



**University of
Leicester**

**A FRONT-TRACKING SOLIDIFICATION
MODEL AND ITS APPLICATION IN
MODELLING ALLOY SOLIDIFICATION**

Thesis submitted for the degree of
Doctor of Philosophy
at the University of Leicester

by

Guanyu Yi

Department of Engineering

University of Leicester

July 2010

Abstract

A front-tracking solidification model has been developed to simulate the dendritic structure evolution during alloy solidification. In the model the growth of dendrites is governed by heat and mass transport and a finite difference technique is employed to solve heat and solute diffusion during solidification. The model incorporates front-tracking technique to calculate and track the exact position of the Solid/Liquid (S/L) interface as a part of solution process and a new capture rule was designed and implemented in the model to efficiently track the growing S/L interface.

The model has been evaluated and verified using simulated data from Al-Cu 4 wt. % alloy solidification. The effect of curvature undercooling on crystal growth was investigated. The simulated results reveal that solute redistribution, curvature of the S/L interface and anisotropy of interface tension are important factors in determining the dendritic morphology. The calculation of the S/L interface curvature and anisotropy of surface tension was found to be particularly important in determining the dendritic growth direction. Based on the above observations and simulated data, the parameters in the developed model have been optimised for predicting the solidification structure in binary alloys.

Simulations of Al-Cu alloy solidification were then performed using the optimised model for single-grain and multi-grain solidification. The simulated results of single-grain growth were compared with the results from the Lipton-Glicksman-Kurz (LGK) model (Lipton *et al.* 1984). Solute profile ahead of the S/L interface was examined using different techniques for approximating solute profile in the growing cell. The solidification segregation in the multi-grain growth was investigated; and the dendritic evolution and solute interaction during multi-grain growth were investigated.

Acknowledgments

I would like to thank the Overseas Research Students Awards Scheme (ORSAS), Rolls-Royce Plc and the Department of Engineering for financial support throughout the program, and the University of Leicester's Centre for Mathematical Modelling (MMC) for the provision of high performance computing facilities.

I would like to express my sincere gratitude to my supervisor, Dr. Hongbiao Dong for his supervision, continuous help and encouragement during this work. Grateful acknowledgement is also made to Prof. Helen Atkinson for her kind assistance, continuous help and supervision. Their painstaking guidance on my PhD study is beneficial not only for my PhD study but also for my future career development. Their help and motivation has certainly provided a huge contribution towards the completion of a successful project.

I also thank Dr. Simon Gill of the Engineering Department for his invaluable and inspiring advices on developing the model. Special appreciation would like to be given to Dr. Neil D' Souza from Rolls-Royce Plc for giving me constructive suggestions. Many thanks to Dr. Wenguang Jiang and Prof. Jinzhe Pan of the Engineering Department for giving me precious advices on process modelling.

I would like to express my appreciation to all the members of the Mechanics of Materials (MOM) Group and the rest of the Department of Engineering who have given me all kinds of help and provided a good environment for study. Special appreciation

would like to be expressed to Yu Xie to give me a lot of help and priceless suggestions on my thesis. All the technicians involving in this project are appreciated for their continued assistance.

Finally, I would like to express my deepest appreciation and warmest regards to my dear parents for their love and their encouragement support in undertaking this project.

Table of Contents

ABSTRACT.....	I
ACKNOWLEDGMENTS	II
TABLE OF CONTENTS.....	IV
LIST OF FIGURES.....	VII
LIST OF TABLES	X
LIST OF PUBLICATIONS	XI
CHAPTER 1 INTRODUCTION.....	1
CHAPTER 2 LITERATURE REVIEW---SOLIDIFICATION THEORY	4
2.1 NUCLEATION	5
2.1.1 Homogeneous Nucleation	6
2.1.2 Heterogeneous Nucleation	9
2.2 KINETICS OF GRAIN GROWTH	10
2.2.1 Diffusion	11
2.2.2 Solute Redistribution	13
2.3 DENDRITIC GROWTH.....	19
2.3.1 Planar Interface Stability.....	20
2.3.2 Formation of Dendrites	22
CHAPTER 3 LITERATURE REVIEW---MODELLING THEORY	24
3.1 NUCLEATION MODELS.....	27
3.2 ANALYTICAL METHOD	29
3.3 CELLULAR AUTOMATA METHOD.....	30
3.4 PHASE-FIELD METHOD	31
3.4.1 The Development of Phase-field.....	32
3.4.2 Derivation of Phase-field Method.....	33
3.5 FRONT-TRACKING-TYPE METHODS	36
3.5.1 Fundamentals of Front-Tracking-Type Methods	37
3.5.2 Front-Tracking Method for Solidification	40
3.5.3 Extended Application of Front-Tracking Model.....	51

3.6 SUMMARY	51
CHAPTER 4 MODEL DESCRIPTION	53
4.1 GOVERNING EQUATIONS	53
4.2 MODEL DESCRIPTION	57
4.2.1 Tracking of the S/L Interface	57
4.2.2 Capture Rules	58
4.3 NUMERICAL TREATMENT	62
4.3.1 System Initialization	63
4.3.2 Main Calculation	63
4.3.3 Grain Growth Calculation	64
4.3.4 Simulation Program	69
CHAPTER 5 MODEL EVALUATION	71
5.1 MODEL ANALYSIS	72
5.1.1 The Movement of S/L Interface	73
5.1.2 Interface Cells Concentration Change with S/L Interface Movement	74
5.1.2.1 Without Curvature Undercooling	75
5.1.2.2 With Curvature Undercooling	75
5.2 EFFECT OF THERMAL UNDERCOOLING AND CURVATURE UNDERCOOLING	78
5.2.1 Dendritic Growth under a Thermal Undercooling of 2K	78
5.2.2 Dendritic Growth under a Thermal Undercooling of 3K	80
5.3 EFFECT OF C_l APPROXIMATION IN A GROWING CELL	84
5.4 EFFECT OF CAPTURE RULE $L\phi$	86
5.5 EFFECT OF OTHER PARAMETERS WITH APPLYING $1.01 * L\phi$	89
CHAPTER 6 MODEL VERIFICATION	96
6.1 EFFECT OF ACCURACY OF INTERFACIAL CURVATURE CALCULATION ON GRAIN GROWTH	97
6.1.1 Interfacial Curvature Solved with Method 1	98
6.1.1.1 Two Layers of Neighbouring Cells Counted with 500×500 Domain	98
6.1.1.2 Two Layers of Neighbouring Cells Counted with 100×100 Domain	100
6.1.2 Interfacial Curvature Solved with Method 2	102
6.1.2.1 Method 2 with 500×500 Domain	102
6.1.2.2 Method 2 with 100×100 Domain	103
6.2 EFFECT OF PARAMETERS IN SOLVING CURVATURE UNDERCOOLING	105
6.2.1 Effect of Anisotropy Degree on Calculation of Interfacial Curvature with Method 1	105
6.2.2 Effect of Anisotropy Degree on Calculation of Interfacial Curvature with Method 2	108
6.3 EFFECT OF ANISOTROPY DEGREE ON MULTI GRAIN GROWTH	112

6.4 MESH SIZE AND TIME STEP DEPENDENCY.....	113
6.4.1 Effect of Mesh Size	114
6.4.2 Effect of Time Step.....	114
6.5 EFFECT OF CURVATURE UNDERCOOLING ON SOLUTE PROFILE AHEAD OF S/L INTERFACE	115
6.6 SIMULATION OF DENDRITE INTERACTIONS	116
CHAPTER 7 SIMULATION OF MICROSTRUCTURE EVOLUTION DURING ALLOY SOLIDIFICATION	119
7.1 SIMULATION OF SINGLE DENDRITIC GROWTH	119
7.1.1 Single Dendritic Growth.....	120
7.1.2 Single Dendritic Morphologies and Composition Fields	122
7.1.3 Solute Profile ahead of Dendritic Tip	124
7.1.4 Comparison of Tip Velocity with the LGK Model	126
7.2 EFFECT OF SOLUTE CONCENTRATION APPROXIMATION IN THE INTERFACE CELLS ON CRYSTAL GROWTH.....	128
7.2.1 Methods for approximating the average concentration of liquid phase in a growing cell ...	129
7.2.2 Simulated Results using Different Approximations	130
7.3 SIMULATION OF EQUIAXED MULTI GRAIN GROWTH	131
7.3.1 Equiaxed Multi Grain Growth.....	132
7.3.2 Solute Interaction	133
7.4 SOLIDIFICATION SEGREGATION	136
7.4.1 Microsegregation during Equiaxed Multi-grain Growth	136
7.4.2 Comparison with the Scheil Model and Lever Rule.....	140
7.4.3 Effect of Different Solid Seed Number and Cooling Rate on Segregation.....	142
7.4.4 Effect of Latent Heat on Segregation	143
7.5 SUMMARY	145
CHAPTER 8 CONCLUSIONS AND FUTURE WORK	147
8.1 CONCLUSIONS	147
8.1.1 Model Development	147
8.1.2 Simulation using the Developed Model.....	148
8.1.2.1 Single-grain Growth	148
8.1.2.2 Multi-grain Growth	149
8.2 FUTURE WORK	149
APPENDIX A. PHASE-FIELD MODELLING OF SOLIDIFICATION	150
APPENDIX B. BASIC MODEL EVALUATION	170
APPENDIX C. MATERIALS AND PROCESS DATA MANAGEMENT PROGRAM.....	197
REFERENCE	202

List of Figures

FIGURE 2.1 UNDERCOOLING DURING SOLIDIFICATION	7
FIGURE 2.2 FREE ENERGY AS A FUNCTION OF THE RADIUS OF NEW PHASE SHAPE.	9
FIGURE 2.3 SCHEMATIC OF HETEROGENEOUS NUCLEATION	10
FIGURE 2.4 A BINARY PHASE DIAGRAM WITH A LIQUID AND A PRIMARY SOLID	13
FIGURE 2.5 SEGREGATION WITH COMPLETE LIQUID MIXING AND SOME SOLID	16
FIGURE 2.6 SEGREGATION CURVES DURING SOLIDIFICATION	19
FIGURE 2.7 TYPICAL DENDRITIC GROWTH MORPHOLOGY IN AN ORGANIC SYSTEM.....	20
FIGURE 2.8 SCHEMATIC DIAGRAM SHOWING THE EQUIAXED AND COLUMNAR GRAIN STRUCTURE	23
FIGURE 3.1 PHASE-FIELD SIMULATION OF SOLIDIFICATION IN PURE METAL.....	36
FIGURE 3.2 SIMULATED DENDRITIC MORPHOLOGY OF AN ALLOY.....	45
FIGURE 3.3 CAPTURING RULES FOR NEW INTERFACE CELLS	48
FIGURE 3.4 SIMULATED EQUIAXED DENDRITE EVOLUTION OF AN AL-10WT.% CU ALLOY	50
FIGURE 3.5 SIMULATED COLUMNAR DENDRITE EVOLUTION OF AN AL-4WT.% CU ALLOY	50
FIGURE 4.1 ILLUSTRATION OF DETERMINING THE SHARP S/L INTERFACE POSITION	58
FIGURE 4.2 CASES OF NEIGHBOURING CELLS.....	59
FIGURE 4.3 CAPTURE RULES FOR NEW INTERFACE CELLS.....	61
FIGURE 4.4 FLOW CHART OF THE MODEL	62
FIGURE 4.5 DEFINITION OF GRAIN SEED	63
FIGURE 4.6 FLOW CHART OF CAPTURE RULES.....	65
FIGURE 4.7 NUMERICAL TREATMENT OF NEIGHBOURING CELLS	66
FIGURE 4.8 CALCULATION OF S/L INTERFACE POSITION	68
FIGURE 4.9 FLOW CHART OF PROGRAM FOR FRONT-TRACKING MODEL	70
FIGURE 5.1 A BINARY PHASE DIAGRAM WITH A LIQUID AND A PRIMARY SOLID	72
FIGURE 5.2 CONCENTRATION IN LIQUID OF INTERFACE CELLS AND SOLUTE DIFFUSION	76
FIGURE 5.3 SOLUTE PROFILE ALONG DENDRITIC ARM.....	80
FIGURE 5.4 LATE STAGES OF GRAIN GROWTH.....	80
FIGURE 5.5 SOLUTE PROFILE ALONG DENDRITIC ARM.....	82
FIGURE 5.6 LATE STAGES OF GRAIN GROWTH.....	83
FIGURE 5.7 COMPARISON WITH USING L_φ AND $1.01 * L_\varphi$	87
FIGURE 5.8 SYSTEM STATUS WHEN GRAIN STOPS GROWING.....	88
FIGURE 5.9 SIMULATED GRAIN GROWTH.....	91

FIGURE 5.10 SIMULATED GRAIN GROWTH WITH $\theta=20^\circ$	92
FIGURE 5.11 SIMULATED GRAIN GROWTH WITH BOTH ANISOTROPY OF SURFACE TENSION AND S/L INTERFACE CURVATURE	93
FIGURE 5.12 STATUS DURING GRAIN GROWTH.....	94
FIGURE 5.13 SIMULATED DENDRITIC GROWTH	95
FIGURE 6.1 SOLUTE PROFILE ALONG DENDRITIC ARM OF CASE 1	99
FIGURE 6.2 SOLUTE PROFILES ALONG DENDRITIC ARM OF CASE 2 AND CASE 3	100
FIGURE 6.3 SOLUTE PROFILES ALONG DENDRITIC ARM OF CASE 2 AND CASE 3	102
FIGURE 6.4 SIMULATION OF TWO GRAINS GROWTH	112
FIGURE 6.5 SIMULATION OF THREE GRAINS GROWTH	113
FIGURE 6.6 STEADY STATE TIP VELOCITY AS A FUNCTION OF MESH SIZE.....	114
FIGURE 6.7 STEADY STATE TIP VELOCITY AS A FUNCTION OF TIME STEP.....	115
FIGURE 6.8 EFFECT OF CURVATURE UNDERCOOLING.....	116
FIGURE 6.9 SIMULATION OF DENDRITE INTERACTION WITH DIFFERENT PACKING OF SEEDS.....	117
FIGURE 6.10 DENDRITE INTERACTIONS AT DIFFERENT SYSTEM TEMPERATURES T_i	118
FIGURE 7.1 SIMULATED SINGLE DENDRITE EVOLUTION.....	121
FIGURE 7.2 TIP VELOCITY EVOLUTION AT EARLY STAGES (FROM 0 SECOND TO 0.08 SECONDS) OF SOLIDIFICATION AT CONSTANT MELT UNDERCOOLINGS	122
FIGURE 7.3 SIMULATED SINGLE DENDRITE EVOLUTION OF AN AL-4WT. %CU ALLOY.....	123
FIGURE 7.4 STEADY-STATE SOLUTE PROFILES ALONG THE DENDRITE ARMS	125
FIGURE 7.5 STEADY-STATE SOLUTE PROFILES AHEAD OF DENDRITIC TIP AT DIFFERENT UNDERCOOLINGS.....	126
FIGURE 7.6 COMPARISON OF THE STEADY-STATE TIP VELOCITY AT DIFFERENT MELT UNDERCOOLINGS BETWEEN PRESENT MODEL AND LGK MODEL PREDICTIONS.....	127
FIGURE 7.7 APPROXIMATIONS OF SOLUTE CONCENTRATION IN THE INTERFACE CELL.....	128
FIGURE 7.8 CALCULATED AVERAGED SOLUTE CONCENTRATION USING DIFFERENT APPROXIMATIONS	131
FIGURE 7.9 SIMULATED EQUIAXED DENDRITE EVOLUTION OF AN AL-4WT. %CU ALLOY	133
FIGURE 7.10 SIMULATED EQUIAXED DENDRITE EVOLUTION OF AN AL-4WT. %CU ALLOY	135
FIGURE 7.11 SIMULATED DENDRITE GROWTH	137
FIGURE 7.12 THE SOLUTE PROFILE ACROSS THE SIMULATED DOMAIN.....	138
FIGURE 7.13 COMPARISON OF THE PRESENT MODEL WITH THE SCHEIL MODEL AND LEVER RULE FOR PREDICTING THE CU CONCENTRATION IN THE LIQUID AT THE S/L INTERFACE AS A FUNCTION OF SOLID FRACTION.....	141
FIGURE 7.14 COMPARISON OF THE PRESENT MODEL WITH THE SCHEIL MODEL AND LEVER RULE FOR PREDICTING THE CU CONCENTRATION IN DENDRITES AS A FUNCTION OF SOLID FRACTION.....	142
FIGURE 7.15 SIMULATED CU CONCENTRATION IN DENDRITES AS A FUNCTION OF SOLID FRACTION.....	143
FIGURE 7.16 SIMULATED CU CONCENTRATION IN DENDRITES AS A FUNCTION OF SOLID FRACTION.....	144
FIGURE 7.17 SIMULATED CU CONCENTRATION IN DENDRITES AS A FUNCTION OF SOLID FRACTION AT LATE STAGES OF SOLIDIFICATION.....	145
FIGURE A0.1 FLOW CHART OF PROGRAM FOR PHASE-FIELD MODEL FOR PURE METAL	156

FIGURE A0.2 FLOW CHART OF CALCULATION LOOP	157
FIGURE A0.3 SIMULATED DENDRITIC STRUCTURE EVOLUTION FOR A PURE METAL	159
FIGURE A0.4 FLOW CHART OF PROGRAM FOR PHASE-FIELD MODEL FOR BINARY ALLOYS	168
FIGURE B0.1 DISTRIBUTION OF SOLID FRACTION	173
FIGURE B0.2 TECHNIQUE FOR CALCULATION OF SOLUTE DIFFUSION	178
FIGURE B0.3 SOLUTE DISTRIBUTION	181
FIGURE B0.4 SCHEME OF DIRECTION CONTROL	182
FIGURE B0.5 SOLUTE DISTRIBUTION WITHOUT Nf	184
FIGURE B0.6 SOLUTE DISTRIBUTION WITH A BIGGER SEED	187
FIGURE B0.7 DISTRIBUTION OF SOLID FRACTION	189
FIGURE B0.8 DISTRIBUTION OF SOLID FRACTION	190
FIGURE B0.9 POSITION OF S/L INTERFACE	192
FIGURE B0.10 EARLY STAGES OF GRAIN GROWTH.....	195
FIGURE C0.1 PROGRAM INTERFACES	198
FIGURE C0.2 INTERFACE FOR INPUTTING CHANGEABLE PARAMETERS.....	199
FIGURE C0.3 MODIFY DATA INTERFACE	200
FIGURE C0.4 DATABASE STRUCTURE.....	201

List of Tables

TABLE 3.1 METHODS FOR SOLIDIFICATION MODELLING.....	26
TABLE 5.1 INVESTIGATION OF GRAIN GROWTH WITH DIFFERENT PREFERENTIAL DIRECTIONS	79
TABLE 5.2 INVESTIGATION OF GRAIN GROWTH WITH DIFFERENT PREFERENTIAL DIRECTIONS	81
TABLE 5.3 PREDICTED CRYSTAL MORPHOLOGIES USING DIFFERENT APPROXIMATION OF C_t	85
TABLE 5.4 INVESTIGATION OF GRAIN GROWTH WITH DIFFERENT PREFERENTIAL DIRECTIONS	89
TABLE 6.1 INVESTIGATION OF GRAIN GROWTH.....	99
TABLE 6.2 INVESTIGATION OF GRAIN GROWTH.....	101
TABLE 6.3 INVESTIGATION OF GRAIN GROWTH.....	103
TABLE 6.4 INVESTIGATION OF GRAIN GROWTH.....	104
TABLE 6.5 INVESTIGATION OF GRAIN GROWTH WITH $\Delta=0.4$	106
TABLE 6.6 INVESTIGATION OF GRAIN GROWTH WITH $\Delta=0.8$	107
TABLE 6.7 INVESTIGATION OF GRAIN GROWTH WITH $\Delta=1.6$	108
TABLE 6.8 INVESTIGATION OF GRAIN GROWTH WITH $\Delta=0.4$	109
TABLE 6.9 INVESTIGATION OF GRAIN GROWTH $\Delta=0.8$	110
TABLE 6.10 INVESTIGATION OF GRAIN GROWTH WITH $\Delta=1.6$	111
TABLE A0.1 MATERIAL PROPERTIES.....	155
TABLE B0.1 INVESTIGATION OF EFFECT OF INTERFACIAL ENERGY PARAMETERS ON GRAIN GROWTH WITH UNDERCOOLING OF 3K	172
TABLE B0.2 INVESTIGATION OF EFFECT OF PARAMETERS IN CAPTURE RULES ON GRAIN GROWTH	174
TABLE B0.3 INVESTIGATION OF EFFECT OF INTERFACIAL CURVATURE ON GRAIN GROWTH WITH UNDERCOOLING OF 3K	175
TABLE B0.4 INVESTIGATION OF EFFECT OF INTERFACIAL ENERGY PARAMETERS ON GRAIN GROWTH.....	180
TABLE B0.5 INVESTIGATION OF EFFECT OF PARAMETERS ηF ON GRAIN GROWTH	185
TABLE B0.6 INVESTIGATION OF GRAIN GROWTH WITH FIXED L_ϕ	193
TABLE B0.7 INVESTIGATION OF GRAIN GROWTH WITH FIXED L_ϕ	194

List of Publications

G.Y. Yi, H.B. Dong, H.A. Atkinson and N. D'souza, "*A Front-Tracking Model for Modelling of Solidification Microstructures in Binary Alloys*", 1st draft ready for journal

G.Y. Yi, H.B. Dong and H.A. Atkinson, "*The Effect of Anisotropy on Solidification Structure Evolution in Front-Tracking Model*", 1st draft ready for journal

G.Y. Yi, H.B. Dong, H.A. Atkinson and N. D'souza, "*A Front-Tracking Model for Modelling of Solidification Microstructures in Binary Alloys*", EUROMAT 2009, Glasgow, UK, 7-10, Sep, 2009(Poster presentation)

G.Y. Yi, H.B. Dong, N. D'Souza and H.V. Atkinson, "*High Efficiency Front-Tracking Modelling of Competitive Crystal Growth during Binary Alloys Solidification*", Second International Conference on Advances in Solidification Processes(ICASP-2), Graz, Austria, 17-20 Jun, 2008(Oral presentation)

G.Y. Yi, and H.B. Dong, "*Front-Tracking Modelling of Competitive Crystal Growth during Alloy Solidification*", 4th Chinese International Conference on Materials, Chongqing, China, 12-16 Oct, 2007(oral presentation)

Chapter 1 Introduction

Microstructures are at the centre of materials science and engineering. It is well known that materials microstructure, including size and shape, spatial arrangement of local structural features, spatially distributed phases of different compositions, spatially distributed phases of crystal structures, *etc.* plays a critical role in determining the mechanical and physical properties. Therefore, microstructure control is essential for any processing activity (Kurz & Fisher 1989). Solidification, which is generally accompanied by the formation of crystals, is one of the most important processing routes for many materials, especially metals and alloys (Kurz & Esaka 1988). During the last few decades, important advances have been made in our fundamental understanding of solidification microstructures (Boettinger *et al.* 2000). On the other hand, with the development of very powerful computers, computer simulations are becoming increasingly used for the modelling of microstructure formation and associated characteristics or defects. Over recent years, with advanced numerical methods and better understanding of the physical phenomena involved in solidification, numerical simulation has emerged as one of the most powerful and efficient methods for studying many types of microstructure evolution processes (Boettinger *et al.* 2000).

The work described in this thesis is on modelling of the microstructure evolution during solidification. A front-tracking model for solidification microstructure evolution has been developed. Using the developed model, the microstructure evolution during alloy solidification was investigated.

In the thesis, reviews of the relevant literature on solidification theory and modelling theory are presented in Chapter 2 and Chapter 3, separately. The background of the project and recent developments in solidification theory are described in Chapter 2. Simulation techniques for solidification and their recent developments are summarised in Chapter 3.

Chapter 4 describes the developed front-tracking solidification model. In the developed model, solidification structure evolution is controlled mainly by mass and heat transport; techniques for tracking the Solid/Liquid (S/L) interface were employed. In this chapter, the numerical treatment used in the model is also presented.

In Chapter 5, model evaluation is presented. The effect of anisotropy of the S/L interfacial energy on solidification structure evolution was examined. Curvature undercooling was included and effects of curvature undercooling on the dendritic morphology development were reported.

Chapter 6 presents the verification of the developed model. Firstly, effects of accuracy of S/L interface curvature calculation on dendritic morphology are presented. Then the effect of interface curvature and anisotropy of surface tension on dendritic growth was analysed. Mesh independency and time step independency in multi-grain growth are described.

Chapter 7 describes simulated results on microstructure evolution during solidification of single-grain and multi-grain growth. Results for single-grain solidification fit well with the results from the Lipton-Glicksman-Kurz (LGK) model (Lipton *et al.* 1984). For the multi-grain growth simulation, solute interaction in multi-grain growth was analysed and solidification segregation was investigated.

Conclusions of this study are drawn in Chapter 8, followed by recommendations for future work.

Chapter 2 Literature Review---

Solidification Theory

The work described in this thesis is about the modelling of microstructure evolution during solidification. To develop such a model, it is essential to understand the microstructure evolution during the process of solidification. Microstructures are at the centre of materials science and engineering. Materials microstructure, including size, shape, spatial arrangement of local structural features, and spatial distribution of phases of different compositions, plays a critical role in determining materials properties. Solidification is one of the most important processing routes to engineer microstructures for many materials, especially for metals and alloys (Kurz & Esaka 1988). In order to better understand the microstructure evolution during solidification process, it is necessary to grasp the basic theory of solidification. It is essential to understand the associated underlying physical principles. The objective in this chapter is to give a literature review of solidification theory, which has been a topic studied by many scientists for years (Boettinger *et al.* 2000). This chapter will focus on the fundamental solidification theory, with particular attention given to dendritic growth.

Solidification is a phase-transformation process in which liquid phase changes into one or several solid phases. Solidification starts with grain nucleation and continues with solid growth. It is well known that solidification is one of the most important processing

routes for many materials, even if the only acquaintance with it involves the making of ice cubes. The manufacture of almost every man-made object involves solidification at some stage. Where the most widely-used group of materials, metallic alloys, are concerned, it is generally accompanied by the formation of crystals.

Solidification is of significant importance. Casting, one of the major practical applications of solidification, is a very economic method of forming a component if the melting point of the metal is not too high. If the properties of castings were easy to control, then solidification would be an even more important process. As a materials solidification microstructure plays a critical role in determining the properties, microstructure control is essential for this processing. In this respect, solidification theory plays a vital role since it forms the basis for influencing the microstructure and hence improving the quality of cast products. Over the past years, important advances have been made in fundamental understanding of solidification microstructures (Boettinger *et al.* 2000). This chapter will outline the fundamental theory of solidification, with main interest placed on the evolution of microstructures during solidification process.

2.1 Nucleation

When a solid is growing into a liquid, the solid phase has to first nucleate followed by subsequent growth. There are three possible mechanisms for nucleation: 1) homogeneous nucleation, 2) heterogeneous nucleation and 3) growth from existing substrates such as gas pockets or metastable particles.

2.1.1 Homogeneous Nucleation

The classical homogeneous nucleation model is developed by calculating a critical degree of deviation from equilibrium required for nucleation. The balance of free energy due to formation of a particle of the new phase is determined. The energy balance is formed by taking into account the decrease in free energy due to the formation of a certain volume of the new phase, and the increase due to the formation of the surface of that phase. In the simplest case, the particle is assumed to be a sphere of radius r . The energy balance is derived by summing the interface and volume terms, which can be given as (Kurz & Esaka 1988):

$$\Delta G = \Delta G_l + \Delta G_v = 4\sigma\pi r^2 + \frac{4}{3}\Delta g\pi r^3 \quad (2.1)$$

where $\Delta G_l = 4\sigma\pi r^2$ is the interface term and $\Delta G_v = \frac{4}{3}\Delta g\pi r^3$ is the volume term. σ is the L/S interfacial energy, r is the radius of a nucleus and Δg is the Gibbs free energy difference between the liquid and solid per unit volume, which is proportional to undercooling ΔT :

$$\Delta g = \Delta s_f \cdot \Delta T \quad (2.2)$$

where Δs_f is the difference in slope of Gibbs free energy-Temperature function of two phases and ΔT is undercooling.

The undercooling ΔT is the sum of solute undercooling, kinetic undercooling, curvature undercooling and thermal undercooling. It can be written as:

$$\Delta T = \Delta T_C + \Delta T_K + \Delta T_R + \Delta T_t \quad (2.3)$$

where ΔT_C is solute undercooling, which arises when the material is not pure, ΔT_K is the kinetic undercooling, ΔT_R is curvature undercooling, which occurs when the interface between the solid and the liquid is curved, and ΔT_t is thermal undercooling, see Figure 2.1 (Kurz & Fisher 1989).

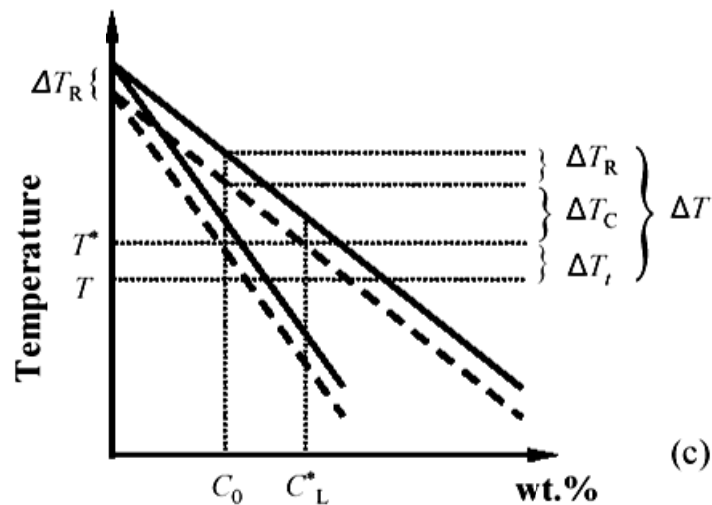


Figure 2.1 Undercooling during solidification

Solute undercooling happens when the material is not pure. During the solidification of alloys, because of the difference of solubility in liquid and solid, the solute is rejected into the liquid at the S/L interface. The diffusion processes are driven by solute gradient in the liquid. Via the equilibrium phase diagram, the difference of solute concentration can be converted into a temperature difference, which is:

$$\Delta T_C = m_l(C_0 - C_l^*) \quad (2.4)$$

where m_l is the liquidus slope, C_0 is the solute concentration in bulk liquid and C_l^* is the concentration in liquid side at the interface.

Curvature undercooling occurs when the interface between the solid and the liquid is curved. The amount of this undercooling can be obtained from the Gibbs-Thomson equation. Usually, it can be given by:

$$\Delta T_R = \Gamma K \quad (2.5)$$

where Γ is the Gibbs-Thomson coefficient and K is the surface curvature.

Thermal undercooling ΔT_t , which is associated with the release of the latent heat, assumes particular significance in pure metal, where constitutional undercooling ΔT_C is absent. The kinetic undercooling reflects the ease by which the atoms from the liquid state can be transformed to the solid state during solidification. In metals, which are characterised by low entropy of fusion, this undercooling is practically absent.

For homogeneous nucleation, if a nucleus is stable, it has to exceed a critical radius, r^0 , as shown in Figure 2.2 (Kurz & Esaka 1988), above which a nucleus will be unstable and may grow. From Eq. 2.1, we can see that the right-hand side is composed of a quadratic and a cubic term. The value of Δg depends on ΔT , and is negative if ΔT is positive, whereas σ is always positive. When the melt is undercooled, this behaviour leads to the occurrence of a maximum in the value of ΔG , which can be given by:

$$\frac{d(\Delta G)}{dr} = 0 \quad (2.6)$$

From Eqs. 2.1 and 2.6, we then obtain the critical radius as:

$$r^0 = \frac{-2\sigma}{\Delta g} \quad (2.7)$$

The occurrence of homogeneous nucleation is limited to very restricted situations and often requires a high degree of undercooling (Turnbull & Cech 1950).

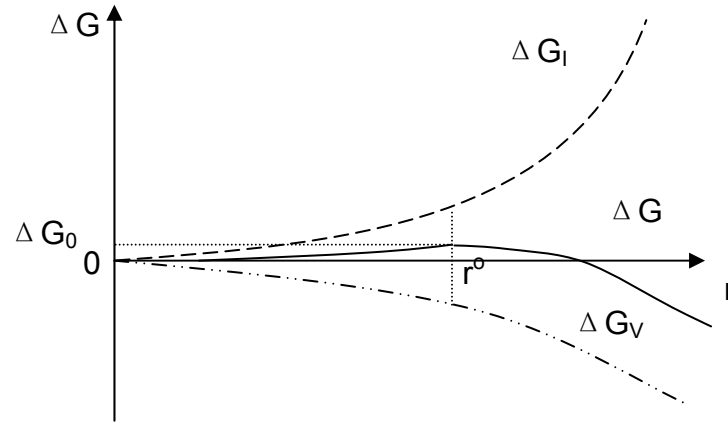


Figure 2.2 Free energy as a function of the radius of new phase shape.

2.1.2 Heterogeneous Nucleation

For heterogeneous nucleation, when the melt contains nucleation agents, e.g. solid particles, crystalline crucible or oxide layer, nucleation may be facilitated if the number of atoms or activation energy required for nucleation, are decreased. Nucleation can be greatly facilitated, as shown in Figure 2.3 (Kurz & Fisher 1989), when the S/L interface of the crystal, A_{LC} , is partly replaced by an area of low-energy S/L interface between the crystal and a foreign solid, A_{CS} .

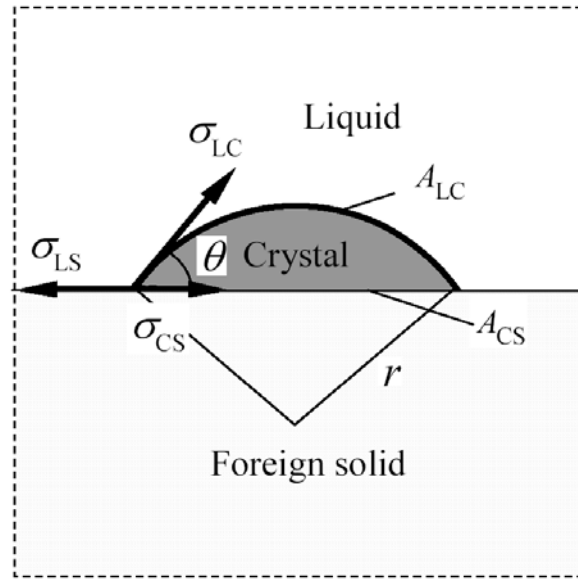


Figure 2.3 Schematic of heterogeneous nucleation

The magnitude of the effect can be calculated by (Kurz & Esaka 1988):

$$f(\theta) = \frac{(2 + \cos\theta)(1 - \cos\theta)^2}{4} \quad (2.8)$$

where θ is the wetting angle between a growing spherical cap of nucleus and particle or mould wall, as shown in Figure 2.3. So the energy required to grow a stable crystal, ΔG_{het} , is

$$\Delta G_{het} = \Delta G \cdot f(\theta) \quad (2.9)$$

2.2 Kinetics of Grain Growth

Following nucleation in undercooled melts, grain growth occurs. Growth kinetics will dominate the solidification processes after nucleation. As dendrite is the typical solidification structure for alloys, with emphasis laid on the principles of dendritic growth, this section gives an instruction of principles of growth kinetics.

2.2.1 Diffusion

Once a nucleus is formed, it will normally continue to grow. Such growth will be limited by the kinetics of atom attachment to the S/L interface, capillarity and especially diffusion of heat and mass. Without considering convection, the transformation from liquid to solid is a diffusion-controlled process. The diffusion of heat and mass are given by the following equations:

a) For solute diffusion:

$$\frac{\partial C}{\partial t} = \nabla(D\nabla C) \quad (2.10)$$

where t is the time, D is the solute diffusion coefficient and C is concentration in solid or liquid.

b) For heat transfer:

$$\frac{\partial T}{\partial t} = \nabla(\alpha\nabla T) \quad (2.11)$$

where T is temperature. The thermal diffusivity, α , can be given by:

$$\alpha = \frac{\kappa}{\rho \cdot C_p} \quad (2.12)$$

where κ is the thermal conductivity, ρ is density and C_p is the specific heat per unit mass.

The solute diffusion in liquid is about two to three magnitude orders faster than that in solid. To solve the solute diffusion in both solid and liquid during solidification, we can apply Eq. 2.10 in both phases:

$$\frac{\partial C_l}{\partial t} = \nabla(D_l \nabla C_l) \quad (2.13)$$

$$\frac{\partial C_s}{\partial t} = \nabla(D_s \nabla C_s) \quad (2.14)$$

where C_l and C_s are the concentrations in liquid and solid phases, and D_l and D_s are the solute diffusion coefficients in the two phases, respectively.

In addition, boundary conditions must be satisfied for both heat and solute diffusion, at the S/L interface.

For heat:

$$\Delta h_f V_n = \alpha_{solid} \left. \frac{\partial T}{\partial \mathbf{n}} \right|_{solid} - \alpha_{liquid} \left. \frac{\partial T}{\partial \mathbf{n}} \right|_{liquid} \quad (2.15)$$

where \mathbf{l} is a vector normal to the interface, Δh_f is the latent heat of fusion, V_n is the growth rate of the interface and α is the thermal diffusivity.

For solute, according to the local thermodynamic equilibrium at S/L interface, as shown in Figure 2.4:

$$C_s^* = k \cdot C_l^* \quad (2.16)$$

where C_0 is the initial composition, C_s^* and C_l^* are the concentrations at solid side and liquid side of the S/L interface respectively, T_l^{eq} is the equilibrium liquidus temperature at the initial composition C_0 , T^* is the interface equilibrium temperature, T_0 is the melting point for pure element and k is the equilibrium partition coefficient.

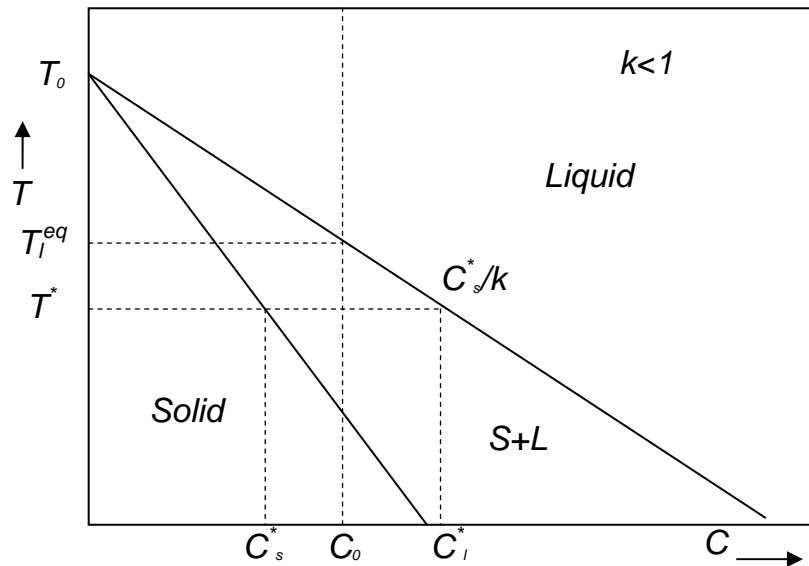


Figure 2.4 A binary phase diagram with a liquid and a primary solid

2.2.2 Solute Redistribution

During the solidification of an alloy, the solute is rejected from solid into liquid at the S/L interface when the solubility of the solute element in the solid is smaller than that in the liquid, when the liquidus slope, m_l , is negative and the distribution coefficient, k , is less than unity. In the other case, when m_l is positive and k is greater than 1, solute will diffuse from the liquid to the solid. In this case, the solubility in the liquid is smaller than that in the solid. The first case will lead to a creation of an enriched zone ahead of the S/L interface, and the latter case to a depleted zone.

As soon as the grain starts growing, local equilibrium is assumed to hold at the S/L interface, where the solid concentration is related to the liquid concentration by the equilibrium distribution coefficient, as Eq. 2.16. This difference between C_s^* and C_l^* always leads to concentration variations in the solidified alloy, which are known as segregation. At the same time, this compositional difference will also lead to solute redistribution. The solute distribution in the liquid ahead of the S/L interface will always lead to the appearance of variations in growth morphologies and will later in turn determine the solute distribution in the solid. Depending on the process involved in the solute redistribution, where the solute can be transported by diffusion or by convection or by both, the segregation pattern will be quite different, as microsegregation, macrosegregation and a mix of both. The macrosegregation is compositional difference over distances equal to the size of a large casting. It is the result of convection, which can lead to mass transport over very large distances. Diffusional process in the solid and liquid, which is solute diffusion related to the dendrite shape and size, will lead to solute transport over small distances and may result in microsegregation, which is compositional difference within a grain, crystal or particle of microscopic size. As convection will not be treated in this thesis, attention will be limited to microsegregation.

The microsegregation reveals the original microstructure of any solidified alloy in regions of locally different composition. Understanding this process is the key to interpreting the influence of solidification on the mechanical properties of cast products.

The segregation that occurs at the scale of the dendrites is always very complicated due to the morphology of these crystals. In order to understand it, it is very useful to start with a description of the solute redistribution during directional solidification of a rod of

constant cross-section with a planar S/L interface. All changes will be easy to analyse as they occur in one dimension. Once this case is fully understood, it will be possible to apply the results to investigate the phenomenon of more complicated cases in a qualitative manner by imagining the changes happening in small volume elements to be the same as those in this case.

In the case of applying a mass balance of equilibrium solidification, it can be reasonably assumed that diffusion in the liquid is sufficiently rapid to avoid the creation of any concentration gradient ahead of the S/L interface, as there are very high diffusion coefficients in the liquid, strong convection, and/or a very small system size, when compared to the diffusion boundary layer thickness, δ_c , as Eqs. 2.17 and 2.18:

$$D_l \gg D_s \gg LV \quad (2.17)$$

$$\delta_c = \frac{2D_l}{V} \gg L \quad (2.18)$$

in which, L is the system size and V is the growth rate of the solid. Considering only the case of diffusion, there will be no concentration gradient existing in condition of Eq.2.18. From the mass balance equation, as Eq.2.19, in which C is expressed as a percentage, the corresponding relationships, Eq.2.20, can be derived.

$$f_s C_s + f_l C_l = 100 \quad (2.19)$$

$$d(f_s C_s) + d(f_l C_l) = 0 \quad (2.20)$$

where f_s is fraction of solid and f_l is fraction of liquid. Applying the condition of $\partial C_l / \partial z = \partial C_s / \partial z \cong 0$ and substituting $C_s = kC_l$, $dC_s = kdC_l$, $f_s = 1 - f_l$ and $df_s = -df_l$, taking

the differential and integral form of Eq.2.20 gives the solution for the lever rule, in which C_0 is the initial composition, as Eq.2.22.

$$\int_{C_0}^{C_l} \frac{dC_l}{(1-k)C_l} = \int_0^{f_s} \frac{df_s}{1-f_s(1-k)} \quad (2.21)$$

$$\frac{C_l}{C_0} = \frac{1}{1-f_s(1-k)} \quad (2.22)$$

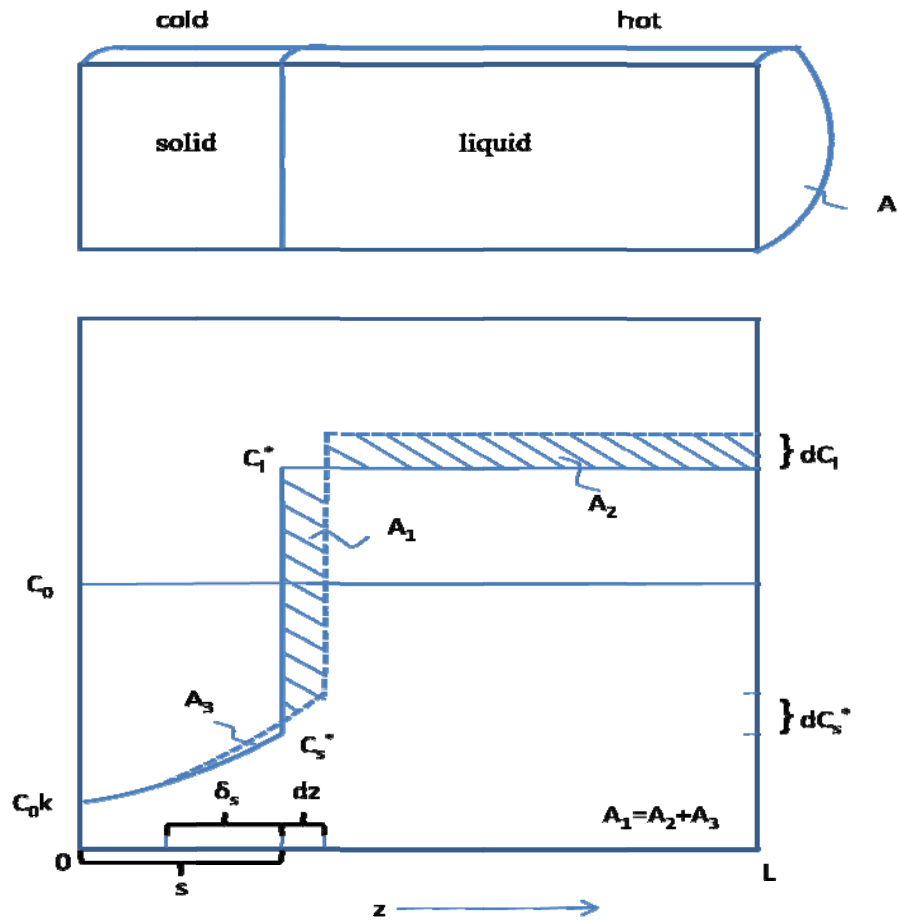


Figure 2.5 Segregation with complete liquid mixing and some solid

In other case, there is solute distribution with back-diffusion in the solid and complete mixing in the liquid, as shown in Figure 2.5. Here, the bar has a constant cross-section, A , and limited diffusion in the solid and a zero concentration gradient in the liquid, due to rapid mass transport in the liquid, where $C_l=C_l^*$. The boundary layer in the solid, δ_s ,

due to back diffusion and accordingly A_3 represents the surface of the equivalent boundary layer in the solid. The diffusion boundary thickness will take a value between zero and infinity depending on the diffusion coefficient in the solid. Brody and Flemings (1966) have developed a flux balance which slightly modified the form of mass balance, $A_1=A_2+A_3$, as Eq.2.23.

$$(C_l - C_s^*)Ads = (L - s)AdC_l + dC_s^*A \frac{\delta_s}{2} \quad (2.23)$$

With the relative interface position as shown in Figure 2.5, it can be recognised that $s/L=f_s=1-f_l$, $\delta_c=2D_s/V$. So, it can be found that $df_s=ds/L$, $\delta_c=2D_s dt/ds$. Also as $C_l=C_l^*$, Eq.2.16 can be rewritten as $C_s^*=kC_l$, then $dC_s^*=k dC_l$. Substituting these equations into Eq.2.23 leads to Eq.2.24.

$$C_l(1 - k)df_sL = L(1 - f_s)dC_l + dC_l k D_s \frac{dt}{ds} \quad (2.24)$$

Assuming that the interface position, s , is a parabolic function of time and dividing by L gives a parabolic growth rate relationship:

$$\frac{s}{L} = f_s = \left(\frac{t}{t_f} \right)^{1/2} \quad (2.25)$$

where, t is time and t_f is the local solidification time. With evaluating ds/dt and substituting the above results, Eq.2.24 can be rearranged to:

$$\frac{dC_l}{(1-k)C_l} = \frac{df_s}{(1-f_s)+2akf_s} \quad (2.26)$$

where, a is dimensionless solid-state back-diffusion parameter(Fourier number), defined as:

$$a = \frac{D_s t_f}{L^2} \quad (2.27)$$

and :

$$\frac{1}{1-k} \int_{C_0}^{C_l} \frac{dC_l}{C_l} = \int_0^{f_s} \frac{df_s}{1-f_s(1-2ak)} \quad (2.28)$$

Integrating Eq.2.28 leads to:

$$\frac{C_l}{C_0} = [1 - f_s(1 - 2ak)]^{\frac{k-1}{1-2ak}} . \quad (2.29)$$

Eq.2.29 is limited to k -values which are smaller than unity due to the simplifying assumptions made. This solution includes two limiting cases:

(1) *Lever rule*: when $a=0.5$. Eq.2.29 becomes Eq.2.22.

(2) *Scheil's equation*: when $a=0$, where $D_s=0$ and $D_l=\infty$. Eq.2.29 leads to:

$$\frac{C_l}{C_0} = f_l^{(k-1)} \quad (2.30)$$

As can be seen, according to Eq.2.27, the lever rule case, where $a=0.5$, does not correspond to the physical characteristics of equilibrium solidification, where a should approach infinity, Clyne & Kurz (1981) have proposed a modified back-diffusion parameter, a' , to replace a in Eq.2.29.

$$a' = a \left[1 - \exp\left(-\frac{1}{a}\right) \right] - \frac{1}{2} \exp\left(-\frac{1}{2a}\right) \quad (2.31)$$

According to the definition of a' , at the low a -range, $a' = a$, and at the high a -range, $a' = 0.5$. Substituting a' into Eq.2.29 gives:

$$\frac{C_l}{C_0} = [1 - f_s(1 - 2a'k)]^{\frac{k-1}{1-2a'k}} \quad (2.32)$$

The segregation curves during solidification of Al-4wt.% Cu alloy are illustrated in Figure 2.6, in which, apart from two limited cases, a realistic case of $a' = 0.2$ is also plotted.

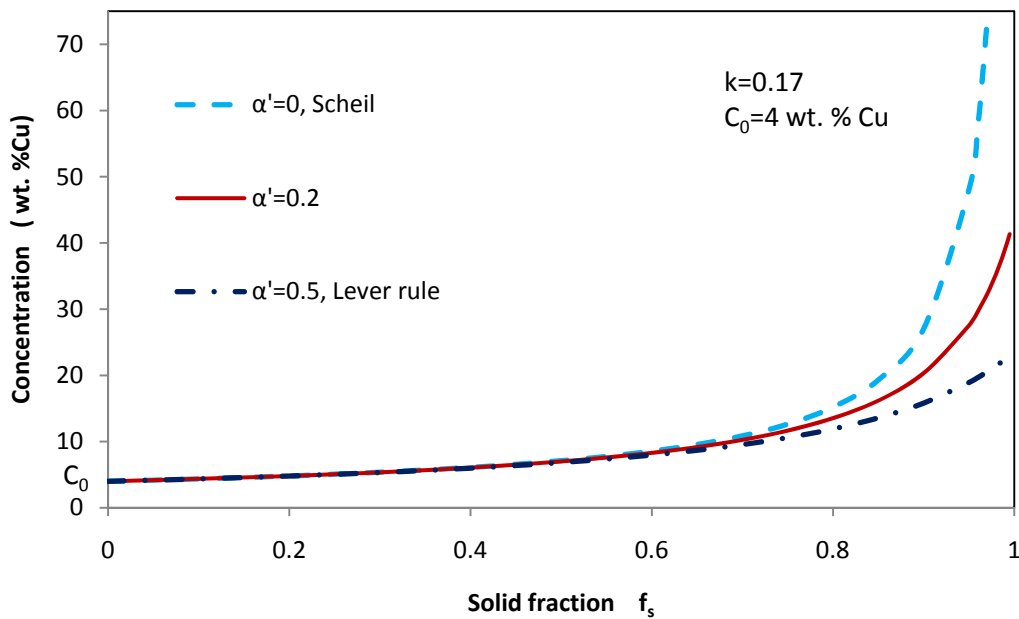


Figure 2.6 Segregation curves during solidification

2.3 Dendritic Growth

Dendrites or cells form once a S/L interface has been broken down. As observed in most metals produced in casting processes (Chilton 2002), the S/L interface is usually broken down from a planar front into a dendritic morphology, as shown in Figure 2.7 (Chilton 2002). This change of interface allows better efficiency in heat extraction through the increased surface area in the dendritic structure.

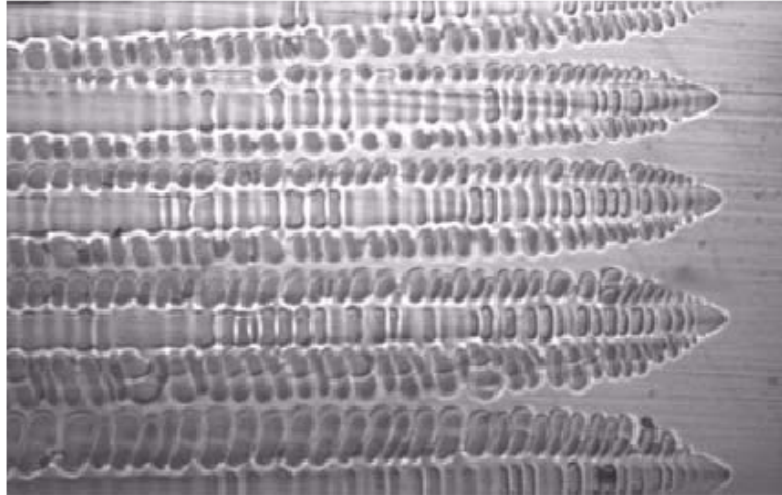


Figure 2.7 Typical dendritic growth morphology in an organic system

2.3.1 Planar Interface Stability

In order to proceed with analyses of growth morphologies, it has been found necessary to understand the stability of the planar interface and the criterion for its break down.

For the case of a pure substance, the conditions which lead to instability can easily be understood. During growth in a pure substance, a stable interface is distinguished from an unstable interface by its response to random disturbances, which are caused by insoluble particles, temperature fluctuations, or grain boundaries. When the temperature gradient is positive, the S/L interface of a pure substance will be stable, in which case the perturbations will be unfavourably situated and tend to disappear. In the case when the temperature gradient is negative, the perturbations will be in a more advantageous situation for the growth and increase in prominence, and therefore the S/L interface becomes unstable.

For alloys, as it is seen from the above that, during the solidification, there is a substantial change in the concentration ahead of the S/L interface which leads to the local equilibrium melting point can vary along the S/L interface, the criterion for stable/unstable behaviour is more complicated. During the solidification of an alloy, when the distribution coefficient is less than unity, solute piles up ahead of the S/L interface due to its smaller solubility in the solid. The excess solute starts to accumulate and finally forms an enriched boundary layer ahead of the S/L interface and constitutional undercooling happens. As the solidification carries on, substantial change in concentration ahead of the interface affects the local equilibrium solidification temperature of the liquid. The local concentration gradient becomes steeper and consequently the local gradient of the liquidus temperature increases. When the liquidus temperature gradient at the S/L interface is greater than the temperature gradient due to the heat flux, a driving force for interface change will be present whenever the slope of the local melting point curve at the interface is greater than the slope of the actual temperature distribution. Therefore, the S/L interface becomes unstable. Considering solute diffusion as well as heat flow effects, the critical conditions for breakdown of a planar interface front can be given as (Flemings 1974):

$$G_l < \frac{m_l C_s V_n (k-1)}{k D_l} \quad (2.33)$$

where G_l is the temperature gradient in liquid at the S/L interface and m_l is the liquidus slope.

2.3.2 Formation of Dendrites

When a planar interface is unstable and breaks down, cells or dendrites will form. During the solidification, the solid forms as a series of arms projecting into the liquid known as primary dendrite arms, with branches extending outward, known as secondary dendrite arms. Further branching may be observed in some situations. Two different morphologies are considered: 1) isolated growth, which is often referred to as unconstrained or equiaxed growth, and array growth, which is often referred to as constrained or columnar growth. An isolated dendrite usually forms by a smooth steady-state needle-like shape solid growing into an infinite undercooled melt, where the latent heat of fusion is extracted through the cooler liquid ahead of the S/L interface. Isolated growth applies equally well with both pure substances, where growth is controlled by heat flow; and alloys, where growth is controlled by solute flow where the temperature can be assumed constant throughout the system. Array growth is not observed in solidification of pure substances. However, in solidification of alloys, it is more frequently observed than isolated growth. Array growth occurs if latent heat can be extracted through the solid from a mould wall or otherwise, where temperature gradient is positive in both solid and liquid phase. In this case, the dendrite growth direction and the heat flow direction are parallel but in opposite directions. Compared with isolated growth, array growth is more complicated as there is interaction between local cells or dendrites, and usually side branching.

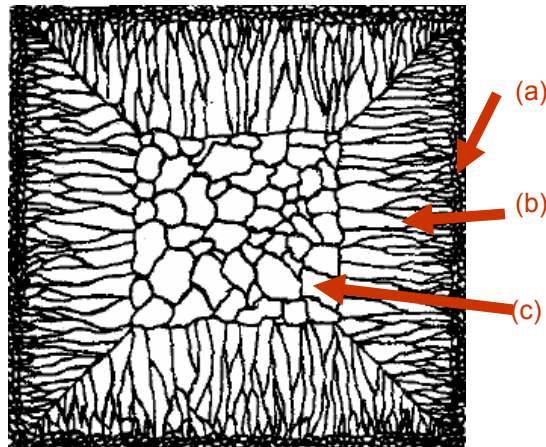


Figure 2.8 Schematic diagram showing the equiaxed and columnar grain structure

(a) Outer equiaxed zone (b) Columnar zone (c) Inner equiaxed zone

After solidification, dendrites make up the grains of most metallic microstructures. As shown in Figure 2.8 (Flemings 1974), under conventional casting conditions in sand casting, the dendrites can be part of either a columnar or equiaxed grain structure depending upon the local thermal and solutal fields. Columnar dendrites (zone b) often grow from near the mould surface (zone a) where the thermal gradients are high, transforming to an equiaxed structure (zone c) when the gradient is reduced near the centre of the casting.

Chapter 3 Literature Review---Modelling

Theory

As microstructures are at the centre of materials science and engineering, on one hand, important advances have been made in our fundamental understanding of solidification microstructures (Boettinger *et al.* 2000) during past years. On the other hand, with the development of very powerful computers, computer simulations are becoming increasingly used for the modelling of microstructure formation and associated characteristics or defects. Over recent years, with advanced numerical methods and better understanding of the physical phenomena involved in solidification, numerical simulation has emerged as one of the most powerful and efficient methods for studying many types of microstructure evolution processes (Boettinger *et al.* 2000). In this Chapter, a critical review of modelling methods for simulation of microstructure evolution of solidification is given. Then, the major methods are discussed, which have been widely used over recent years.

Several methods for solidification modelling have been developed during the past years, including analytical method, cellular automata, front-tracking and phase-field method. Here, a brief comparison of these methods is given in Table 3.1 (Rappaz 2003). Analytical method is the earliest and most theoretical one used for simulation of solidification, which is based on simplified geometry and cannot give visualized results.

All the other three methods can simulate the competitive growth of dendrites during solidification. Phase-field and front-tracking-type methods are now the most powerful approaches for modelling many types of microstructure evolution processes. Front-tracking-type approach has recently emerged as one of the most efficient methods, especially in term of computational cost, which is mainly determined by cell size. In the following section, introduction of these methods is given in detail.

Table 3.1 Methods for Solidification Modelling

	Analytical	Cellular Automata	Front-Tracking-Type	Phase-field
Basic Principles	Simplified geometry and average values	Each spatial cell can have three states: liquid, solid and growing determined by a nucleation event or due to growth proceeding from a neighbouring cell.	The exact position of the S/L interface is calculated and tracked as part of solution process.	The state of the entire microstructure is represented continuously by an order parameter Φ . At the interface the Φ changes from 0 to 1 over a couple of computing layers
Typical Scale	Can be very large and small	5 μ m--mm	In order of microns to mm	In order of microns
Dendritic Geometry	Simplified: plate, sphere, column	Real geometry through competitive growth	Real geometry through competitive growth	Real geometry through competitive growth
Interface	Sharp	Sharp	Sharp interface	Diffuse interface
Stochastic	Deterministic	Probabilistic models	Probabilistic models	Probabilistic models
Visualization	No	Yes	Yes	Yes

A lot of work on numerical simulation has been done during the past years. Many contributions have been made to the development of modelling of microstructure evolution, including: (1) modelling of microstructure formation using phase-field or front-tracking-type methods; (2) modelling of grain structure formation using Cellular Automata or “Granular Dynamics” methods; and (3) modelling of solidification processes and microstructural features using averaging methods.

This section starts with a brief review of nucleation models followed by grain growth models, and covers analytical, phase-field and front-tracking-type methods.

3.1 Nucleation Models

Based on observations on eutectic cast iron, a nucleation model relating the undercooling to the number of nuclei, which has been proposed by Oldfield (1966), can be given as:

$$N = Ka(\Delta T)^2 \quad (3.1)$$

where N is the number of nuclei, Ka is a constant, which varies with different alloy system and can be determined by measurement of nucleation and undercooling, and ΔT is the undercooling. The nucleation increases continuously as the undercooling increases. While, at large undercoolings, nucleants which should become active have no chance because they have already been incorporated into the solid phase. This mechanism agrees with Tronche & Greer’s (2001) experimental observations, in which the distribution of particle sizes of grain refiner at the centre of grains are measured to compare to the distribution of all refiner particles. The former population occupies only the upper slope of the distribution curve, which means that only the most active

nucleants actually result in nucleation events. This phenomenon can be explained by a growth mechanism as proposed by Greer et al.(2000).

Physically, to represent a system in which the embryo population contains a number of particles growing at different times, we can obtain from Eq. 3.1:

$$\frac{dN}{dt} = 2Ka \cdot \Delta T \cdot \frac{d\Delta T}{dt} \quad (3.2)$$

Where dt is the time step. So dN is directly proportional to undercooling, ΔT .

Another model, which assumes the nucleation density has a Gaussian distribution of onset undercooling, is also widely used. As observed at the situation of small undercooling, an abrupt burst of nucleation appears as soon as a critical undercooling is reached. The model incorporates this phenomenon very well. In fact it seems that the rapid growth of the grains first nucleated would overtake nuclei which are activated only at the lower temperature. The model can be given as (Thevoz *et al.* 1989; Rappaz & Gandin 1993):

$$N(\Delta T) = \frac{N_{MAX}}{\sqrt{2\pi}\Delta T} \int_0^{\Delta T} \exp\left[-\frac{1}{2}\left(\frac{\Delta T - \Delta T_N}{\Delta T_\sigma}\right)^2\right] \cdot d(\Delta T) \quad (3.3)$$

where N_{Max} is the maximum density of grains, ΔT_σ and ΔT_N are the standard deviation and the mean value of Gaussian distribution, respectively. It is derived using the assumption that the grain density observed in a sample cooled to a particular temperature is due strictly to nucleation.

3.2 Analytical Method

Analytical method for simulation of solidification is usually based on simplified geometry. It is the earliest and theoretical method, which cannot give visualized results. The microstructure of most alloys consists of both columnar and/or equiaxed dendrites and both types of growth are forms of free dendritic growth. The analytical models are developed to describe free dendritic growth.

Free dendritic growth in pure substances is controlled by heat transport, while in alloys by both heat and mass transport. Earliest models describing free dendritic growth in alloys taking into account the coupled processes of heat and mass transport have been proposed by Temkin (1962) and by Trivedi & Tiller (1978) using the extremum approach. As the operating point of a dendrite may be determined by the limit of morphological stability of its tip rather than by extremum arguments, Langer (1980) developed a theory of dendrite growth in dilute alloys, which showed that the dendrite tip is growing close to the condition of marginal stability.

Lipton *et al.* (1984) developed another model (LGK model) for describing a free dendritic crystal growing into an undercooled binary alloy melt. The LGK model assumes that the dendrite grows freely and steadily into a melt at a constant undercooling and the heat and mass transport in the solid and liquid is only controlled by diffusion. The LGK model predicts the steady-state growth rate and the tip radius of a free growing dendrite using the stability criterion, as tip radius equals to the shortest wavelength:

$$\Delta T = \frac{\Delta h_f}{C_p} Iv(P_t) + m_l C_0 \left\{ 1 - \frac{1}{1 - (1-k)Iv(P_c)} \right\} + \frac{2\Gamma}{R} \quad (3.4)$$

$$R = \frac{\Gamma/\sigma^*}{\frac{P_t \Delta h_f}{c_p} - \frac{P_c m_l c_0 (1-k)}{1-(1-k)Iv(P_c)}} \quad (3.5)$$

in which V is the interface growth rate and R is the tip radius. $Iv(\cdot)$ is the Ivantsov function. P is the Peclet number, where for the thermal field:

$$P_t = \frac{VR}{2\alpha} \quad (3.6)$$

and for the solutal field:

$$P_c = \frac{VR}{2\tilde{D}} \quad (3.7)$$

in which \tilde{D} is the interdiffusion coefficient.

For describing microstructural development during rapid solidification, a theoretical model (KGT model) for directional solidification of Al-Cu system under high cooling rate conditions was developed by Kurz *et al.* (1986). The KGT model applies an appropriate stability criterion coupled with the solute trapping effect to predict microstructural features. As the undercooling in rapid solidification is very large, both the effect of the temperature dependant diffusion coefficient and the velocity and temperature dependant partition coefficient on microstructural characteristics are considered in the model. The KGT model predicts the sharp increase in tip radius near the absolute stability limit and the possible transition from dendritic to cellular structure at high velocity.

3.3 Cellular Automata Method

In a cellular automata model, the domain is divided into a grid of cells with states. Each cell may be thought of as a simple automaton which calculates the new state of the cell

based on the states of itself and its neighbouring cells. It is assumed that the behaviour of each cell is influenced only by the conditions in neighbouring cells. The majority of cellular automata models limit the transition rule to depend on the immediately preceding time step and on the nearest neighbours only.

As for materials modelling, the cellular automata technique has been used for the modelling of solid state phenomena, such as recrystallization and grain growth during annealing and solidification. Cellular automata solidification models try to produce physical phenomena with simple rules at a microstructure level. The simulated domain is divided into a grid of cells characterized by a state and several variables, such as temperature, composition and crystallographic orientation. Each cell can be in liquid, solid or growing status by setting a state index of number. Time is divided into finite steps and the evolution of the given cell during one time step is determined by the transition rules according to the states and conditions of itself and its neighbours. In most diffusion controlled cellular automata solidification models, the growth velocity of the S/L interface is calculated by solving the solute conservation equation subject to the boundary conditions at the S/L interface, therefore, they are able to predict dendrite growth without the need of introducing a kinetic parameter.

3.4 Phase-field Method

The phase-field method employs a phase-field variable, $\Phi(\vec{r}, t)$, a function of position and time, to characterize the physical state of the system at each position and time. In this method, the diffuse nature of the S/L interface of metallic alloys is considered. The phase-field variable, Φ , changes steeply but smoothly at the interface region between solid and liquid, which avoids direct tracking of the interface position. The variable

varies continuously between fixed values over a certain thickness, d . Usually, the fixed values are given as 0 and 1, which represent solid and liquid respectively, and the values from 0 to 1 stand for the S/L interface. Therefore, the model can be regarded as a type of a diffuse interface model, which assumes that the interface has a finite thickness and that the physical properties of the system vary smoothly through the interface.

However, phase-field model has some disadvantages. Firstly, in phase-field model, it is difficult to relate the physical parameters in the equation for the field variable to physical parameters, such as the surface tension. Secondly, the cell size is limited by the surface thickness. So results mainly depend on the prescribed interface thickness.

3.4.1 The Development of Phase-field

The basic idea is to introduce a phase-field that varies continuously over S/L interfacial layers and is mostly uniform in the liquid and solid regions. On considering fluid density as an order parameter, Van der Waals (Rowlinson 1979) developed the first diffuse interface model. By the mid 1980s, this model was applied to the equilibrium properties of the interface (Cahn & Hilliard 1958) and antiphase boundary migration by curvature (Allen & Cahn 1979; Ginzburg & Landau 1950). Langer (1986) proposed that the diffuse interface model could be applied to solidification phenomena.

By using the singular perturbation method (O'Malley 1991), Caginalp (1989) proved that the phase-field model could be reduced to the Stefan problem, in which the boundary of the domain has to be found as part of the solution, in the limit that the thickness of the interface approaches zero and Kobayashi (1993) studied the dendritic growth of a pure melt by using the phase-field model for pure materials. The model which was proposed for simulating dendritic growth in pure undercooled melt (Karma

& Rappel 1996, 1998; Kobayashi 1993; Penrose & Fife 1990; Wang & Sekerka 1993, 1996) has been extended to modelling of alloy solidification (Caginalp & Xie 1993; Cha *et al.* 2001; Kim *et al.* 1998, 1999; Losert *et al.* 1998; Löwen *et al.* 1992; McFadden *et al.* 1993; Tiaden *et al.* 1998; Wheeler *et al.* 1992, 1993, 1996) and recently has been used extensively for the simulation of dendritic growth and the prediction of microstructures (Boettinger *et al.* 2000; Ode *et al.* 2001; Wheeler *et al.* 1995). Over past few years, the model has been developed to do quantitative simulation of microstructure evolution (Echebarria *et al.* 2004; Foch & Plapp 2005; Lan *et al.* 2005; Zhu *et al.* 2004).

3.4.2 Derivation of Phase-field Method

Phase-field models can be divided into various intersecting classes and there are also different approaches to phase-field modelling (Boettinger *et al.* 2002). It may involve a single scalar order parameter or involve multiple order parameters; and can be derived from a thermodynamic formulation or derived from geometrical arguments. To build a phase-field model, we can use a thermodynamic treatment with gradient flow or only be concerned with reproducing the traditional sharp-interface approach. Here, a thermodynamic treatment approach, which is widely used in many papers (Bi & Sekerka 1998; Boettinger *et al.* 1994; Caginalp & Xie 1993; Wheeler *et al.* 1992, 1993), is described in detail.

Using thermodynamic treatment, there are also different ways to build the phase-field model. The phase-field governing equations can be derived from entropy or a free energy formulation. An introduction using a free energy formulation is given in following part.

We start from a free energy equation. For heat diffusion, we append a heat flow equation to a simpler isothermal formulation. The enthalpy density is given as:

$$h = C_{pp}T + L\Phi + h_0 \quad (3.8)$$

where C_{pp} is the heat capacity per unit volume, T is the temperature, L is the latent heat per unit volume and h_0 is a constant. This equation yields an equation for thermal diffusion with a source term given by:

$$C_{pp} \frac{\partial T}{\partial t} + L \frac{\partial \Phi}{\partial t} = \nabla \cdot (\kappa \nabla T) \quad (3.9)$$

where κ is the thermal conductivity. From Eq. 3.9, we can see that the latent heat evolution only occurs when Φ is changing with time, which happens in the S/L interface area.

For solute diffusion, we firstly give the free energy functional F , which decreases during any processes, as:

$$F = \int_V \left[f(\Phi, C, T) + \frac{\varepsilon_C^2}{2} |\nabla C|^2 + \frac{\varepsilon_\Phi^2}{2} |\nabla \Phi|^2 \right] \cdot dV \quad (3.10)$$

where $f(\Phi, C, T)$ is the free energy density, C and Φ are concentration and phase field, respectively, with ε_C and ε_Φ being the associated gradient energy coefficients.

And for equilibrium, if the gradient energy coefficients are constants, the variational derivatives of F must satisfy the following equations:

$$\frac{\delta F}{\delta \Phi} = \frac{\partial f}{\partial \Phi} - \varepsilon_\Phi^2 \nabla^2 \Phi = 0 \quad (3.11)$$

$$\frac{\delta F}{\delta C} = \frac{\partial f}{\partial C} - \varepsilon_c^2 \nabla^2 C = \text{constant} \quad (3.12)$$

The constant in Eq. 3.12 occurs because the total amount of solute in the volume is a constant, such as concentration is a conserved quantity.

Then, for time-dependent situations, in the simplest case, the evolution equations of phase field and concentration can be obtained as following, which guarantees a decrease in total free energy with time.

$$\frac{\partial \Phi}{\partial t} = -M_\Phi \left[\frac{\partial f}{\partial \Phi} - \varepsilon_\Phi^2 \nabla^2 \Phi \right] \quad (3.13)$$

$$\frac{\partial C}{\partial t} = \nabla \cdot \left[M_c C(1-C) \nabla \left(\frac{\partial f}{\partial C} - \varepsilon_c^2 \nabla^2 C \right) \right] \quad (3.14)$$

where M_Φ and M_c are positive mobilities related to the interface kinetic coefficient and solute diffusion coefficient respectively. As composition is a conserved quantity and phase-field is not, these two governing equations have different forms.

To reduce computational cost, adaptive grid methods have been applied for phase-field simulation in recent years (Rosam *et al.* 2007).

A simulation result for pure material with phase-field model is shown in Figure 3.1(Kobayashi 1993).

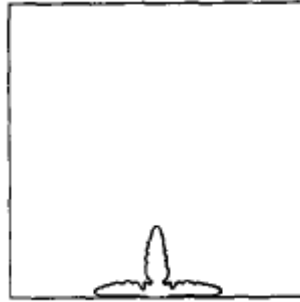


Figure 3.1 Phase-field simulation of solidification in pure metal

At simulation time 0.2s, with 4-mode anisotropy

3.5 Front-Tracking-Type Methods

In solidification of most metallic alloys under normal conditions, microstructure formation is controlled by solute diffusion and interfacial curvature of the S/L interface, while heat diffusion occurs over much longer distances. Simulation at this level normally requires front tracking, which means following the S/L interface. Although this has been achieved successfully in simple geometry using either the boundary element method (BEM) (Satio *et al.* 1988), in which only the interface is enmeshed and Greens functions are used to solve the diffusion problem, or the finite element method (FEM) (Sullivan *et al.* 1987), in which dynamic remeshing of the domain is needed, it is very difficult to implement even in two dimensions. Furthermore, topological changes, such as merging of two dendrite arms, cannot be handled. To seek more efficient ways to solve the problems, during the last decade, front-tracking-type methods have been developed.

The front-tracking-type methods calculate the S/L interface position as part of the solution process. The presence of an interface between solid and liquid complicates the solution of an otherwise manageable problem. The interface position must be calculated

as part of the solution process, and interface conditions must be satisfied at this interface. This leads to a highly nonlinear problem that is very sensitive to numerical error and prone to numerical instability. Early numerical models of solidification were mainly developed for the stable Stefan problem and avoided the actual calculation of the interface position, while still being able to calculate the thermal field. For unstable solidification, such as a crystal growing into an undercooled liquid, it is very necessary to accurately calculate the interface position. This led to the development of diffuse-interface models, phase-field model and front-tracking-type models. As phase-field model has some disadvantages, particular attention has been laid on the development of front-track-type models during the last few years. A number of models of this type have been developed for simulation of pure metal solidification (Clyne 1984; Giovanola & Kurz 1986; Wang & Matthys 1992; Zhang & Atrens 1992), considering as plane front solidification. The basic front-tracking-type model is the front-tracking method, based on which pseudo-front-tracking method (Jacot & Rappaz 2002), level-set method (Zabaras & Tan 2006) and some other methods, somewhat in between front-tracking and phase-field, have been developed. Recently, simulations of microstructure evolution for alloy solidification have been carried out with these methods.

3.5.1 Fundamentals of Front-Tracking-Type Methods

Generally, during phase-change and materials processing, the moving S/L interface encountered may be highly distorted. The calculation of both shape and position of such an interface must be considered as part of the problem solution. In such cases, solution for thermal, compositional, or flow fields at each time step, must consist of not only a correct calculation of the governing equations in both phases but also an accurate tracking of the S/L interface (Li *et al.* 2003).

In the literature (Floryan & Rasmussen 1989), the interface between solid and liquid phases has dealt with interface-capturing and interface-tracking methods. In the interface-capturing method, the details of the structure of the interface are resolved with only a minimal effort. Without any specific modelling for the interface, it is treated as only that the actual physical discontinuity is known to be someplace near the middle of the temperature gradient. Basically, the interface itself is not tracked. As an example of this in one-domain, in the enthalpy method, both phases are considered together in the solution, and the properties are either changed continuously over a range near the interface or changed discretely across the interface. Interface-tracking methods may be divided into front-tracking and volume-tracking approaches. Interface-tracking method was reviewed in the literature (Chen *et al.* 1997) with reference to the simulation of bubble rise and distortion. In front-tracking (Glimm *et al.* 1981), the interface is represented by the distance between the points and some reference surface, such as the interface of previous time step.

Front-tracking methods identify the interface by an ordered set of marker points located on the interface. To represent the interface front, a line connecting the marker points is applied, usually a piecewise polynomial. Front-tracking is used in the vicinity of the interface with an irregular grid. In an extension to this method, Unverdi & Tryggvason (1992) represented the interface by an indicator function, which takes a value of unity in one phase and zero in the other. To explicitly track the interface and move through the stationary grid, an additional Eulerian grid is generated on the front. More efforts are made on improving the accuracy of interface tracking, which may also be considered to fall under the front-tracking category (Udaykumar *et al.* 1994). The method they proposed is in two dimensions, with tracking the position of the interface explicitly by a

Lagrangian translation of marker particles and solving the field equations on an underlying fixed grid as in Eulerian methods.

Most of the interface-tracking researches in the literature focus on two dimensions. A number of serious complications are introduced when these methods are extended to three dimensions. Despite some studies of front-tracking methods, (Chen *et al.* 1997; Lafaurie *et al.* 1994; Nobari & Tryggvason 1996) successfully applying this to model three-dimensional bubble dynamics, the solution methodologies become quite complex and computationally intensive. As the accuracy of the tracking is particularly important in accounting properly for surface-tension effects, the interface position must be obtained accurately to represent the states properly at the interface in simulation. An adaptive-grid approach may be applied to obtain a sharp resolution of the interface, where the grid is adjusted locally to coincide with the interface. However, to adjust the grids to track highly deformed interfaces is extremely difficult. Using body-fitted coordinates, Yeoh *et al.* (1992) have successfully developed another mapping method to maintain a sharp resolution of the interface, which transforms the deformed physical domain into a regular, fixed-grid computational domain. Theoretically, it provides a true tracking of the interface. However, in practice, as the switching between the original and transformed coordinate systems is required at each time step, it leads to extremely expensive computations. More importantly, this method can only handle geometries which will not lead to singular mappings. Jayaraman *et al.* (1997) present a promising method for tracking in three dimensions with adaptive unstructured grids to represent the three dimensional interfaces. However, it is true that a fixed-grid approach in two dimensions lends itself to simplified computations, in addition to being able to handle large deformations and multiple interfaces.

3.5.2 Front-Tracking Method for Solidification

For simulation of alloy solidification, the state of a cell can be either liquid, solid, or interface at each time step. At beginning, one or several crystal seeds with a randomly selected growth orientation are assigned in the domain. During solidification, when the crystal seed is suspended in an undercooled melt, the local equilibrium composition is larger than the local actual liquid composition. To reach the equilibrium composition, solidification continues. Therefore, the driving force for dendritic growth is considered to be the difference between the local equilibrium composition and the local actual liquid composition. As solidification carries on, at the S/L interface, latent heat is released and solute is rejected into liquid, which results in a thermal and a solutal gradient ahead of the interface, leading to heat and mass transport in the domain. The mass transfer also results in a new solute field, which determines the local actual interface liquid composition. The kinetics of dendritic growth is thus governed by the heat and mass transport in the domain. In turn, the dendrite growth also leads to the heat and mass transport through rejecting latent heat and solute at the S/L interface. This interaction between heat/mass transport and dendritic growth continues to the end of solidification.

When the interface tracking method is applied to the solidification process for liquid melts, it requires the solution of a system of equations for the conservation of mass, momentum, energy, and, perhaps, species. In such a problem, the movement of the interface is controlled by an energy balance, and by additional conditions if an alloy is considered. As observed in solidification of most commercial metallic alloys, dendritic growth is the primary form of crystal growth. Dendritic growth is governed by the complex interplay of thermal, solutal, capillary, crystallographic anisotropy,

thermodynamics and kinetics properties which occur on different length scales (Amar & Pelce 1989; Glicksman & Koss 1994; Koss *et al.* 1999; McFadden *et al.* 2000; Meiron 1986; Trivedi & Kurz 1994; Trivedi & Mason 1991).

Based on the cellular automaton (CA) concepts, Belteran-Sanchez & Stefanescu (2003, 2004) developed a model by using virtual tracking of the sharp S/L interface to simulate solutal dendrite growth. In this model, a methodology is introduced by calculating growth kinetics from the complete solution of the solute and heat transport equations and by incorporating the boundary condition of solute conservation. The most important novel aspect of this model is a solution proposed to avoid grid effects. In this model, the artificial anisotropy due to mesh is eliminated for any grain orientation by applying new calculating methods of S/L interface curvature, normal velocity and method of capturing rules for new interface cells. As the mesh dependency of calculations is eliminated, the model can describe dendrites growth at an arbitrary crystallographic orientation. In this model, the growth kinetics is based on the assumption of local solute conservation at the S/L interface. Therefore, this method is able to calculate growth velocity of the S/L interface without introducing kinetic parameters. As the assumption is actually equivalent to the concept of steady-state growth that is characterized by equilibrium diffusion of the rejected solute away from the S/L interface, this method can only describe reasonable well of the growth velocity of the S/L interface during steady-state growth. However, this method cannot accurately predict the growth velocity during unstable growth, such as growth at the initial stage. The reason is that during the initial unstable growth stage the rejected solute from solid is greater than that can be transported away from the interface by diffusion. Therefore, the condition of solute balance at the S/L interface cannot be satisfied at the initial stage.

Front-tracking models (Juric & Tryggvason 1996; Zhao & Heinrich 2001, 2002; Zhao *et al.* 2003; Jacot & Rappaz 2002) try to calculate time-dependent dendritic growth following the dynamics of the sharp S/L interface directly by solving the heat and species conservation equations with appropriate interface conditions. In this model, the location and shape of the S/L interface are provided explicitly by a set of extra marker nodes, which are defined at every time and move according to the interface conditions and therefore independently of the mesh. Front-tracking models are able to deal with the discontinuous properties at the interface, interfacial anisotropy and topology changes.

a) Front-tracking method

Zhu & Stefanescu (2006) proposed a front-tracking model to simulate dendritic growth. In the model, the dendritic growth of binary alloys is considered to be governed by heat and mass transport. The relevant governing equations are as follows.

For heat transport, the governing equation is given by

$$\rho C_p \frac{\partial T}{\partial t} = \nabla(\kappa \nabla T) + \rho L \frac{\partial f_s}{\partial t} \quad (3.15)$$

where ρ is density, C_p is specific heat, T is temperature, t is time, κ is thermal conductivity, L is latent heat during solidification and f_s is the solid fraction. The second term on the right-hand side denotes the latent heat released when cells change from liquid to solid.

For mass transport, the governing equation is given by

$$\frac{\partial C}{\partial t} = \nabla(D \nabla C) + C(1-k) \frac{\partial f_s}{\partial t} \quad (3.16)$$

where C is composition, t is time, D is the solute coefficient and f_s is solid fraction. Using a constant partition coefficient, k , the solute partition between liquid and solid at the S/L interface is considered according to $C_s = k \cdot C_l$. The second term on the right-hand side of the Eq. 3.16 denotes the amount of solute rejected at the S/L interface.

During the solidification of binary alloys, solute of alloy elements is rejected at the S/L interface due to the difference in solubility between the two phases. The composition in the solid follows that of the solidus, C_s^* , and that of the liquid follows that of the liquidus, C_l^* . This is illustrated in a schematic equilibrium phase diagram on Figure 2.4. During the solidification, solute and latent heat are released at the S/L interface, and also the interface curvature changes. A thermal and a solute gradient come into being ahead of the interface, which leads to heat and mass transport in the domain. The new interface curvature and thermal field result in new interface equilibrium composition. At the same time, the mass transfer also generates new solute field, determining the local actual interface liquid composition. The new difference between the local actual liquid composition and the local interface equilibrium composition drives the dendrite to continue growing. This cycle of interaction between dendrite growth and mass and heat transport continues to the end of solidification.

At this stage, the driving force for dendrite growth is only considered to be controlled by the difference of composition between local actual liquid and local interface equilibrium. Based on the phase diagram, the interface equilibrium composition C_l^* can be given by

$$C_l^* = C_o + \frac{T^* - T_l^{eq}}{m_l} \quad (3.17)$$

where C_o is the initial composition, T^* is the current interface temperature, T_l^{eq} is the equilibrium liquidus temperature at C_o and m_l is the liquidus slope. T_l^{eq} can be calculated by

$$T_l^{eq} = T_o + m_l \cdot C_E \quad (3.18)$$

where C_E can be calculated by

$$C_E = f_s \cdot C_s + (1 - f_s)C_l \quad (3.19)$$

Then, compare the calculated interface equilibrium composition C_l^* with the local actual liquid composition C_l , which is controlled by Eq. 3.16. When C_l^* is more than C_l , the solid fraction of the current calculating cell will increase.

$$\Delta f_s = (C_l^* - C_l) / (C_l^* - (1 - k)) \quad (3.20)$$

To avoid moving the interface out of the cell in one time step for numerical stability, the following limiting condition is applied for the calculation of the increase in solid fraction:

$$\Delta f_s(Nt) = \min(\Delta f_s, 1 - \sum_{i=1}^{Nt-1} \Delta f_s(i)) \quad (3.21)$$

where Nt indicates the number of iterations(time step intervals) after the cell became an interface cell. In other words, when the cell is captured as an interface cell, $Nt=1$. As Nt increases, the solid fraction in this interface cell increases.

If at time $t=t_N$, the sum of the solid fraction in an interface cell equals one, this interface cell has fully solidified. Then, the interface cell changes its state to solid. From the calculated increase in solid fraction at each time step, the normal growth velocity of the interface V_n can be obtained by

$$V_n = \Delta f_s \frac{\Delta x}{\Delta t} \quad (3.22)$$

where Δx is the cell size and Δt is the time step.

Figure 3.2 (Zhu & Stefanescu 2006) shows the simulated dendrite morphology of Al-4wt. %Cu alloy with front tracking model.

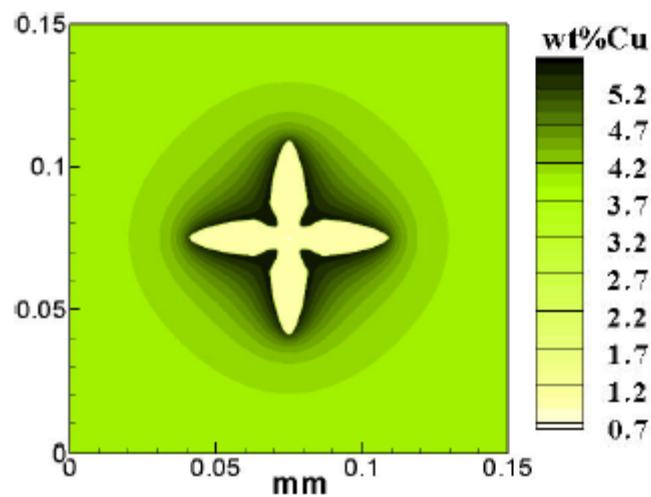


Figure 3.2 Simulated dendritic morphology of an alloy

At melt undercooling of $\Delta T=4K$, after 0.08s, 600×600 , $\Delta x = 0.25 \mu m$.

b) Pseudo-front-tracking method

The pseudo-front-tracking method allows calculations of the primary phase formation to be performed at lower undercooling without the non-equilibrium effects. In this method (Dilthey & Pivlik 1998; Jacot & Rappaz 1997; Juric & Tryggvason 1998), the S/L interface is spread over a layer of only one mesh of the finite difference (FDM) or finite volume (FVM) enmeshment. To introduce the concept of the volume fraction of solid (or liquid), a variable, ϕ , is employed. For meshes of solid status, ϕ equals to unity, zero for liquid and $0 < \phi < 1$ for interface meshes. With the advantage of such a method, fairly easy implementation and computation speed can be obtained. However, this technique usually involves fairly large grid anisotropy, such that the growth direction and kinetics of the dendrites tend to be influenced by the orientation and size of the mesh. Therefore, such numerical effects are often not very well characterised in simulations of dendritic solidification based upon such methods. Since preferred growth directions and dendrite tip kinetics are governed by the small anisotropy of the interfacial energy, such methods can only give qualitative results.

c) Level set method

The level set method was devised by Sethian (1996) and Osher & Fedkiw (2003) as a simple and versatile method for computing and analyzing the motion of an interface in two or three dimensions. It has recently been developed further by Zabaras (2006). As an alternative method to handle the sharp S/L interface front directly, avoiding the asymptotic analysis needed in phase-field models, the method has been shown to be a promising mathematical tool for tracking the interface with low computational cost. It

has been widely used in various applications such as two-phase flow, crack propagation, computer vision and image processing.

In this method, a level set variable ϕ is employed, which is the signed distance from the interface. This signed distance is the shortest distance to phase boundary, with minus sign within the phase and plus sign outside the phase. Interfacial geometric quantities such as curvature and outward normal can be easily calculated using the signed distance. Also, the velocity of the evolution of interface can be obtained by solving the level set equation.

d) Virtual Front-Tracking Model

Zhu & Stefanescu (2007) develop a computationally efficient quantitative virtual front-tracking model to simulate the formation of both multi-equiaxed and columnar dendrites in alloy solidifying under normal practical conditions. In this model, a solution of the kinetics of dendritic growth is proposed, which allows the accurate simulation of dendrite growth from the initial unstable stage to the steady-state stage. The model adopts an interface tracking method previously proposed by Belteran-Sanchez & Stefanescu (2004) for explicitly capturing the new interface cells. The exact S/L front is implicitly scaled by the solid fraction within each interface cell. This hybrid scheme provides straightforward handling of complex topology changes, meanwhile the concept of a sharp transition between liquid and solid is maintained.

The virtual front-tracking model adopts solutions for the evaluation of local curvature and interface capturing rules with a virtual interface tracking scheme, which make the model virtually mesh-independent. The kinetics of dendritic growth is considered to be driven by the difference between local equilibrium composition and local actual liquid

composition, which can be calculated from the local temperature and curvature and obtained by solving the solutal transport equation separately. The virtual interface tracking scheme for capturing new interface cells is shown as Figure 3.3 (Zhu & Stefanescu 2007).

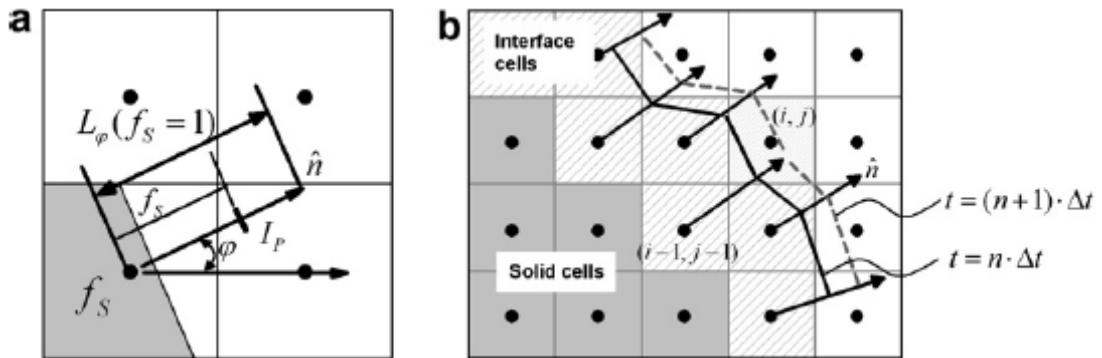


Figure 3.3 Capturing rules for new interface cells

(a) Determining the sharp S/L interface position (b) Capturing rules for new interface cells

First, for all interface cells, the length L_φ , measured from the cell centre along the direction normal to the local S/L interface, where φ is the local growth angle and is assumed equivalent to $f_s = 1$. Then the position of the sharp S/L interface I_p can be calculated from the cell centre along this line at a distance proportional to the solid fraction f_s in this cell, as shown in Figure 3.3(a). Connecting the point I_p of all interface cells of current time step and next time step separately, the S/L sharp interface of current time step and next time step can then be obtained. In Figure 3.3(b), the solid line is the interface of current time step and dash line is the one of next time step. Then, the liquid neighbouring cells of the interface cell are scanned. If the centre of one of these cells lies inside the area between the two sharp interface lines, meanwhile also satisfying the condition that at least one of its eight closest neighbouring cells is solid,

this liquid cell is then captured as a new interface cell. For example, at current time, $t = n\Delta t$, the state of cell (i, j), whose centre of this cell is located outside the interface line, is liquid. Then, at next time, $t = (n+1)\Delta t$, the new interface line has moved past the centre of cell (i, j). And also, one of its neighbours, cell (i-1, j-1), has been solid. Therefore, the cell (i, j) changes its state from liquid to interface and becomes a newly captured interface cell.

As shown in capturing rules, dendrite growth is directly calculated from solid fraction, eliminating the need to first calculate the growth velocity. Thus, the computational time is decreased. This computationally efficient front-tracking model has been successfully applied to simulate the formation of both multi-equiaxed and columnar dendrites in alloy solidifying under normal practical conditions. Figure 3.4 (Zhu & Stefanescu 2007) shows the simulated evolution of multi-equiaxed dendritic growth of an Al-10 wt.% Cu alloy with a cooling rate of 5 K s^{-1} . It can be seen that most dendrites develop the main arms along their crystallographic orientations during the early stage of solidification. During the late stages, growing and coarsening of the primary trunks occurs, together with the branching and coarsening of the secondary arms. Figure 3.5 (Zhu & Stefanescu 2007) presents the simulation of columnar dendrites evolution for an directionally solidified of an Al-4 wt.% Cu alloy, with a thermal gradient $G = 2000 \text{ K m}^{-1}$. At beginning, several nuclei are assigned at the bottom wall with random crystallographic orientation and location.

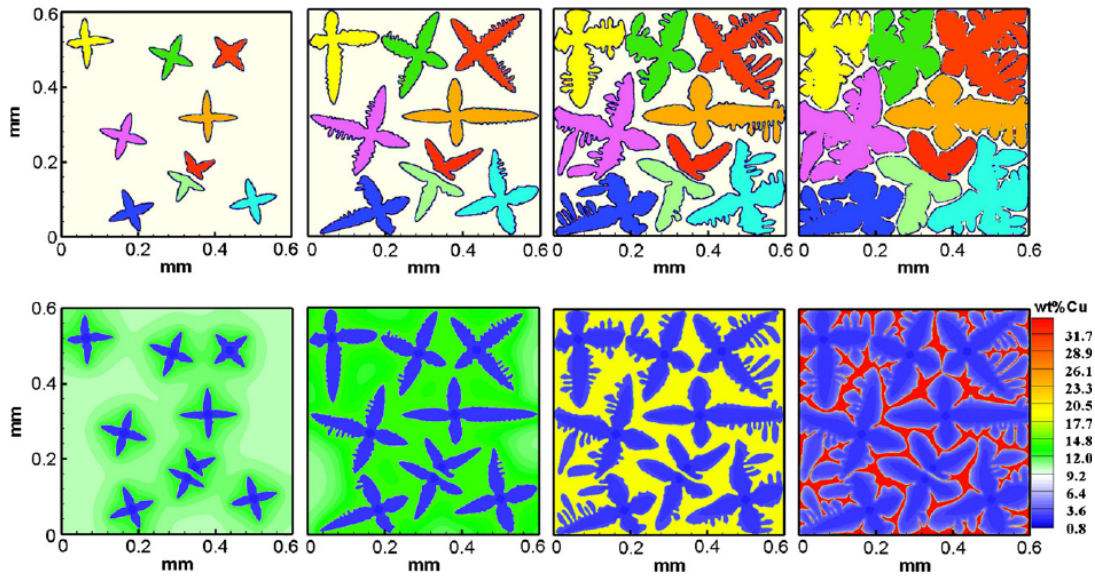


Figure 3.4 Simulated equiaxed dendrite evolution of an Al-10wt.% Cu alloy with upper row showing grain boundary formation and bottom row showing composition fields, 600×600 meshes, $dx = 1 \mu\text{m}$, cooling rate at 5 K s^{-1} , from left to right after 1.4 s, 2.2 s, 4.6 s and 17 s

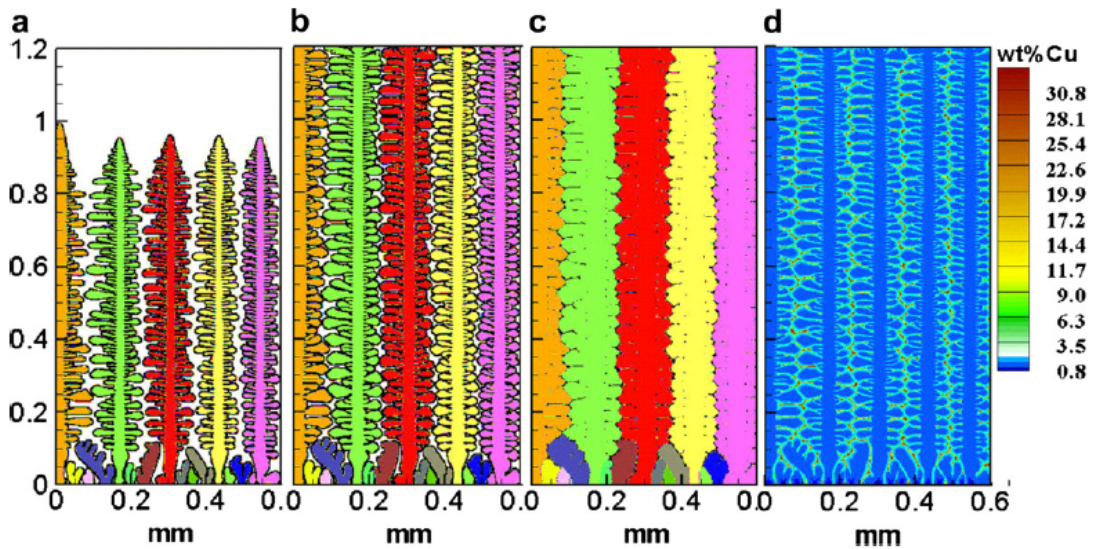


Figure 3.5 Simulated columnar dendrite evolution of an Al-4wt.% Cu alloy with a thermal gradient of 2000 K m^{-1} , initial undercooling of 3 K, cooling rate of 5 K s^{-1} , after (a) 2 s, (b) 3.2 s, (c) and (d) 12 s; (a-c) show grain boundary formation, and (d) shows the solute map.

3.5.3 Extended Application of Front-Tracking Model

A meso-scale front-tracking model of nonequilibrium binary alloy dendritic solidification has been extended by Banaszek *et al.* (2007) to incorporate KGT (Kurz *et al.* 1986) dendrite kinetics and a Scheil solidification path. The model has been applied to predict natural convection and columnar-to-equiaxed transition of binary alloy solidification controlled by both conduction and thermal natural convection.

In the extension of front-tracking model, it is assumed that the growth kinetics is not influenced by velocity field. To calculate concurrent fluid flow and heat-transfer phenomena occurring in the superheated melt, undercooled liquid, mushy and fully solidified regions, the control volume difference method is directly coupled with the front-tracking technique on a fixed grid. The computational model is based on the staggered grid approach (Patankar 1980), to avoid checkerboard pressure modes. The velocity and pressure correction method (Van Doormal & Raithby 1984) is used to separately calculate pressure and velocity fields. And finally, the iterative segregated solution strategy is used, where linearized directional momentum and energy equations are solved consecutively.

3.6 Summary

In this chapter, several simulation techniques for solidification process have been reviewed. As in cellular automata model, when calculating the growth of the S/L interface, the solute conservation is actually equivalent to the concept of steady-state growth, it neglects the fact that the condition of solute balance at the S/L interface cannot be satisfied in the initial transition period, during which the solute rejected by the growing dendrite cannot be fully diffused away from the the interface by diffusion only.

Therefore, the cellular automata can describe reasonably well the kinetics for steady-state growth, but fail to offer an accurate solution for the growth velocity during unstable growth. Phase-field and front-tracking are widely used methods to simulate microstructure formation of solidification. For solidification, front-tracking (Juric & Tryggvason 1996) techniques have been successfully applied to model dendritic growth of alloys. Advantage of the front-tracking method has been shown in the computation of several important physical problems, such as the study of fluid interface instabilities. However, both phase-field and front-tracking (in tracking the S/L interface front) models have some disadvantages such as in computational cost. Therefore, considering computational efficiency and accuracy, in this study a (virtual) front-tracking method is chosen based on a cellular automata model coupling with a front-tracking technique to simulate the solidification structure evolution. By applying an accurate solution for growth velocity, the model can describe well the kinetics for both steady-state and unstable growth. Model description, model validation and simulated results using the developed front tracking model will be presented in following chapters.

Chapter 4 Model Description

The main modelling work described in this thesis is the development of a front-tracking model for simulation of the microstructure evolution of alloy solidification. In this chapter, a detailed description of the developed front-tracking model will be presented.

4.1 Governing Equations

In the present study, solutal dendritic growth of binary alloys is considered to be governed by heat and mass transport. Governing equations for heat and solute diffusion are as Eqs. 3.15 and 3.16 respectively.

To take into account both constitutional and curvature undercooling, according to the thermodynamic concept of local equilibrium between the liquid and solid phases, Eq 3.17 can be extended to

$$C_l^* = C_0 + \frac{T^* - T_l^{eq}}{m_l} + \frac{\Gamma K f(\varphi, \theta)}{m_l} \quad (4.1)$$

where Γ is the Gibbs-Thomson coefficient, K is mean curvature of the S/L interface and function $f(\varphi, \theta)$ accounts for the anisotropy of the surface tension. The assumption of local equilibrium means that the liquid and solid compositions at the S/L interface can be obtained by reference to the equilibrium phase diagram when the S/L interface temperature is known, but not that the whole system in which temperature and composition gradients exist is at equilibrium. The reason that the local equilibrium can

be assumed is that in solidification of most alloys, it is assumed that the S/L interface behaves locally as if it were in a state of equilibrium, which means that the reaction rates are rapid in comparison with the S/L interface advance rate, as the reaction makes up a very thin but finite interface layer in the small volume. Therefore, the transfer of atoms and changes in their arrangement which are required in order to maintain the constancy of the chemical potentials in both phases are relatively rapid and can hence be neglect. The creation of a crystal from an alloy melt causes the formation of curved S/L interfaces and local change in composition, which leads to microscopic flow of heat and solute. The change in melting point due to the existing of the curvature effect is called the curvature undercooling, which can be given as Eq. 2.5. For a portion of S/L interface which is convex towards the liquid phase, K and Γ are defined to create a positive undercooling, which decreases the equilibrium melting point. The Gibbs-Thomson coefficient is defined as interface energy divided by entropy of fusion, as $\Gamma = \sigma / \Delta s_f$. As Γ is of the order of 10^{-7} Km for most metals, the effect of the S/L interface energy σ only is important for morphologies which have a radius of less than about $10\mu\text{m}$.

So we can obtain

$$T^* = T^{eq} + (C_l^* - C_0)m_l - \Gamma K f(\varphi, \theta) \quad (4.2)$$

in which the second item of the right hand accounts for constitutional undercooling and the third one for curvature undercooling.

The S/L interface curvature K and anisotropy of the surface tension $f(\varphi, \theta)$ can be calculated respectively by (Nastac 1999)

$$K = \frac{1}{a} \left(1 - 2 \frac{f_s + \sum_{i=1}^N f_s(i)}{N+1} \right) \quad (4.3)$$

$$f(\varphi, \theta) = 1 - \delta \cos[\lambda(\varphi - \theta)] \quad (4.4)$$

where \mathcal{C} is the cell size, f_s is the solid fraction of the cell, $f_s(i)$ is the solid fraction of a neighbouring cell and N is the number of neighbouring cells counted, φ is the growth angle, between interface normal and x-axis and θ is preferential crystallographic orientation angle and δ is the degree of anisotropy. The values of the curvatures calculated with Eq. 4.3 vary from a maximum of $1/a$ to zero for convex surfaces and from zero to a minimum of $-1/a$ for concave surfaces.

To model free dendritic growth in two dimensions, both Eqs. 3.15 and 3.16 are solved numerically using an explicit finite difference scheme.

For heat transport

$$\frac{\partial T}{\partial t} = \frac{\kappa}{\rho c_p} \nabla^2 T + \frac{\Delta H}{c_p} \cdot \frac{\partial f_s}{\partial t} \quad (4.5)$$

Where, in finite discretization form, in which $T_{i,j}^k$ is temperature of cell(i,j) at time step k .

$$\frac{T_{i,j}^{k+1} - T_{i,j}^k}{\Delta t} = \frac{\kappa}{\rho c_p} \left(\frac{\partial^2 T}{\partial x^2} + \frac{\partial^2 T}{\partial y^2} \right) + \frac{\Delta H}{c_p} \cdot \frac{f_s^k - f_s^{k-1}}{\Delta t} \quad (4.6)$$

And finally, the temperature for next time step can be given by

$$T_{i,j}^{k+1} = \frac{\Delta t \cdot \kappa}{\rho C_p} \left(\frac{T_{i-1,j}^k + T_{i+1,j}^k - 2T_{i,j}^k}{\Delta x^2} + \frac{T_{i,j-1}^k + T_{i,j+1}^k - 2T_{i,j}^k}{\Delta y^2} \right) + \frac{\Delta H}{C_p} (f_s^k - f_s^{k-1}) + T_{i,j}^k \quad (4.7)$$

where Δx and Δy are the size of the cell.

Accordingly, with assumption of the solute diffusion coefficient D as constant, the governing equation for solute diffusion Eq. 3.16 can be written as, in finite discretisation form

$$\frac{C_{i,j}^{k+1} - C_{i,j}^k}{\Delta t} = D(\nabla^2 C) + C_{i,j}^k(1 - k) \frac{f_s^k - f_s^{k-1}}{\Delta t} \quad (4.8)$$

Finally, the mass concentration for next time step can be obtained by

$$C_{i,j}^{k+1} = D \cdot \Delta t \left(\frac{C_{i-1,j}^k + C_{i+1,j}^k - 2C_{i,j}^k}{\Delta x^2} + \frac{C_{i,j-1}^k + C_{i,j+1}^k - 2C_{i,j}^k}{\Delta y^2} \right) + C_{i,j}^k \cdot ((1 - k) \cdot (f_s^k - f_s^{k-1}) + 1) \quad (4.9)$$

For calculation of both temperature field and composition field, the choice of the Δt must be made in such a way that the equations remain stable under time-step iteration. To ensure stable results in the explicit calculation of the two fields in two dimensions it can be shown that (suppose that $\Delta x = \Delta y$)

$$\Delta t < \min\left(\frac{\Delta x^2}{D}, \frac{\Delta x^2}{\alpha}\right) / 4 \quad (4.10)$$

where $\alpha = \frac{\kappa}{\rho C_p}$.

4.2 Model Description

In solving a solid–liquid phase-change problem during the solidification or melting process, the governing conservation equations must be solved at each time step. It is also necessary to compute the exact position and the movement of the S/L interface. Two distinct steps, solution of the governing equations and interface reconstruction and advection (tracking), are involved. The first step involves the imposition of boundary conditions and matching conditions at the interface, and the second step hence follows and depends on the first step.

4.2.1 Tracking of the S/L Interface

The front-tracking model calculates the exact S/L interface position and movement of the S/L interface together with solving governing equations. As capturing of new S/L interface cells is based on the S/L interface position, calculation of the S/L interface position becomes very important and therefore is the key calculation in the front-tracking model.

To calculate the S/L interface position, L_φ , a parameter to describe length is introduced for all interface cells. As illustrated schematically in Figure 4.1(a), L_φ , which equals to $\Delta x / \max(|\cos\varphi|, |\sin\varphi|)$, is dependent on the local growth angle φ and assumed equivalent to $f_s = 1$. It represents the distance to be covered by a point on the S/L interface so that it could be considered solid. Notice that L_φ is measured from the cell center along the direction normal to the local S/L interface, as shown in Figure 4.1(b), so as to minimize the effect of the artificial mesh anisotropy on the rate of advance of the interface. The position of the sharp S/L interface I_p can be scaled from the cell

center along L_φ at a distance proportional to the solid fraction f_s in this cell. The sharp interface can thus be obtained by connecting the point I_p of all adjacent interface cells. The liquid cells found inside the area drawn by lines connecting the positions of the sharp S/L interface are considered captured, becoming interface cells able to change their solid fraction.

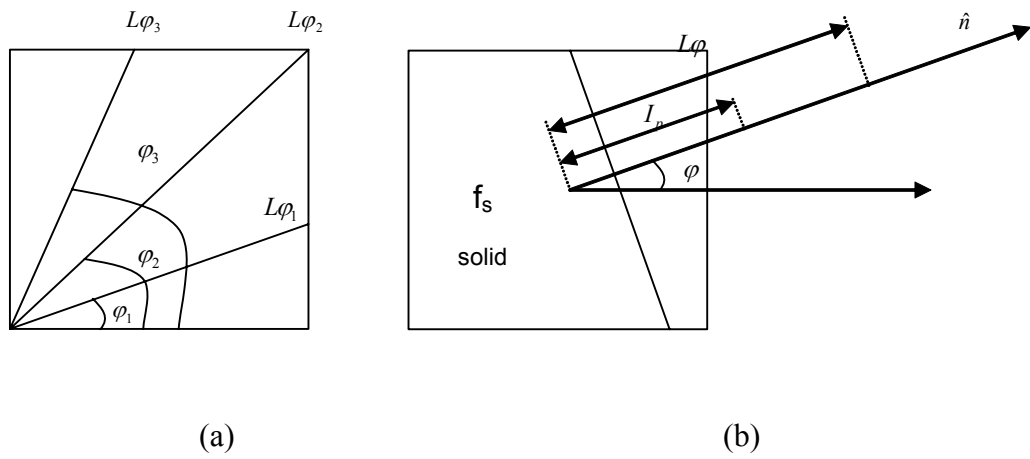


Figure 4.1 Illustration of determining the sharp S/L interface position

4.2.2 Capture Rules

In the front-tracking model, grains grow by capturing new S/L interface cells during solidification, where capture rules are applied. In capture rules, conditions for capturing new S/L interface cells are defined.

The virtual front-tracking model described in Chapter 3 can solve capturing new interface cells. However, during dendritic growth, for a growing cell, there are several sorts of neighbouring status. As shown in Figure 4.2, among neighbouring cells of a growing cell (i, j), there could be 2-4 interface cells, 1-5 solid cells and 1-5 liquid cells. When applying the capture rules, these different situations must be solved separately, as

for each of them, different kinds of neighbouring interface cells are involved when calculating the position of the S/L interface and different kinds of liquid cells are scanned when determining new interface cells. Therefore, when looking at a growing cell, not only the status of all its neighbouring cells should be checked, but also which kind of situation should also be checked out. Different solutions must be applied for these situations. This method not only leads to difficulty in numerical treatment but also seriously increases computational cost.

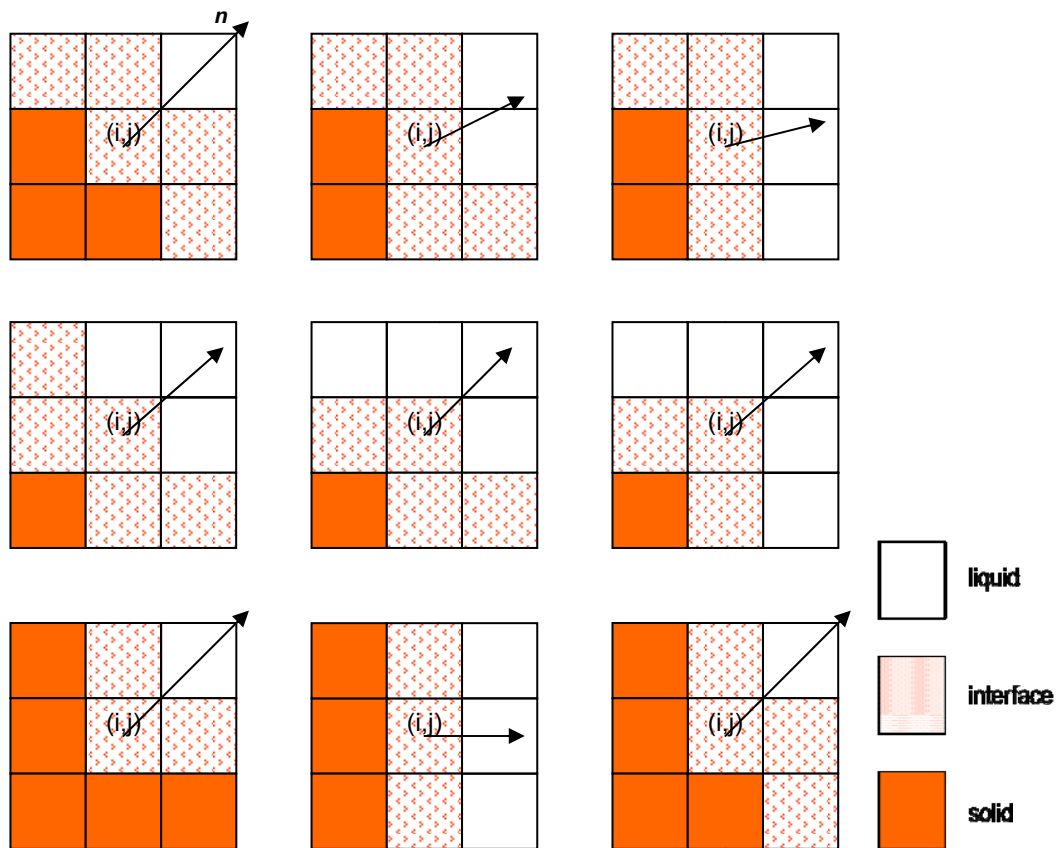
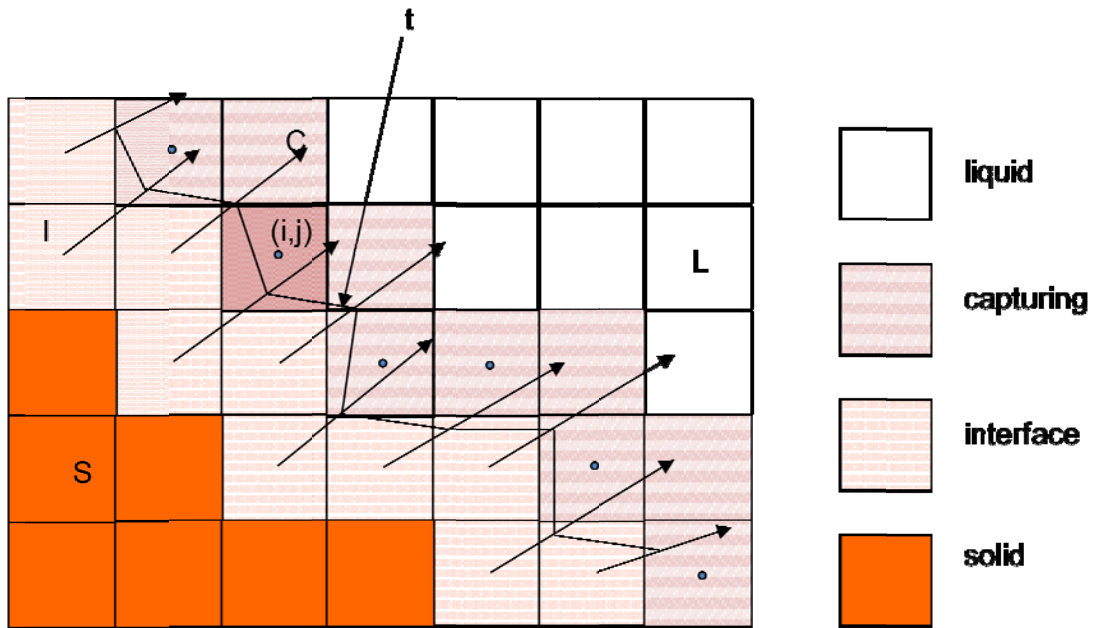
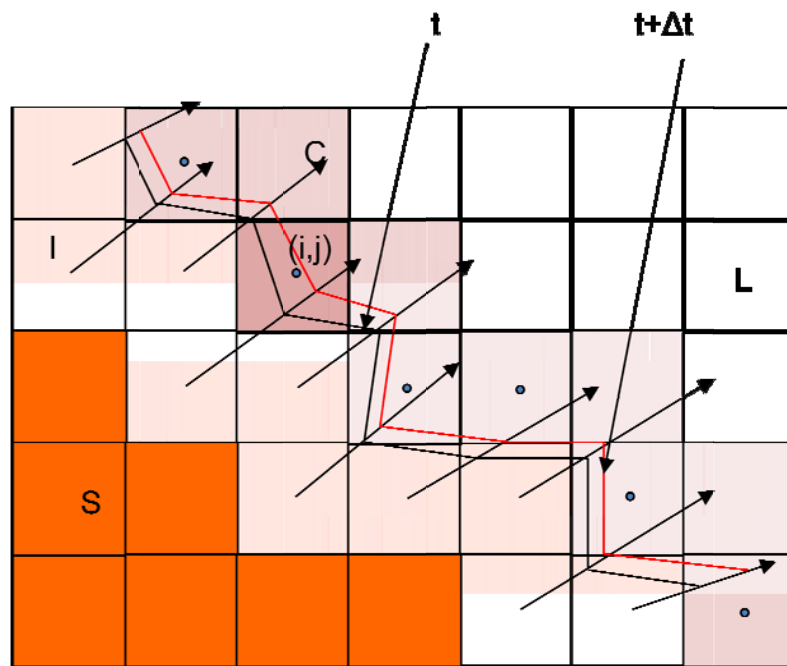


Figure 4.2 Cases of neighbouring cells

To solve the above problems, a new capture rule is proposed and implemented. A 2D rectangular computation domain is divided into a uniform orthogonal arrangement of cells. At present, cell spacing equals mesh size. Each cell is characterized by several variables, such as status, temperature, concentration, crystallographic orientation, solid

fraction, etc. As shown in Figure 4.3, the whole domain is divided into four states: liquid ($f_s = 0$), solid ($f_s = 1$), S/L interface ($0 < f_s < 1$) and capturing cells ($f_s = 0$). The capturing cells are all those liquid cells that can possibly be captured as new interface cells at the current time step. These cells are located between liquid and S/L interface cells. During grain growth calculation, capturing cells are scanned. If the center of a capturing cell lies inside the area surrounded by the sharp interface lines and meanwhile satisfying the condition that at least one of its eight closest neighbouring cells is solid, this capturing cell becomes a newly captured interface cell. For example, as shown in Figure 4.3(a), cell (i, j) remains in capturing at time step t , since its center is located outside the interface line. However, at next time step $t + \Delta t$, the interface line has moved past the center of cell (i, j), as shown in Figure 4.3(b). Meanwhile, one of its neighbours, cell (i-1, j-1), has been solid. Thus, the cell (i, j) changes its state from capturing to interface and can start growing in time step thereafter.

(a) Time step t (b) Time step $t + \Delta t$ **Figure 4.3 Capture rules for new interface cells**

S-solid cells, I-interface cells, C-capturing cells, L-liquid cells

4.3 Numerical Treatment

The flow chart of program built based on the model is shown in Figure 4.4. It mainly contains three modules, initialization, main calculation and results output. In main calculation module, it involves temperature field calculation, solute field calculation, solid fraction calculation for growing cells and grain growth calculation.

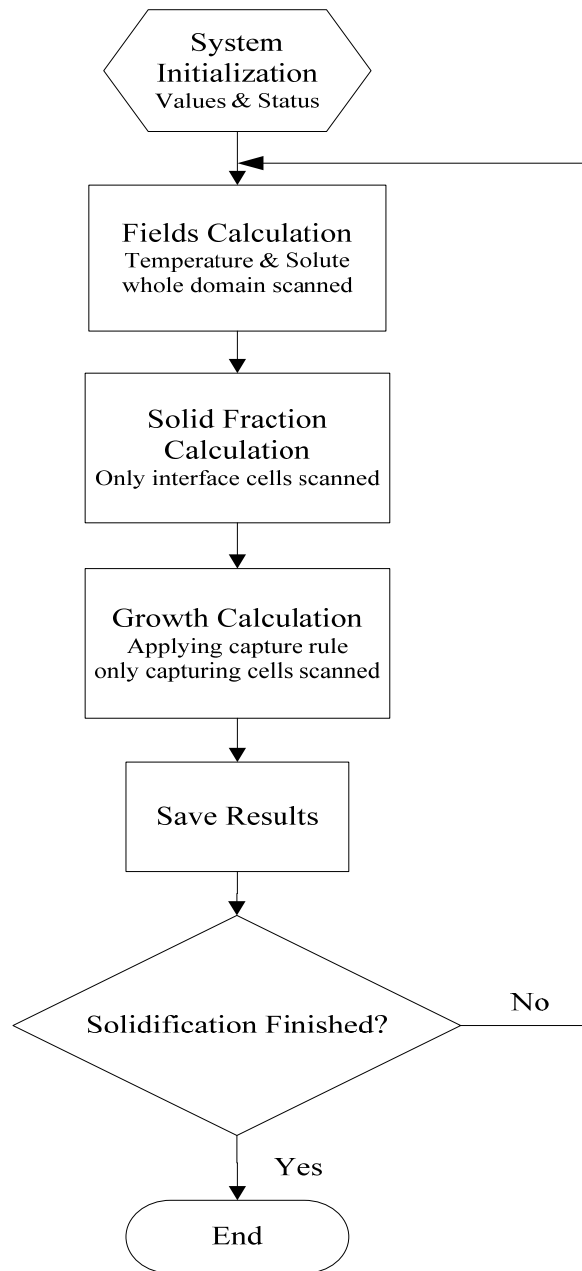


Figure 4.4 Flow chart of the model

4.3.1 System Initialization

At the beginning of the simulation, the system is initialized. All variables and parameters are given initial values. Also, one or more seed(s) of grain are set in the domain, following which cells of the domain are given status according to their positions regarding to the seed cells. The definition of a seed is shown in Figure 4.5. The seed is set to be a circle with radius of r_0 , which is defined as a number of cells. The value of r_0 varies with seed and mesh size.

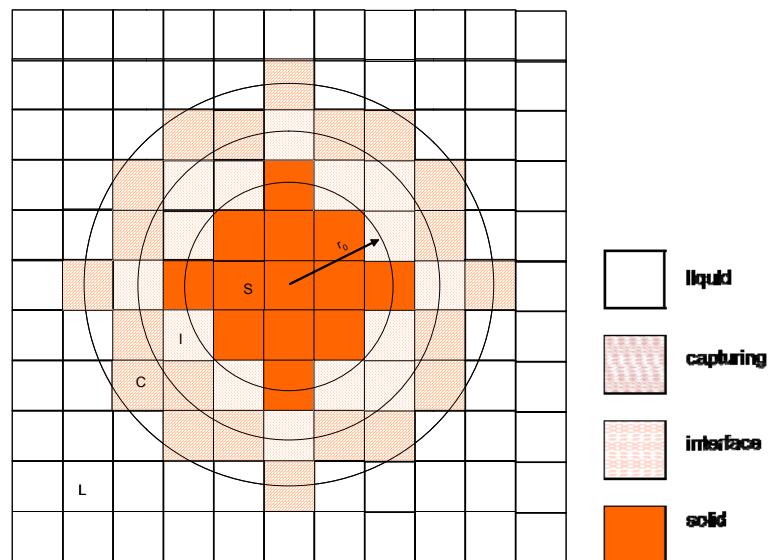


Figure 4.5 Definition of grain seed

S-solid cells, I-interface cells, C-capturing cells, L-liquid cells

4.3.2 Main Calculation

After initialization of the system, the main calculation loop starts. In this part, the temperature field, solute field, solid fraction of interface cells and growth are solved. With a preset time interval, results, including temperature, solute composition, solid fraction, and system status, are saved into different data files. As the solid fraction of interface cells, which is needed for new interface capture calculation, must be calculated

with the values of temperature and solute composition, temperature and solute field, solid fraction of interface cells and grain growth are calculated in turn separately. During each time step, the whole domain is firstly scanned. For each cell, parameters needed for calculation of heat and mass transport are solved and then calculation of temperature and solute field is done with these parameters. Secondly, with the values of temperature and solute composition, all interface cells are scanned and solid fraction of these cells is calculated. At last, new interface cell capturing is calculated based on the solid fraction of interface cells of current time.

4.3.3 Grain Growth Calculation

According to the capture rules, to calculate new interface cell capture, only capturing cells need to be scanned. The flow chart of capture rules is shown as Figure 4.6. During solidification, for cells in capturing layer, only those cells whose centre is covered by new S/L interface of current time and at least one of neighbouring cells is fully solidified currently can be captured as new interface cells. To improve computational efficiency, the neighbouring cells' status is checked firstly when scanning a capturing cell. If the capturing cell doesn't satisfy the condition that at least one of its eight closest neighbouring cells is solid, there is no need to calculate new S/L interface position and the cell will be neglected and next capturing cell will be scanned. Otherwise, calculation of new S/L interface position from solid fraction of neighbouring cells will be carried out. If the capturing cells satisfies both conditions of the capture rules, then it can be captured as a newly interface cell.

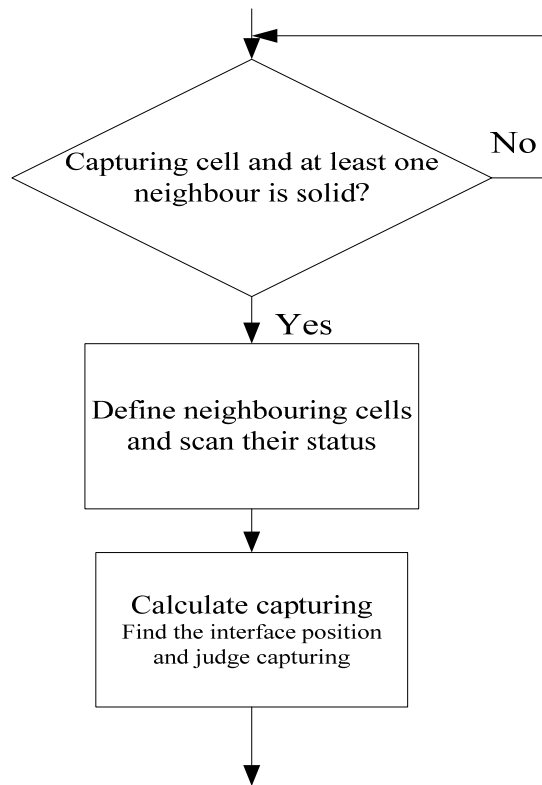


Figure 4.6 Flow chart of capture rules

As defined in the model, among eight closest neighbouring cells of a capturing cell, there must be capturing, liquid and S/L interface cells. However, there can be several kinds of situations, such as different numbers of cells of each kind of status and different positions of these cells. As shown in Figure 4.7 (a), the new S/L interface position is calculated from the center position and solid fraction of those neighbouring cells which are in interface status. Therefore, when checking status of a capturing cell's neighbouring cells, number and position of interface cells must be found out. Considering efficient numerical treatment, a 2 dimensional array with 9 rows and 2 columns is defined to store the information of 8 neighbouring cells. As shown in Figure 4.7(b), rows 1 to 7 are designed for each individual neighbouring cell and rows 0 and 8 for one same cell. By this setting, when scanning neighbouring cells or calculating interface position from neighbouring cells, in each loop scanning from rows 0 to 7, both

present and next elements can be read or write without distinguishing the position in the array.

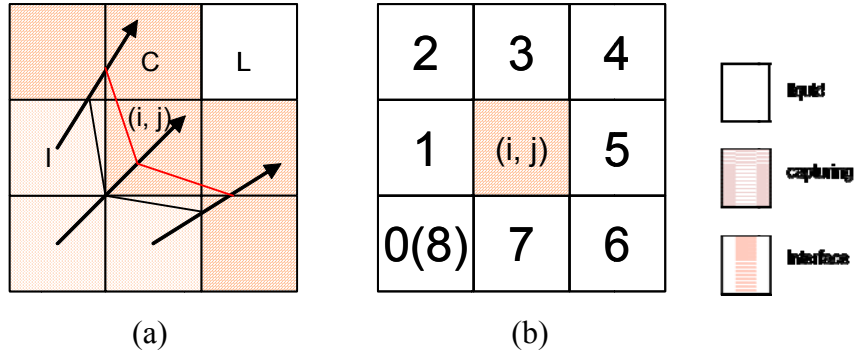


Figure 4.7 Numerical treatment of neighbouring cells

(a) Calculate S/L interface position from neighbouring cells (b) Setting of neighbouring cells

The S/L interface positions are calculated from 2 adjacent neighbouring interface cells of cell(i,j). There are also different kinds of situations when calculating interface position. As shown in Figure 4.8(a), the old S/L interface position L1 can be gained from points P10(x_1,y_1) and P20(x_2,y_2), which are the S/L interface positions at current time step of 2 neighbouring interface cells separately. The new S/L interface position L2 can be obtained in same way from points P11(x_3,y_3) and P21(x_4,y_4), which are the Ip positions at next time step of these 2 neighbouring interface cells separately. Normally, the equations for L1 and L2 can be given as Eqs 4.13 and 4.14 separately.

$$y = y_1 + \frac{y_2 - y_1}{x_2 - x_1} (x - x_1) \quad (4.13)$$

$$y = y_3 + \frac{y_4 - y_3}{x_4 - x_3} (x - x_3) \quad (4.14)$$

Together with the center position of cell(i,j), it can be found out if the center of the cell is located between these 2 S/L interfaces. However, during grain growth, the S/L

interfaces can be of any directions. Although L1 and L2 cannot be one in horizontal and other one in vertical direction, there are many kinds of situations. When looking at L1, there are 2 special positions, horizontal and vertical as shown in Figure 4.8(b) and (c) separately. For the horizontal case, Eqs. 4.13 and 4.14 can still be applied as normal situation. For the vertical case, where these 2 equations cannot be used, there are also different kinds of situations as shown in Figure 4.8(d) and (e). Besides, there is also another case as shown in Figure 4.8 (f), where L2 is vertical. All cases involved vertical position must be treated separately, where comparison of coordinates of P10, P20, P11, P21 and cell (i,j) is needed.

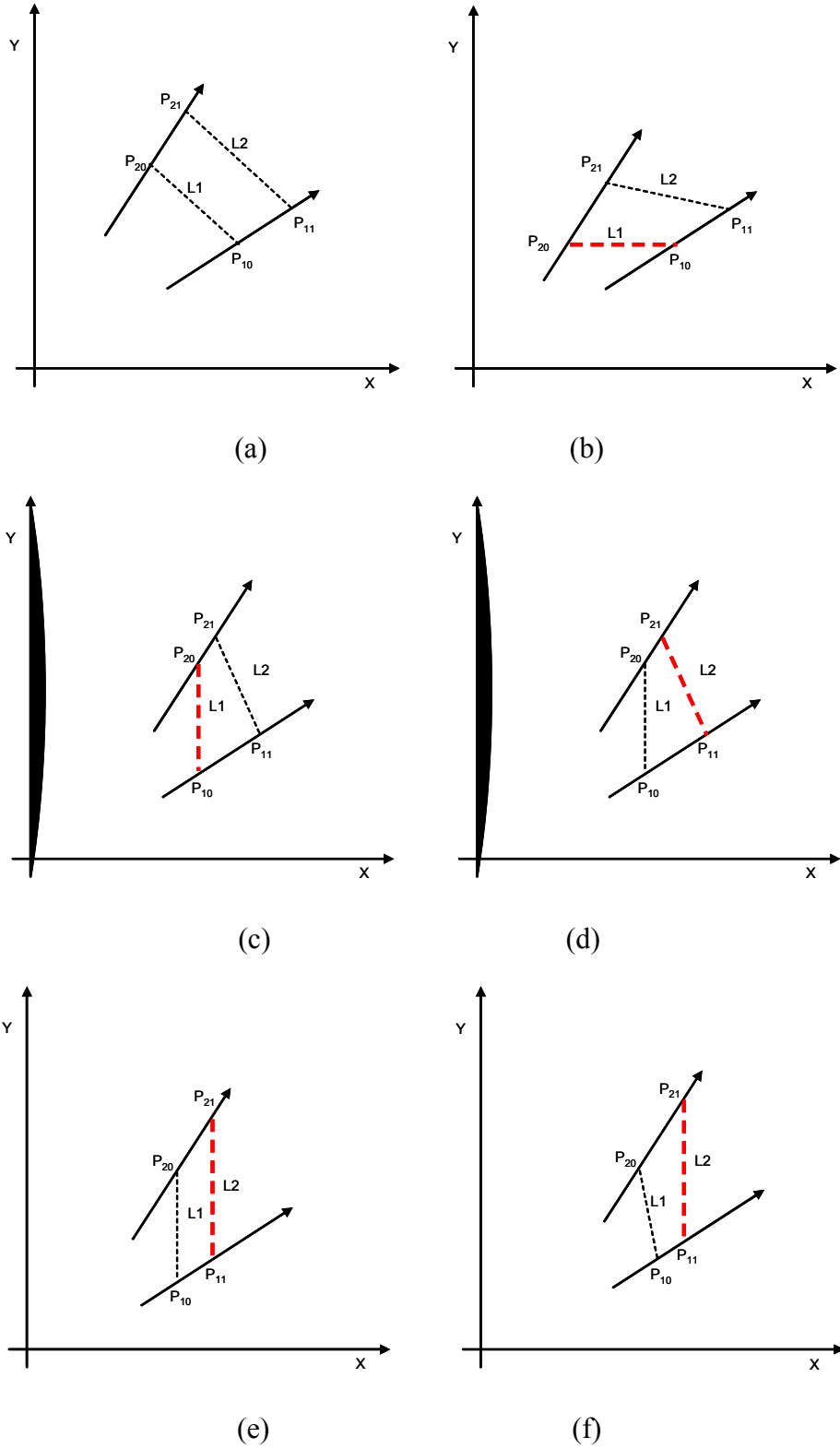


Figure 4.8 Calculation of S/L interface position

4.3.4 Simulation Program

The program, based on front-tracking model for solidification of binary alloys is written in C language under Linux system, and its structure mainly contains three sections: initialization module, calculation module and result outputting module. In the initialization module, both initial conditions and boundary conditions are defined, including defining size of sample and cell, initializing variables for temperature field and phase field and setting thermodynamic and kinetic parameters. All the calculations for heat transfer, solute diffusion and some relevant parameters are made in the calculation module. For each time step, the parameters which vary with the change of the temperature field and mass concentration are calculated firstly. With these new values, the new temperature field and mass concentration are then calculated. Finally, with a preset time interval, the results are saved into hard disk in text file in the outputting module.

At this stage, the grain is pre-fixed at the starting of calculation. Once the pre-fixed grain is chosen, a growth number (0-90 for angle $0-\pi/2$) for growth direction of the grain is given as well, which can also be used to identify different cells. During the calculation, the pre-fixed grain begins to grow. When the grain has grown big enough, one or several of its neighbour cells are then captured and become new growing points, with the same growth number and growth direction as the current grain.

The Flow chart of the main program is as following.

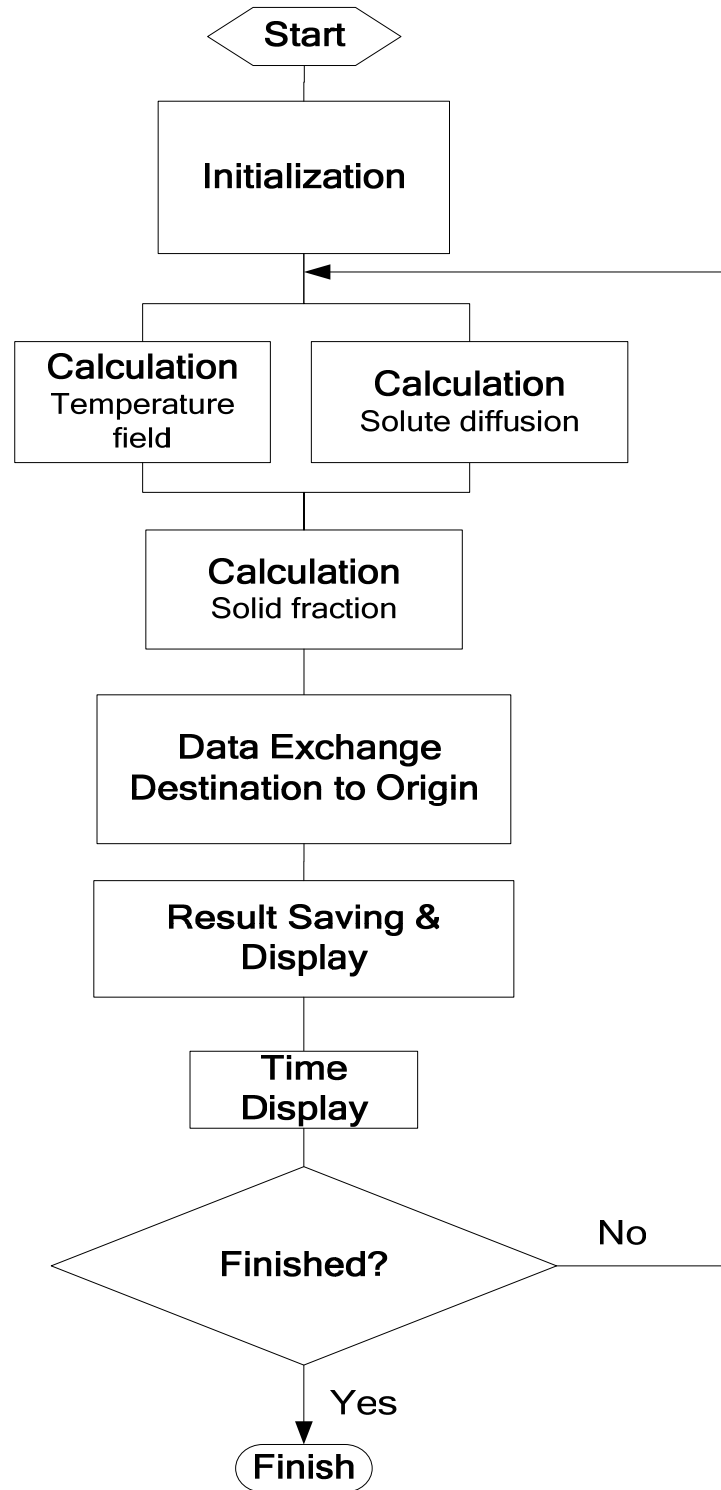


Figure 4.9 Flow chart of program for front-tracking model

Chapter 5 Model Evaluation

According to the model definition, the crystal growth rate is mainly governed by heat and mass diffusion and the S/L interfacial curvature. The growth direction, shape and kinetics of dendrites are influenced by the anisotropy of the chemical potential, which is linked to the anisotropy of the interfacial energy. In this chapter, the model evaluation will be carried out. In the early model developed, the crystal could not grow along the given preferential crystallographic orientation. To solve this problem, firstly, model analysis will be given based on some initial simulation trials. Secondly, according to the analysis results, effect of possible factors on dendritic morphology development will be examined in details. These factors include undercoolings, approximation in solving the solute redistribution during solidification, parameters in capture rule and parameters in solving curvature undercooling. By analysis of all these factors step by step, the model will be improved. In this chapter, solidification of an Al-4wt. %Cu alloy is calculated. For all simulations, the grid size is used as 1e-6m and the time step is used as 1e-6s. Materials parameters used are from literature (Echebarria *et al.* 2004; Rebow&Browne 2007).

Simulations have been performed for basic model evaluation with the developed model with some initial trials. The detailed results and discussions are given in Appendix B. According to the results and discussions, it can be found that the anisotropy of surface tension has no significant effect on grain growth, and, therefore, the crystal could not grow along the preferential crystallographic orientation even with one order magnitude

bigger of anisotropy. As a solute field controlled model, the contribution of anisotropy of surface tension to the solute distribution is introduced via curvature undercooling. In following section, analysis and investigation will start from the solution of solute redistribution.

5.1 Model Analysis

In the model, solute concentration at the S/L interface is calculated using the Eq. 5.1 for a simplified binary system, as shown in Figure 5.1.

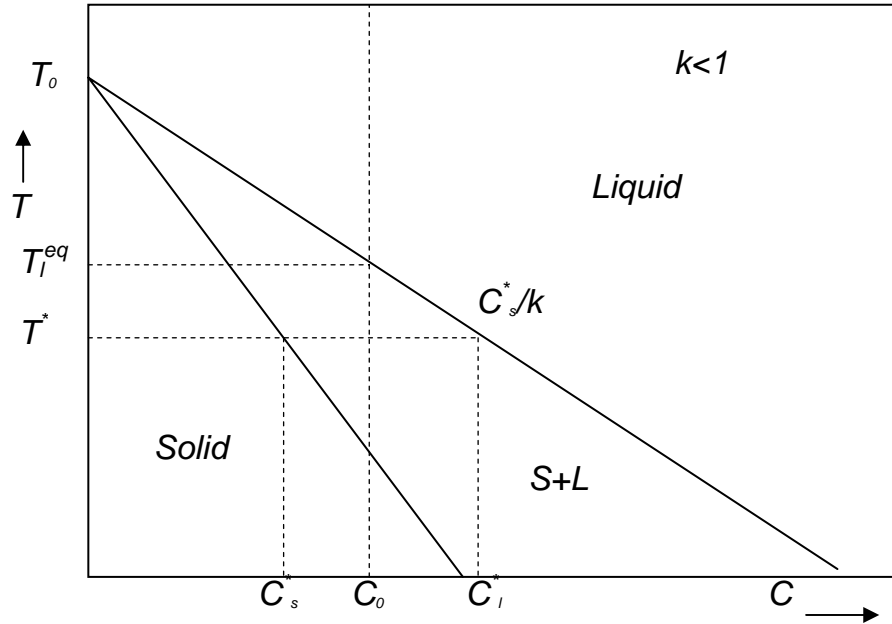


Figure 5.1 A binary phase diagram with a liquid and a primary solid

$$C_l^* = C_0 + \frac{T^* - T_l^{eq}}{m_l} + \frac{\Gamma K f(\varphi, \theta)}{m_l} \quad (5.1)$$

$$f(\varphi, \theta) = 1 - \delta \cos[\lambda(\varphi - \theta)] \quad (5.2)$$

$$K = \frac{1}{a} \left(1 - 2 \frac{f_s + \sum_{i=1}^N f_s(i)}{N+1} \right) \quad (5.3)$$

Where, Γ is the Gibbs-Thomson coefficient. K is the S/L interface curvature which is determined using Eq. 5.3; in Eq. 5.3, a is the cell size, f_s is the solid fraction of the cell, $f_s(i)$ is the solid fraction of neighbouring cell and N is the number of neighbouring cells counted. Anisotropy of the surface tension $f(\varphi, \theta)$ can be calculated using Eq. 5.2, where ζ is the local growth angle between the local S/L interface normal and x-axis; θ is the preferential crystallographic orientation; ζ is the degree of anisotropy; λ controls the number of dendritic arms. The value of interface curvature calculated using Eq. 5.3 varies from a maximum of $1/a$ to zero for convex surfaces, from zero to a minimum of $-1/a$ for concave surfaces.

5.1.1 The Movement of S/L Interface

During solidification, the S/L interface moves into liquid in an undercooled melt. As defined in the model, the S/L interface position is calculated directly by the solid fraction f_s of the interface cells. Therefore, for a certain time period, the movement of the S/L interface is determined by the increase of solid fraction in the interface cells.

For a certain time period such as one time step, the S/L interface moves forward a certain distance according to the solid fraction increase in the interface cells, where the increase of solid fraction can be calculated by:

$$\Delta f_s = \frac{C_l^* - C_l}{C_l^*(1-k)} \quad (5.5)$$

where C_l is the local actual composition (average liquid concentration in the growing cell) in liquid of the interface cell. The solute rejected accordingly, due to the difference in solubility between solid and liquid, can be calculated by:

$$\Delta C = (1 - k) * C_l * \Delta f_s \quad (5.6)$$

In return, during the next time step, C_l will be modified by the solute redistribution due to the rejected solute.

It can be seen from Eq. 5.5 where k is constant, the solid fraction increase is therefore determined by C_l^* and C_l . For a uniform system, where the current interface temperature T^* and the equilibrium liquidus temperature T_l^{eq} are both constant, C_l^* varies only with

$\frac{\Gamma K f(\varphi, \theta)}{m_l}$

curvature undercooling contribution, in which the preferential crystallographic orientation φ is introduced. The increase of solid fraction is supposed to vary with curvature undercooling in different directions, and therefore the growth rate of the S/L interface varies which will lead crystal to grow along φ . To check this variation, it is need to check how C_l^* and C_l of the interface cells change during calculation.

5.1.2 Interface Cells Concentration Change with S/L Interface Movement

To check how the solute field is redistributed during calculation, it is necessary to start from the calculation of composition in interface cells from the beginning of the calculation. For a given condition as $T_l^{eq}=921.15K$, $k=0.17$, $T^*=917K$, $C_0=4.0wt.\%$ and $m_l=-2.6$, where uniform undercooling can be obtained, calculations have been performed without and with considering curvature undercooling separately.

5.1.2.1 Without Curvature Undercooling

For the case of not considering curvature undercooling, for all interface cells, where there is a uniform undercooling ($T^* - T_l^{eq}$), C_l^* can be determined by Eq. 5.1 as:

$$C_l^* = 4.0 + \frac{917 - 921.15}{-2.6} = 5.596 \text{ wt. \%} \quad (5.7)$$

Therefore, the increase of solid fraction of the interface cells depends on C_l , as both C_l^* and k are constants.

$$\Delta f_s = \frac{5.596 - 4.0}{5.596 * (1 - 0.17)} = 0.3436 \quad (5.8)$$

Accordingly, the solute rejected from solid into liquid is:

$$\Delta C = (1 - 0.17) * 4.0 * 0.3436 = 1.1408 \text{ wt. \%} \quad (5.9)$$

It can be seen, when an interface cell has a lower concentration C_l , it will have a larger solid fraction increase Δf_s . As a result, there will be more solute rejected into the liquid. In the following time step of calculation, this cell will still have a relatively higher C_l , which will lead to less solid fraction increase.

5.1.2.2 With Curvature Undercooling

For the case of considering curvature undercooling, calculation has been carried out with applying the same conditions as above. In order to track the change of solid fraction in interface cells, interface cells have been recorded step by step from the beginning of the calculation, with applying a time step of $dt = 1e-6 \text{ s}$.

Step1:

A solid seed with surrounding interface cells is set in the system. All these interface cells have same curvature undercooling, and therefore they have same increase of solid fraction. After the first step calculation, they have the same solid fraction as:

$$f_s = 0.3436 \quad (5.10)$$

Accordingly, for all these interface cells, there is same amount of solute rejected into liquid.

Step2:

But, after the calculation of solute diffusion, depending on the position as shown in Figure 5.2, the local composition in liquid of interface cells becomes:

$$C_l = 4.6338 \text{ or } 4.8872 \text{ wt. \%} \quad (5.11)$$

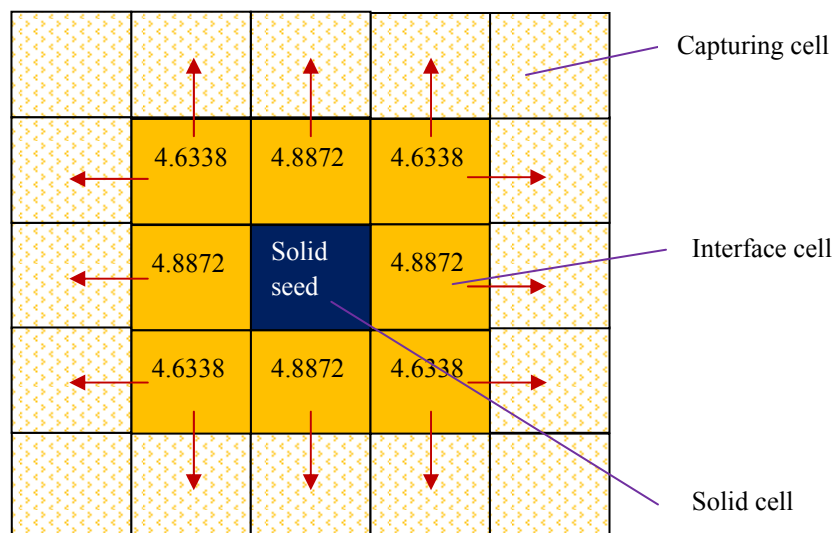


Figure 5.2 Concentration in liquid of interface cells and solute diffusion

The difference is caused by the method of solute transport calculation. In the model, the calculation of solute diffusion is solved by an explicit finite difference scheme, in which the left, right, up and down neighbouring cells are involved. The arrows in Figure 5.2 show the directions of solute diffusion. It can be seen, for those interface cells in which solute can be diffused away into two capturing cells, there is lower concentration in the liquid. There is higher concentration in the liquid for other interface cells which can only diffuse solute away into one capturing cell. Therefore, after the first step calculation, for interface cells, there are different compositions in liquid. This difference will be eliminated as calculation carries on. Meanwhile, C_l^* in different interface cells varies due to curvature undercooling. Finally, there is same increase of solid fraction.

$$f_s = 0.3636 \quad (5.12)$$

Step3:

As calculation carries on, in the third step calculation, the local composition in liquid of interface cells becomes

$$C_l = 4.4648 \text{ or } 4.7463 \text{ wt. \%} \quad (5.13)$$

And, again, all interface cells have same solid fraction increase as:

$$f_s = 0.5636 \quad (5.14)$$

From the above calculation, it can be found that the increase of solid fraction in interface cells, which determines the growth rate of the S/L interface, is decided by both the calculation of both C_l and C_l^* . As the curvature undercooling contribution is

supposed to dominate the dendritic growth direction and this contribution is much smaller compared with that of undercooling due to concentration difference, where curvature undercooling is about a few percent of the undercooling due to compositional difference, high accuracy is required for the calculations of not only C_l^* but also C_l . For the calculation of C_l^* , it involves solving interfacial curvature, anisotropy of surface tension and curvature undercooling. As for C_l , the calculation accuracy mainly depends on approximation for solving C_l and the accuracy of solute diffusion calculation. In the following section, investigation will be carried out on these aspects.

5.2 Effect of Thermal Undercooling and Curvature Undercooling

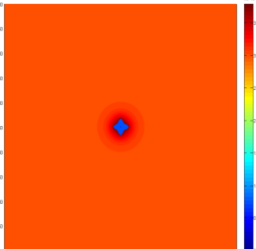
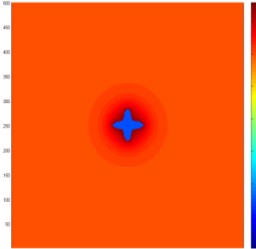
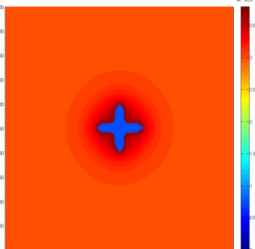
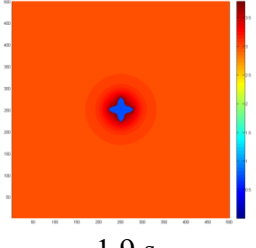
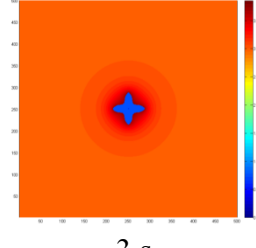
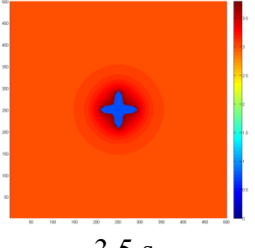
In the model, the curvature undercooling is introduced when solving the current composition in liquid of interface cells, as the third item of right hand of the Eq. 5.1. To

investigate the curvature effect, the item $\frac{\Gamma K f(\varphi, \theta)}{m_l}$ has been solved with different values of parameters under different thermal undercooling.

5.2.1 Dendritic Growth under a Thermal Undercooling of 2K

Simulations have been performed for the Al – 4wt. % Cu alloy at undercooling of 2K. In the calculation, $\delta=0.08$, $\lambda=4$ and $\Gamma=1e-6Km$ were applied for solving curvature undercooling. The other conditions are the same as those used in previous calculations. The simulated dendritic morphologies and composition fields, in which different colours represent different compositions, are as shown in Table 5.1.

Table 5.1 Investigation of grain growth with different preferential directions

Case No.	θ	Simulation results		
1	25°	 0.8 s	 2.3 s	 4.3 s
2	1°	 1.9 s	 3 s	 3.5 s

For case 1 in Table 5.1, it can be seen, under the current conditions, the crystal cannot grow along the given preferential crystallographic orientation of $\theta=25^\circ$, which is not as expected. For case 2 in Table 5.1, Figure 5.3 shows the solute profile along the central of dendritic arm at simulation time of 1.9 s and Figure 5.4 shows the late stages of grain growth. During the late stages of grain growth, more and more solute is rejected through the S/L interface from solid side into liquid side, which leads to solute enriched in the liquid. As the undercooling is constant, the thermal undercooling becomes smaller in the concentrated solution when compared to that in dilute solution at the early stages of the grain growth. Consequently, the dendritic tips become more and more flat.

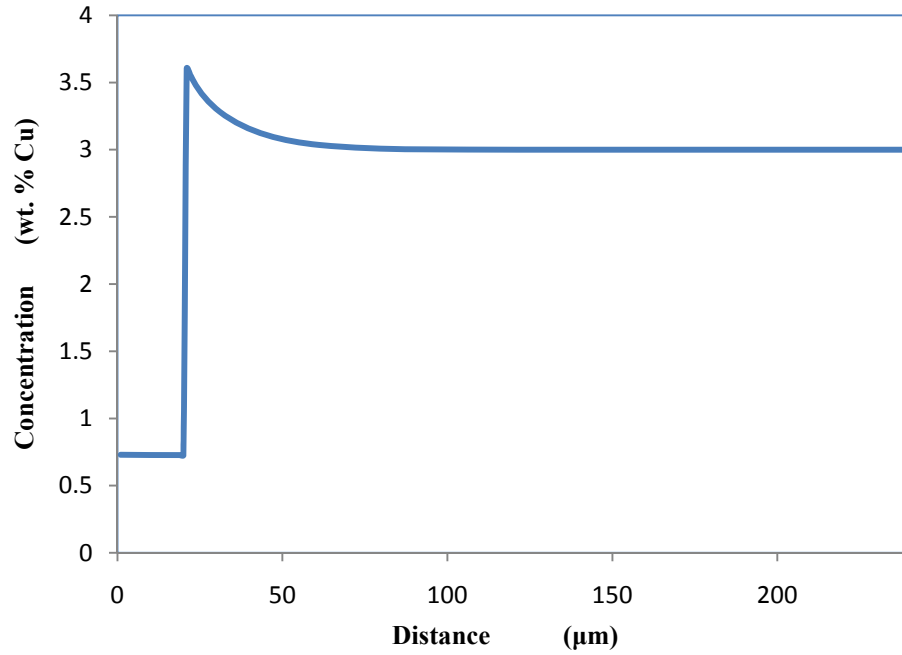


Figure 5.3 Solute profile along dendritic arm

Simulation time: 1.9 s

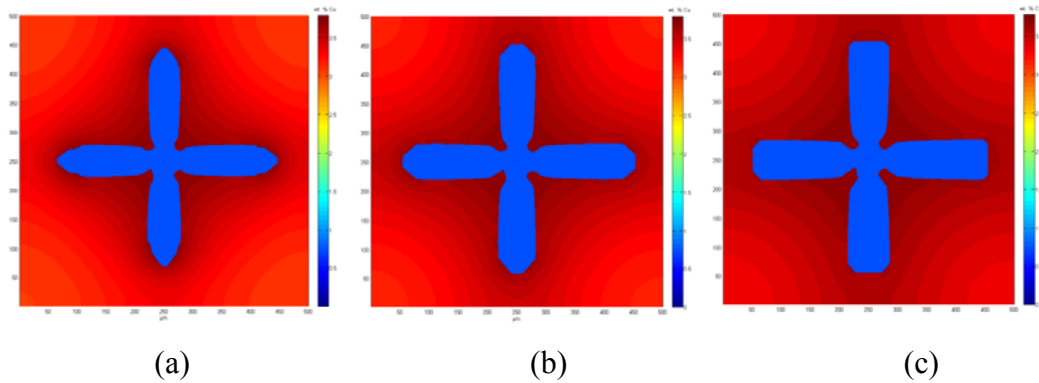


Figure 5.4 Late stages of grain growth

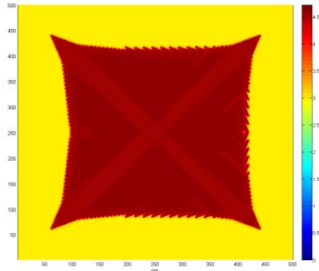
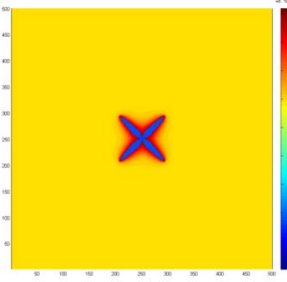
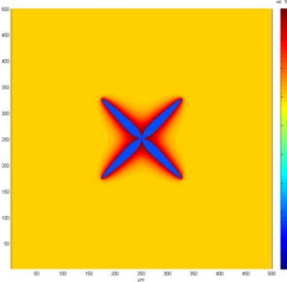
Simulation time: (a) 35 s, (b) 45 s and (c) 60 s

5.2.2 Dendritic Growth under a Thermal Undercooling of 3K

For the case of undercooling of 3K, $\delta=0.08$, $\lambda=4$ and $\Gamma=1e-6Km$ were applied for the calculation of curvature undercooling. Other conditions are as same as used in previous

calculations. The simulated dendritic morphologies and composition fields are as shown in Table 5.2.

Table 5.2 Investigation of grain growth with different preferential directions

Case No.	θ	Simulation results	
1	1°	 <p style="text-align: center;">30 s</p>	
2	45°	 <p style="text-align: center;">3 s</p>	 <p style="text-align: center;">6 s</p>

As it is known, for convex surface, the curvature undercooling will slow down the S/L interface growth rate. Therefore, there is largest deduction on the S/L interface growth rate at dendritic tip due to the most convex surface. To check if the curvature undercooling functions as it is expected in the current model, calculation has been performed with a particular situation, where the reversed curvature effect condition has been applied. This can be achieved by applying $\Gamma = -1e-6Km$.

The simulated results with reversed curvature undercooling effect are shown as case 2 in Table 5.2. Compared with the results of case 2 in Table 5.1, it can be found, at same simulation time of 3s, the dendrite arms become much longer and thinner, which means

that the S/L interface growth rate at the dendritic tip is significantly increased by the reversed curvature undercooling effect. Figure 5.5 shows the solute profile along the central of dendritic arm. It can be found that the slope ahead of the S/L interface is very deep which means the enriched solute layer ahead of the S/L interface is very thin. The solute rejected into liquid from solid during grain growth has not been distributed enough into the liquid far away from the S/L interface. An interesting thing is that during late stage of the grain growth, the prior growth direction changes from 45° degree to 0° degree, as shown in Figure 5.6. In the model, the growth velocity of the S/L interface is calculated from the increase of solid fraction in growing cells, which is determined by C_l^* and C_l according to Eq. 5.5. As the calculations of both C_l^* and C_l involve curvature undercooling, which is in a small value but dominates the dendritic growth direction, this unexpected phenomenon could be caused by the poor curvature model, which weakens the curvature effect and makes the grid effect become the main factor in controlling the dendritic growth direction.

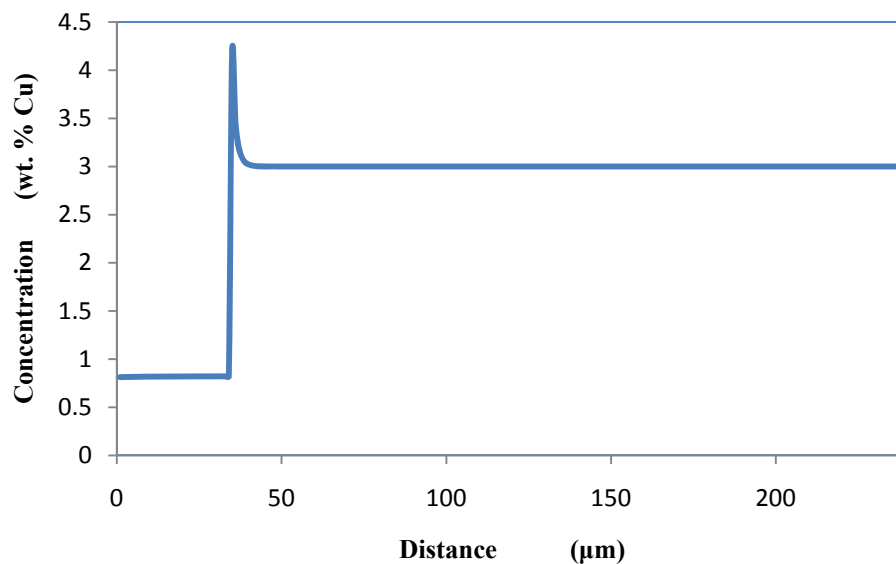


Figure 5.5 Solute profile along dendritic arm

Simulation time: 3 s

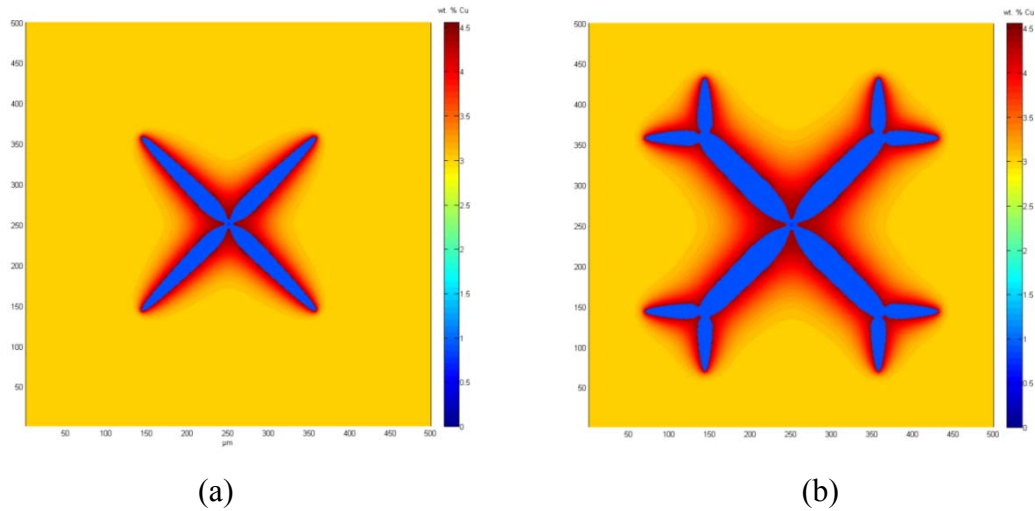


Figure 5.6 Late stages of grain growth

Simulation time: (a) 10 s and (b) 20 s

Furthermore, during the simulation, sometimes, it can be found that the grain stops growing. On checking the debugging information, it can be found that the local interface equilibrium composition C_l^* is smaller than the local actual liquid composition C_l , and therefore, there is no solid fraction increase. This particular situation happens in the solidification under small thermal undercooling, and when the curvature undercooling is very large. During the calculation, when C_l^* is smaller than C_l , the cell will not grow within the current time step.

From the above simulation results and discussion in this chapter, it can be found that, besides the calculation of curvature undercooling, the solute redistribution in the remaining liquid during solidification plays an important role in determining the grain growth. As the calculation of solute transport during solidification is so important, it is necessary to investigate the effect on grain growth under different methods for solving solute diffusion. In the following study, simulations will be carried out applying different ways to solve the solute diffusion problem.

5.3 Effect of C_l Approximation in a Growing Cell

In solving the solute redistribution during solidification, the key issue is the calculation of the local actual liquid composition C_l . On one hand, the increase in solid fraction is directly calculated from C_l , which means the growth velocity of the S/L interface is dominated by C_l . On the other hand, the local actual liquid composition is also affected by the increase in solid fraction in return, as released solute due to solid fraction increase is added to the remaining liquid in the same interface cell. Furthermore, the local actual liquid composition is very important in the interaction between growing dendrites. During solidification, the growing grains affect each other by the solute field in liquid between them. The solute redistribution is calculated directly from the local actual liquid composition C_l , where C_l determines the solute gradient in liquid ahead of the S/L interface.

Simulations with applying different methods of solving C_l have been carried out with the developed model. For comparison, a simulation is performed for each model. In the following study, different treatments for calculation of C_l in interface cell have been applied, including the solution to solid fraction increase Δf_s and solute rejected from solid to liquid crossing S/L interface ΔC and how to add ΔC into the liquid ahead of the S/L interface. Basic parameters used here are the same as those used in the previous simulation. The simulation results are as shown in Table 5.3.

Table 5.3 Predicted crystal morphologies using different approximation of C_l

Case No.	Solution	Simulation results	
		1 s	20 s
1	Zhu's model: $\Delta f_s = (C_l^* - C_l) / [C_l^*(1 - k)]$ $\Delta C = (1 - k) * C_l * \Delta f_s$ To add the rejected solute to the remaining liquid of current interface cell.		
2	Developed model: $\Delta f_s = (C_l^* - C_l) / [C_l^*(1 - k)]$ $\Delta C = (1 - k) * C_l^* * \Delta f_s$ To add the rejected solute to liquid of the current interface cell and its surrounding liquid cells.		
3	Developed model: $\Delta f_s = (C_l^* - C_e) / [C_l^*(1 - k)]$ where $C_e = C_l * (1 - f_s) + C_s * f_s$ $\Delta C = (1 - k) * C_l * \Delta f_s$ To add the rejected solute to liquid of the current interface cell and its surrounding liquid cells.		

Case 1 shows the simulation results from Zhu & Stefanescu's (2007) model. It can be found that the grain does not grow when adding the rejected solute to the remaining liquid of the current cell. When checking the status of the system, it can be found the calculated composition of most cells is out of range, where *NaN* (not a number) appears. Whenever *NaN* appears, the calculation of solute redistribution and grain growth cannot be carried on. Therefore, the grain stops growing.

In case 2, the solute released during solidification is calculated using the local interface equilibrium composition C_l^* , instead of the local actual liquid composition C_l . As C_l^* is larger than C_l , there will be more solute rejected into liquid ahead of S/L interface, which will lead to smaller solid fraction increase.

Compared with case 2, the grain grows much faster in case 3. In case 3, the solid fraction increase is calculated using equilibrium composition C_e instead of C_l . As C_e is smaller than C_l , usually even smaller than the initial composition, there will be bigger solid fraction increase leading fast grain growth. An interesting thing can be found is that as the grain grows too fast liquid can be found among solid cells.

5.4 Effect of Capture Rule L_ϕ

During the simulation in chapter 5.3, according to the debugging information, at most time the cell centre of a capturing cell is exactly located on the S/L interface, when capturing happens. Sometimes the capturing cell failed to be captured as a new interface cell, due to the accuracy of numerical treatment. For example, when the location of a capturing cell centre is (10, 10) and the new S/L interface is also located at this point, in which case the capturing cell should be captured as new S/L interface cell, the calculated position of new S/L interface could be (9.99999, 9.99999). In this case, the capturing cell will not be captured as new interface cell. This phenomenon will lead to incorrect grain growth. One of the solutions is to improve the accuracy of capture calculation, and the other way is to use larger value of the parameter L_ϕ in capture rule.

L_φ in capture rule is defined as $L_\varphi = \Delta x / \max(|\cos\varphi|, |\sin\varphi|)$, simulation has been performed with applying the L_φ and $1.01 * L_\varphi$. The simulation results are shown in Figure 5.7.

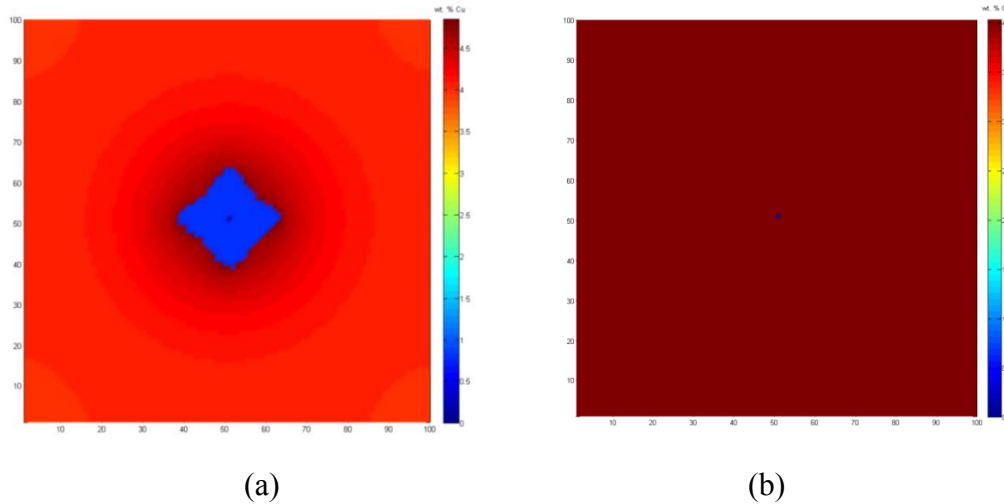


Figure 5.7 Comparison with using L_φ and $1.01 * L_\varphi$

(a) calculation using $1.01 * L_\varphi$, and (b) calculation using L_φ at simulation time of 4 s

It can be found that the crystal stops growing when applying L_φ in the calculation, where grain growth calculation is correct with applying $1.01 * L_\varphi$. On checking the debugging information during calculation, it has been found calculation of new S/L interface cell capture was correct with $1.01 * L_\varphi$. For the L_φ case, the grain stopped growing. When checking the debugging information, the status of the system around the grain seed is as shown in Figure 5.8.

$f_s=0.0$	$f_s=1.0$	$f_s=1.0$	$f_s=0.0$
$f_s=1.0$	(52,52) $f_s=1.0$	(53,52) $f_s=1.0$	$f_s=1.0$
$f_s=1.0$	$f_s=1.0$	$f_s=1.0$	$f_s=0.0$

Figure 5.8 System status when grain stops growing

As L_φ is used exactly as $\Delta x / \max(|\sin(\varphi)|, |\cos(\varphi)|)$, when an interface cell becomes totally solid, where the solid fraction $f_s=1$, the new S/L interface reaches exactly the centre of its neighbouring capturing cells. The capturing cell should be captured theoretically. However, in term of numerical calculation, this sometimes could not be captured. As a result, the surrounding status of cell (53, 52) appears as shown in Figure 5.10. Cells with $f_s=0.0$ in the figure should be captured as new S/L interface cell, but fail to be captured. This failure leads to trouble to calculate local growth angle for cell (53, 52) and therefore error occurs when calculating the S/L interface position.

It can be concluded that the fault of failing capturing new S/L interface cell can be avoided by applying $1.01 * L_\varphi$ for capture of new interface cell during calculation. In the following part, investigation of grain grow with other different parameters will be carried out, with applying $1.01 * L_\varphi$ for calculation of capturing new S/L interface cell.

5.5 Effect of Other Parameters with Applying $1.01 * L_\phi$

Firstly, simulations have been performed for solidification under undercooling of 2K. For the calculation of curvature undercooling, $\delta=0.08$, $\lambda=4$ and $\Gamma=1e-6Km$ were applied. The simulated dendritic morphologies and composition fields are as shown in Table 5.4.

Table 5.4 Investigation of grain growth with different preferential directions

Case No.	θ	Simulation results	
		1 s	3.5 s
1	5°		
2	30°		

From the above results in Table 5.4, it can be seen that the dendrite keeps growing along a certain direction, for both θ directions. As discussed at the beginning in this chapter, by increasing the effect of curvature undercooling, there will be larger increase of solid fraction for growing cell along θ direction. The increase of the curvature

undercooling effect can be achieved by using bigger value of Gibbs-Thomson coefficient.

Simulation has been performed with $\Gamma=5e-6Km$. The grain does not grow at all. The following calculations have been applied using different values of the Gibbs-Thomson coefficient. The reason is as follows. When using $\Gamma=5e-6Km$, according to the calculation of the local interface equilibrium composition C_l^* , it can be found $C_l^*=4.0+2/(2.6)+(-1.35)wt. \%$ when $\theta=45^\circ$ and $\varphi=45^\circ$, $C_l^*=4.0+2/(-2.6)+(-1.56)$ when $\theta=45^\circ$ and $\varphi=0^\circ$. So, $C_l^*=3.41wt. \%$ or $3.20wt. \%$ separately. These values are even smaller than the initial composition of the system, where $C_0=4.0wt. \%$, therefore, must be smaller than the local actual liquid composition C_l . As a result, there is no increase of solid fraction Δf_s and the grain will not grow.

Based on the above analysis, it can be seen that the Gibbs-Thomson coefficient Γ can't be too large. For a certain Gibbs-Thomson coefficient, the effect of curvature undercooling is also affected by the parameter δ and λ in solving anisotropy of surface tension. Another simulation has been performed for solidification under undercooling of 2K. In solving curvature undercooling, $\delta=0.8$, $\lambda=4$ and $\Gamma=5e-7Km$ have been applied. The simulated dendritic morphologies and composition fields are as shown in Figure 5.9.

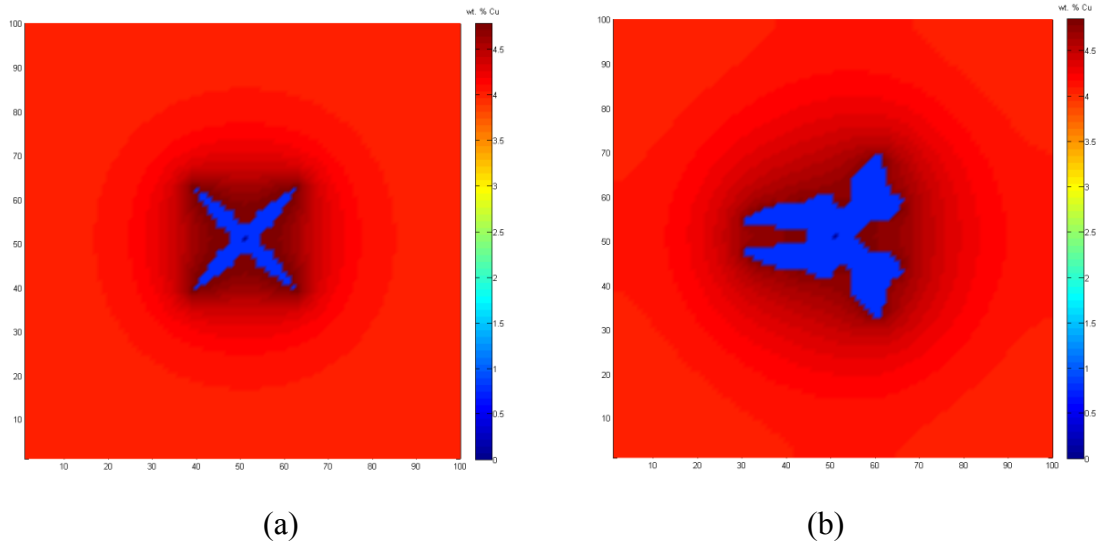


Figure 5.9 Simulated grain growth

(a) $\theta=45^\circ$, and (b) $\theta=20^\circ$ at simulation time of 2 s

From the simulated result with $\theta=20^\circ$, as shown in Figure 5.9 (b), it can be seen that at these conditions, the grain growth direction changes. In Eqs. 5.1 and 5.2, we can see that the curvature undercooling varies with S/L interface curvature and anisotropy of the surface tension, where the other two parameters are constant. In these two variable parameters, the preferential crystallographic orientation θ is only involved in the solution to anisotropy of the surface tension, which means in the curvature undercooling, anisotropy of the surface tension is the main item controlling the dendritic arm growth direction.

To investigate the effect of S/L interface curvature and anisotropy of the surface tension, simulations for solidification under undercooling of 3K have been performed. Firstly, calculation has been performed with applying only anisotropy of surface tension, where all S/L interface cells are assumed to have the same curvature. The effect of different S/L interface curvature can then be eliminated. Secondly, calculation has been performed with applying both S/L interface curvature and anisotropy of surface tension.

The simulated dendritic morphologies and composition fields are as shown in Figure 5.10.

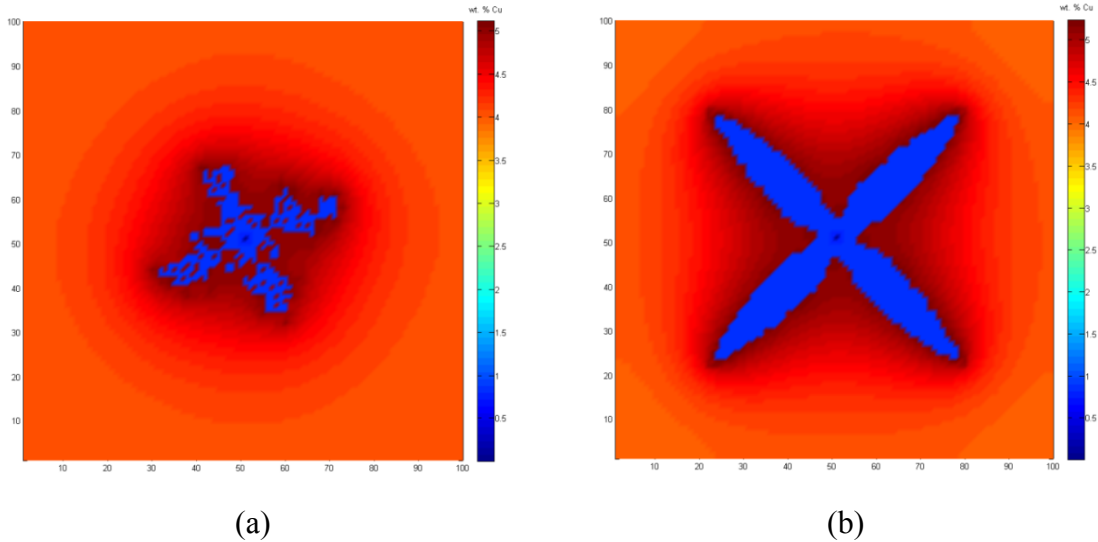


Figure 5.10 Simulated grain growth with $\theta=20^\circ$

(a) with anisotropy of surface tension only, and (b) with both anisotropy of surface tension and S/L interface curvature

In Figure 5.10 (a), it is found that the dendritic arms grow along θ angle with only taking into account of the anisotropy of surface tension. When adding curvature effect, the dendritic arm grows along 45° again, in Figure 5.10 (b). From Eq 5.1, it can be noticed, when using undercooling of 3K, the contribution due to undercooling increased (the second item on the right hand side of the equation) while contribution due to curvature undercooling keeps same value as smaller undercooling. Comparing the simulated results in Figure 5.10 (a) and (b), it can be found that, during dendrite growth, the anisotropy effect tries to pull the grain to grow along θ direction, while the effect of the poor curvature model is forcing the grain to grow along 45° . This phenomenon can also be found in the simulation for solidification under undercooling of 2K, where the contribution due to undercooling becomes smaller, as shown in Figure 5.11.

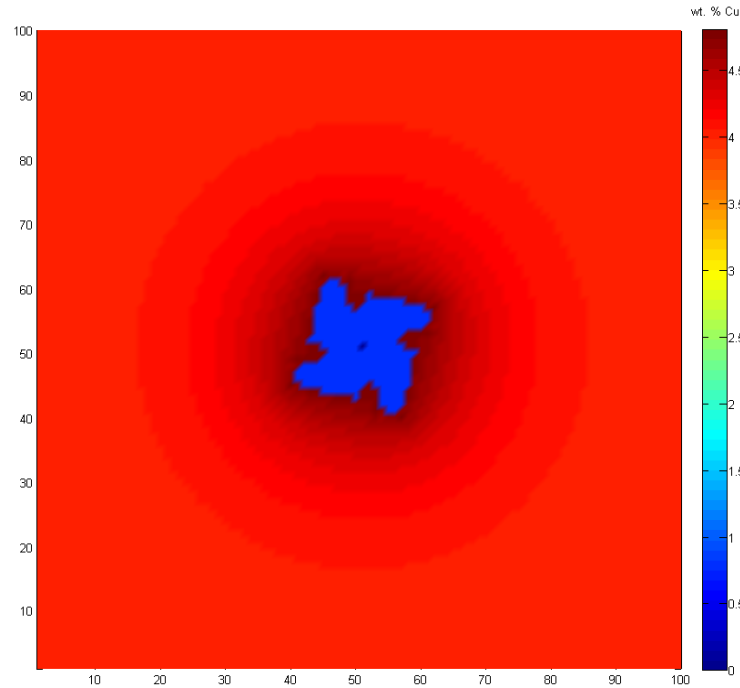


Figure 5.11 Simulated grain growth with both anisotropy of surface tension and S/L interface curvature

From above results, it can be found that during dendritic growth, the curvature effect always forces the grain to grow along 0° or 45° direction. Furthermore, growing along 0° or 45° mainly depends on the value of given angle θ . When the given θ is closer to 0° , the grain will grow along 0° and if closer to 45° then grow along 45° . To check why grain grows like this, it is necessary to check how this geometry is formed.

At the beginning of grain growth, the status of the system is shown in the Figure 5.12. For given $\theta=0^\circ$ and $\theta=45^\circ$, the formation of the dendritic tip will start from cell (i,j) as shown in the (a) and (b) separately. In these two situations, although the S/L interface is the sharpest at cell (i,j) , cell (i,j) can still become dendrite tip. However, for other given θ angle, to try to grow along θ direction, the grain must form its tip from somewhere as shown in (c). In this situation, it is more difficult for cell (i,j) to start growing, as the interface is sharper here than that in situation (a) and (b). Similar

situation will happen again during the following growth and finally the dendrite will grow to the geometry as shown in Figure 5.11. During this process, it can be noticed that the accuracy of interface curvature is very important.

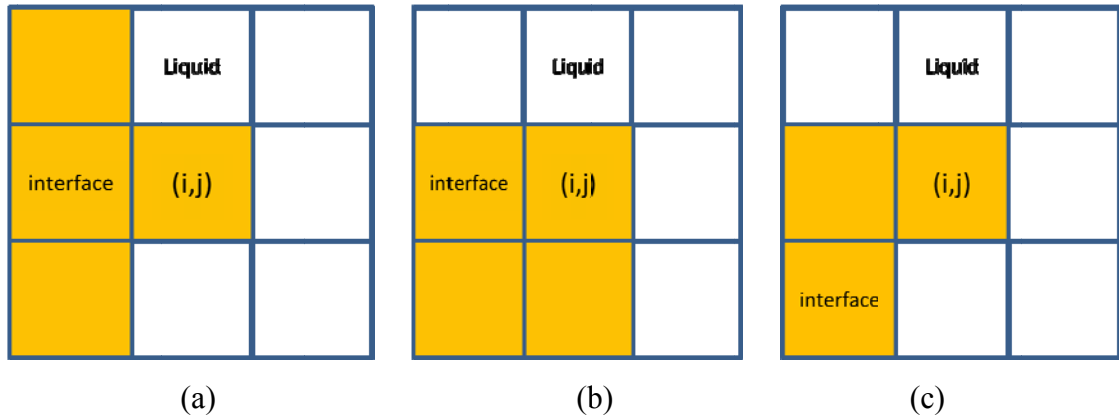


Figure 5.12 Status during grain growth

Currently, the curvature of the S/L interface has been calculated by a method checking and counting neighbouring cells status, as shown in Eq. 5.3, where, a is the cell size and N is the number of neighbouring cells counted. When using one layer of neighbouring cells, where only the nearest neighbours are counted, $N=8$ and $N=24$ for using two layers of neighbouring cells, where next-nearest neighbours are also counted. For all above calculation, one layer of neighbouring cells were used, where $N=8$. For this method, the accuracy of the calculation can be partially improved by counting two layers of neighbouring cells, where $N=24$.

Simulation of solidification under undercooling of 2K has been performed with counting two layers of neighbouring cells to calculate interfacial curvature. The simulated dendritic morphologies and composition fields are as shown in Figure 5.13. To avoid possible influence due to small domain size, a 500×500 domain has been used. It can be seen, in this situation, the dendritic arm can grow along the preferential crystallographic orientation $\theta=70^\circ$.

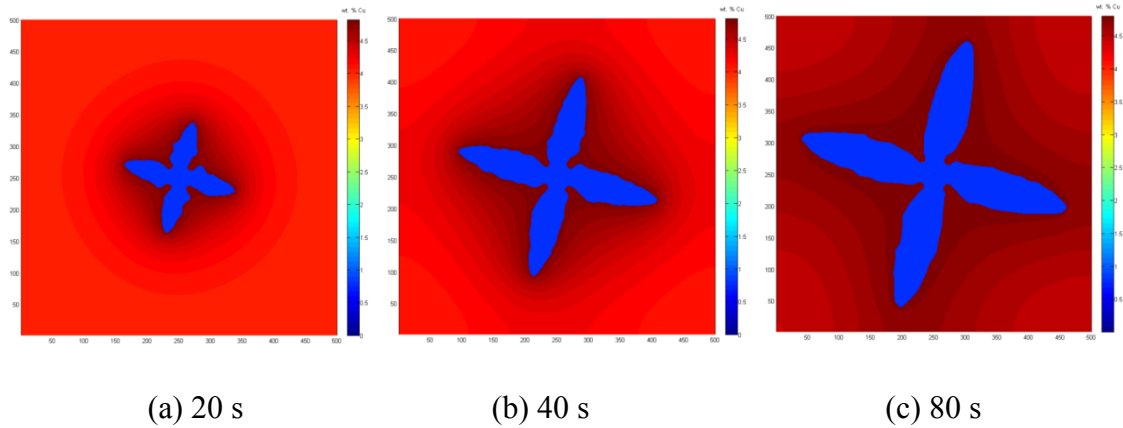


Figure 5.13 Simulated dendritic growth

In this chapter, the model evaluation has been carried out. From the analysis and discussion, it can be found that the calculation of solute redistribution, curvature of the S/L interface and anisotropy of interface tension are very important in the simulation solidification. They determine the development of dendritic morphology. In determining the dendritic growth direction, the calculation of the S/L interface curvature and anisotropy of surface tension is particularly important. In the next chapter, a detailed investigation of the effects of accuracy of interface curvature and anisotropy of surface tension calculation will be carried out.

Chapter 6 Model Verification

This chapter will focus on the verification of the developed model. According to the definition of the model, it can be seen that variation of the S/L interface growth in different directions, which will lead the dendrite to develop different morphologies, is due to the third item of the right hand side in Eq. 5.1, which is related to curvature undercooling. As in this item, the Gibbs-Thomson coefficient Γ and the liquidus slope m_l are used as constant, the value of the item varies with interfacial curvature K and function $f(\varphi, \theta)$. Therefore, the calculation of K and $f(\varphi, \theta)$ is vital important in the model. Firstly, investigation of effect of accuracy of the S/L interface curvature calculation on dendritic morphology development will be carried out. Secondly, the effect of detailed parameters used in solution to curvature undercooling, including interface curvature and anisotropy of surface tension on dendritic growth will be investigated. Thirdly, multi-grain growth will be investigated. Finally, mesh independency and time step independency of the developed model will be demonstrated.

Investigation in this chapter will be carried out mainly with single-grain growth. Parameters will be optimised during the study, followed by simulation of multi grain growth during solidification with optimised parameters. As a quantitative model, the solution must converge to a finite value when grid size and time step are refined. The model has been applied to simulate the solidification of a binary Al-4wt. % Cu alloy at a constant melt undercooling of 3K with various grid sizes and time steps. Simulations have been performed for a single dendrite freely growing to test the model sensitivity to

grid size and time step. In this chapter, for all simulations except chapter 6.4, fixed grid size of 1e-6m and time step of 1e-6s have been used.

6.1 Effect of Accuracy of Interfacial Curvature Calculation on Grain Growth

Discussions in the last chapter show that grain growth is seriously affected by the accuracy of the interfacial curvature calculation. To check the effect of accuracy of interfacial curvature calculation on grain growth, particularly on dendritic morphology development, two methods for calculation of interfacial curvature are applied for simulation of single-grain growth into an undercooled melt:

Method 1:

$$K = \frac{1}{a} \left(1 - 2 \frac{f_s + \sum_{i=1}^N f_s(i)}{N+1} \right), \quad (6.1)$$

which has been widely applied in CA model; And,

Method 2:

$$K = \left[\left(\frac{\partial f_s}{\partial x} \right)^2 + \left(\frac{\partial f_s}{\partial y} \right)^2 \right]^{-3/2} \times \left[2 \frac{\partial f_s}{\partial x} \frac{\partial f_s}{\partial y} \frac{\partial^2 f_s}{\partial x \partial y} - \left(\frac{\partial f_s}{\partial x} \right)^2 \frac{\partial^2 f_s}{\partial y^2} - \left(\frac{\partial f_s}{\partial y} \right)^2 \frac{\partial^2 f_s}{\partial x^2} \right], \quad (6.2)$$

which has been proposed by Beltran-Sanchez & Stefanescu (2003).

Comparing these two methods, it can be seen Method 1 is more computationally efficient but mesh dependent, while, according to literature, Method 2 can provide better calculation accuracy. Although the calculation accuracy of Method 1 can be partially improved by counting more layers of neighbouring cells, according to the

analysis and discussion in the previous chapter. To check the effect of domain size on grain growth, simulations with both methods have been performed in two different domains.

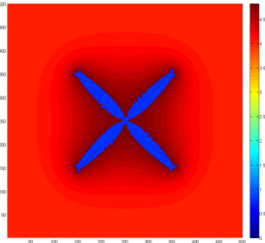
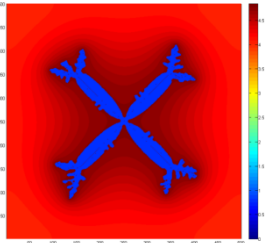
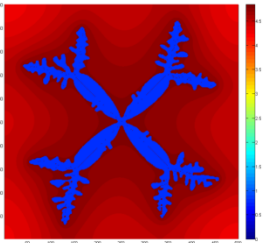
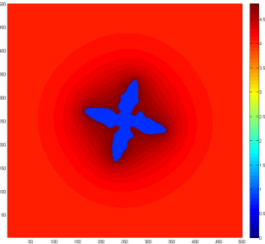
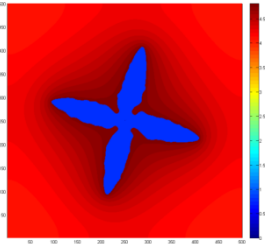
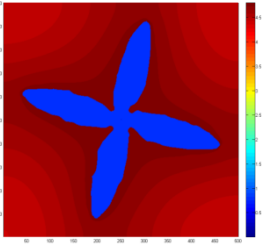
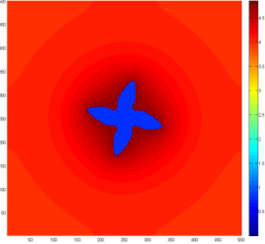
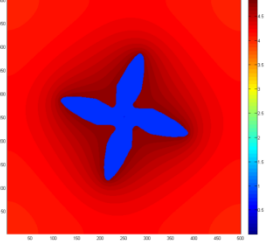
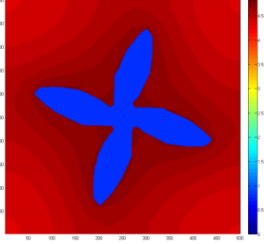
6.1.1 Interfacial Curvature Solved with Method 1

6.1.1.1 Two Layers of Neighbouring Cells Counted with 500×500 Domain

With two layers of neighbouring cells counted, more accurate calculation of interfacial curvature can be obtained with Method 1. Simulations have been performed for simulating a single-grain growing into melt with constant undercooling of 2K in a domain of 500×500. The preferential crystallographic angle of the grain was set as $\theta=70^\circ$. In solving the function of anisotropy of the surface tension, $\delta=0.8$ and $\lambda=4$ have been applied. Besides, in order to check the effect of curvature undercooling strength on grain growth, simulations with different values of Gibbs-Thomson coefficient Γ have been performed. Part of the simulated results are listed as shown in Table 6.1

It can be seen from Table 6.1, at the beginning, the crystal grew at 45° and not at the given preferential crystallographic orientation, when using smaller Γ -value as shown in case 1. At late stage, the dendritic arms split to grow along the preferential crystallographic orientation. When plotting the solute profile along the dendritic arm, as shown in Figure 6.1, it can be found the dendritic arms split when the composition in the remaining liquid increased. As for larger Γ -value, as shown in case 2 and case 3 in Table 6.1, the dendrite can grow along the preferential angle. Comparing these two cases, it can be found that the dendritic arms are longer and thinner with smaller Γ -value. The solute profiles along dendritic arm of these two cases are plotted in Figure 6.2. It can be seen there is no significant difference on peak value and slope.

Table 6.1 Investigation of grain growth

Case No.	Γ ($\times 1e-6Km$)	Simulation results		
1	1	 1.5 s	 2.5 s	 4 s
2	5	 2 s	 4 s	 8 s
3	10	 2 s	 4s	 8 s

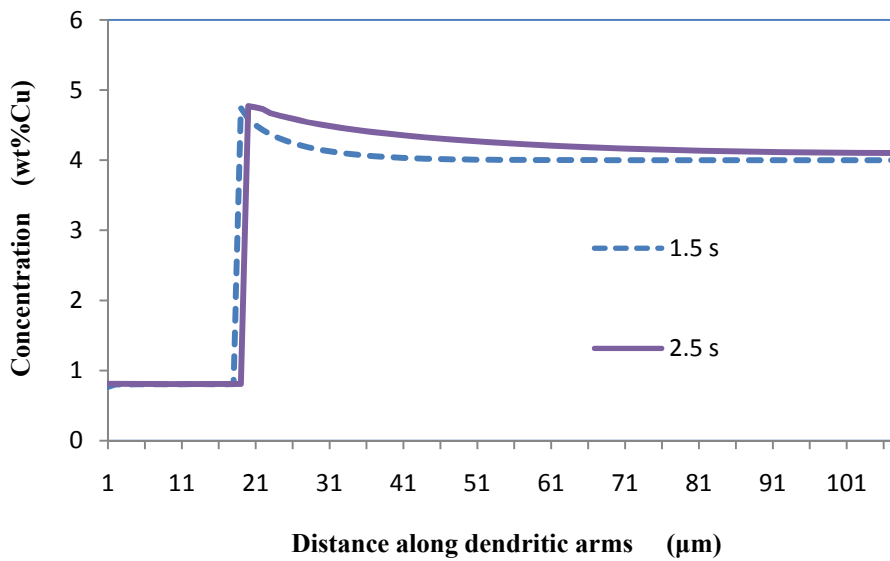


Figure 6.1 Solute profile along dendritic arm of case 1

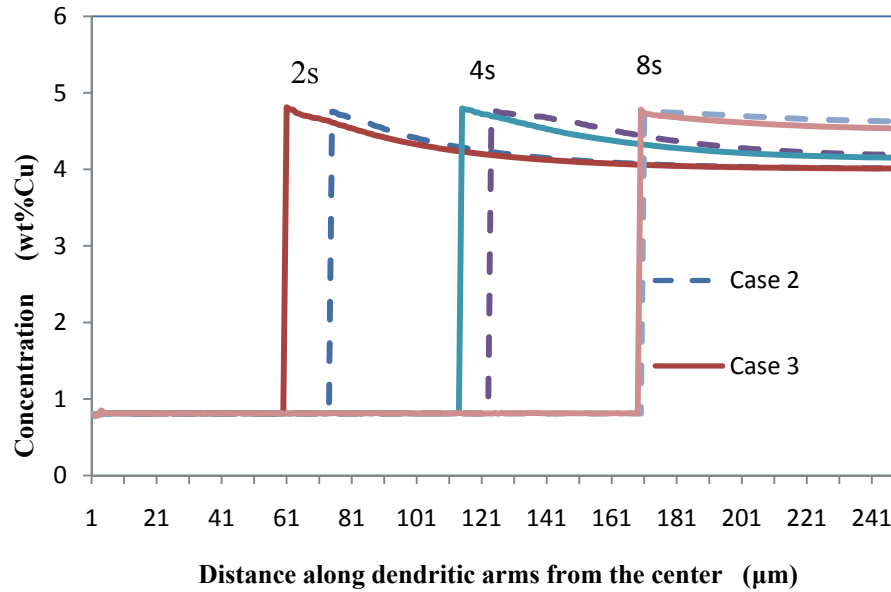


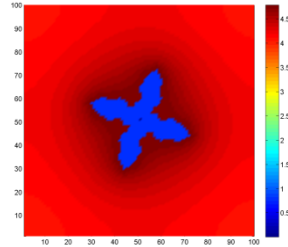
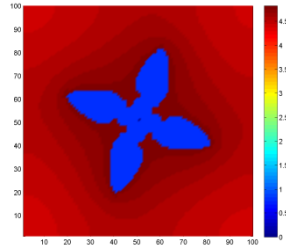
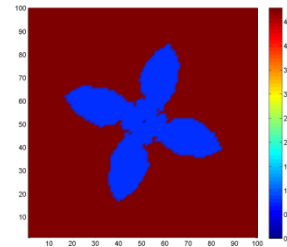
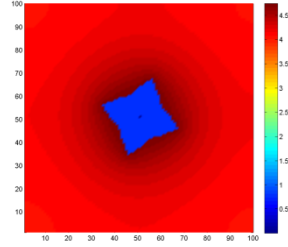
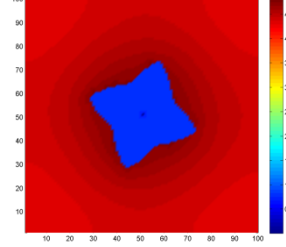
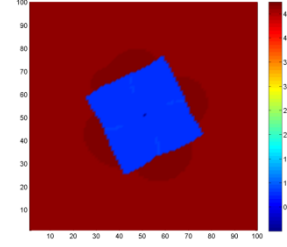
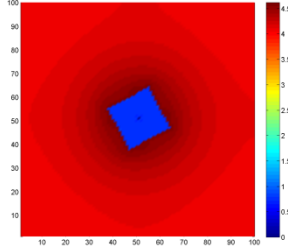
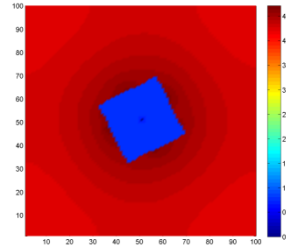
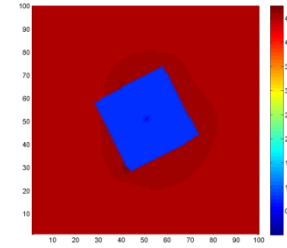
Figure 6.2 Solute profiles along dendritic arm of case 2 and case 3

6.1.1.2 Two Layers of Neighbouring Cells Counted with 100×100 Domain

For a comparison, simulations with same conditions and parameters have been performed for a 100×100 domain. With same conditions, the dendrite will grow close to the domain boundaries earlier in smaller simulation domain, which means the solutal field is easier to be modified by the domain boundaries. The simulated results are shown in Table 6.2. Compared with case 1 in Table 6.1, for smaller simulation domain in case 1 in Table 6.2, the solutal field in the remaining liquid is much earlier and easier to be modified by the growing dendrite. This means the composition in the remaining liquid can be earlier and easier increased to the level of that of case 1 in Table 6.1 when dendritic arms splitting happens, as it can be found at the bottom of the dendritic arms in case 1 in Table 6.2.

It can be noticed that for smaller domain, although there is no significant difference on solute profiles along the dendritic arms, as plotted in Figure 6.3, larger Γ -value modifies the width of dendritic arms more than the length.

Table 6.2 Investigation of grain growth

Case No.	Γ ($\times 10^{-6} \text{Km}$)	Simulation results		
1	1	 <p data-bbox="582 705 646 739">0.2 s</p>	 <p data-bbox="901 705 965 739">0.4 s</p>	 <p data-bbox="1220 705 1284 739">0.8 s</p>
2	5	 <p data-bbox="582 1008 646 1041">0.2 s</p>	 <p data-bbox="901 1008 965 1041">0.4 s</p>	 <p data-bbox="1220 1008 1284 1041">0.8 s</p>
3	10	 <p data-bbox="582 1303 646 1337">0.2 s</p>	 <p data-bbox="901 1303 965 1337">0.4s</p>	 <p data-bbox="1220 1303 1284 1337">0.8 s</p>

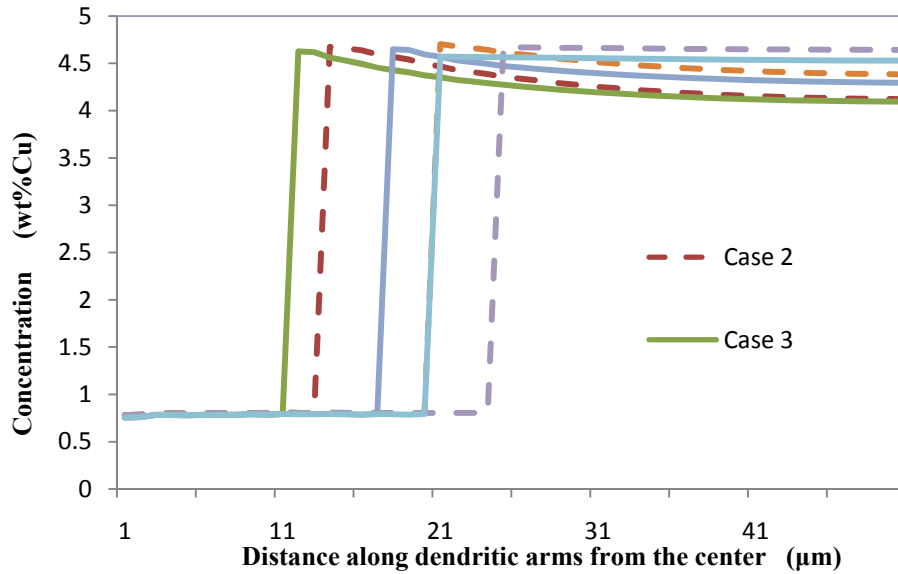


Figure 6.3 Solute profiles along dendritic arm of case 2 and case 3

6.1.2 Interfacial Curvature Solved with Method 2

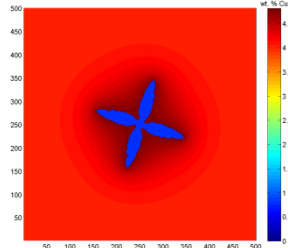
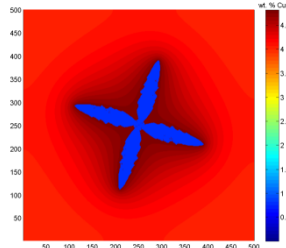
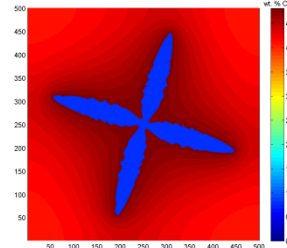
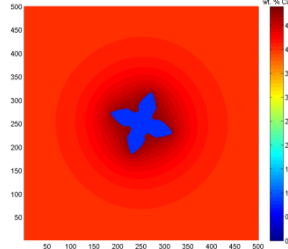
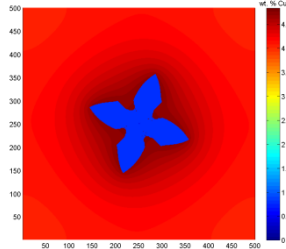
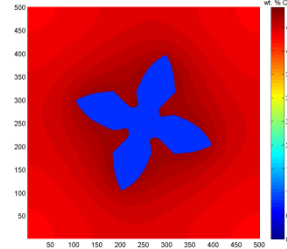
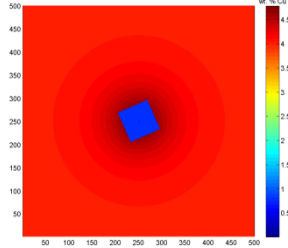
For a comparison purpose, simulations have been performed using calculation method 2 with same conditions and parameters as in chapter 6.1.1.

6.1.2.1 Method 2 with 500×500 Domain

The simulated results with applying Method 2 for 500×500 domain are shown in Table 6.3. Compared with the results of case 1 in Table 6.1, it can be seen, with method 2 for interfacial curvature calculation, the dendrite can always grow along the given preferential crystallographic angle at smaller Γ -value, as shown in case 2 in Table 6.3.

Also, with Method 2, effect of Γ -value on dendritic morphology can be found. The trend of the effect is same, but more significant with using Method 2, where the simulated dendrite in case 1 in Table 6.3 has longest and thinnest primary arms while dendrite in case 3 has shortest and thickest ones.

Table 6.3 Investigation of grain growth

Case No.	Γ ($\times 10^{-6} \text{Km}$)	Simulation results				
1	1	 15 s	 25 s	 40 s		
		2	5	 20 s	 40 s	 80 s
				3	10	 20 s

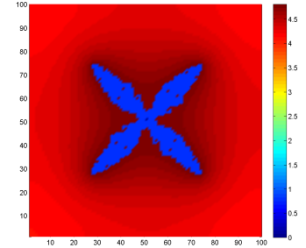
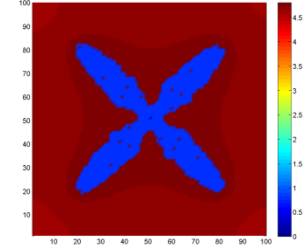
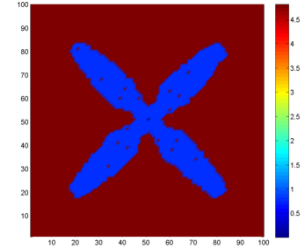
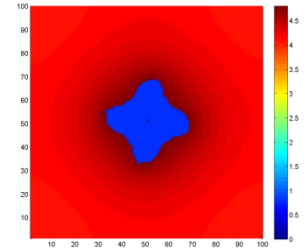
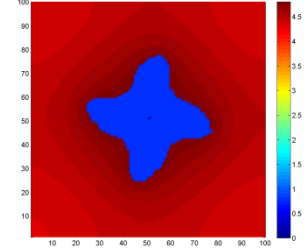
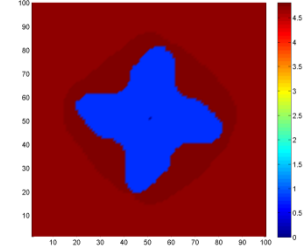
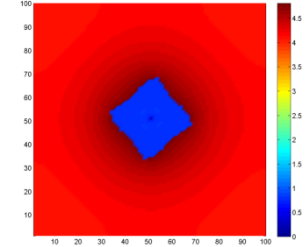
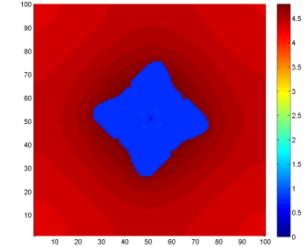
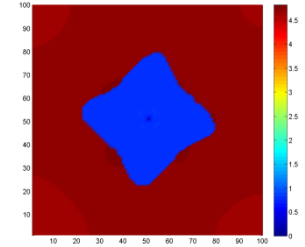
6.1.2.2 Method 2 with 100×100 Domain

Simulations with Method 2 using same conditions and parameters have been performed. The simulated results are shown in Table 6.4. Compared with the results in chapter 6.1.1.1 and 6.1.1.2, it can be found, for smaller domain, the solutal field in the liquid is earlier to be modified by the growing dendrite.

The effect of calculation of interfacial curvature on dendrite growth in large and small domains is similar, while it affects the grain growth earlier in smaller domain due to

smaller mass volume of the remaining liquid and smaller space between dendritic arms and domain boundaries.

Table 6.4 Investigation of grain growth

Case No.	Γ ($\times 10^{-6} K/m$)	Simulation results		
1	1	 <p data-bbox="576 869 639 898">0.2 s</p>	 <p data-bbox="898 869 962 898">0.4 s</p>	 <p data-bbox="1220 869 1284 898">0.8 s</p>
2	5	 <p data-bbox="576 1167 639 1196">0.2 s</p>	 <p data-bbox="898 1167 962 1196">0.4 s</p>	 <p data-bbox="1220 1167 1284 1196">0.8 s</p>
3	10	 <p data-bbox="576 1464 639 1494">0.2 s</p>	 <p data-bbox="898 1464 962 1494">0.4 s</p>	 <p data-bbox="1220 1464 1284 1494">0.8 s</p>

6.2 Effect of Parameters in Solving Curvature Undercooling

As it can be seen in chapter 6.1, although the domain size can affect the dendritic morphologies, there is no significant difference on grain growth directions with different domain size, simulations have been performed using 100×100 domain in this section to check the effect of other parameters on grain growth. To make systematic comparisons, all simulations have been performed with three different Γ -values using both Method 1 and Method 2 for interfacial curvature.

6.2.1 Effect of Anisotropy Degree on Calculation of Interfacial Curvature with Method 1

For comparison, calculations for a domain of 100×100 with different levels of degree of anisotropy also have been performed. All solidification conditions are same. Method 1 for calculation of interfacial curvature has applied with counting two layers of neighbouring cells. Calculations have been performed for uniform undercooling of 2K and $\theta=70^\circ$, where $\lambda=4$ has been applied for the calculation of function f . The results are shown in Tables 6.5, 6.6 and 6.7.

Table 6.5 Investigation of grain growth with $\delta=0.4$

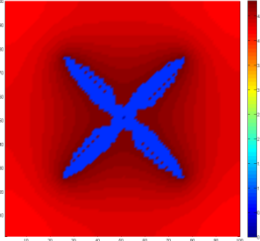
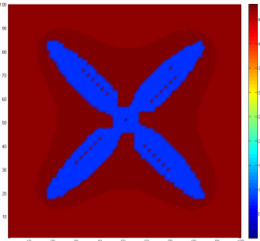
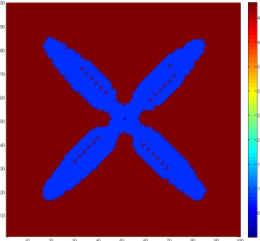
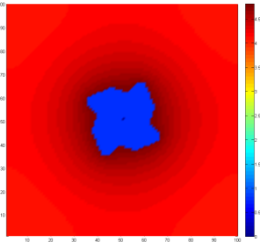
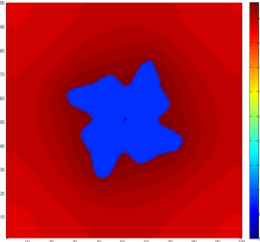
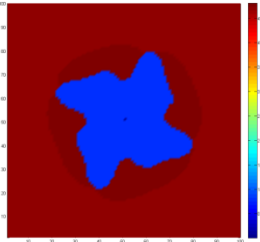
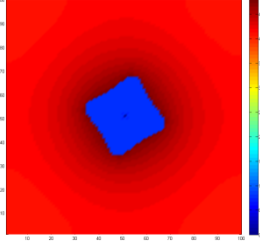
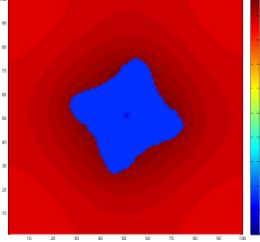
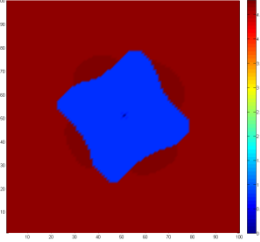
Case No.	Γ ($\times 1e-6Km$)	Simulation results		
1	1	 <p data-bbox="603 658 671 689">0.2 s</p>	 <p data-bbox="914 658 983 689">0.4 s</p>	 <p data-bbox="1230 658 1299 689">0.8 s</p>
2	5	 <p data-bbox="603 958 671 990">0.2 s</p>	 <p data-bbox="914 958 983 990">0.4 s</p>	 <p data-bbox="1230 958 1299 990">0.8 s</p>
3	10	 <p data-bbox="603 1258 671 1290">0.2 s</p>	 <p data-bbox="914 1258 983 1290">0.4 s</p>	 <p data-bbox="1230 1258 1299 1290">0.8 s</p>

Table 6.6 Investigation of grain growth with $\delta=0.8$

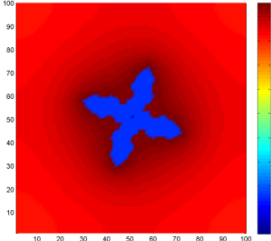
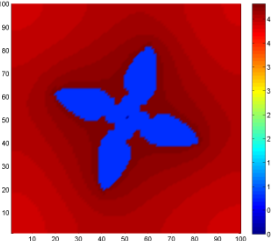
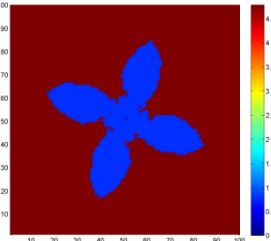
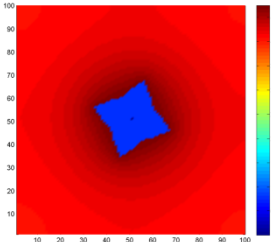
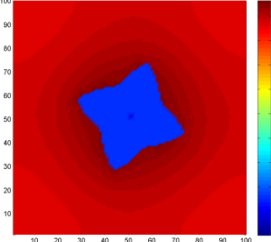
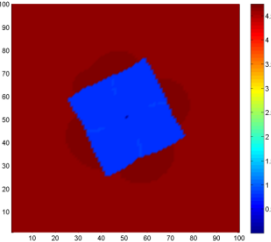
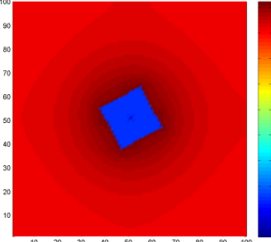
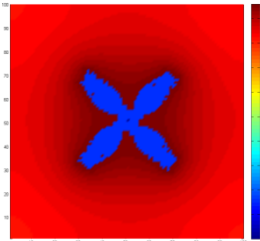
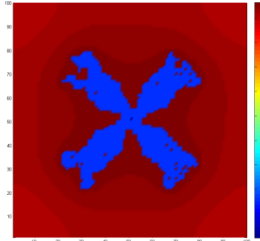
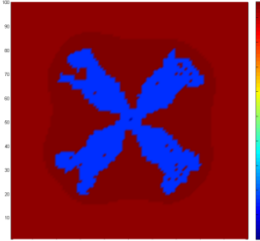
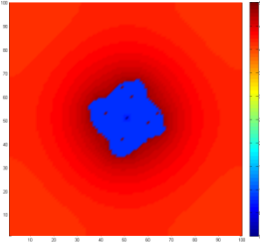
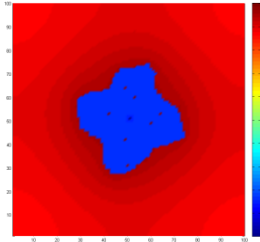
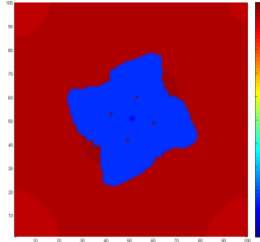
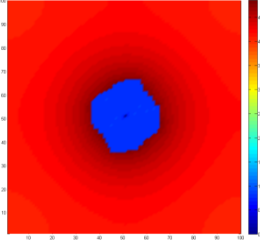
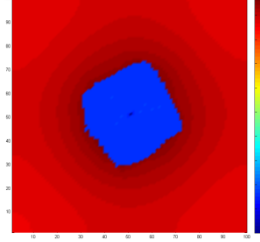
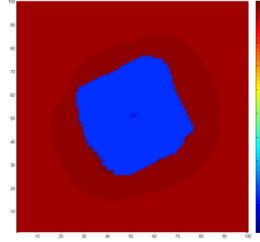
Case No.	Γ ($\times 10^{-6} \text{Km}$)	Simulation results				
1	1	 <p data-bbox="580 689 639 719">0.2 s</p>	 <p data-bbox="906 689 965 719">0.4 s</p>	 <p data-bbox="1232 689 1291 719">0.8 s</p>		
		2	5	 <p data-bbox="580 987 639 1016">0.2 s</p>	 <p data-bbox="906 987 965 1016">0.4 s</p>	 <p data-bbox="1232 987 1291 1016">0.8 s</p>
				3	10	 <p data-bbox="580 1285 639 1314">0.2 s</p>

Table 6.7 Investigation of grain growth with $\delta=1.6$

Case No.	Γ ($\times 1e-6 Km$)	Simulation results		
1	1	 <p data-bbox="603 658 671 689">0.2 s</p>	 <p data-bbox="911 658 979 689">0.4 s</p>	 <p data-bbox="1222 658 1291 689">0.8 s</p>
2	5	 <p data-bbox="603 958 671 990">0.2 s</p>	 <p data-bbox="911 958 979 990">0.4 s</p>	 <p data-bbox="1222 958 1291 990">0.8 s</p>
3	10	 <p data-bbox="603 1258 671 1290">0.2 s</p>	 <p data-bbox="911 1258 979 1290">0.4s</p>	 <p data-bbox="1222 1258 1291 1290">0.8 s</p>

6.2.2 Effect of Anisotropy Degree on Calculation of Interfacial Curvature with Method 2

Calculations also have been performed with Method 2 using same condition as in chapter 6.2.1. The results are shown in Tables 6.8, 6.9 and 6.10.

Table 6.8 Investigation of grain growth with $\delta=0.4$

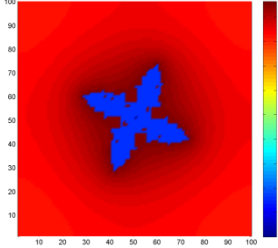
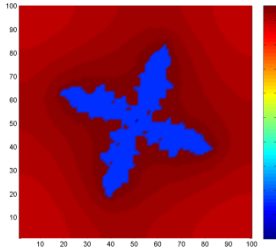
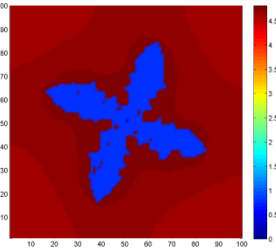
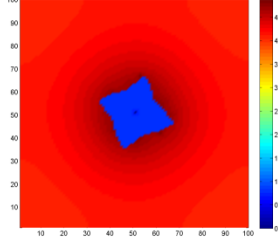
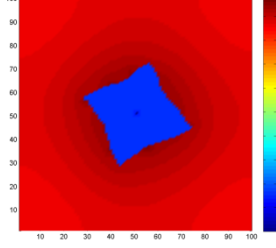
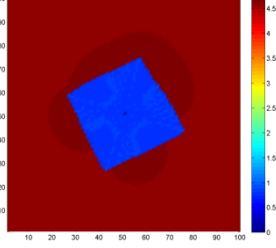
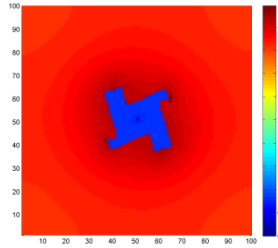
Case No.	Γ ($\times 10^{-6}$)	Simulation results				
1	1	 <p data-bbox="577 654 641 689">0.2 s</p>	 <p data-bbox="896 654 960 689">0.4 s</p>	 <p data-bbox="1232 654 1295 689">0.8 s</p>		
		2	5	 <p data-bbox="577 956 641 992">0.2 s</p>	 <p data-bbox="896 956 960 992">0.4 s</p>	 <p data-bbox="1232 956 1295 992">0.8 s</p>
				3	10	 <p data-bbox="577 1247 641 1283">0.2 s</p>

Table 6.9 Investigation of grain growth $\delta=0.8$

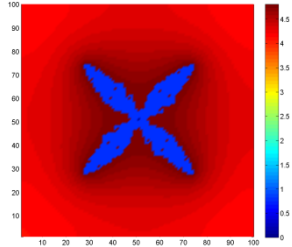
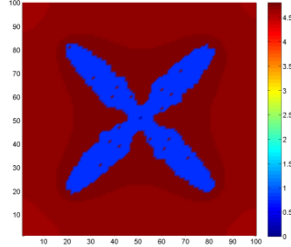
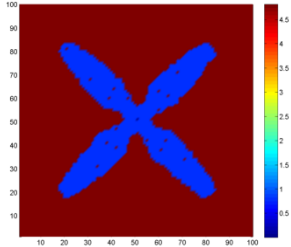
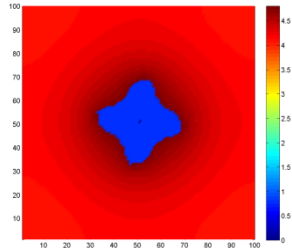
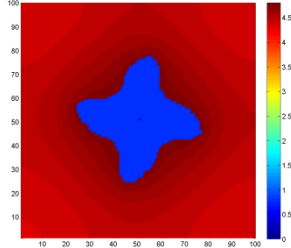
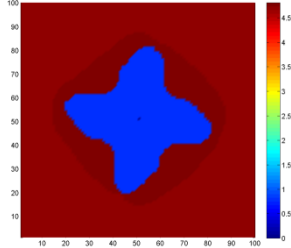
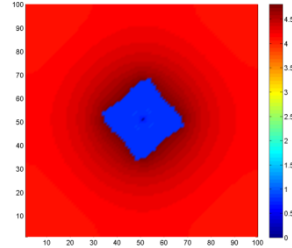
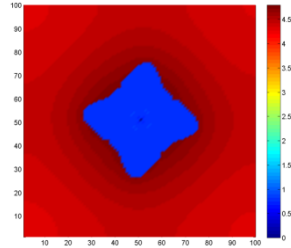
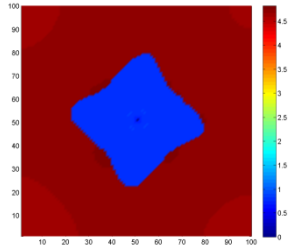
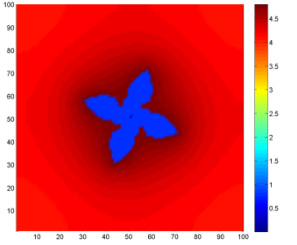
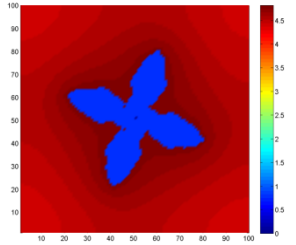
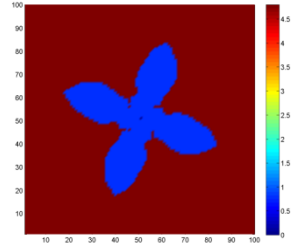
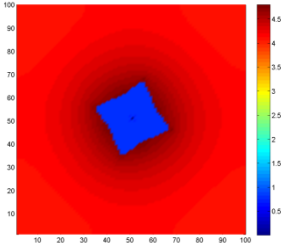
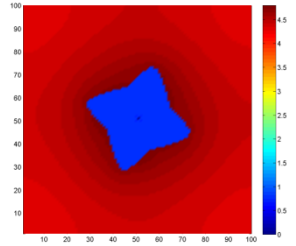
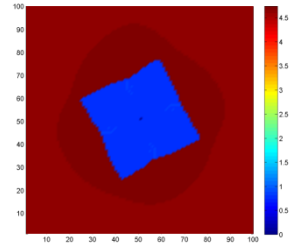
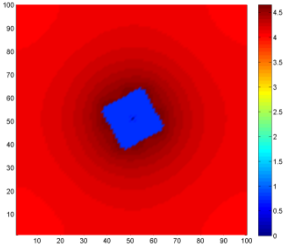
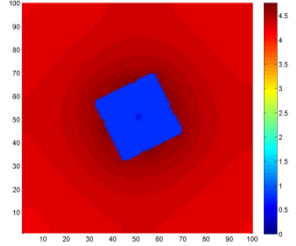
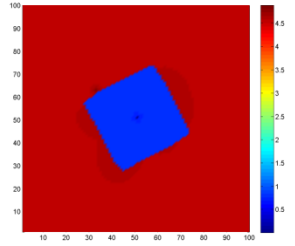
Case No.	Γ ($\times 10^{-6} \text{Km}$)	Simulation results		
1	1	 <p data-bbox="576 689 644 719">0.2 s</p>	 <p data-bbox="900 689 968 719">0.4 s</p>	 <p data-bbox="1224 689 1292 719">0.8 s</p>
		 <p data-bbox="576 987 644 1016">0.2 s</p>	 <p data-bbox="900 987 968 1016">0.4 s</p>	 <p data-bbox="1224 987 1292 1016">0.8 s</p>
		 <p data-bbox="576 1285 644 1314">0.2 s</p>	 <p data-bbox="900 1285 968 1314">0.4s</p>	 <p data-bbox="1224 1285 1292 1314">0.8 s</p>

Table 6.10 Investigation of grain growth with $\delta=1.6$

Case No.	Γ ($\times 10^{-6} Km$)	Simulation results		
		0.2 s	0.4 s	0.8 s
1	1			
2	5			
3	10			

From the above results, in both curvature models, the Γ -value is of high importance in determining the grain morphology development. It can be seen that the grain can grow along the preferential angle with using $\delta=0.8$ and $\Gamma=5e-6Km$ or $\delta=0.4$ and $\Gamma=1e-5Km$. This means by choosing proper Γ -values, the artificial anisotropy due to mesh can be eliminated and the grain can grow along the crystallographic orientation.

6.3 Effect of Anisotropy Degree on Multi Grain Growth

From the results in chapter 6.1 and 6.2, it can be found that the dendritic morphology developed well when using two groups of parameters for calculation of anisotropy of interfacial energy. To investigate the multigrain growth cases, simulation of multigrain growth applying these two groups of parameters are also carried out.

Case 1: simulation of two grain growth using $\delta=0.4$ and $\Gamma=1e-5Km$. Both the location of seeds in the domain and grain preferential growth angle were generated randomly.

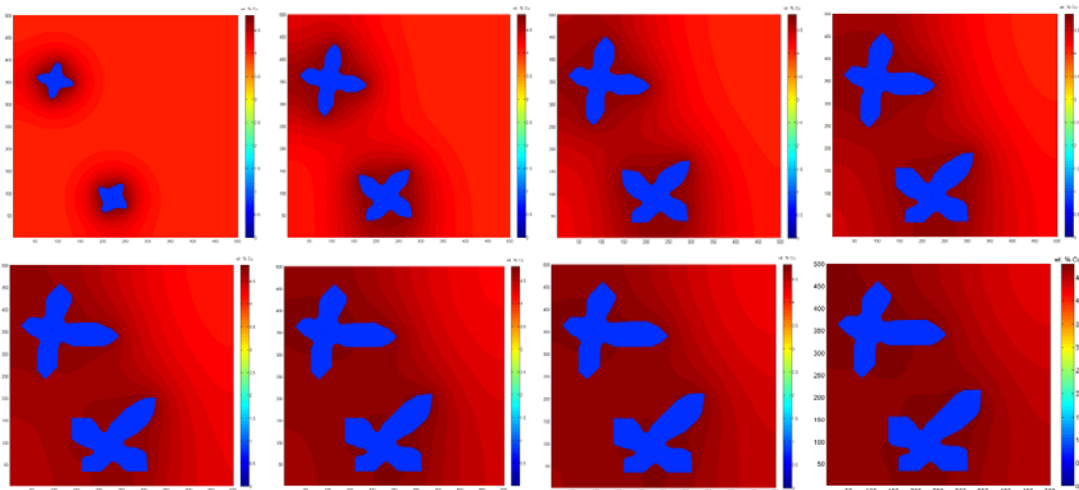


Figure 6.4 Simulation of two grains growth

Case 2: simulation of three grain growth using $\delta=0.8$ and $\Gamma=5e-6Km$. Both the location of seeds in the domain and grain preferential growth angle were generated randomly.

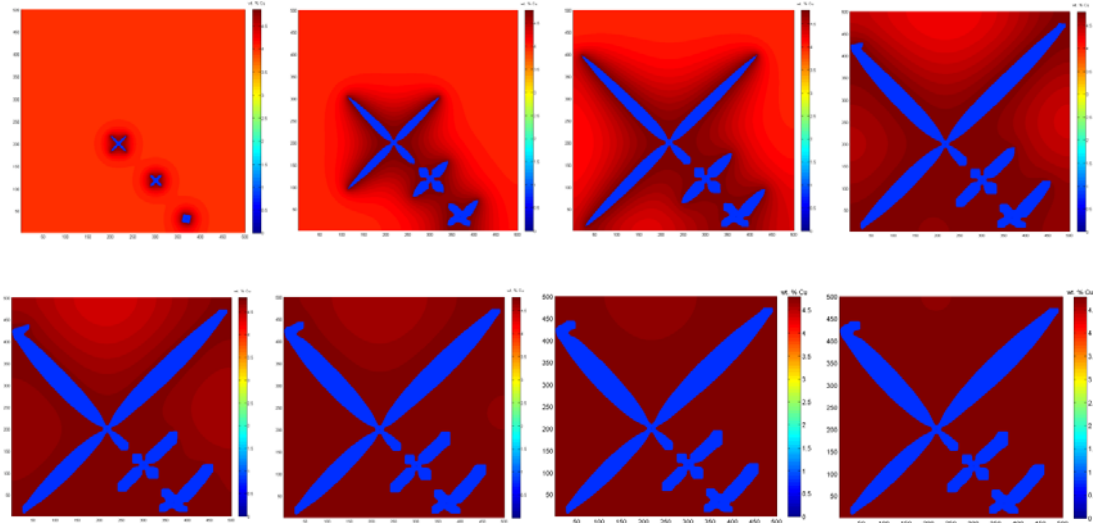


Figure 6.5 Simulation of three grains growth

In both cases, parameters used for simulations are the same as those used in single grain growth cases. Different from single grain growth, solutal interaction occurs during multigrain growth when grains are close to each other due to their locations and preferential growth directions. The solutal interaction seriously modifies the grain morphology development. A detailed investigation on multi grain growth during solidification is given in following part in this chapter.

6.4 Mesh Size and Time Step Dependency

As a quantitative model, it must demonstrate both mesh independency and time step independency. The solution must converge to a finite value when grid size and time step are refined. The model was used to simulate the solidification of a binary Al-4wt. % Cu alloy at a constant melt undercooling of 3K with various grid sizes and time steps. Simulations were performed for a single dendrite freely growing to test for sensitivity to the basic modelling parameters of grid size and time step to ensure that the model approaches a steady result as it is refined. The velocity of the dendrite tip recorded when the growth time was around 0.4 seconds as a function of grid size and time step.

6.4.1 Effect of Mesh Size

For a constant time step, simulations were performed with various grid sizes. The steady state tip velocity was plotted as a function of mesh size in Figure 6.6.

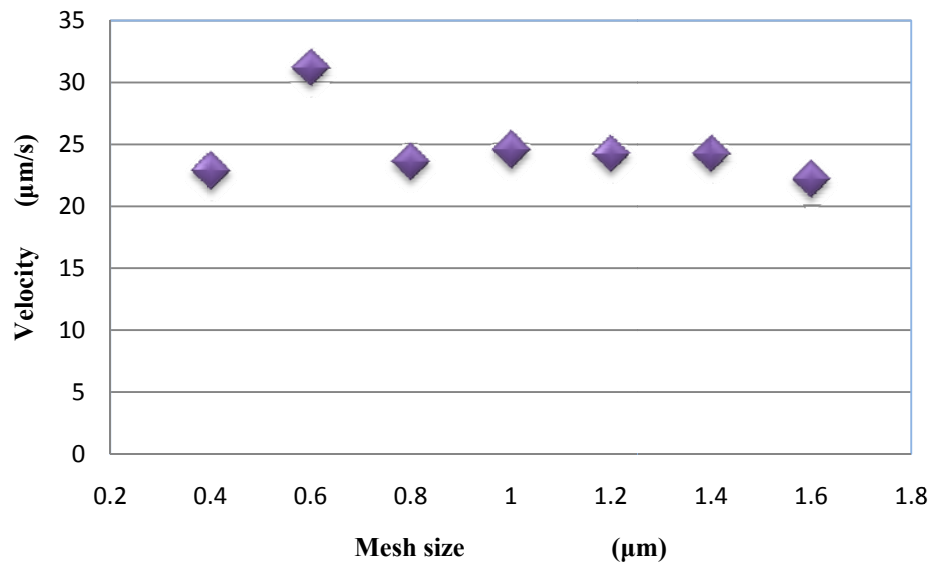


Figure 6.6 Steady state tip velocity as a function of mesh size.

It can be seen that resulting velocity of dendrite tip at steady state converges in a stable range of value.

6.4.2 Effect of Time Step

To check time step dependency, various time steps were applied with a constant mesh size. A plot of tip velocity as a function of time step is presented as Figure 6.7.

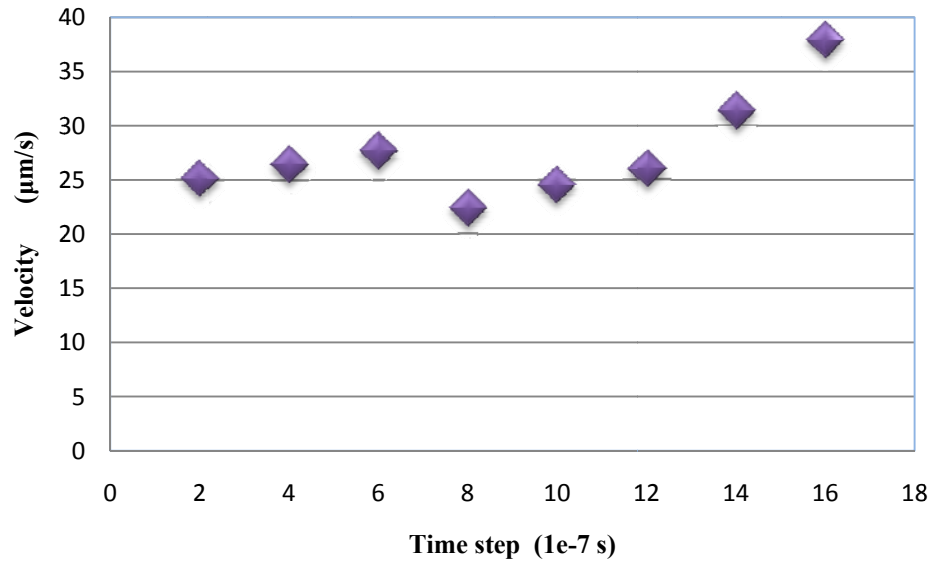


Figure 6.7 Steady state tip velocity as a function of time step.

It can be seen that velocity of dendrite tip at steady state converges very stable for time step smaller than 1.4×10^{-6} second. When above this value, the steady state tip velocity increases with bigger time step.

6.5 Effect of Curvature Undercooling on Solute Profile ahead of S/L Interface

Curvature undercooling occurs when the S/L interface is curved. The curvature of S/L interface plays an important role in determining the solute distribution ahead of the interface, especially at the head of the dendrite tip. Curvature undercooling must be taken into account during the simulation. The effect of curvature undercooling on solute profile ahead of S/L interface of dendrite tip is shown in Figure 6.8. We can see, without curvature undercooling, the dendrite grow faster than with curvature undercooling. Also, more solute piles up ahead of S/L interface when the curvature undercooling is not calculated.

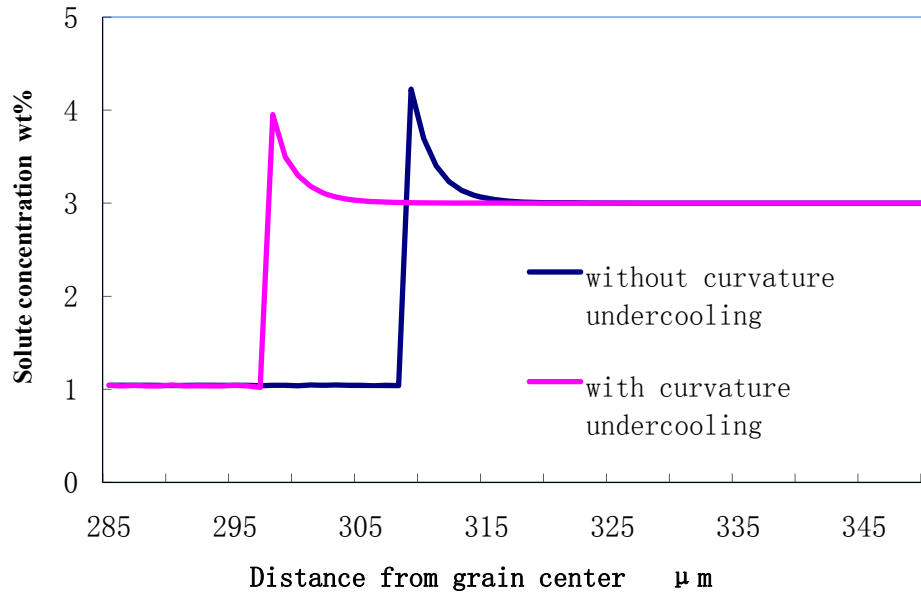


Figure 6.8 Effect of curvature undercooling

Simulation time of 2s at melt undercooling of $\Delta T = 6K$, 500×500 , cell size = $1 \mu m$.

The zero of x-axis is put on the grains centre and there is about 3% difference.

6.6 Simulation of Dendrite Interactions

To investigate the solute interaction between dendrites, multiple grains were simulated in the computation domain as shown in the following figures. Seeds with different packing patterns (square, diamond shape, parallelogram and triangle) were prefixed in the computation domain, at constant undercooling of 5K. Different solute interaction patterns are shown in the Figures 6.9. An interesting observation in the figure is orientation variation of dendrite arm and this is probably due to different solute interaction. Detailed study on this analysis will be carried out in the future.

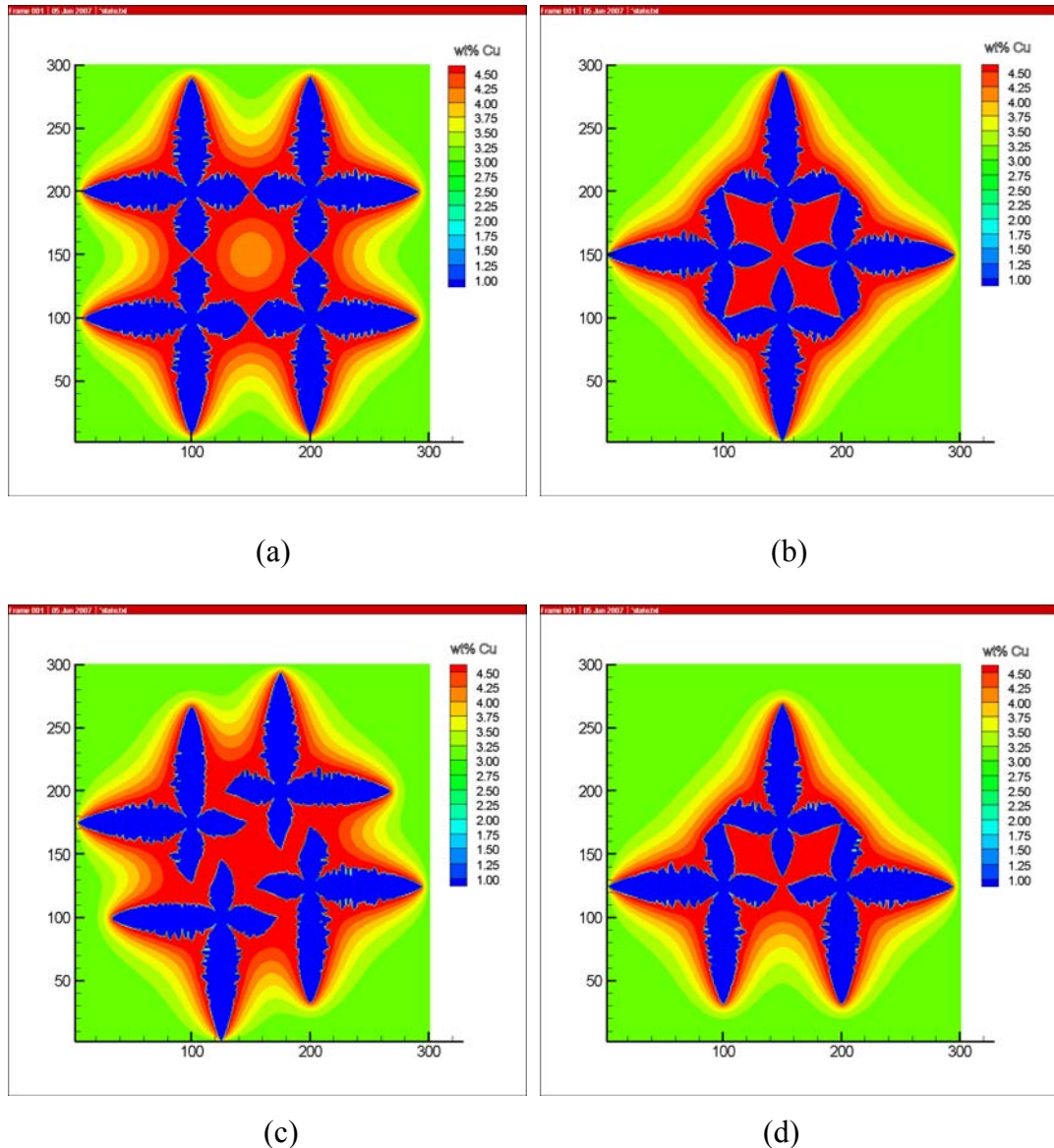


Figure 6.9 Simulation of dendrite interaction with different packing of seeds

At melt undercooling of $\Delta T = 5K$, 300×300 , cell size = $1\mu m$.

(a) Square (b) Diamond shape (c) Parallelogram (d) Triangle

The effect of undercooling of the solute interaction is illustrated in Figure 6.10. Under a large undercooling in Figure 6.10(a), dendrites grow at a high growth rate with a thin solute diffusion layer. Under a small undercooling, (Figure 6.10(d)), dendrites grow at a slow rate with a thick diffusion layer. A quantitative analysis is planned to further investigate the effect of undercooling on solute interaction.

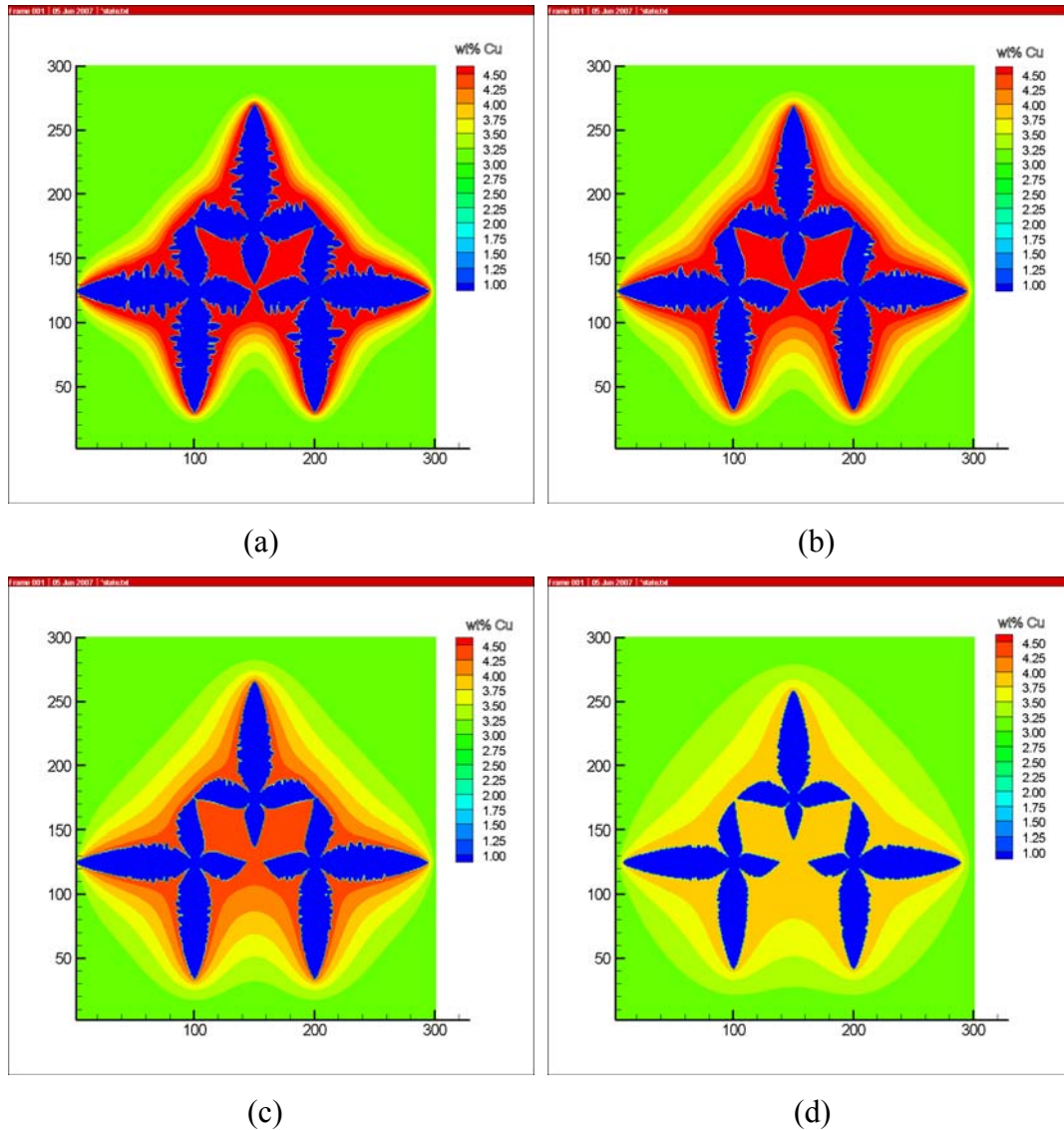


Figure 6.10 Dendrite interactions at different system temperatures T_i

(a) $\Delta T = 6K$ (b) $\Delta T = 5K$ (c) $\Delta T = 4K$ (d) $\Delta T = 3K$

Quantitative analysis on simulation of dendrite interactions will be presented in next chapter.

In this chapter, the developed model has been verified. Effect of interfacial curvature, anisotropy and calculation of curvature undercooling on crystal morphology development has been investigated, where the effect of accuracy of interface curvature and anisotropy of surface tension calculation on dendritic morphology development has been examined.

Chapter 7 Simulation of Microstructure Evolution during Alloy Solidification

Evolution during Alloy Solidification

In this Chapter, results on microstructure evolution during alloys solidification will be reported. Firstly solidification structure evolution and solute interaction for single dendritic growth will be presented; then the effect of solute concentration approximation in the interface cells on crystal growth will be examined; the microstructure evolution and solute interaction for multi-grain growth will be analyzed; solidification segregation will be simulated.

Based on the discussion in the last chapter, $\delta=0.4$ and $\Gamma=1e-6Km$ are chosen for the simulations in this chapter.

7.1 Simulation of Single Dendritic Growth

In this section, the features of single dendritic growth at constant melt undercooling will be examined with the developed model. Simulations of single-grain solidification with the developed model were performed in a square domain of 500×500 meshes with a mesh size of $1 \mu\text{m}$. The temperature field was assumed to be homogeneous in the entire simulated domain. The square domain was initialized at the liquidus temperature and then decreased to the eutectic temperature with constant cooling. The simulated features were compared with the predictions of the LGK model for unconstrained steady-state

growth as a function of melt undercooling. To maintain the constant melt undercooling and to avoid the interference of the wall on solute diffusion, simulation results were only selected when the dendrite size is less than 1/3 of the domain size.

7.1.1 Single Dendritic Growth

Simulations of single dendritic growth were performed for an Al-4wt. %Cu alloy solidified at constant melt undercoolings. A solid seed with the composition of kC_0 and a preferential crystallographic orientation of zero degree with respect to the positive x -axis was set at the centre of the domain at the beginning of the simulation. The cells in the first layer surrounding the seed were assigned as interface cells and the cells in the second layer were assigned as capturing cells. Both interface cells and capturing cells were initialized with the composition of C_0 . The other cells in the domain were set as undercooled melt liquid with the initial composition of C_0 .

Simulation of single dendritic growth at a constant melt undercooling of 4K was performed. The simulated evolution of single dendritic morphology and composition fields at different times are presented in Figure 7.1. To examine the evolution of dendritic tip growth velocity, simulations were performed with constant melt undercoolings of 4K, 5K and 6K. The tip velocities *versus* time were recorded at the early stages (from 0 second to 0.08 seconds) of solidification and are plotted in Figure 7.2. Velocities in the plot are average values calculated from the measured velocities with a time step of 0.001 seconds, and the velocities were measured from the interface cells at the dendritic tip. Note, in the initial growth stage, the condition of solute balance at the S/L interface cannot be satisfied, as the solute rejected by the growing crystal is more than can be diffused away from the S/L interface into the far away liquid. It can be

seen from the figure that the dendrite grows at a very high velocity at the start of solidification. Then, the growth velocity decreases rapidly and finally reaches a steady-state level after a transient period from 0-0.04 seconds. When the dendrite growth velocity comes to a steady-state level after 0.04 seconds, the condition of solute balance at the S/L interface can then be satisfied.

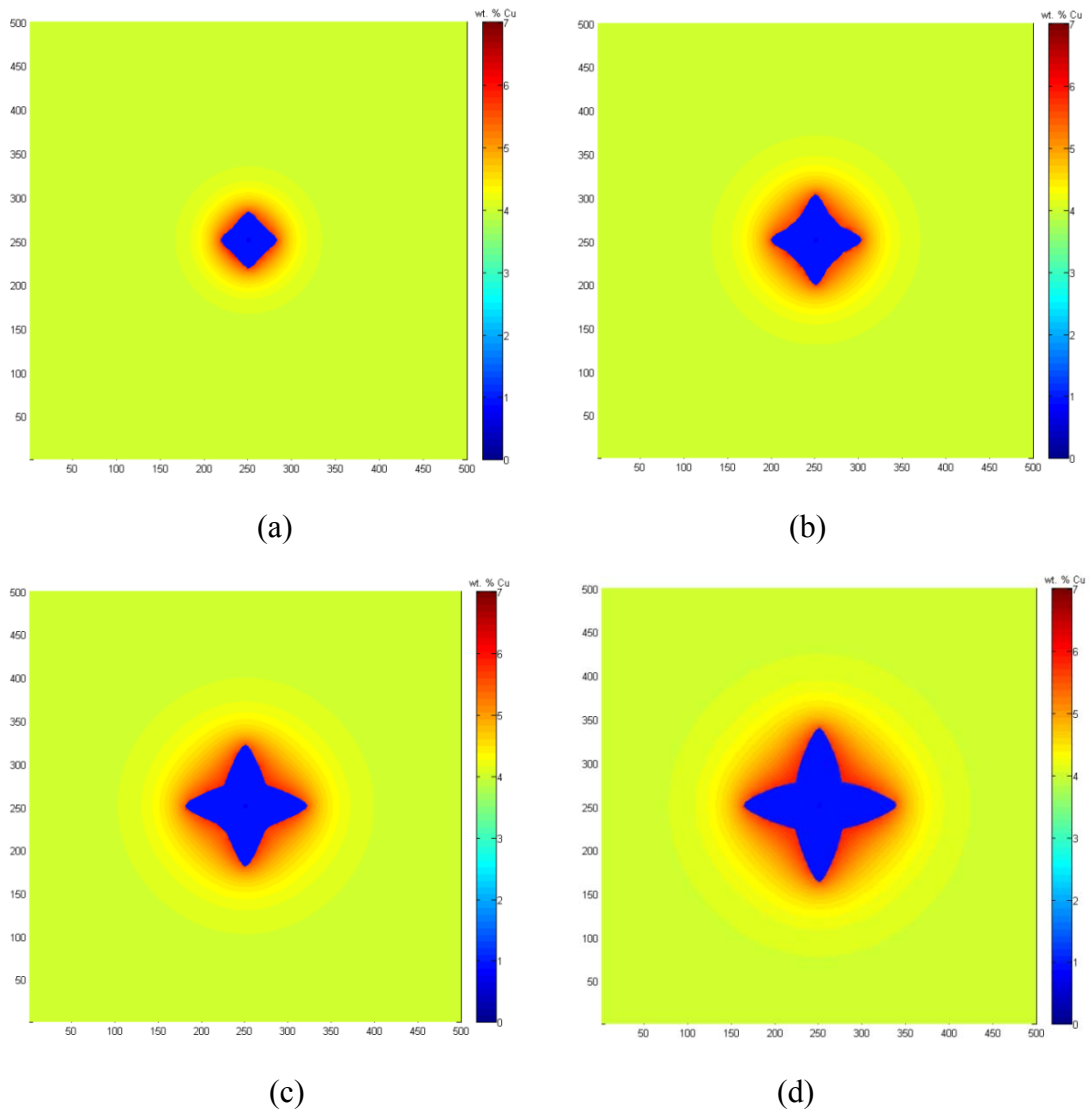


Figure 7.1 Simulated single dendrite evolution.

Melt undercooling of 4K, at time of (a)0.02s, (b)0.04s, (c)0.06s and(d)0.08s

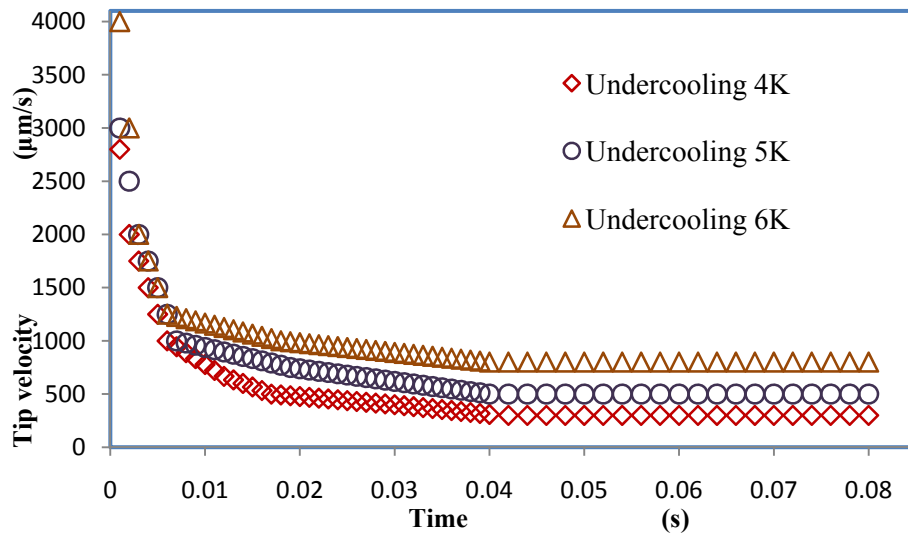


Figure 7.2 Tip velocity evolution at early stages (from 0 second to 0.08 seconds) of solidification at constant melt undercoolings

7.1.2 Single Dendritic Morphologies and Composition Fields

To examine the single dendritic morphologies and composition fields under different conditions, simulations of single dendritic growth with various preferential crystallographic orientations and at various melt undercoolings for Al-4wt. %Cu alloy solidification were performed.

Figure 7.3 shows some of the simulated dendritic morphologies and composition fields for an Al-4wt. %Cu alloy at various constant melt undercoolings and different preferential crystallographic orientations with respect to the positive x -axis. Figure 7.3(a) and (b) present the simulated dendrite with preferential crystallographic orientation of zero degree at time of 0.06s, where the melt undercooling for (a) and (b) are 3K and 6K, separately. Obviously, the dendrite arm at melt undercooling of 3K is thicker than that at 6K. Two simulated dendrites with preferential crystallographic orientation of 30

degree at time of 0.08s are shown as Figure 7.3(c) and (d), where the undercooling for (c) is 6K and (d) is 5K. Note, at same solidification time, the arm length of dendrite solidified at larger undercoolings is longer than that at smaller undercoolings, when comparing (a) and (b) or (c) and (d). This means the growth velocity of dendritic tip increases with melt undercooling. Also, it can be seen that the composition fields vary at different melt undercoolings, especially in the liquid ahead of the dendritic tip. Composition fields and steady-state tip velocity at different melt undercoolings will be examined quantitatively in the following sections.

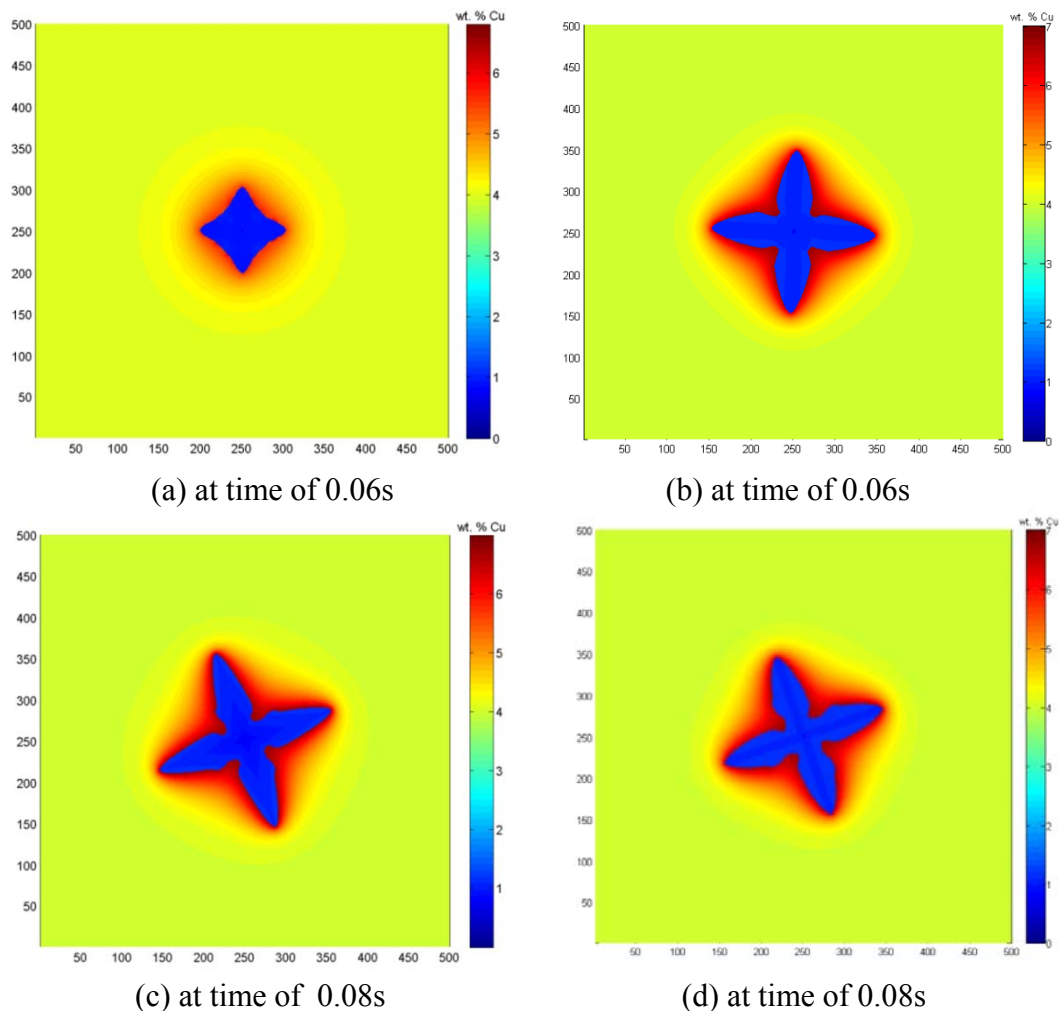


Figure 7.3 Simulated single dendrite evolution of an Al-4wt. %Cu alloy.

At constant undercooling and with growth orientation: (a)3K and 0 degree, (b)6K and 0 degree, (c) 6K and 30 degree and (d)5K and 30 degree

7.1.3 Solute Profile ahead of Dendritic Tip

As discussed in some detail in previous Chapters, for the solidification of alloys, the growth velocity of dendritic tip is mainly governed by the solute field in the liquid ahead of S/L interface. To examine the compositions along the dendrite arms at different undercoolings, simulations were performed for Al-4wt. %Cu alloy solidification at different melt undercoolings from 4K to 9K. The steady-state solute profiles along the dendrite arms from the centre of the dendrite at various constant melt undercoolings were plotted in Figure 7.4 (a) and (b).

It can be seen from the figure, the composition in the solid remains nearly constant and is higher for solidification at larger melt undercooling. The composition increases suddenly at the S/L interface due to the solute rejected into liquid by the growing crystal, and decays exponentially until it reaches the initial composition. As the detailed solute profiles in liquid shown in Figure 7.5, it can be seen that composition gradient in the liquid ahead of the S/L interface is steeper at larger melt undercooling. This phenomenon can be explained as followings:

- (1) On one hand, according to Eq.5.1, the composition in the liquid at the S/L interface C_l^* is higher at larger melt undercooling, which can be seen in the figure.
- (2) On the other hand, the growth velocity is higher at larger melt undercooling, which leads to less time for the rejected solute to diffuse away into the liquid far way of the S/L interface. As a result, there is a steeper solute gradient in front of the S/L interface at larger melt undercooling.

Investigation on steady-state tip velocity at different melt undercoolings will be carried out in next section.

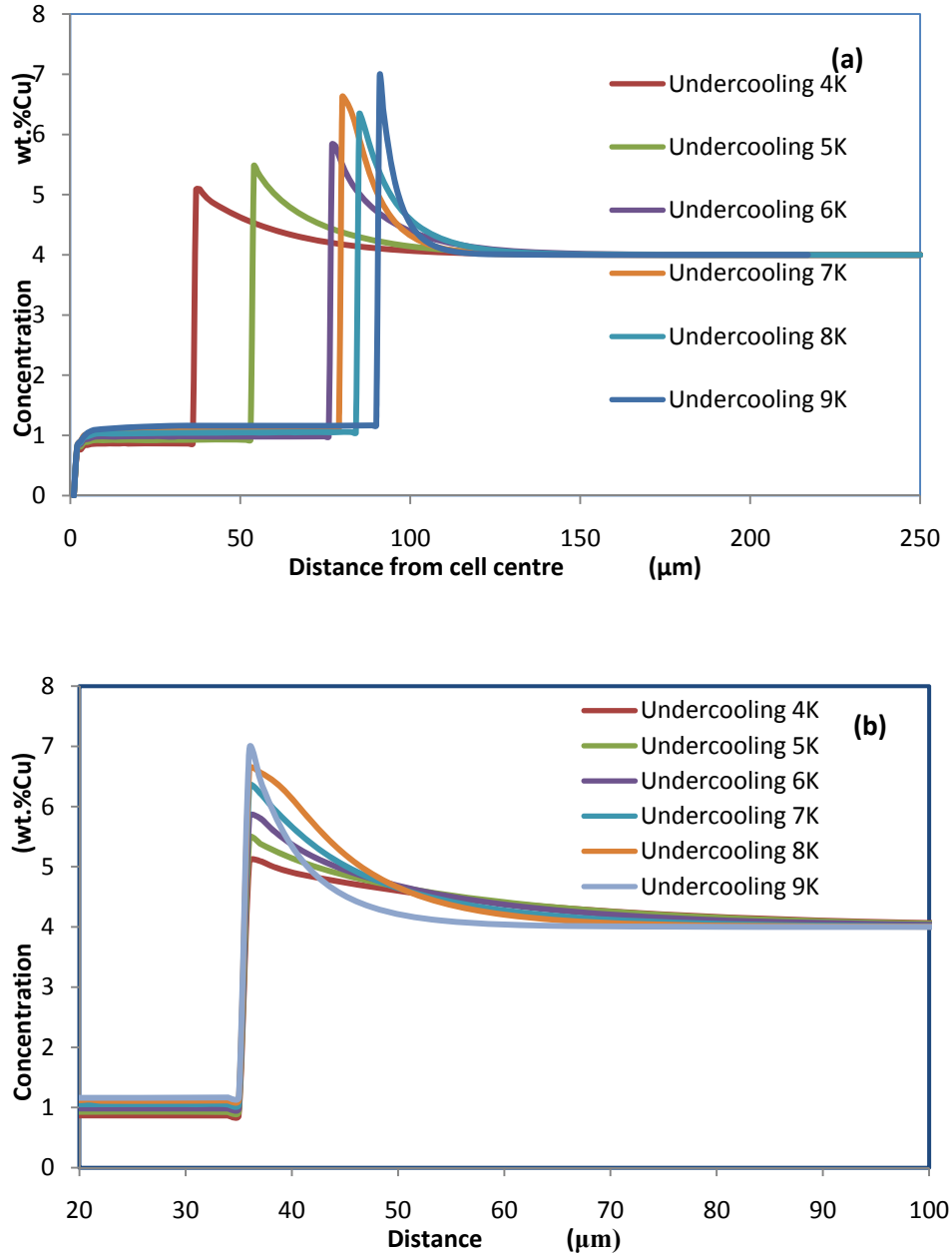


Figure 7.4 Steady-state solute profiles along the dendrite arms

- (a) Steady-state solute profiles along the dendrite arms at different undercoolings at time of 20 seconds;
 (b) displaced solute profiles at interfaces in (a) to illustrate the concentration variation for different undercooling.

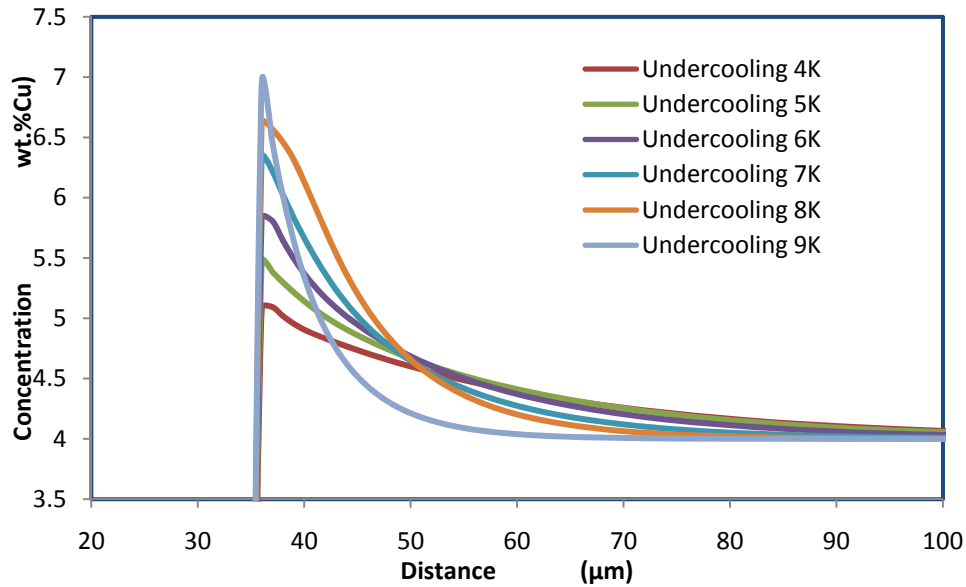


Figure 7.5 Steady-state solute profiles ahead of dendritic tip at different undercoolings.

7.1.4 Comparison of Tip Velocity with the LGK Model

The tip velocity of steady-state single dendritic growth during Al-4wt. %Cu alloy solidification as a function of melt undercooling is examined in this section. The simulated steady-state tip velocities at different constant melt undercoolings were compared with predictions of the LGK analytical model.

The LGK model predicts the steady-state growth of a dendrite growing unconstrainedly at a given constant melt undercooling and constant initial composition. The basic assumptions of the LGK model are that the dendrite grows steadily into an undercooled melt of constant undercooling and the heat and mass transport in the solid and liquid is only controlled by diffusion. To satisfy these conditions, simulations were performed in a domain of 500×500 with a solid seed set in the centre. In such a case, the domain size is more than four times bigger than the dendrite size when the dendrite growth reaches

steady-state. The recorded steady-state tip velocity is an average value calculated from the measured steady-state values of several computation time step intervals. The values were measured when the simulation domain was more than three times bigger than the dendrite length, in which case the melt far away from the dendritic tip remained at the initial composition. Figure 7.6 shows the comparison of simulated steady-state tip velocity at different constant melt undercoolings with predictions of the LGK model for Al-4wt. %Cu alloy solidification, which can be given (Dantzig & Rappaz 2009) as:

$$V = 49.14 \times \frac{\Delta T^{2.5}}{C^{1.5}} \quad (7.1)$$

in which V is the steady-state tip velocity, ΔT is melt undercooling and C is the composition.

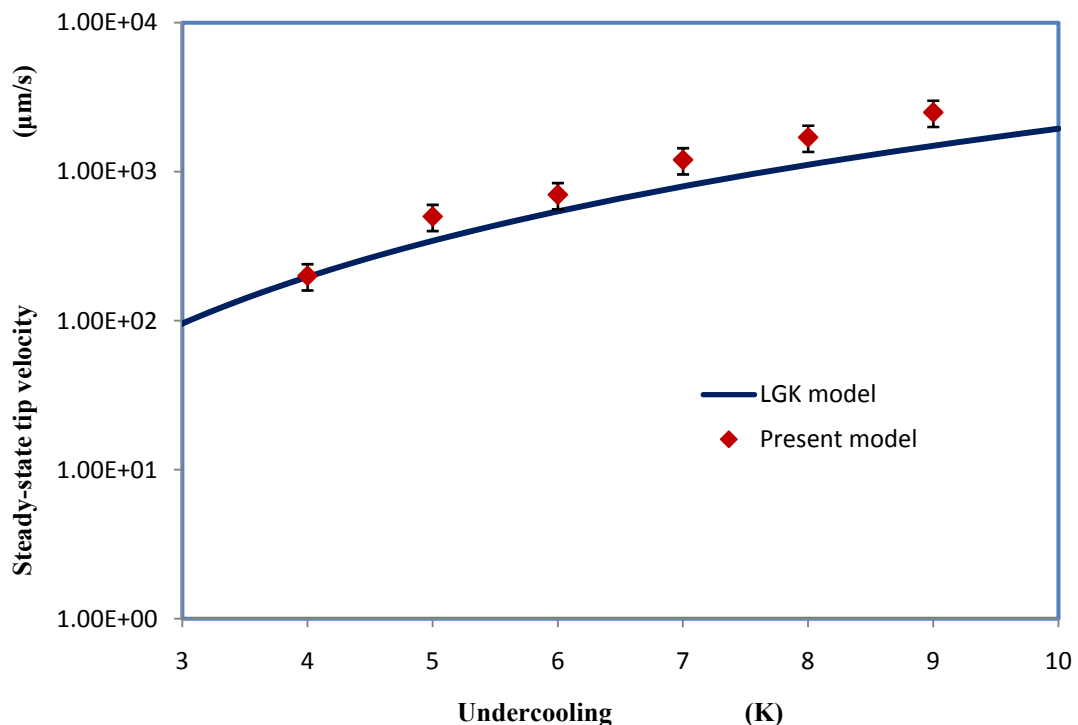


Figure 7.6 Comparison of the steady-state tip velocity at different melt undercoolings between present model and LGK model predictions.

The figure shows excellent agreement at lower melt undercoolings. As for larger melt undercoolings, the agreement is reasonably good. The simulated steady-state tip velocities are slightly larger than the predictions of the LGK model at larger melt undercoolings, but they follow the same trend.

7.2 Effect of Solute Concentration Approximation in the Interface Cells on Crystal Growth

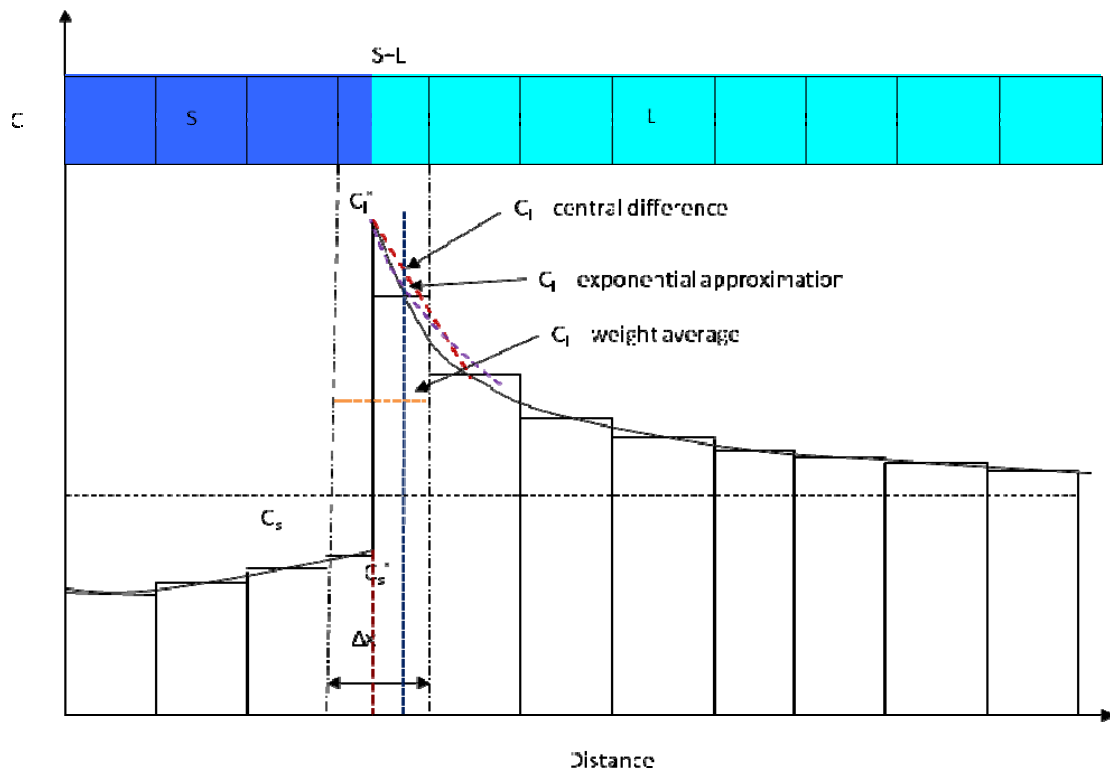


Figure 7.7 Approximations of solute concentration in the interface cell.

As shown in Figure 7.7, in a growing cell, C_l^* (interface concentration of liquid phase) and C_s^* (interface concentration of solid phase) are determined by the phase diagram. The average composition of the liquid phase in the growing cell, C_l , plays an important role in determining the growth rate of dendrites and the development of dendritic morphology, because C_l is used to calculate the undercooling. Therefore C_l is required

to be calculated with a high accuracy. Various methods have been applied to approximate the averaged liquid composition, in this section three different methods will be used to approximate the liquid concentration and the effect of liquid concentration approximation on solute interaction will be examined in detail.

7.2.1 Methods for approximating the average concentration of liquid phase in a growing cell

(1) *Weighted average*: This method is commonly used in front-tracking model by taking weighted average of S/L interface composition in a growing cell. C_l is defined as:

$$C_l = C_l^*(1 - f_s) + C_s f_s \quad (6.5)$$

(2) *Central difference approximation*: This assumes the composition to be the arithmetic average between the compositions of the S/L interface and that of the cell next adjacent to the wall. The composition is given by:

$$C_l = C_l^* - \frac{1 - f_s}{2} \Delta x \cdot G_c \quad (6.6)$$

Where Δx is the cell size and G_c is the solute gradient between the growing cell and its adjacent cell. The solute gradient is calculated using values from previous time step.

(3) *Exponential approximation*: This approximation assumes an exponential composition profile between the growing cell and its adjacent cell. The curvature of the exponential profile is determined by the sign and the magnitude of the *Peclet* number (Shin 2001):

$$C_l = \frac{C_l^* - C_l^{i-1} \exp(-P)}{1 - \exp(-P)} \quad (6.7)$$

where C_l^{i-1} is the solute concentration in the adjacent cell. For a given component, the *Peclet* number in the growing cell is given by: $P = v \times \Delta x / D_i$, where v is the growth velocity in previous time step, D_i is the diffusion coefficient for the given component at the current temperature.

7.2.2 Simulated Results using Different Approximations

To investigate the effect of different calculation methods of solute concentration in a growing cell, calculations using the three methods described above were carried out. Figure 7.8 shows the solute concentration ahead of the solidification interface using (1) the weighted average, (2) the central difference approximation and (3) the exponential approximation. In method (1), as the composition of interface cell is an equivalent value, *i.e.* $C_l = C_l^*(1 - f_s) + C_s f_s$, the weighted average solute concentration is used to calculate solute diffusion. Comparing with other two methods, this method gives lower solute concentration. Using central difference approximation method, C_l has a close value to C_l^* , the composition at the wall between the growing cell and its adjacent cell has highest value. Using exponential approximation, the solute profile has an exponential decay from the S/L interface, the composition at the wall between the growing cell and its adjacent cell is lower than that calculated using central difference approximation and is higher than that of the weighted average method.

It shall be noted that the exponential approximation assumes exponential decay from the solidification interface and theoretically it shall provide closer approximation to the solute profile within the growing cell. Weight average method can provide a high

efficiency solution for solute redistribution where the entire domain can be treated as a single phase for solute diffusion calculation. However, the accuracy in the weighted average method seems lower than that of exponential and central approximations. The predicted results using the central approximation is close to those predicted using the exponential approximation, but the central approximation is much more efficient than the exponential approximation. Therefore the central approximation was used in following studies.

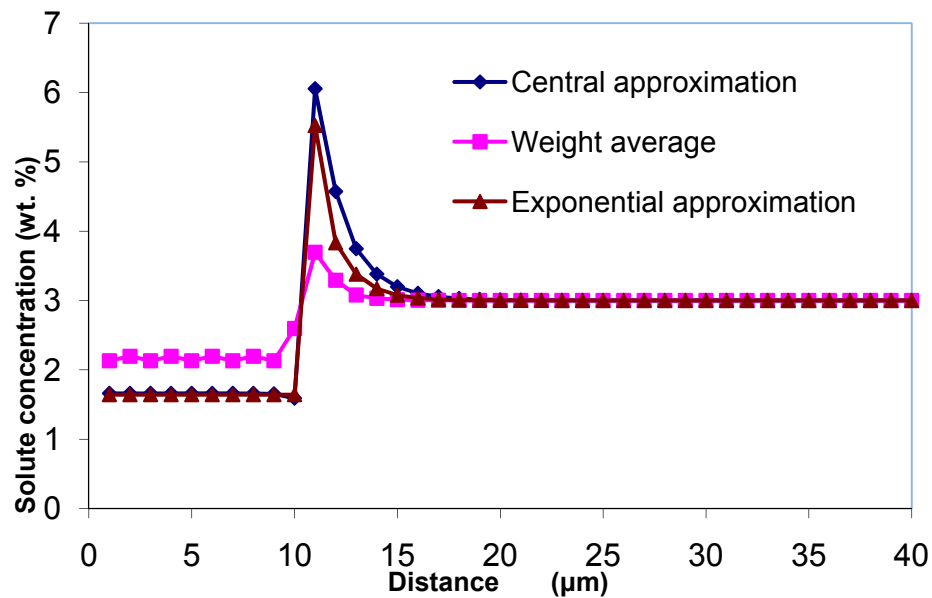


Figure 7.8 Calculated averaged solute concentration using different approximations

7.3 Simulation of Equiaxed Multi Grain Growth

During solidification of an alloy, if the partition coefficient is less than unity, solute will pile up ahead of the S/L interface due to the smaller solubility of the solute in the solid phase. The solute rejected from the solid will accumulate in an enriched boundary layer ahead of the S/L interface. Compared with single-grain growth, during the multi-grain

growth the concentration in liquid from S/L interface will increase if it is close to another grain. This is because solutal fields of different grains interact. As a result, the solute diffusion will decrease due to the shallower concentration gradient and the local liquid composition will become higher. According to the definition of the present model, the driving force for grain growth is directly related to the difference between the local interface equilibrium composition and the local actual liquid composition. Therefore, the dendrite growth velocity will decrease with an increased local liquid composition. The interaction of solutal fields in multi-grains growth plays an important role in determining microstructure development during alloy solidification.

In this section, simulations with the built model were performed in a square domain of 500×500 meshes with a mesh size of $1 \mu\text{m}$. The temperature field was assumed to be homogeneous in the entire simulated domain. The square domain was initialized at the liquidus temperature and then decreased to the eutectic temperature with constant cooling rates. The liquid was initialized with bulk alloy composition C_0 , and the solid seeds with C_0k .

7.3.1 Equiaxed Multi Grain Growth

Al-4wt. %Cu alloy was used in this section. As an example, one of the simulated equiaxed multi-grain morphology and composition field are as shown in Figure 7.9, in which twenty solid seeds, with randomly-generated preferred growth orientations, were assigned in the domain with randomly-generated locations.

In Figure 7.9, different colours represent grains with different preferred growth orientations as shown in figure (a). Figure (b) is concentration plot from the same simulation, which shows the compositional difference within dendrites. Due to solute

rejection at the S/L interface, the concentration in the liquid increases as solidification carries on. Therefore the solid which forms at a later stage has a higher concentration. It can be seen in the figure that the concentration near the dendrite boundary is higher than that of the area in the dendrite core. This is the called solidification microsegregation, or coring. A quantitative investigation of the microsegregation during multi-grain growth during solidification is analysed in the following Chapter 7.4.

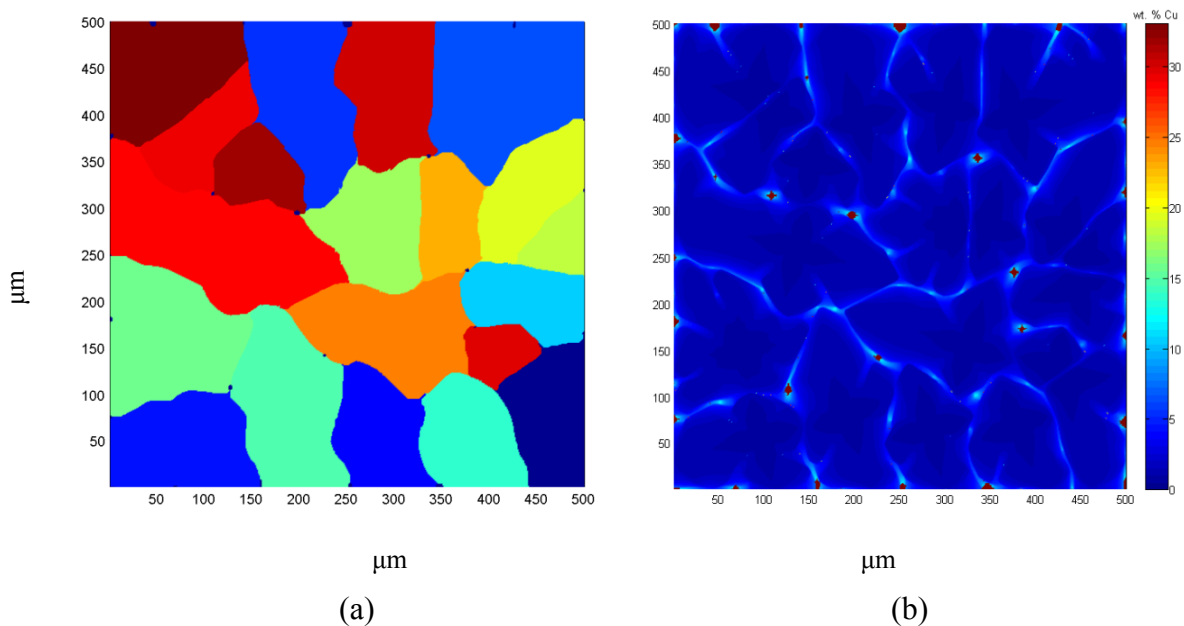


Figure 7.9 Simulated equiaxed dendrite evolution of an Al-4wt. %Cu alloy

With a cooling rate of 10 K/s, at time of 18s; (a) showing grain boundary formation, where different colours represent grains with different crystallographic orientations, and (b) showing composition field.

7.3.2 Solute Interaction

Figure 7.10 shows simulated structure evolution of multi-grain morphology and composition field of Al-4wt. %Cu alloy. Eight solid seeds with randomly-generated preferred growth orientations were assigned in the domain with randomly-generated locations.

The left column of Figure 7.10 shows the simulated dendrite boundaries at different time, which eventually form the grain boundaries. Three grains are labelled in the left column. Grain 1 grows with secondary branching, while the branching in grain 3 was suppressed due to its seed location and preferred growth orientation relative to the surrounding dendrites. Grain 2 is located at a very particular position where is fully and closely surrounded by other dendrites. This special location leads to the dendrite grow with globular morphology. It can also be noticed that at the end of solidification, the grain boundaries are formed. Meanwhile, the main arms of dendrites are distorted at the end of solidification.

The right column shows the simulated composition fields at different times. It can be found, at the beginning of solidification, dendrites grow following the pre-set preferred orientation at a similar pattern. If dendrites are close to each other, the interaction of the solutal fields surrounding the dendrites occurs at very early stage of solidification. As solidification carries on, the interaction is then significantly affecting the growth of individual dendrite and therefore their structure evolution. Depending on the location and preferred orientation, some of the dendrites finally are able to develop secondary arms, while for others, the secondary arms are suppressed. At some particular position, some dendrites eventually grow as globular dendrites.

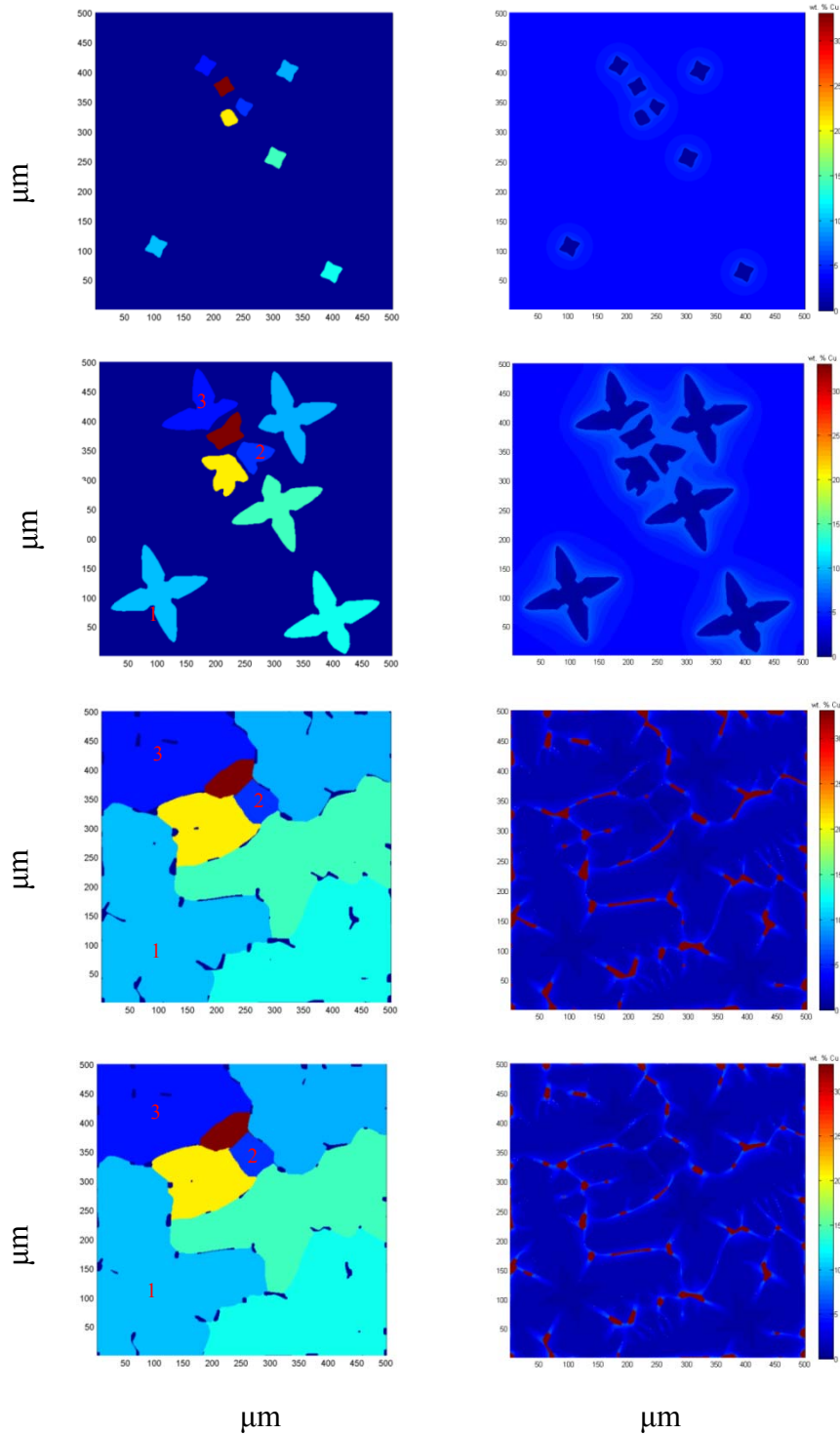


Figure 7.10 Simulated equiaxed dendrite evolution of an Al-4wt. %Cu alloy
 With a cooling rate of 10 K/s, the left column showing grain boundary formation, where different colours represent grains with different crystallographic orientations, and the right column showing composition field. From up to bottom after 0.1s, 0.4s, 8s and 10s.

7.4 Solidification Segregation

In the model, local equilibrium is assumed at the S/L interface, where the solid concentration, C_s^* , is related to the liquid concentration, C_l^* , by the equilibrium distribution coefficient k , as $C_s^* = kC_l^*$. The difference between C_s^* and C_l^* leads to concentration variations in the solidified solid phase, which is known as solidification segregation. Depending on the process involved in the solute redistribution, where the solute can be transported by diffusion or by convection or by both, the segregation pattern will be quite different, as microsegregation, macrosegregation or a mix of both. Because convection will not be treated in this thesis, attention will be limited to microsegregation.

In this section, simulations of Al-4wt. % Cu alloy solidification were performed in a domain of 500×500 meshes with a mesh size of 1 μm . Solid seeds with randomly generated preferred growth orientations were assigned randomly in the domain. To analyze the effect of amount of solid seeds and cooling rate on segregation, simulations of the solidification with different number of solid seeds and different cooling rates were performed. The effect of latent heat on structure evolution and solidification segregation will be examined as well.

7.4.1 Microsegregation during Equiaxed Multi-grain Growth

Simulated dendritic structures of an Al-4wt. %Cu alloy at time of 6s are shown in Figure 7.11. It can be found that some dendrites have fully developed secondary arms, while some dendrites have suppressed secondary arms due to their seeds location and preferred growth orientation relative to the surrounding dendrites. For some particular locations, some other dendrites finally grow with globular morphology. Figure 7.12 (a),

(b) and (c) show solute concentration at three positions as shown Line1, Line2 and Line3 in Figure 7.11. In Figure 7.12.(d), solute profiles for the 3 positions are plotted with line 2 being shifted 20 wt% and line 3 being shifted 40 wt% in y-axis direction, for a comparison purpose.

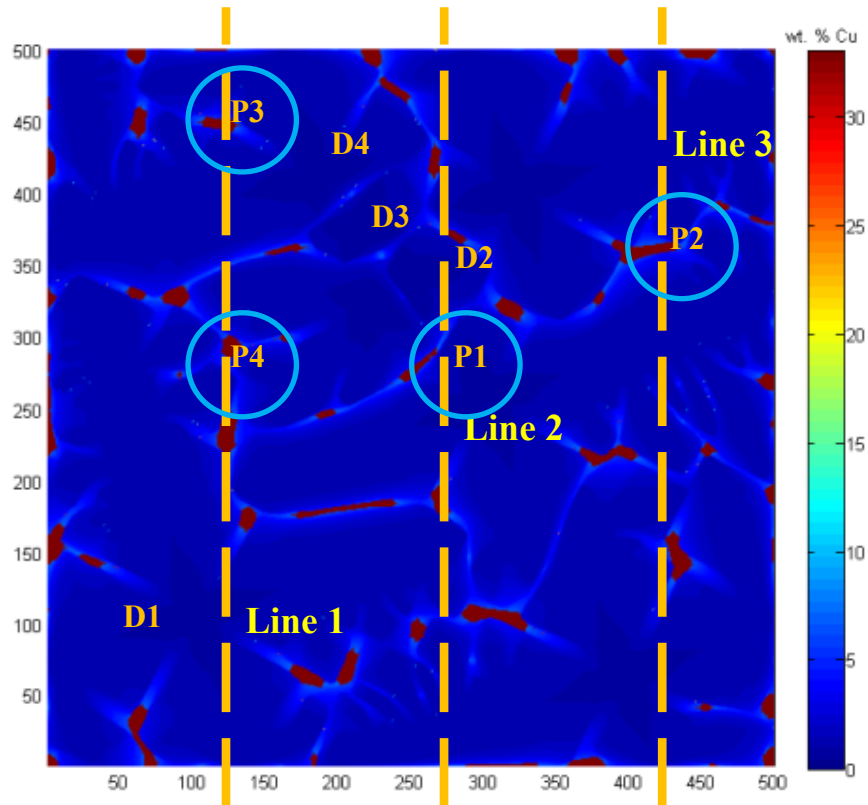


Figure 7.11 Simulated dendrite growth

Of solidification of an Al-4wt. %Cu alloy with a cooling rate of 10 K/s,
8 grain seeds, at time of 6s

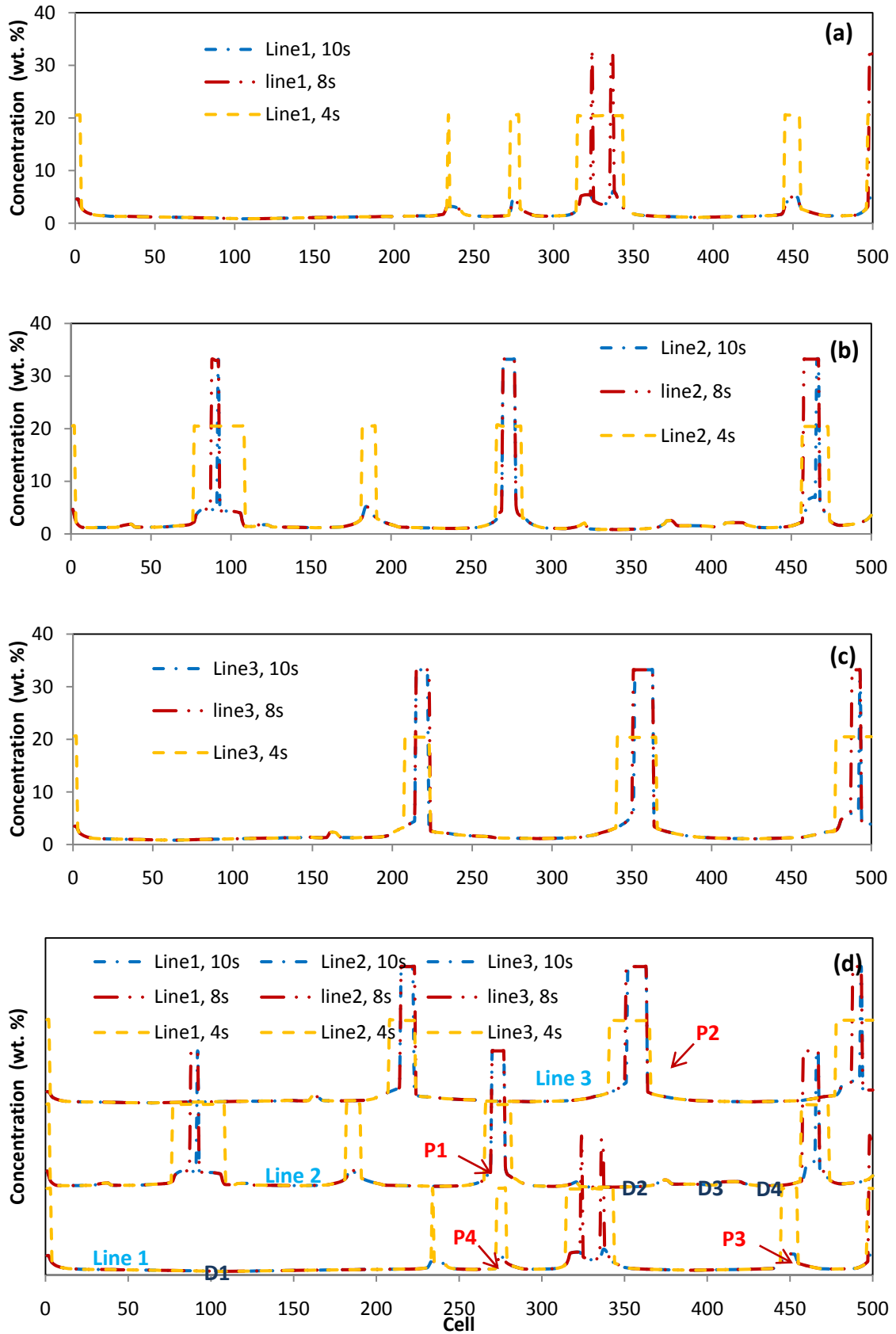


Figure 7.12 The solute profile across the simulated domain.

Firstly, it can be seen from the solute profiles, no significant composition gradient develops in solid located away from the dendritic boundaries. While deep gradient only forms in the solid regions close to the dendritic boundaries. These regions solidified at the late stages of the solidification and therefore are in contact with the last-to-freeze region. The reasons for this phenomenon are analyzed as followings:

During the solidification of Al-Cu alloys, solute is rejected into the liquid at the S/L interface, which leads to the creation of a solute enriched layer ahead of the S/L interface. At the early stages of the solidification, on one hand, the undercooling is smaller than that of the late stages of solidification due to the constant cooling rate applied to the system. On the other hand, for a same volume change of solid phase, the radius change is smaller near the dendrite boundary than that near the dendrite core.

Secondly, on solute profiles shown in Figure 7.12, it can also be noticed that the extent of microsegregation varies in different grains. Detailed concentration analysis was carried at four positions as indicated in Figure 7.11. At the positions P1 and P2, as shown in Figure 7.12, the composition gradient is much deeper than that at the positions P3 and P4. Comparing the concentration in liquid of these positions, it can be found that, at a same time during solidification, the concentration in the liquid at the positions P1 and P2 is much higher than that at the positions P3 and P4. Examining the simulated result in Figure 7.11, it can be found that, during the late stages of solidification, isolated liquid pools are formed. For regions like P1 and P2, where the liquid has a very small volume, as the solidification carries on during the last stages of solidification, the continuous release of solute at the S/L interface leads to rapid increases of concentration in smaller liquid pools. Accordingly, the solid formed in these regions has higher

concentration. As for regions with larger volume of liquid, such as P3 and P4, the composition increasing rate in the liquid is much smaller. Therefore, the concentration in the liquid is much smaller than that in regions P1 and P2, and solid formed in these regions also increases but not as much as that in regions P1 and P2.

Note that at the last stages of solidification, the compositional gradient in the liquid is not significant. As shown in Figure 7.12, in each isolated liquid area, the liquid has a nearly uniform concentration.

7.4.2 Comparison with the Scheil Model and Lever Rule

Figure 7.13 shows a comparison of simulated compositions in the liquid at the S/L interface with those predicted using the Scheil model and lever rule. The agreement is excellent at early stages of solidification. As for the final stages of solidification, the deviation becomes large between the Scheil model and lever rule. As discussed in detail in Chapter 2, in Eq.2.32, for the case of lever rule, where $\alpha' = 0.5$, the composition in the liquid increases from C_0 to C_0/k , while it increases from C_0 to infinity in the case of the Scheil model, where $\alpha' = 0$. The Scheil model is not able to predict the final liquid composition, since the maximum liquid concentration is infinite if no eutectic reaction occurs. While for the lever rule case, equilibrium solidification leads to a final liquid concentration, C_0/k , is also unrealistic diffusivity in the solid. For all of intermediate cases, parameter α' can take values between 0 and 0.5, which gives good approximation to the final composition for realistic cases. Comparing the simulated composition in the liquid at the S/L interface with predictions of the case of $\alpha' = 0.2$, the agreement is pretty good at the last stages of solidification.

The simulated composition profiles in dendrites as a function of solid fraction for cooling rates of 5, 10 and 15K/s are compared with the predictions of the Scheil model and lever rule in Figure 7.14. As the simulations with the present model were performed using realistic diffusion coefficients both in the solid and liquid, it can be noted that at the late stages of solidification, the simulated solid composition profiles agree very well with the predictions of the case of $\alpha'=0.2$, where the solid composition is higher than the prediction of the lever rule and lower than the prediction of the Scheil model.

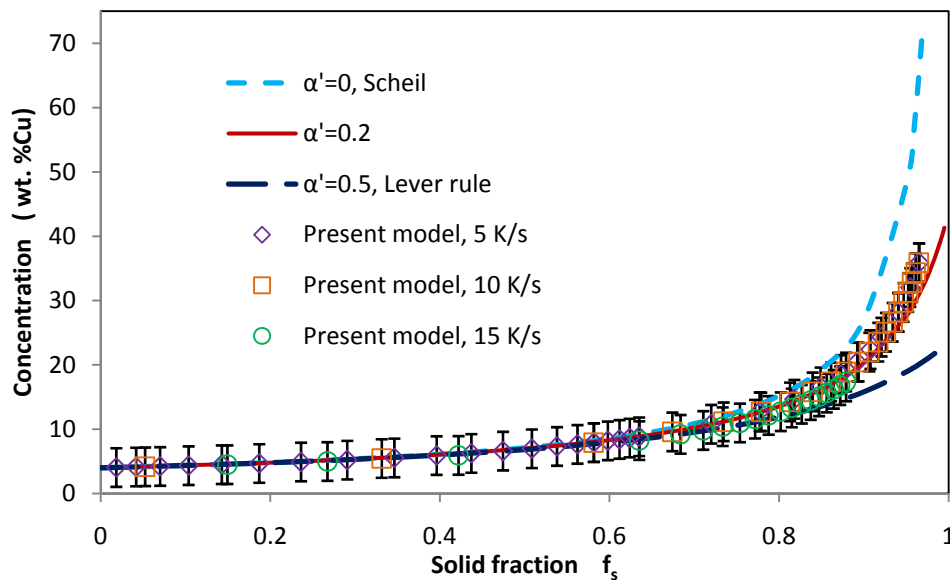


Figure 7.13 Comparison of the present model with the Scheil model and lever rule for predicting the Cu concentration in the liquid at the S/L interface as a function of solid fraction.

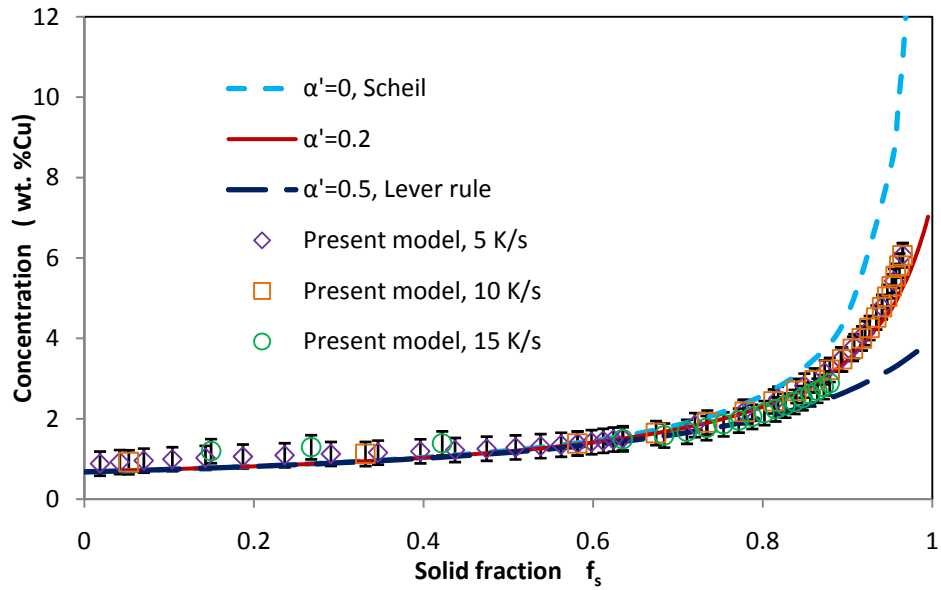


Figure 7.14 Comparison of the present model with the Scheil model and lever rule for predicting the Cu concentration in dendrites as a function of solid fraction.

7.4.3 Effect of Different Solid Seed Number and Cooling Rate on Segregation

Simulations of Al-4wt. % Cu alloy solidification were performed with different solid seed numbers and cooling rates. In this section, the effect of number of solid seeds and cooling rate on solidification segregation will be examined in detail.

To examine the effect of seed number on solidification segregation, simulations were performed for solidification at a cooling rate of 10 K/s with eight and twenty solid seeds assigned in the domain. The simulated composition profiles in dendrites as a function of solid fraction for solidification are plotted in Figure 7.15. It can be seen that the composition profiles are not affected by the number of solid seeds.

To examine the effect of cooling rate on solidification segregation, simulations were performed for solidification with eight solid seeds at cooling rates of 5 and 10 K/s. It can be noted that the composition profiles are not sensitive to the changes of cooling rate from 5K/s to 10K/s, as shown in Figure 7.15.

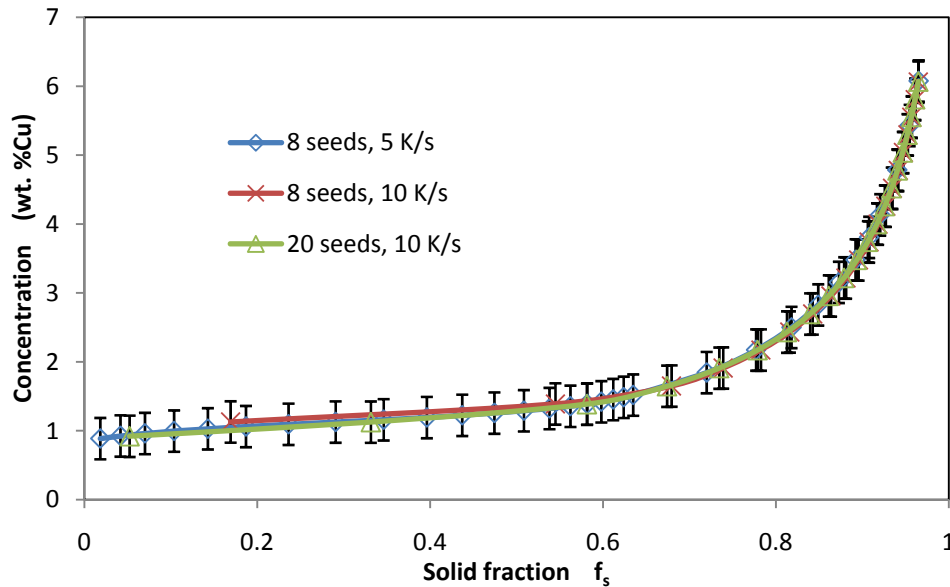


Figure 7.15 Simulated Cu concentration in dendrites as a function of solid fraction

7.4.4 Effect of Latent Heat on Segregation

In this section, the effect of latent heat on solidification segregation will be examined. Simulations of different cases of Al-4wt. % Cu alloy solidification were performed under the same conditions except considering latent heat or not. Simulations were performed for the solidification at a cooling rate of 10 K/s, in one case, with eight solid seeds, while in the other case, with twenty solid seeds.

The simulated composition profiles in dendrites as a function of solid fraction are plotted in Figure 7.16. It can be seen that the solidification segregation is not affected by

latent heat. To examine the effect of latent heat on segregation at late stages of solidification in details, the simulated composition profiles are plotted in Figure 7.17. It can be found that the solid concentration in the case of solidification without considering latent heat, where eight solid seeds and the cooling rate of 10 K/s are used, is a little bit lower than other cases. However, the deviation is not significant. In general, the solidification segregation is not significantly affected by latent heat inclusion in calculation.

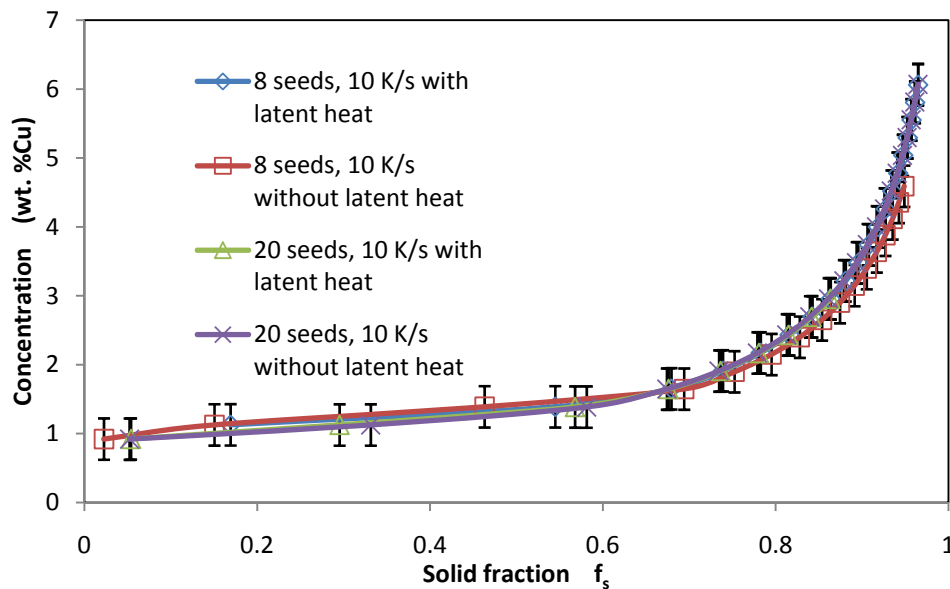


Figure 7.16 Simulated Cu concentration in dendrites as a function of solid fraction.

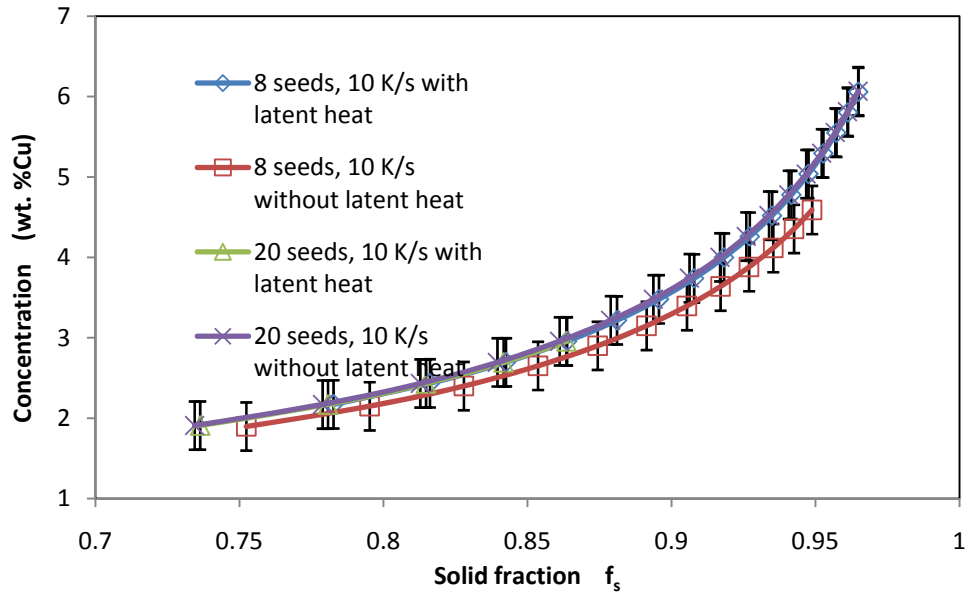


Figure 7.17 Simulated Cu concentration in dendrites as a function of solid fraction at late stages of solidification.

7.5 Summary

In this chapter, simulations of Al-Cu alloy solidification were carried out for single-grain under constant undercoolings and multi-grain growth under constant cooling rates using the optimised model.

The evolution of dendritic tip velocity from the initial stage to steady-state under different undercoolings was analysed. Single dendritic morphology was predicted. The solute profiles ahead of dendritic tip under different undercoolings were analyzed. Comparisons of the steady-state tip velocity at different melt undercoolings between the developed model and the LGK model predictions was carried out. A reasonably good agreement was obtained. Different techniques for calculating solute concentration in the interface cells were. Exponential decay of solute concentration in liquid away from the S/L interface was observed for all three methods. However, it is found that the accuracy

in the weighted average method is lower than that of exponential and central approximations. The predicted results using the central approximation is close to those predicted using the exponential approximation, but the central approximation is much more efficient than the exponential approximation.

Multi-grain microstructure evolution was simulated and the solutal interaction was examined. The solidification segregation during multi-grain growth was investigated in detail. Comparison with the solidification segregation predictions of the Scheil model and lever rule was carried out and the predicted data were found to fall between the results from the two extreme cases. Effect of different conditions, such as cooling rate, solid seed number and latent heat, on segregation was examined and found to have little effect.

Chapter 8 Conclusions and Future Work

A front-tracking model of microstructure evolution during alloy solidification has been developed. It can predict the dendritic structure evolution during alloy solidification. Using the proposed new capture rule, the S/L interface can be tracked efficiently.

8.1 Conclusions

8.1.1 Model Development

A front-tracking solidification model has been developed to simulate the dendritic structure evolution during alloy solidification. In the model the growth of dendrites was governed by heat and mass transport and a finite difference technique is employed to solve heat and solute diffusion during solidification; the model incorporates a front-tracking technique to calculate and track the exact position of the S/L interface as a part of solution process and a new capture rule was designed and implemented in the model to efficiently track the growing S/L interface.

The model has been evaluated and verified using simulated data from Al-Cu 4 wt. % alloy solidification. The effect of curvature undercooling on crystal growth was investigated. First, the accuracy of S/L interfacial curvature estimation was examined using different methods for solving interfacial curvature. Then, the effect of parameters used in anisotropy calculation of interface tension during dendrite growth was examined. The simulated results reveal that solute redistribution, curvature of the S/L interface and

anisotropy of interface tension are important factors in determining the dendritic morphology. The calculation of the S/L interface curvature and anisotropy of surface tension is found to be particularly important in determining the dendritic growth direction. Based on the above observations and simulated data, the parameters in the developed model have been optimised for predicting the solidification structure in binary alloys.

8.1.2 Simulation using the Developed Model

Using the optimised model, simulations of Al-Cu alloy solidification were carried out for single-grain under constant undercoolings and multi-grain growth under constant cooling rates.

8.1.2.1 Single-grain Growth

Single-grain growth under constant undercoolings was simulated. The evolution of dendritic tip velocity from the initial stage to steady-state under different undercoolings was analysed. Single dendritic morphology was predicted. The solute profiles ahead of dendritic tip under different undercoolings were analyzed. Comparisons of the steady-state tip velocity at different melt undercoolings between the developed model and the LGK model predictions was carried out. A reasonably good agreement was obtained.

Different techniques for calculating solute concentration in the interface cells were examined using (1) central difference method, (2) exponential approximation and (3) weighted average method. Exponential decay of solute concentration in liquid away from the S/L interface was observed for all three methods. However, it is found that the accuracy in the weighted average method is lower than that of exponential and central approximations. The predicted results using the central approximation are close to those

predicted using the exponential approximation, but the central approximation is much more efficient than the exponential approximation.

8.1.2.2 Multi-grain Growth

Multi-grain growth with different cooling rates has been simulated and the solutal interaction was examined. The solidification segregation during multi-grain growth was investigated in detail. Comparison with the solidification segregation predictions of the Scheil model and lever rule were carried out and the predicted data fall between the results from the two extreme cases. Effect of different conditions, such as cooling rate, solid seed number and latent heat, on segregation was examined.

8.2 Future Work

The developed model is based on binary alloy system, where the crystal growth is considered to be governed by heat and mass transport. The liquidus and solidus lines are assumed to be straight, where the constant partition coefficient is used in the model.

Firstly, the suggested improvement to the model is to take into account of convection. As convection happens in the liquid during solidification at most times, which can modify the solute and heat fields significantly, the crystal growth is affected by convection. Secondly, the parameters such as partition coefficient, solute diffusivity in the liquid and solid are used as constant. More accurate parameters can be used by linking the model to material property database.

Furthermore, as every computer modeller in materials science will agree, more experiments should be done to determine better values for all the physical properties used as inputs to the model and optimise the parameters used in the model.

Appendix A. Phase-Field Modelling of Solidification

The modelling method in this thesis focuses on front-tracking method for microstructure evolution during alloy solidification. However in the early stages of the PhD study, the phase field method was also investigated and a preliminary phase field code was written. Therefore in this appendix chapter, the developed Phase-Field programme will be described briefly.

In this chapter, a full introduction of investigation on modelling of microstructure evolution of solidification with phase-field models will be given. Two models have been developed for studying simulation of microstructure evolution during solidification: phase-field model for simulation of pure substance solidification and phase-field model for simulation of binary alloy solidification. Two programs based on above models have been developed using Microsoft Visual C++[®] 6.0 in Microsoft Windows XP[®] system.

1 Simulation of Pure Metal Solidification

A phase-field model for simulation of solidification of pure metal has been developed. And a program based on this model has been written with Microsoft Visual C++[®] 6.0 to simulate the microstructure evolution during the solidification of pure metal.

1.1 Phase-field Model

The phase-field model for simulation of pure metal solidification is based on free-energy of system. For governing equation, we use Eq. 3.10 with solute concentration $C=0$, which means pure metal.

Various choices of the free-energy density have been suggested. One of them can be written as (Boettinger *et al.* 2002):

$$f(\Phi, T) = \frac{1}{8a}(1 - \Phi^2)^2 - (T - T_M)\Phi \quad (\text{a.1})$$

in which a is a positive constant, and T_M is the melting temperature of the material. The solid and liquid phases are presented by Φ in neighbourhood -1 and +1 respectively.

From Eq. 3.13, we can obtain the following dimensionless governing equations for phase-field, Φ , and temperature, u , as Eqs. a.2 and a.3. To include anisotropy, we apply an anisotropy function $\varepsilon(\psi) = \bar{\varepsilon}\eta(\psi) = \bar{\varepsilon}(1 + \gamma \cos \zeta\psi)$, in which γ is the strength of the surface tension anisotropy, ζ is the mode number and $\psi = \arctan(\Phi_y / \Phi_x)$ is the angle between the normal to the interface and the x-axis.

$$\begin{aligned} \frac{\bar{\varepsilon}^2}{m} \frac{\partial \Phi}{\partial t} = & \Phi(1 - \Phi) \left[\Phi - \frac{1}{2} + 30\bar{\varepsilon}b\Omega u \Phi(1 - \Phi) \right] \\ & - \bar{\varepsilon}^2 \frac{\partial}{\partial x} \left(\eta(\psi)\eta'(\psi) \frac{\partial \Phi}{\partial y} \right) + \bar{\varepsilon}^2 \frac{\partial}{\partial y} \left(\eta(\psi)\eta'(\psi) \frac{\partial \Phi}{\partial x} \right) \end{aligned} \quad (\text{a.2})$$

$$\frac{\partial u}{\partial t} + \frac{1}{\Omega} p'(\Phi) \frac{\partial \Phi}{\partial t} = \nabla^2 u \quad (\text{a.3})$$

where Ω is the dimensionless undercooling which can be defined as $\Omega = \frac{C_p \Delta T}{L}$ (in which C_p is the specific heat and L is the latent heat per unit volume) and $p(\Phi) = \Phi^3(10 - 15\Phi + 6\Phi^2)$ (an interpolating function). $\bar{\varepsilon}$, m and l can be defined as:

$$b = \frac{\sqrt{2}wL^2}{12c\sigma T_M} \quad (\text{a.4})$$

$$m = \frac{\mu\sigma T_M}{\alpha L} \quad (\text{a.5})$$

$$\bar{\varepsilon} = \frac{\delta}{w} \quad (\text{a.6})$$

where σ is the interfacial energy, μ is the mobility, δ is an estimate of the S/L interface thickness, α is the thermal diffusivity and W is the characteristic length scale.

With the definitions of Eqs a.4, a.5 and a.6, these three model parameters are related to the physical parameters which characterize the interface dynamics (i.e., interfacial energy and mobility) and to an estimate of the interface thickness, which is a consequence of the phase field approach.

Once the W has been chosen, according to the physical properties, one degree of freedom $\bar{\varepsilon}$ is then used to set the interface thickness. In order to model the physical behaviour correctly, the interface thickness must be sufficiently small compared to the interfacial macrostructures which we wish to model. But, from a viewpoint of computation, it is better for the interface thickness to be as large as possible in order to obtain accurate solution of the phase field equations for practical computational effort.

Numerical procedures

To model the microstructure evolution of pure metal solidification in two dimensions, the governing equation for phase-field, Eqs. a.2, is solved numerically using explicit finite difference scheme. For the temperature field equation, Eq. a.3, the Alternating Direction Implicit method (ADI) is applied. As ADI is unconditional conservative, the condition convergence of the system therefore only depends on the calculation of phase field, which can be given as:

$$\Delta t \leq (\Delta x)^2 / 4D \quad (\text{a.7})$$

in which Δx is the size of the cell. Using a square grid with cells of size Δx by Δy , the parameter in cell(i, j) at time step k is shown as $\Phi_{i,j}^k$.

For the phase-field variable, from Eq. a.2, we can obtain:

$$\begin{aligned} \Phi_{i,j}^{k+1} = \Phi_{i,j}^k + \frac{m \cdot \Delta t}{\bar{\varepsilon}^2} & \left\{ \Phi_{i,j}^k (1 - \Phi_{i,j}^k) \left[\Phi_{i,j}^k - \frac{1}{2} + 30\bar{\varepsilon}b\Omega u \Phi_{i,j}^k (1 - \Phi_{i,j}^k) \right] \right\} \\ & + m \cdot \Delta t \left\{ \begin{aligned} & 16\gamma [\cos 4\theta + \gamma \cos 8\theta] [\theta_x \cdot \Phi_y - \theta_y \Phi_x] \\ & - [\theta_x \cdot \Phi_x - \theta_y \Phi_y] [8\gamma \sin 4\theta + 4\gamma^2 \sin 8\theta] \\ & + [\Phi_{xx} + \Phi_{yy}] [1 + \gamma \cos 4\theta]^2 \end{aligned} \right\} \quad (\text{a.8}) \end{aligned}$$

with the definitions of:

$$\begin{aligned} \theta_x &= \frac{\Phi_x \Phi_{xy} - \Phi_y \Phi_{xx}}{\Phi_x^2 + \Phi_y^2} & \theta_y &= \frac{\Phi_x \Phi_{yy} - \Phi_y \Phi_{xy}}{\Phi_x^2 + \Phi_y^2} \\ \Phi_x &= \frac{\Phi_{i+1,j}^k - \Phi_{i,j}^k}{\Delta x} & \Phi_y &= \frac{\Phi_{i,j+1}^k - \Phi_{i,j}^k}{\Delta y} \end{aligned}$$

$$\Phi_{xy} = \frac{\Phi_{i+1,j}^k - \Phi_{i+1,j-1}^k - \Phi_{i,j}^k + \Phi_{i,j-1}^k}{\Delta x \Delta y} \quad \Phi_{xx} = \frac{\Phi_{i+1,j}^k - 2\Phi_{i,j}^k + \Phi_{i-1,j}^k}{\Delta x^2}$$

$$\theta = \arctan(\Phi_y / \Phi_x) \quad \Phi_{yy} = \frac{\Phi_{i,j+1}^k - 2\Phi_{i,j}^k + \Phi_{i,j-1}^k}{\Delta y^2}$$

And for the temperature field, using ADI, we can obtain from Eq a.3:

$$U_{i,j}^{k+1} = \frac{\Delta x^2 - 2\Delta t}{\Delta x^2 + 2\Delta t} U_{i,j}^k - \frac{\Delta x^2}{\Delta x^2 + 2\Delta t} \frac{30}{\Omega} [\Phi_{i,j}^k]^2 [1 - \Phi_{i,j}^k]^2 [\Phi_{i,j}^{k+1} - \Phi_{i,j}^k] + \frac{\Delta t}{\Delta x^2 + 2\Delta t} [U_{i+1,j}^{k+1} + U_{i-1,j}^{k+1} + U_{i,j+1}^k + U_{i,j-1}^k] \quad (\text{a.9})$$

$$U_{i,j}^{k+2} = \frac{\Delta x^2 - 2\Delta t}{\Delta x^2 + 2\Delta t} U_{i,j}^{k+1} - \frac{\Delta x^2}{\Delta x^2 + 2\Delta t} \frac{30}{\Omega} [\Phi_{i,j}^{k+1}]^2 [1 - \Phi_{i,j}^{k+1}]^2 [\Phi_{i,j}^{k+2} - \Phi_{i,j}^{k+1}] + \frac{\Delta t}{\Delta x^2 + 2\Delta t} [U_{i+1,j}^{k+1} + U_{i-1,j}^{k+1} + U_{i,j+1}^{k+2} + U_{i,j-1}^{k+2}] \quad (\text{a.10})$$

Then, with the definitions of A_i , B_i , C_i , D_i and D_j as

$$A_i = C_i = \Delta t, \quad B_i = \Delta x^2$$

$$D_i = -A_i U_{i,j-1}^k + (B_i + 2A_i) U_{i,j}^k - C_i U_{i,j+1}^k - F_i [\Phi_{i,j}^k]^2 [1 - \Phi_{i,j}^k]^2 [\Phi_{i,j}^{k+1} - \Phi_{i,j}^k]$$

$$D_j = -A_i U_{i-1,j}^k + (B_i + 2A_i) U_{i,j}^{k+1} - C_i U_{i+1,j}^{k+1} - F_i [\Phi_{i,j}^{k+1}]^2 [1 - \Phi_{i,j}^{k+1}]^2 [\Phi_{i,j}^{k+2} - \Phi_{i,j}^{k+1}]$$

we can obtain

$$A_i U_{i-1,j}^{k+1} + (B_i - 2A_i) U_{i,j}^{k+1} + C_i U_{i+1,j}^{k+1} = D_i \quad (\text{a.11})$$

$$A_i U_{i,j-1}^{k+2} + (B_i - 2A_i) U_{i,j}^{k+2} + C_i U_{i,j+1}^{k+2} = D_j \quad (\text{a.12})$$

Material parameters used for calculation are as shown in Table A0.1 (Long *et al.* 2003).

Table A0.1 Material properties

Material name	Copper
Density ρ g/m ³	8.96e+6
Melting point T_M K	1356
Latent heat of fusion L J/g	205
Specific heat C_p J/(K·g)	0.385
Thermal conductivity λ W/(m·K)	401
System parameter $\bar{\epsilon}$	0.005
Strength of surface tension anisotropy	$10^{-2} \leq \gamma \leq 3 \times 10^{-2}$
Mode of surface tension anisotropy ζ	4
Interface energy σ J/m ²	0.37

1.2 Simulation Program

The program, based on phase-field model for solidification of pure metal is written in Microsoft Visual C++ 6.0[®]. It contains three sections: initialization module, calculation module and result outputting module. Both initial conditions and boundary conditions are defined in the initialization module, including defining size of sample and cell, initializing variables for temperature field and phase field and setting thermodynamic and kinetic parameters. All the calculations for heat transfer, phase-field evolution and some relevant parameters are made in the calculation module. During the calculation, parameters which vary with the change of the temperature field and status of the system are calculated firstly. Then with these new values, the new temperature field and phase-field are calculated. Finally, with a preset time interval, the results are saved into hard disk in text file in the outputting module.

The flow charts of the program are shown as followings:

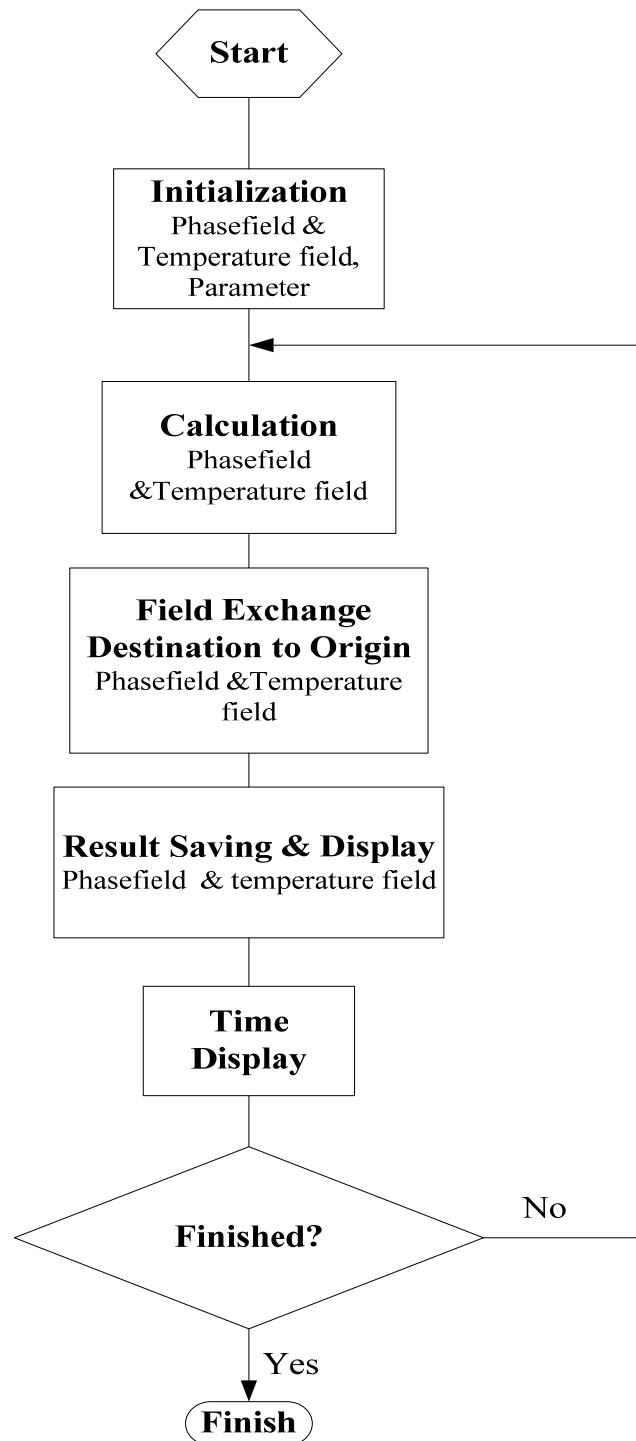


Figure A0.1 Flow chart of program for phase-field model for pure metal

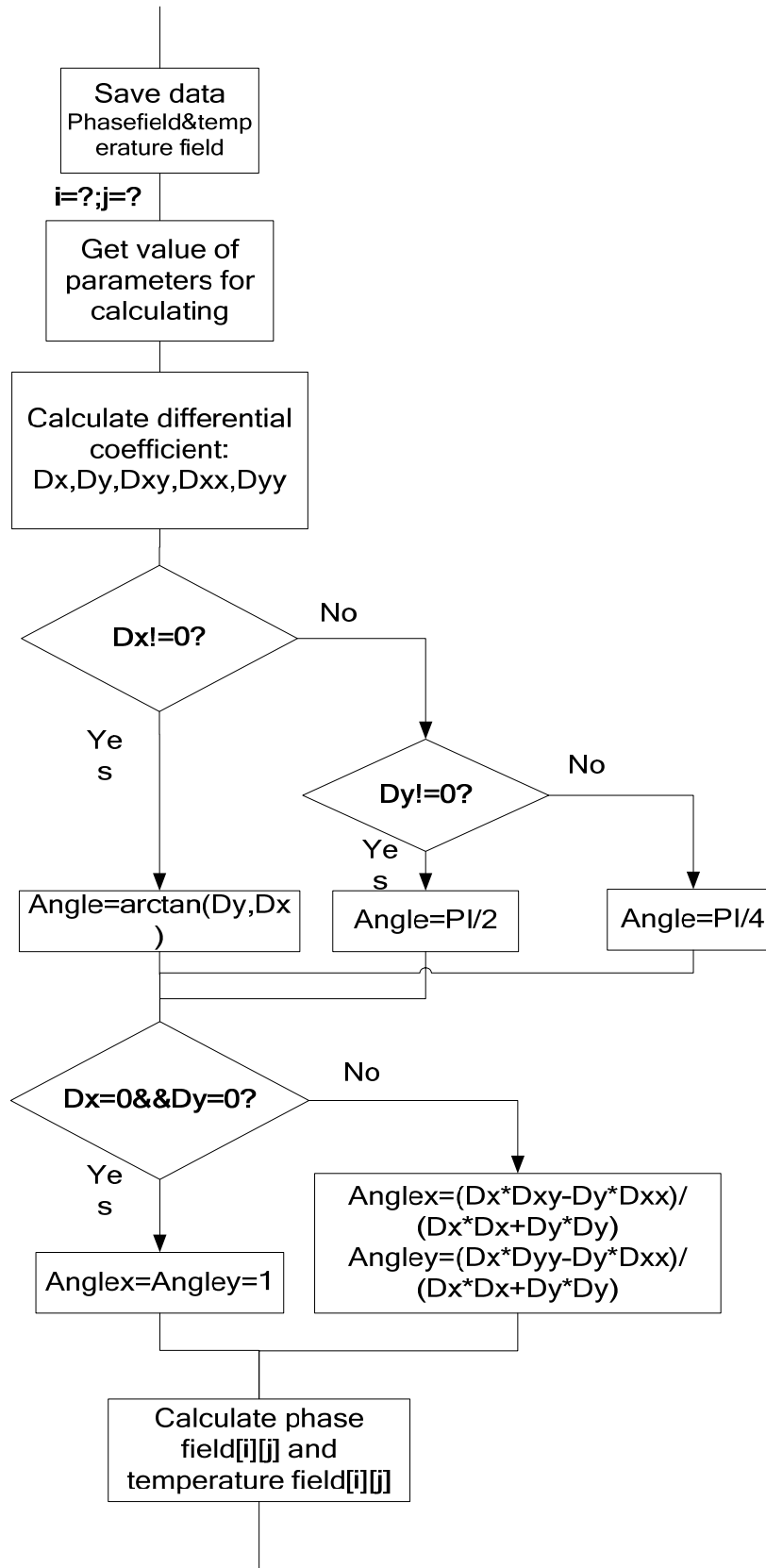


Figure A0.2 Flow chart of calculation loop

1.3 Results and Discussion

With the developed program, the dendrite growth of pure copper during solidification is calculated. Parameters used are as shown in Table a.1. The simulation results are saved in text file on hard disk. With the software of Tecplot[®] 9.0, the results can be transferred to pictures. Some results are shown in Figure A0.3 for different stages of dendrite evolution. In the pictures, the region with blue colour stands for liquid and region with red colour stands for solid. The region between solid and liquid is the S/L interface. The dendritic morphology agrees with Kobayashi's (1993).

As the application of alloys is much wider than that of pure metals, more attention has been paid on simulation of microstructure evolution of alloy solidification in the following work. Both phase-field and front-tracking models for solidification of binary alloys has been developed. In the following section, details of these two models are presented.

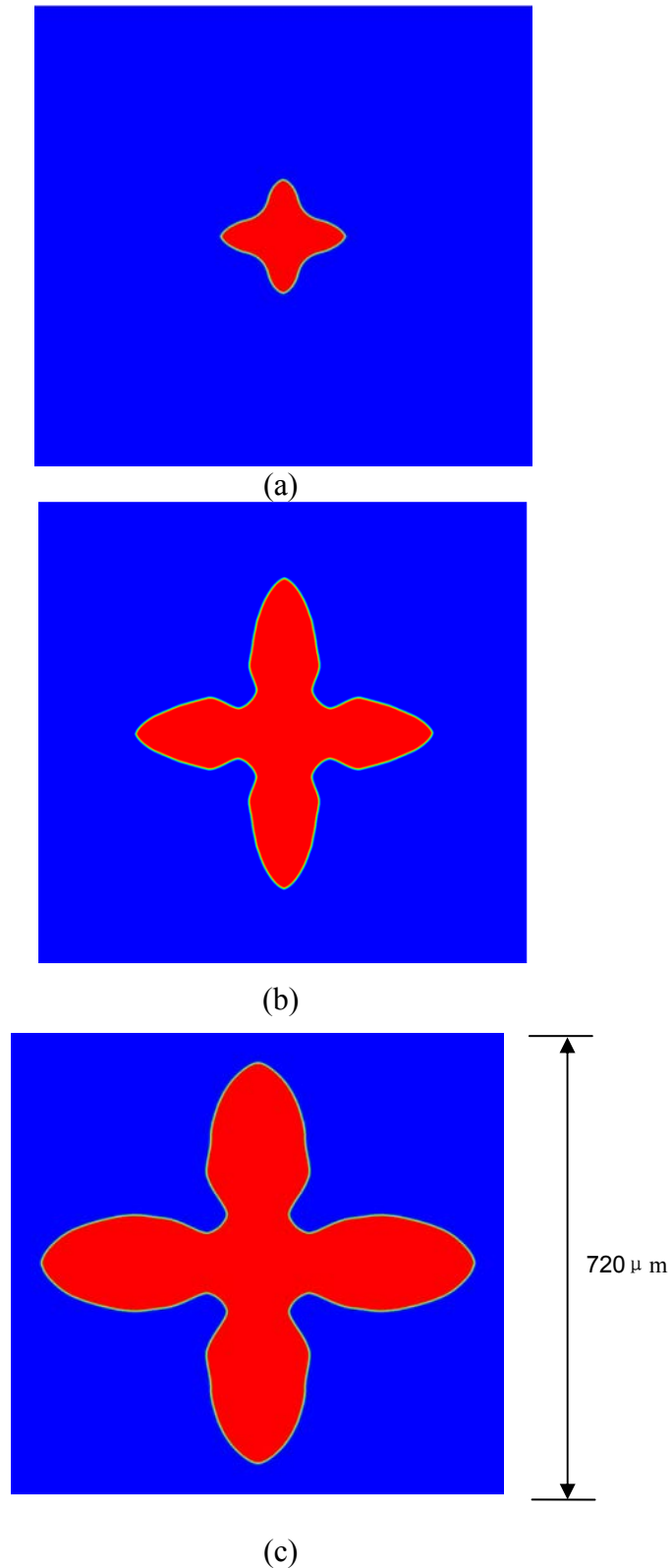


Figure A0.3 Simulated dendritic structure evolution for a pure metal

Under constant undercooling (2K) at simulation domain 1800×1800 at cell size = $0.4 \mu\text{m}$

(a) Growth time=5 s (b) Growth time=10 s (c) Growth time=15 s

2 Phase-field for Simulation of Binary Alloy Solidification

To construct a phase-field model for solidification of binary alloys, we start from an expression for the total free energy of the system.

The phase-field equations considered are as shown in Eqs. 3.10, 3.13 and 3.14.

In the total free energy of the system, Eq. 3.11, the free energy density can be given as the bulk free energy density of a binary mixture of A and B atoms/molecules (Boettinger *et al.* 2002).

$$f_{AB}(\Phi, C, T) = f(\Phi, T_M) + f_T(\Phi)\Delta T + \frac{RT_M}{v_0}(C \ln C - C) + \bar{\varepsilon}C + \bar{g}(\Phi)\frac{\Delta\varepsilon}{2}C \quad (\text{a.13})$$

where C is the solute concentration defined as the mole fraction of B . It is the sum of the free energy of the pure material $f(\Phi, T_M)$ and the contribution due to solute addition. The latter is the sum of the standard entropy of mixing $RTv_0^{-1}(C \ln C - C)$, where R is the universal gas constant and v_0 is the molar volume assumed constant, and the change $\bar{\varepsilon}C$ of the energy density due to solute addition. $\bar{\varepsilon}$ can be given as:

$$\bar{\varepsilon}(\Phi) = \frac{1 + \bar{g}(\Phi)}{2} \varepsilon_s + \frac{1 - \bar{g}(\Phi)}{2} \varepsilon_l \quad (\text{a.14})$$

which interpolates between the values ε_s and $\varepsilon_l < \varepsilon_s$ in the solid and liquid, respectively.

$\bar{g}(\Phi)$ is a monotonously increasing function of Φ with limits $\bar{g}(\pm 1) = \pm 1$, with $\Phi = +1$ ($\Phi = -1$) corresponding to solid (liquid). respectively.

The free energy of pure metal has the standard form of a double-well potential with a barrier height H , as:

$$f(\Phi, T_M) = H(-\Phi^2/2 + \Phi^4/4) \quad (\text{a.15})$$

Moreover, this pure part has been expanded to first order in $\Delta T = T - T_M$ by defining the function $f_T(\Phi) \equiv \partial f(\Phi, T) / \partial T \big|_{T=T_M}$, and RT/v_0 has been replaced by RT_M/v_0 .

Numerical procedures

The equilibrium properties of the model follow from the following conditions, which determine the spatially varying stationary profiles of c and Φ in the diffuse interface region equations, as (Boettinger *et al.* 2002):

$$\frac{\delta F}{\delta c} = \mu_E \quad (\text{a.16})$$

$$\frac{\delta F}{\delta \Phi} = 0 \quad (\text{a.17})$$

where μ_E is the spatially uniform equilibrium value of the chemical potential. Eq. a.17 is equivalent to requiring that the chemical potential and the grand potential be equal in the solid and liquid, or, respectively,

$$\left. \frac{\partial f_s(C, T)}{\partial C} \right|_{C=C_s^0} = \left. \frac{\partial f_l(C, T)}{\partial C} \right|_{C=C_l^0} = \mu_E \quad (\text{a.18})$$

$$f_s(C_s^0, T) - \mu_E C_s^0 = f_l(C_l^0, T) - \mu_E C_l^0 \quad (\text{a.19})$$

Applying the first equilibrium condition Eq. a.16, we can obtain

$$\frac{RT_M}{v_0} \ln C + \bar{\varepsilon} + \bar{g}(\Phi) \frac{\Delta \varepsilon}{2} = \mu_E \quad (\text{a.20})$$

With Eq a.20, we can then obtain the expressions for the equilibrium partition coefficient and the stationary concentration profile as the following respectively:

$$k \equiv \frac{C_s^0}{C_l^0} = \exp\left(-\frac{v_0 \Delta \varepsilon}{RT_M}\right) \quad (\text{a.21})$$

$$C_0(x) = C_l^0 \exp\left(\frac{\ln k}{2} \{1 + \bar{g}[\Phi(x)]\}\right) \quad (\text{a.22})$$

Applying the second equilibrium condition Eq. a.17, we can obtain

$$\sigma \frac{d^2 \Phi_0}{dx^2} + H(\Phi_0 - \Phi_0^3) = f'_T(\Phi_0) \Delta T + \bar{g}'(\Phi_0) \frac{\Delta \varepsilon}{2} c_0 \quad (\text{a.23})$$

where $f_T(\Phi)$ is chosen as:

$$f_T(\Phi) = \frac{RT_M}{v_0 m} \exp\left(\frac{\ln k}{2} [1 + \bar{g}(\Phi)]\right) \quad (\text{a.24})$$

For Eq. a.23, choosing

$$T = T_M + m C_l^0 \quad (\text{a.25})$$

the right-hand side of vanishes.

As $f_T(+1) - f_T(-1) = L/T_M$, the right-hand side of Eq. a.24 is such that the Van't Hoff relation

$$\frac{L}{T_M} = \frac{RT_M(1-k)}{v_0 m} \quad (\text{a.26})$$

is recovered by subtracting Eq. a.24 evaluated at $\Phi = +1$ from the same equation evaluated at $\Phi = -1$. This relation is a special case of the Gibbs-Konovalov rule when applied to dilute alloys.

In addition, to make Eq. 3.14 reduce to Fick's law of diffusion in the liquid, we then obtain

$$K_c = \frac{v_0}{RT_M} Dq(\Phi)C \quad (\text{a.27})$$

where $q(\Phi)$ is a dimensionless function dictating how the solute diffusivity varies through the diffuse interface.

Now, we obtain the governing equations for phase-field and solute diffusion, as

$$\begin{aligned} \tau \frac{\partial \Phi}{\partial t} = & W^2 \nabla^2 \Phi + \Phi - \Phi^3 + \frac{RT_M \ln k}{vH} \bar{g}'(\Phi) \\ & \times \left[C - \frac{T - T_M}{m} \exp\left(\frac{\ln k}{2} [1 + \bar{g}(\Phi)]\right) \right] \end{aligned} \quad (\text{a.28})$$

$$\frac{\partial C}{\partial t} = \bar{\nabla} \left(Dq(\Phi) C \bar{\nabla} \left[\ln C - \frac{1-k}{2} \bar{g}(\Phi) \right] - \vec{j}_{at} \right) \quad (\text{a.29})$$

where $\tau = 1/(K_\Phi H)$. To rewrite the above equations in terms of the dimensionless variable, we make

$$\mu = \frac{v_0}{RT_M} (\mu - \mu_\infty) = \ln(C/C_\infty) - \frac{\ln k}{2} [\bar{g}(\Phi) + 1] \quad (\text{a.30})$$

which measures the departure of the chemical potential from its value μ_∞ for a flat interface at the equilibrium liquidus temperature. Accordingly, we make

$$\exp\left(\frac{\ln k}{2}[1 + \bar{g}(\Phi)]\right) = \frac{1+k}{2} - \frac{1-k}{2}\tilde{g}(\Phi) \quad (\text{a.31})$$

which has the same limits $\tilde{g}(\pm 1) = \pm 1$.

Therefore, Eqs. a.28 and a.29 become

$$\tau \frac{\partial \Phi}{\partial t} = W^2 \nabla^2 \Phi + \Phi - \Phi^3 - \frac{RT_M(1-k)C_\infty}{2\nu_0 H} \tilde{g}(\Phi) \times \left(\exp(u) - \frac{T-T_M}{mC_\infty}\right) \quad (\text{a.32})$$

$$\frac{\partial C}{\partial t} = \bar{\nabla} \left(Dq(\Phi) C \bar{\nabla} u - \bar{j}_{at} \right) \quad (\text{a.33})$$

where $u = \ln(2(C/C_\infty)/[1+k-(1-k)\tilde{g}(\Phi)])$. To replace the function $\tilde{g}(\Phi)$ in this last expression for u by another function $h(\Phi)$ that has the same limits at $\Phi = \pm 1$. The simplest choice is $h(\Phi) = \Phi$, which yields the new expression

$$\mu = \ln\left(\frac{2C/C_\infty}{1+k-(1-k)\Phi}\right) \quad (\text{a.34})$$

The phase-field model is now completely defined by Eqs. a.32–a.34 and 3.9, together with the additional choices

$$\bar{j}_{at} = -\frac{C_\infty(1-k)W}{2\sqrt{2}} \exp(u) \frac{\partial \Phi}{\partial t} \frac{\bar{\nabla} \Phi}{|\bar{\nabla} \Phi|} \quad (\text{a.35})$$

$$q(\Phi) = \frac{1-\Phi}{1+k-(1-k)\Phi} \quad (\text{a.36})$$

Consider the solidification of a dilute binary alloy with equal thermal diffusivity (α) and specific heat at constant pressure (C_p) in solid and liquid, for solute and heat diffusion, we define, respectively,

$$U = \frac{C - C_\infty}{(1-k)C_\infty} \quad (\text{a.37})$$

$$\mathcal{G} = \frac{T - T_M - mC_\infty}{L/C_p} \quad (\text{a.38})$$

Then, we obtain the final governing equations of phase-field, solute diffusion and heat transfer:

$$\tau \frac{\partial \Phi}{\partial t} = W^2 \nabla^2 \Phi + \Phi - \Phi^3 - \lambda g'(\Phi)(\mathcal{G} + MC_\infty U) \quad (\text{a.39})$$

$$\frac{1+k}{2} \frac{\partial U}{\partial t} = \bar{\nabla} \left(D \frac{1-\Phi}{2} \bar{\nabla} U + \frac{W}{2\sqrt{2}} [1 + (1-k)U] \frac{\partial \Phi}{\partial t} \frac{\bar{\nabla} \Phi}{|\bar{\nabla} \Phi|} \right) \quad (\text{a.40})$$

$$\frac{\partial \mathcal{G}}{\partial t} = \alpha \nabla^2 \mathcal{G} + \frac{1}{2} \frac{\partial \Phi}{\partial t} \quad (\text{a.41})$$

where $\tau = \frac{1}{K_\Phi H}$, in which H is double well potential barrier height, and W is width of

the diffuse interface. To take into account the interface anisotropy, we choose W as:

$$W = W_0 A(\hat{n}) = W_0 (1 + \varepsilon \cos B\varphi) \quad (\text{a.42})$$

in which ε is the strength of anisotropy, B is the anisotropy mode and φ is the angle between the interface normal and the x-axis, as $\varphi = \arctan(\partial y / \partial x)$.

The explicit finite difference method is employed to solve phase field and solute diffusion calculation. And for temperature calculation, the Alternating Direction Implicit (ADI) method is applied. Because ADI is unconditional conservative, the

condition of convergence only depends on the calculation of solute diffusion:

$$\Delta t < \Delta x^2 / 4D_l.$$

From the phase-field governing equation, we obtain:

$$\tau \frac{\Phi_{i,j}^{k+1} - \Phi_{i,j}^k}{\Delta t} = W^2 \left(\frac{\partial^2 \Phi}{\partial x^2} + \frac{\partial^2 \Phi}{\partial y^2} \right) + \Phi - \Phi^3 - \lambda g'(\Phi)(\mathcal{G} + MC_\infty U) \quad (\text{a.43})$$

$$\Phi_{i,j}^{k+1} = \frac{\Delta t \cdot W^2}{\tau} \left[\left(\frac{\partial^2 \Phi}{\partial x^2} + \frac{\partial^2 \Phi}{\partial y^2} \right) + \Phi - \Phi^3 - \lambda g'(\Phi)(\mathcal{G} + MC_\infty U) \right] + \Phi_{i,j}^k \quad (\text{a.44})$$

For solute diffusion, the equation can be written as:

$$\frac{1+k}{2} \frac{\partial U}{\partial t} = \bar{\nabla} \left(D \frac{1-\Phi}{2} \bar{\nabla} U + \frac{W}{2\sqrt{2}} [1 + (1-k)U] \frac{\partial \Phi}{\partial t} \cdot \frac{\bar{\nabla} \Phi}{|\bar{\nabla} \Phi|} \right) \quad (\text{a.45})$$

$$\begin{aligned} \frac{1+k}{2} \frac{U_{i,j}^{k+1} - U_{i,j}^k}{\Delta t} &= \left(D \frac{1-\Phi}{2} \left(\frac{\partial^2 U}{\partial x^2} + \frac{\partial^2 U}{\partial y^2} \right) + \right. \\ &\quad \left. \frac{W}{2\sqrt{2}} [1 + (1-k)U_{i,j}^k] \frac{\Phi_{i,j}^{k+1} - \Phi_{i,j}^k}{\Delta t} \cdot \frac{\left(\frac{\partial^2 \Phi}{\partial x^2} + \frac{\partial^2 \Phi}{\partial y^2} \right)}{|\bar{\nabla} \Phi|} \right) \end{aligned} \quad (\text{a.46})$$

$$\begin{aligned} U_{i,j}^{k+1} &= \frac{2\Delta t}{1+k} \left(D \frac{1-\Phi}{2} \left(\frac{\partial^2 U}{\partial x^2} + \frac{\partial^2 U}{\partial y^2} \right) + \right. \\ &\quad \left. \frac{W}{2\sqrt{2}} [1 + (1-k)U_{i,j}^k] \frac{\Phi_{i,j}^{k+1} - \Phi_{i,j}^k}{\Delta t} \cdot \frac{\left(\frac{\partial^2 \Phi}{\partial x^2} + \frac{\partial^2 \Phi}{\partial y^2} \right)}{|\bar{\nabla} \Phi|} \right) + U_{i,j}^k \end{aligned} \quad (\text{a.47})$$

For temperature, applying ADI method, we can obtain

$$\frac{\mathcal{G}_{i,j}^{k+1} - \mathcal{G}_{i,j}^k}{\Delta t} = \alpha \left(\frac{\mathcal{G}_{i-1,j}^k - 2\mathcal{G}_{i,j}^k + \mathcal{G}_{i+1,j}^k}{\Delta x^2} + \frac{\mathcal{G}_{i,j-1}^k - 2\mathcal{G}_{i,j}^k + \mathcal{G}_{i,j+1}^k}{\Delta y^2} \right) + \frac{1}{2} \cdot \frac{\Phi_{i,j}^{k+1} - \Phi_{i,j}^k}{\Delta t} \quad (\text{a.48})$$

and furthermore, the final equations can be obtained as followings:

$$\begin{aligned} g_{i,j}^{k+1} = g_{i,j}^k \left(1 - \frac{2\alpha\Delta t}{\Delta x^2} - \frac{2\alpha\Delta t}{\Delta y^2} \right) + \frac{\alpha\Delta t}{\Delta x^2} (g_{i-1,j}^{k+1} + g_{i+1,j}^k) + \\ \frac{\alpha\Delta t}{\Delta y^2} (g_{i,j-1}^{k+1} + g_{i,j+1}^k) + \frac{1}{2} (\Phi_{i,j}^{k+1} - \Phi_{i,j}^k) \end{aligned} \quad (\text{a.49})$$

$$\begin{aligned} g_{i,j}^{k+2} = g_{i,j}^{k+1} \left(1 - \frac{2\alpha\Delta t}{\Delta x^2} - \frac{2\alpha\Delta t}{\Delta y^2} \right) + \frac{\alpha\Delta t}{\Delta x^2} (g_{i-1,j}^{k+1} + g_{i+1,j}^{k+2}) + \\ \frac{\alpha\Delta t}{\Delta y^2} (g_{i,j-1}^{k+1} + g_{i,j+1}^{k+2}) + \frac{1}{2} (\Phi_{i,j}^{k+2} - \Phi_{i,j}^{k+1}) \end{aligned} \quad (\text{a.50})$$

2.1 Simulation Program

The program with phase-field model for solidification of binary alloys is written in Microsoft Visual C++ 6.0[®]. It contains initialization module, calculation module and result outputting module.

In initialization module, all variables needed for calculation are defined and initialized, including defining the domain and cell size, initializing variables for temperature field, solute diffusion and phase field and setting thermodynamic and kinetic parameters. Boundary conditions are defined in the initialization model as well. All the calculations for the three fields and some relevant parameters are made in the calculation module. During each loop of the calculation, parameters which vary with the change of the temperature field and mass concentration are calculated firstly. Then with these new values, the new temperature field, mass concentration and phase-field are then calculated. Finally, with a preset time interval, the results are saved into hard disk in text file in the outputting module

The flow chart of the main program is as following.

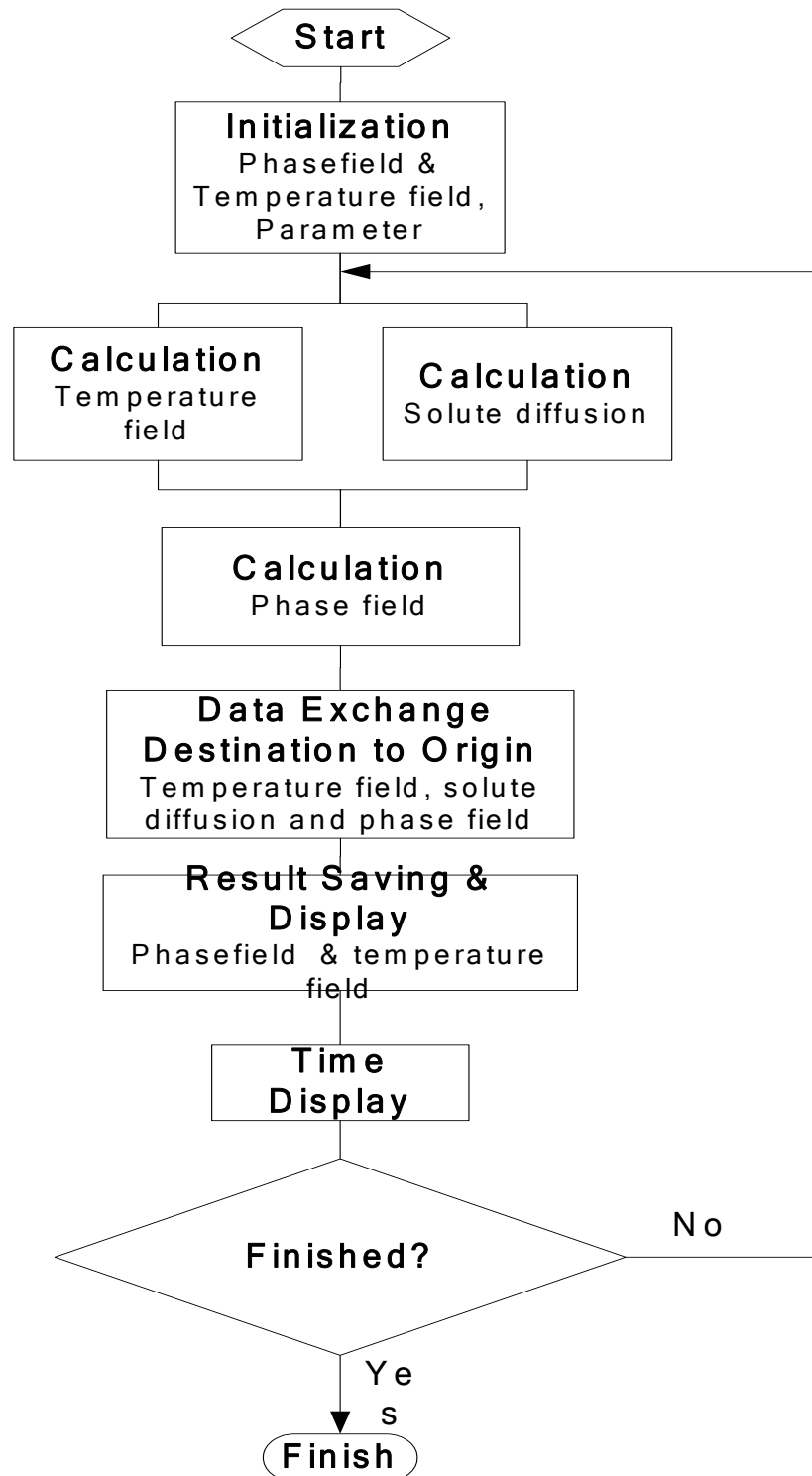


Figure A0.4 Flow chart of program for phase-field model for binary alloys

Phase-field model for solidification of pure metal has been fully developed and debugged. For the phase-field model for alloys solidification, development has been accomplished and some debug work has been done, where some further debugging need be carried out in the future.

Appendix B. Basic Model Evaluation

According to the model definition, the crystal growth rate is mainly governed by diffusion and curvature. The growth direction, shape and kinetics of dendrites are influenced by the anisotropy of the chemical potential, which is linked to the anisotropy of the interfacial energy.

In the model, the anisotropy of the interfacial energy is introduced by curvature undercooling as the third part of the right hand of Eq. b.1.

$$C_L^* = C_0 + \frac{T^* - T_l^{eq}}{m_l} + \frac{\Gamma K f(\varphi, \theta)}{m_l} \quad (\text{b.1})$$

$$f(\varphi, \theta) = 1 - \delta \cos[\lambda(\varphi - \theta)] \quad (\text{b.2})$$

$$K = \frac{1}{a} \left(1 - 2 \frac{f_s + \sum_{i=1}^N f_s(i)}{N+1} \right) \quad (\text{b.3})$$

Where, Γ is the Gibbs-Thomson coefficient. K is the S/L interface curvature which is determined using Eq. b.3; in Eq. b.3, a is the cell size, f_s is the solid fraction of the cell, $f_s(i)$ is the solid fraction of neighbouring cell and N is the number of neighbouring cells counted. Anisotropy of the surface tension $f(\varphi, \theta)$ can be calculated using Eq. b.2, where φ is the local growth angle between the local S/L interface normal and x-axis; θ is the preferential crystallographic orientation; δ is the degree of

anisotropy; λ controls the number of dendritic arms. For four-fold symmetry, $\lambda=4$ and $\delta=0.04$ (Warren & Boettinger 1995). The value of interface curvature calculated with Eq. b.3 varies from a maximum of $1/a$ to zero for convex surfaces and from zero to a minimum of $-1/a$ for concave surfaces.

From Eq. b.1, it can be seen that the S/L interface curvature and anisotropy of interfacial energy work with contribution to the solute concentration of liquid at the S/L interface. To check to what extent the S/L interface curvature and anisotropy affect the grain growth direction in the model, different values of parameters are investigated.

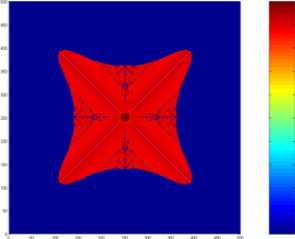
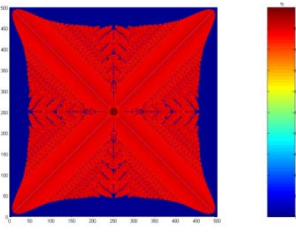
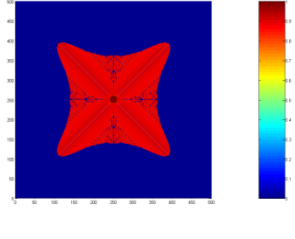
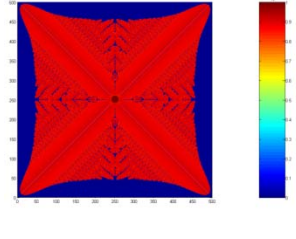
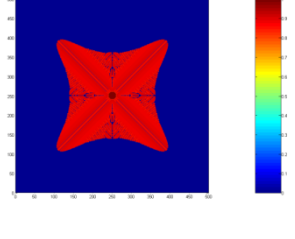
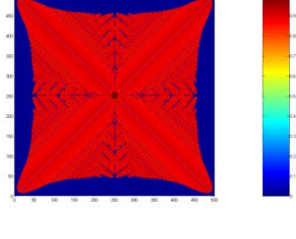
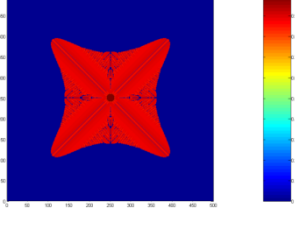
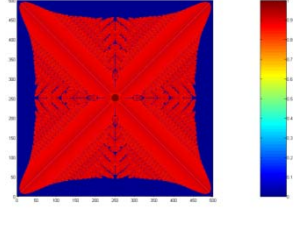
Basic parameters used for the simulation are as the following: mesh size $dx=dy=1e-6$ m and time step $dt=1e-6$ s.

1 Parameters on Solving Anisotropy of Surface Tension

In the function $f(\varphi, \theta)$, the preferential growth direction θ is applied to control grain growth direction. Usually, $\lambda=4$ and $\delta=0.04$ are used for four fold Al-Cu alloys. As in the results shown in Chapter 3, the preferential growth direction doesn't work at all during grain growth. To check to what extent the preferential growth direction affect the grain growth direction, different values of parameters are used in function $f(\varphi, \theta)$, where the effect of θ can be enhanced.

Simulation results of solute fraction distribution with different values of δ and λ are shown in Table B0.1. Except these two parameters, all other parameters are used same values in these results. In these results, the grain morphology doesn't change at all, where the number of dendrite arms should be controlled by λ and dendritic growth direction should along angle θ .

Table B0.1 Investigation of effect of interfacial energy parameters on grain growth with undercooling of 3K

Case No.	Parameters Applied			Results	
	δ	λ	θ	Simulation time= 4 s	Simulation time= 7 s
1	0.4	4	$5\pi/96$		
2	4	4	$5\pi/96$		
3	4	8	$5\pi/96$		
4	4	6	$5\pi/96$		

Besides, case of two seeds is also calculated. At the beginning of the calculation, two grain seeds with same preferential growth direction are set in the domain. As shown in Figure B0.1, the grains still can't grow along the preset crystallographic orientation.

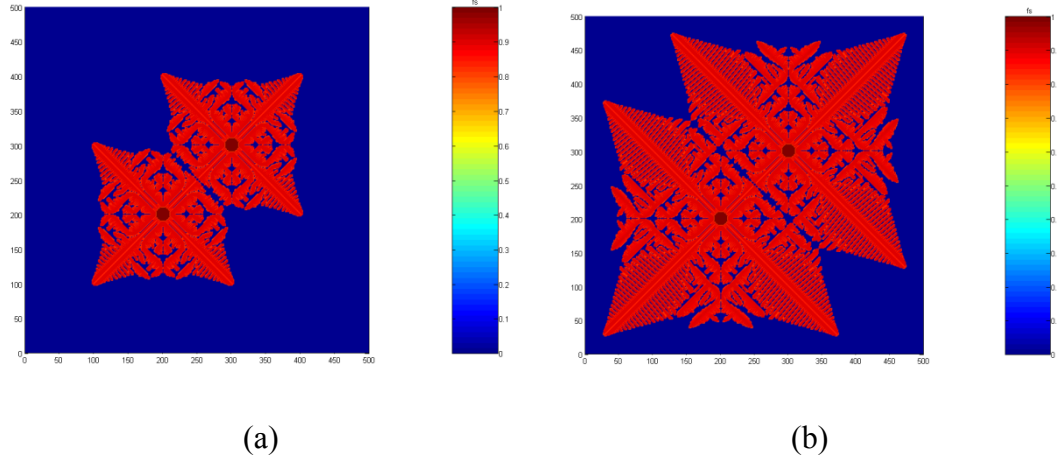


Figure B0.1 Distribution of solid fraction

$\delta=0.04$, $\lambda=4$, $\theta=5\pi/96$, undercooling of 3K

(a) calculation time 4s (b) calculation time 7s

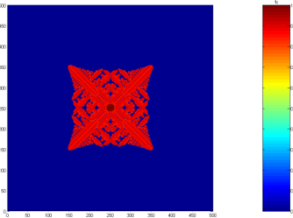
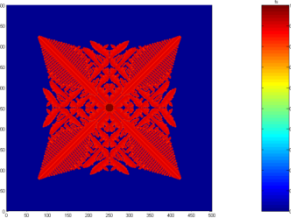
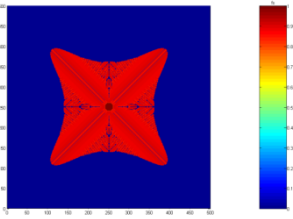
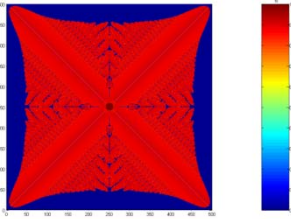
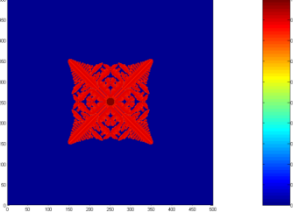
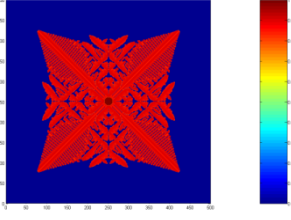
From the above results, it can be seen that the dendrite could not grow along the preferential angle, where the effect of the angle is amplified by using bigger values of δ . Also, the dendrite keeps four arms with different values of λ . Since even the arm amount doesn't change, the anisotropy of interfacial energy makes less or no contribution during grain growth. As the undercooling associated with S/L curvature and anisotropy of interfacial energy is very small, if the numerical noise due to numerical treatment of capture rule is bigger, the effect of interface curvature and anisotropy of interfacial energy can possibly neglected.

2 Parameters in Capture Rules

In definition of capture rule, L_φ is the length along local growth direction used to find the interface position with the solid fraction of a growing cell. The interface position

calculated varies with value of L_ϕ . Here, modification is done on capture rule with calculation of L_ϕ and simulation is done with different parameters (for example, $L_\phi = n \cdot \Delta x / \max(|\cos\phi|, |\sin\phi|)$, where n varies from 0.9 to 1.2). Results at simulation time of 4 and 7 seconds with different parameters are shown in Table B0.2.

Table B0.2 Investigation of effect of parameters in capture rules on grain growth

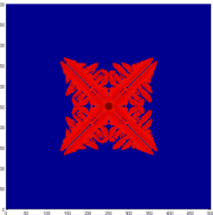
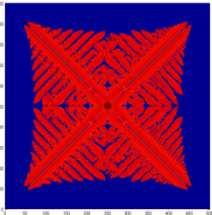
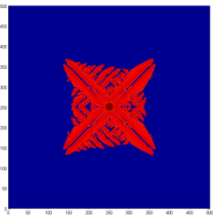
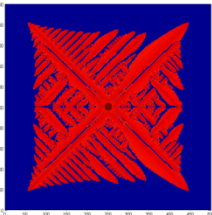
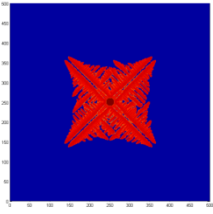
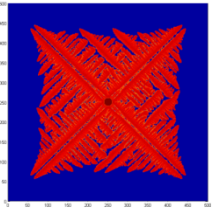
Case No.	Parameters Applied				Results	
	δ	λ	θ	ΔT	Simulation time= 4 s	Simulation time= 7 s
1	0.04	4	$5\pi/96$	3K		
2	0.04	6	$5\pi/96$	4K		
3	0.04	6	$5\pi/96$	3K		

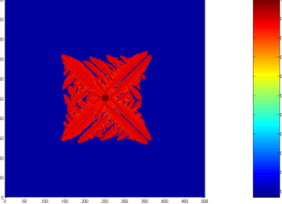
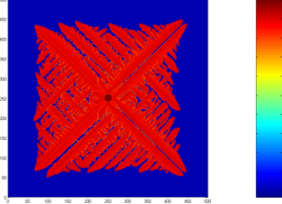
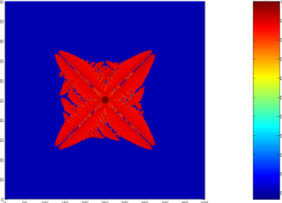
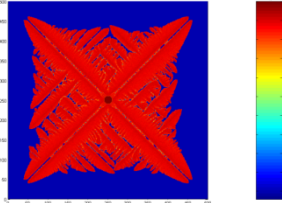
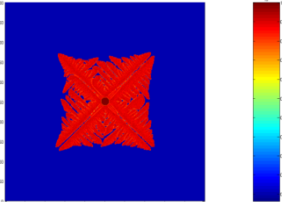
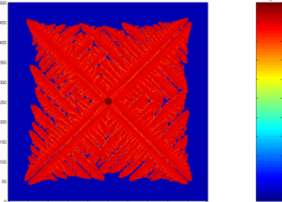
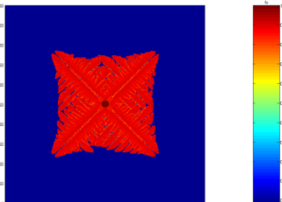
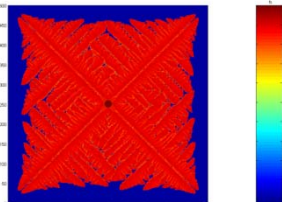
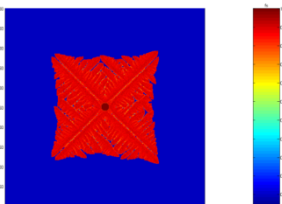
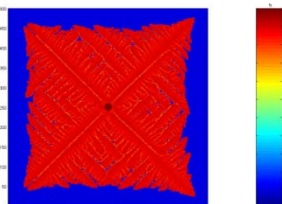
In results of cases 1 and 3 shown in Table B0.2, there is no change with different values of δ and λ . In Eq. b.1, curvature undercooling involves the S/L interface curvature and anisotropy of interfacial energy.

3 Parameters in Interfacial Curvature Calculation

The value of the curvatures calculated in Eq. b.3 varies from a maximum of $1/a$ to zero for convex surfaces and from zero to a minimum of $-1/a$ for concave surfaces. To check the influence of interface curvature, calculation is done with $a=dx/2$, where the value of interface curvature is amplified.

Table B0.3 Investigation of effect of interfacial curvature on grain growth with undercooling of 3K

Case No.	Parameters Applied			Results	
	δ	λ	θ	Simulation time= 4 s	Simulation time= 7 s
1	0.04	4	$5\pi/96$		
2	0.4	6	$5\pi/96$		
3	10	4	$5\pi/96$		

4	10	6	$5\pi/96$		
5	10	8	$5\pi/96$		
6	20	4	$5\pi/96$		
7	20	6	$5\pi/96$		
8	20	8	$5\pi/96$		

Comparing results of case 1 in Table B0.2 and case 1 in Table B0.3, there are changes in dendritic morphology with bigger difference in interface curvature. With amplified difference in interface curvature, there are also changes in morphology of dendrite with

different values of λ , as shown of cases 1 and 2 in Table B0.3. An interesting thing with results of these two cases is that the centre of dendritic arm keeps liquid during the growth of dendrite and twinned dendrite forms. In case 2, with $\delta=0.4$ and $\lambda=6$, although dendrite keeps grow in four directions, there are changes in morphology of dendrite and the twinned dendrite disappears by one side of the arm over growth of the other one.

Cases 3, 4 and 5 show results with different values of λ , where same values are used for other parameters. It can be found that dendrite arms become stronger with bigger values of λ , the arms become wider. In case 5, different from results in case 1, the centre of arm is total liquid.

Results with $\delta=20$ are shown in case 6, 7 and 8. In these results, there is less liquid between dendritic arms (including second order arms), compared with results calculated from smaller values of δ . However, the dendrite could not grow along preferential angle and the amount of arms is not consistent with value of λ .

From the above results, it can be found that there are changes in morphology of dendrite with different parameters values in calculation of S/L interface curvature and anisotropy of the surface tension. However, the dendrite could not grow along the preferential direction. According to literature (Jacot & Rappaz's 2002), the growth direction, shape and kinetics of dendrites are strongly influenced by the anisotropy of chemical potential, which is linked to the anisotropy of the interfacial energy (and its second derivative). But the anisotropy of the interfacial energy is very small (a few percents in most common metals). Undercooling associated with diffusion (typically a few degrees) is usually two orders of magnitude higher than that associated with curvature for primary phase solidification. As a result, if the numerical noise of the system is bigger than the anisotropy of the interfacial energy, the later one will take no or less effect on

controlling grain shape and the growth direction. For example, when calculating the interface position, the system always gives a very close value instead of the exact value. Therefore, it requires high accuracy on solute diffusion calculation, especially in liquid ahead of S/L interface.

4 Improvement on Solute Diffusion Calculation

In front-tracking model for solidification, it is assumed that the phase transformation is mainly governed by diffusion and curvature (Gibbs-Thomson effect). Therefore, high accuracy of solute diffusion calculation is required. Considering both accuracy and efficiency of calculation, a technique combined with Finite Element and Finite Difference is proposed.

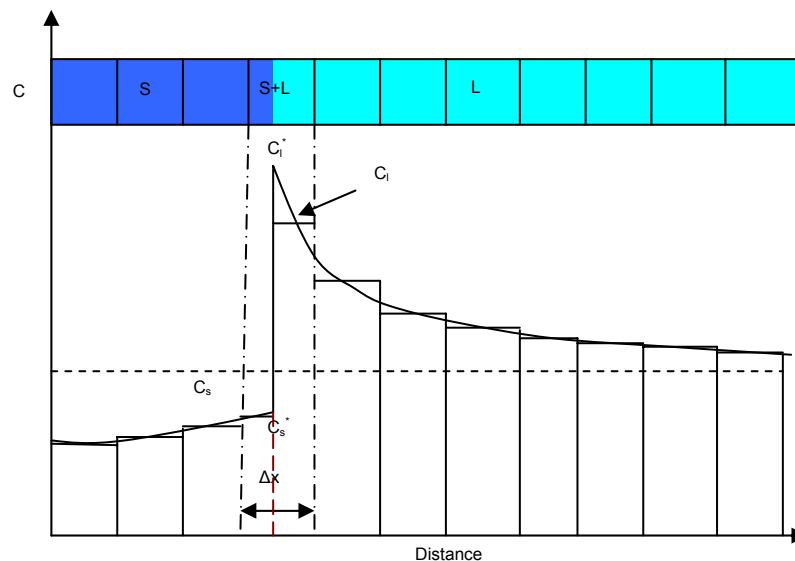


Figure B0.2 Technique for calculation of solute diffusion

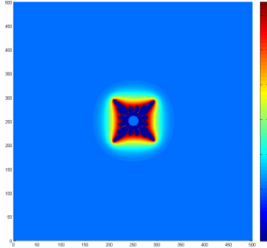
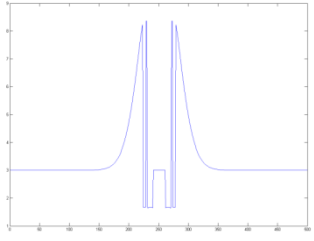
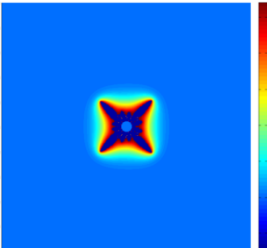
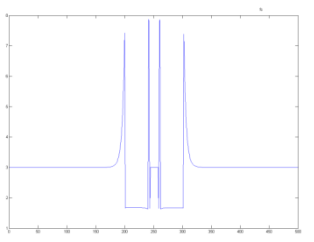
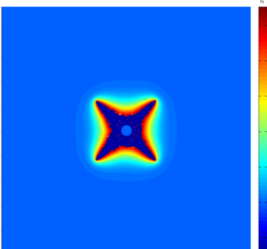
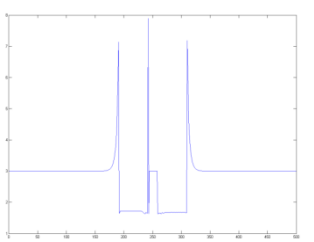
During solidification, equilibrium is assumed in a growing cell at the S/L interface and solute partitioning occurs at the S/L interface, *i.e.* $C_s^* = k \cdot C_L^*$, where C_s^* and C_L^* are the concentrations of the solid and liquid sides at S/L interface separately. As shown in Figure B0.2, for liquid and solid cells, Finite Difference method is applied for

calculation of solute diffusion, where the average solute concentration is used to describe the whole cell. Differ from that, at the S/L interface, a growing cell is treated as liquid part and solid part separately, where C_L and C_S are the average solute concentration of liquid part and solid part separately. C_L and C_S can be calculated using various methods. As the solute gradient at solid side of S/L interface is very small and solute diffusivity in solid is about two orders of magnitude smaller than that in liquid side, there is no significant difference on calculation of solute redistribution in solid side with different methods on solving C_S . However, in liquid side, the amount of solute diffused away from S/L interface to liquid, which changes with C_L , may vary with C^*_L . As a result, solute profile ahead of dendritic tips varies and finally can affect morphology of dendrites.

With this improvement on calculation of solute diffusion, simulations have been done using different parameters for S/L interface curvature and anisotropy of interfacial energy.

As solute diffusion in solid is much smaller than that in liquid, which can be neglected, a calculation is done with only solving solute diffusion in liquid. The results are shown as case 1 in Table B0.4. The solute distribution at simulation time of 4s is shown in the table. The solute profile across the grain centre along dendritic arm is also shown in the table.

Table B0.4 Investigation of effect of interfacial energy parameters on grain growth

Case No.	Parameters Applied				Results	
	δ	λ	θ	ΔT	4 s	
1	0.04	4	$5\pi/96$	3K		
2	4	4	$5\pi/96$	4K		
3	20	4	$5\pi/96$	3K		

Simulation results with different values of parameters are shown as cases 2 and 3.

5 Gibbs-Thomson Coefficient

To amplify curvature undercooling, calculation is done by using thirty times of Gibbs-Thomson coefficient. The solute distribution is shown in Figure b.3. In this condition, the dendritic arms could not form and the grain grows at almost same speed to all directions.

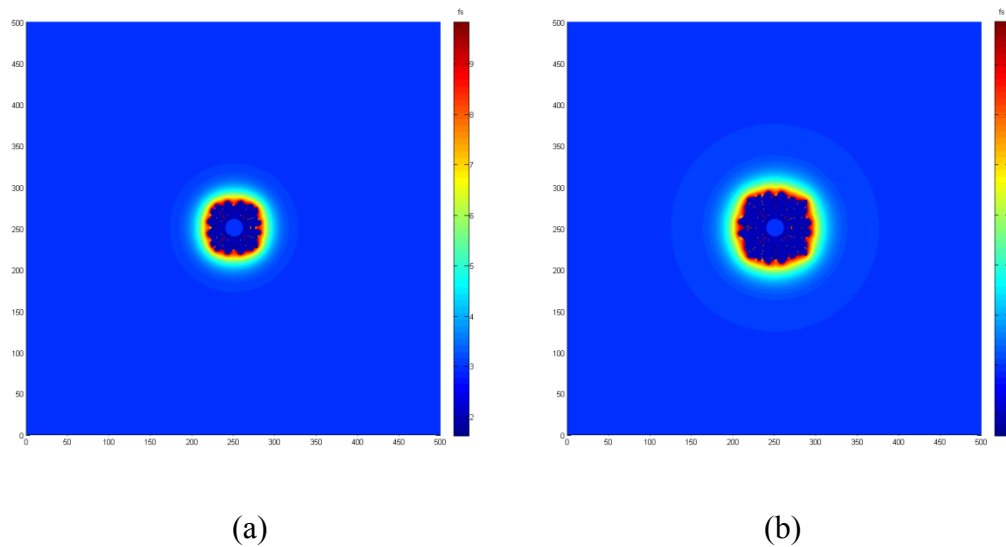


Figure B0.3 Solute distribution

$\delta=0.04$, $\lambda=4$, $\theta=5\pi/96$, undercooling of 3K

(a) calculation time 2s (b) calculation time 4s

6 Numerical Treatment-Control Parameter for Growth Direction

As front-tracking is a probabilistic model, a technique based on statistics is proposed to help controlling grain growth direction. The idea of this technique is that cells located less off crystallographic direction have more chances to be captured as new interface cell. A parameter is introduced to store information of cells position relative to

crystallographic angle. This technique will ensure that cells located along crystallographic direction have most chances to grow.

For four-fold symmetry, as shown in Figure B0.4, the crystallographic directions are shown as black lines, where the preferential angle is θ . For cell (x,y) , A parameter nf (0-1) is given as Eq. b.4, where la is the angle between pink line and x-axis.

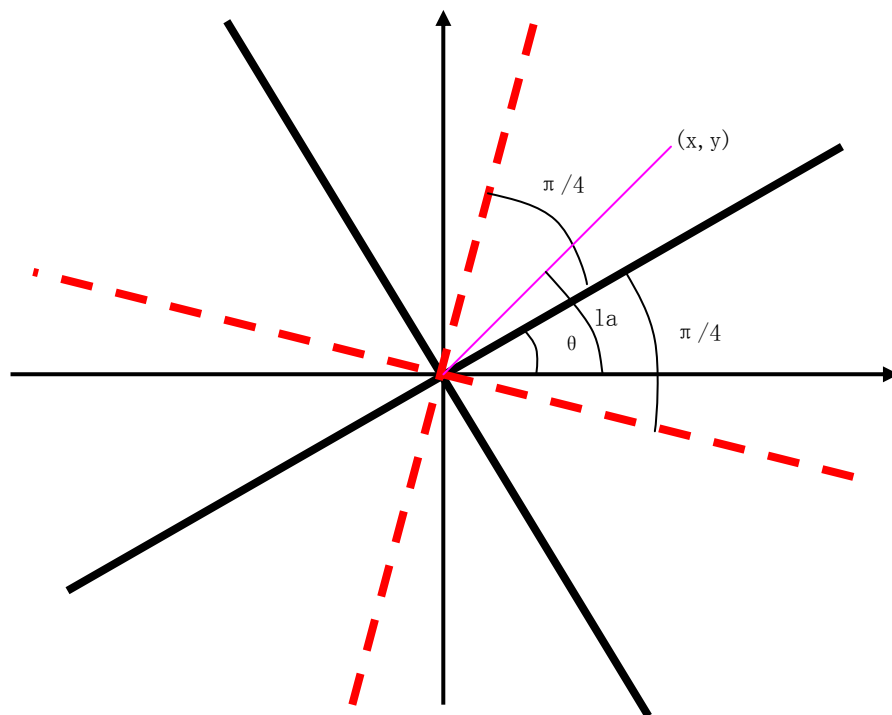


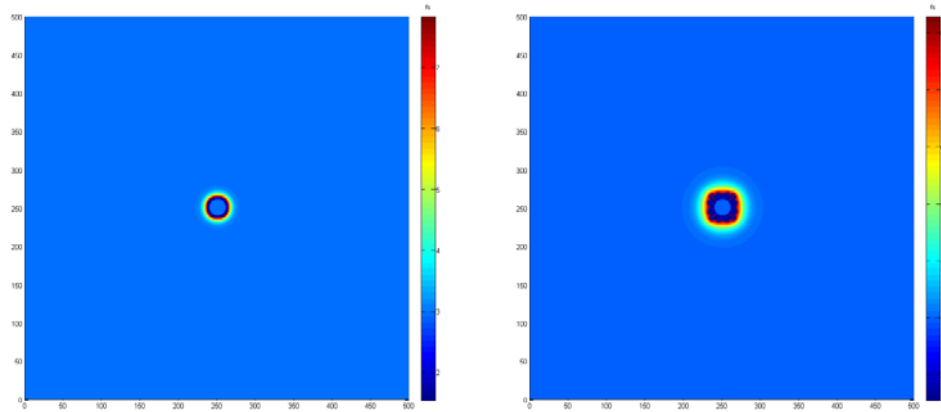
Figure B0.4 Scheme of direction control

By the definition, nf has biggest value (1) when cell is located on the red lines, and has smallest value (0) when cell is located on black lines.

$$nf = \frac{|la - \theta|}{\pi/4} \quad (\text{b.4})$$

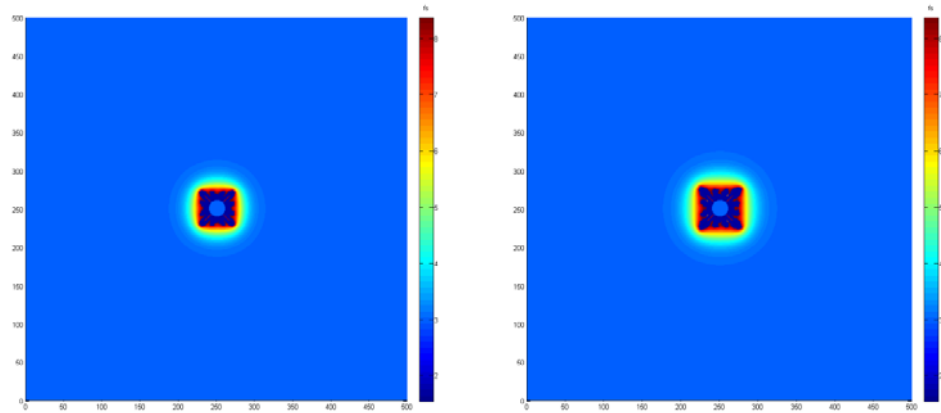
During calculation of new interface cell capture, firstly, the normal capture rule is applied. When a cell satisfies the conditions of being captured as a new interface cell, the angle la is then calculated, from which the parameter can be solved out. Secondly, a random number, $rannf$ varies from 0 to 1, is generated. If $nf > rannf$, then the cell is change to new interface cell.

For comparison purpose, calculation is firstly done without applying the direction control parameter. To check more details about how dendritic arm forms during grain growth, more results of early stages are plotted, as shown in Figure B.5. It can be seen that at simulation time of 0.85s, as shown in Figure B0.5(b), the grain grows nearly at same speed at all directions. After that, the dendritic arms formation occurs, as shown in Figure B0.5(c). As at the dendritic tips, the solute rejected from solid is diffused into liquid faster than in other areas, the solute composition in liquid ahead of dendritic tips keeps smaller than that of other areas, which leads to bigger constitutional undercooling in liquid ahead of dendritic tips. With bigger undercooling, dendrite tips have bigger growth speed and finally the dendritic arms form.



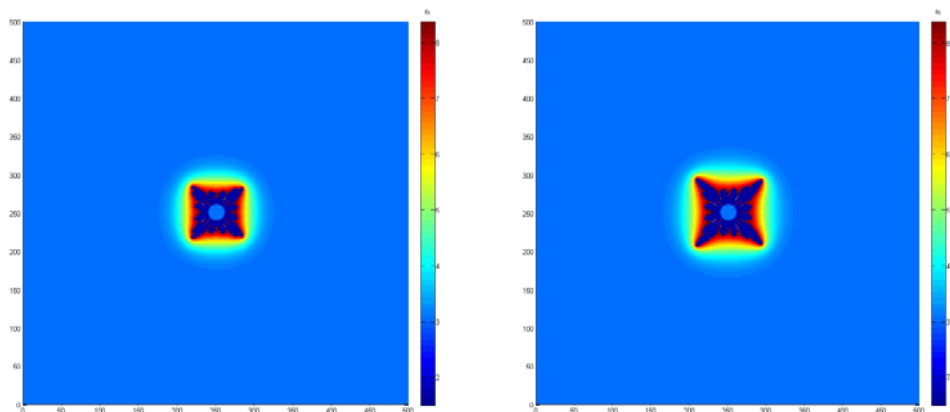
(a)

(b)



(c)

(d)



(e)

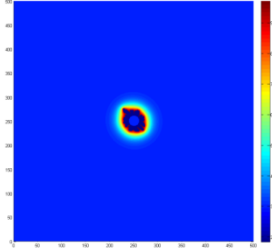
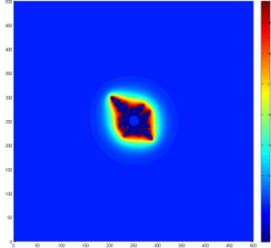
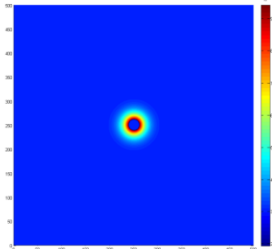
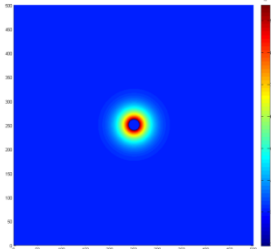
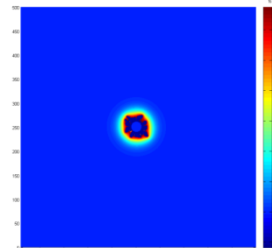
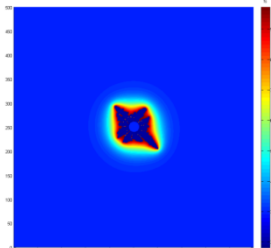
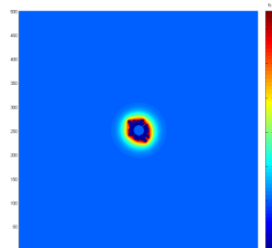
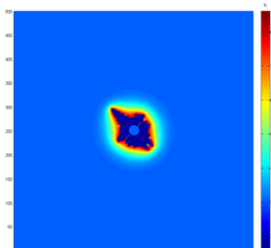
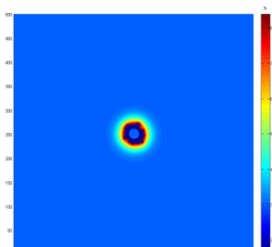
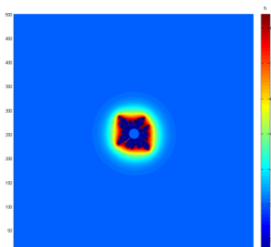
(f)

Figure B0.5 Solute distribution without nf

$\delta=0.04$, $\lambda=4$, $\theta=5\pi/96$, undercooling of 3K

calculation time (a) 0.15s (b) 0.85s (c) 1.55s (d) 2.2s (e) 3s (f) 4s

Table B0.5 Investigation of effect of parameters nf on grain growth

Case No.	Parameters Applied			Results	
	δ	λ	nf	1.55 s	4 s
1	0.04	4	$nf < rannf$		
2	0.04	4	$nf < rannf/2$		
3	4	4	$nf < rannf$		
4	20	4	$nf < rannf$		
5	0.04	n/a	$nf < rannf$		

In Table B0.5, case 1 shows simulation results with introduction of direction control parameter nf , where the criterion $nf < rannf$ is applied. With the contribution of direction

control parameter, more dendritic arms form. It can be seen that the direction control parameter affects the grain growth to some extent, but still could not eliminate the effect cause by bigger growth speed at $\pi/4$ direction. To enlarge the effect of direction control parameter, calculation is done with criterion of $nf < rannf/2$, where random control effect is enlarged when capturing new interface cells. The simulation results are shown as case 2. With this criterion, it becomes harder to capture new interface cells and the grain stops growing.

Calculations with different values of δ and λ are also done together with the direction control parameter. Case 3 shows simulation results with $\delta=4$, $\lambda=4$ and $nf < rannf$, where effect of angle difference in anisotropy of surface tension is amplified. It can be found that the effect of direction control parameter is enhanced. However, if continue to increase δ , simulation results as shown as case 4, the direction control parameter keeps taking effect and arms along $\pi/4$ direction still form, but in other areas, there is no clearly growth orientation.

From the above results, it can be seen the effect of angle difference in anisotropy of surface tension on grain growth direction. Here, two cases of calculations with particular conditions are done.

The first calculation is done without effect of angle difference in anisotropy of surface tension by applying $\theta=\varphi$ in Eq. b.2, where the curvature undercooling is still taken into account. The simulation results are shown as case 5. All though direction control parameter takes effect, the whole grain growth still has priority at $\pi/4$ direction. As the seed size could be a factor influencing the grain growth direction, especially at the beginning of grain growth, the second calculation is to investigate the results with a bigger seed. Figure B0.6 (a) and (b) show simulation results without direction control

parameter and Figure B0.6 (c) and (d) show simulation results with $nf < rannf$. The effect of direction control parameter is about same as in small seed situation.

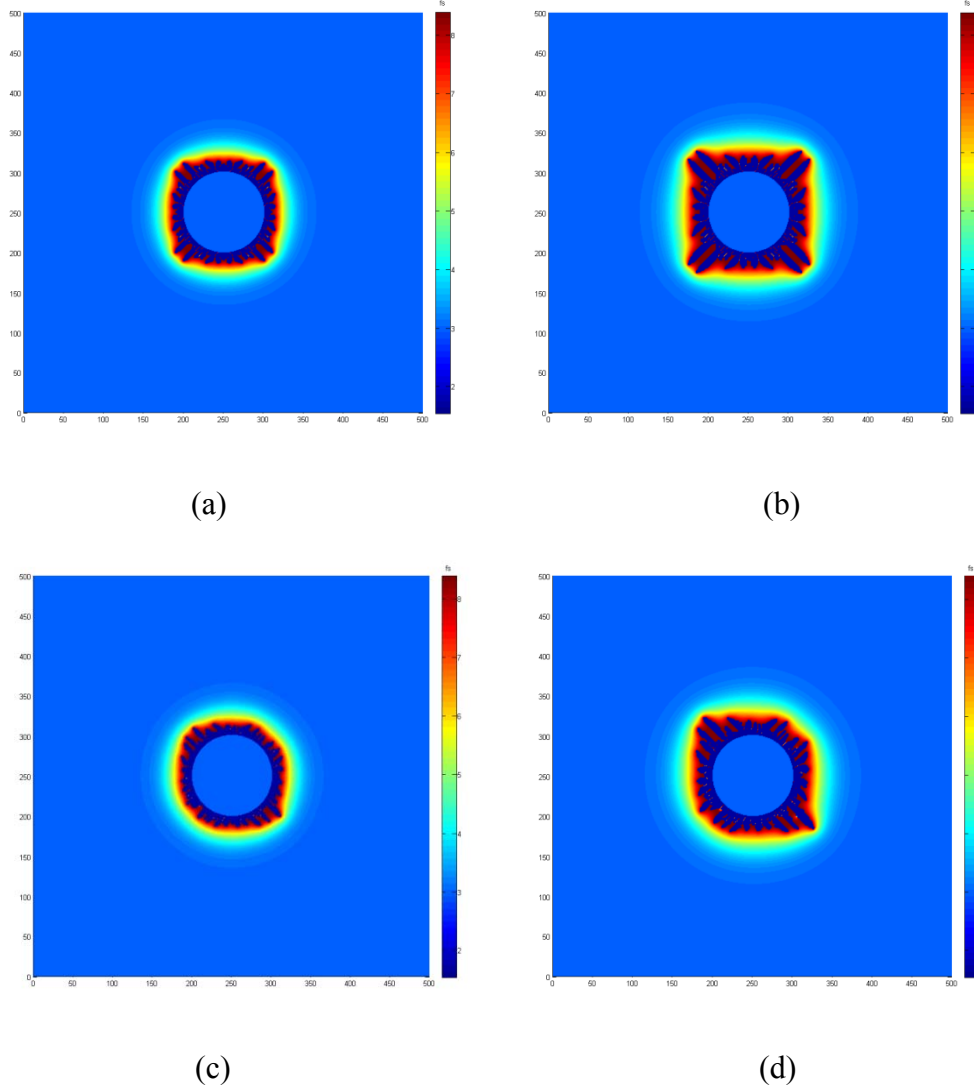


Figure B0.6 Solute distribution with a bigger seed

$\delta=0.04$, $\lambda=4$, $\theta=5\pi/96$, undercooling of 5K

(a) and (b) without nf , (c) and (d) with $nf < rannf$

calculation time (a) and (c) 2s, (b) and (d) 4s

In the above results, the dendrite could not grow along the preferential orientation. There are some changes in morphology of dendrite when using different values of some parameters. However, the main growth direction keeps at $\pi/4$ angle. In the model, the grain growth is a complicated evolution process involved many factors, which may

affect the solute diffusion and therefore affect local growth speed or directly affect new interface cells capturing. As there are so many aspects making contribution to grain growth, to investigate the reason that grain has priority in growth at $\pi/4$ direction, it is necessary to simplify the model and only keep essential calculation.

7 Simplified Model

To simplify the model, only solute field is calculated and 300×300 domain size is used. Instead of calculation of temperature field, unified temperature is used for the entire domain. Calculations are done with simplified model. Some typical results from these calculations plotting solid fraction are shown in Figure B0.7.

In these results, dendritic arms finally form along $\pi/4$ direction. As there is no temperature calculation involved, the shape of dendrite is mainly controlled by solute undercooling and curvature undercooling, where anisotropy of interface tension is taken into account. According to Jacot & Rappaz's (2002) work, the growth direction, shape and kinetics of dendrites are strongly influenced by the anisotropy of chemical potential, which is linked to the anisotropy of the interfacial energy (and its second derivative). The undercooling associated with diffusion (typically a few degrees) is usually two orders of magnitude higher than that associated with curvature for primary phase solidification. In most common metals, the anisotropy of the interfacial energy is very small (a few percents). Therefore, the effect of interfacial curvature and anisotropy of surface tension on grain growth is investigated firstly. Following that, details of capture rules are investigated, as grain growth can also be controlled by some aspects in capture rules.

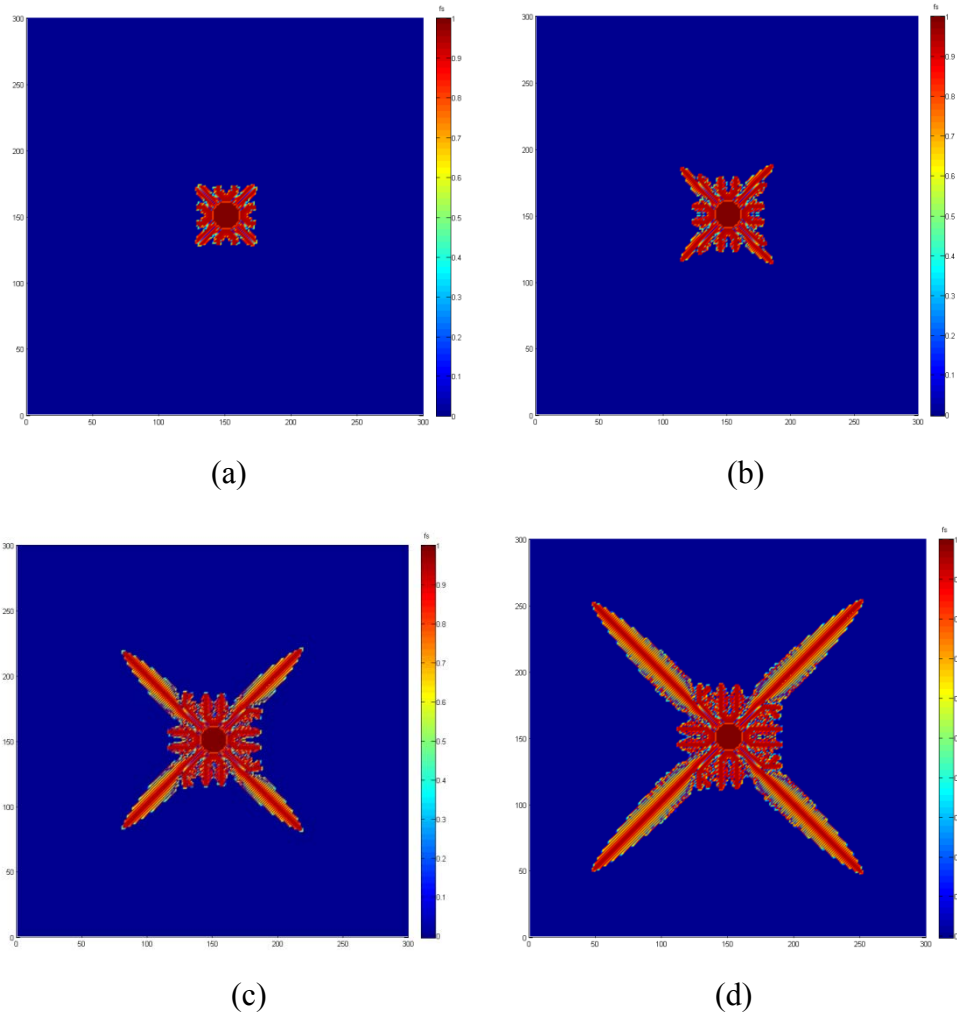


Figure B0.7 Distribution of solid fraction

$\delta=0.04$, $\lambda=4$, $\theta=5\pi/96$, undercooling of 4K

Simulation time (a) 2s, (b) 4s, (c) 6s, (d) 8s

In the model, the anisotropy of surface tension, in which the preferential orientation is involved, is introduced by curvature undercooling. If the curvature undercooling is not taken into account, the grain growth is then controlled by solute undercooling, where, theoretically, the grain should grow as a circle. Calculations are done without calculating curvature undercooling. To check when and how the dendritic arms form, simulation results are plotted step by step. Typical results from these calculations are shown in Figure B0.8.

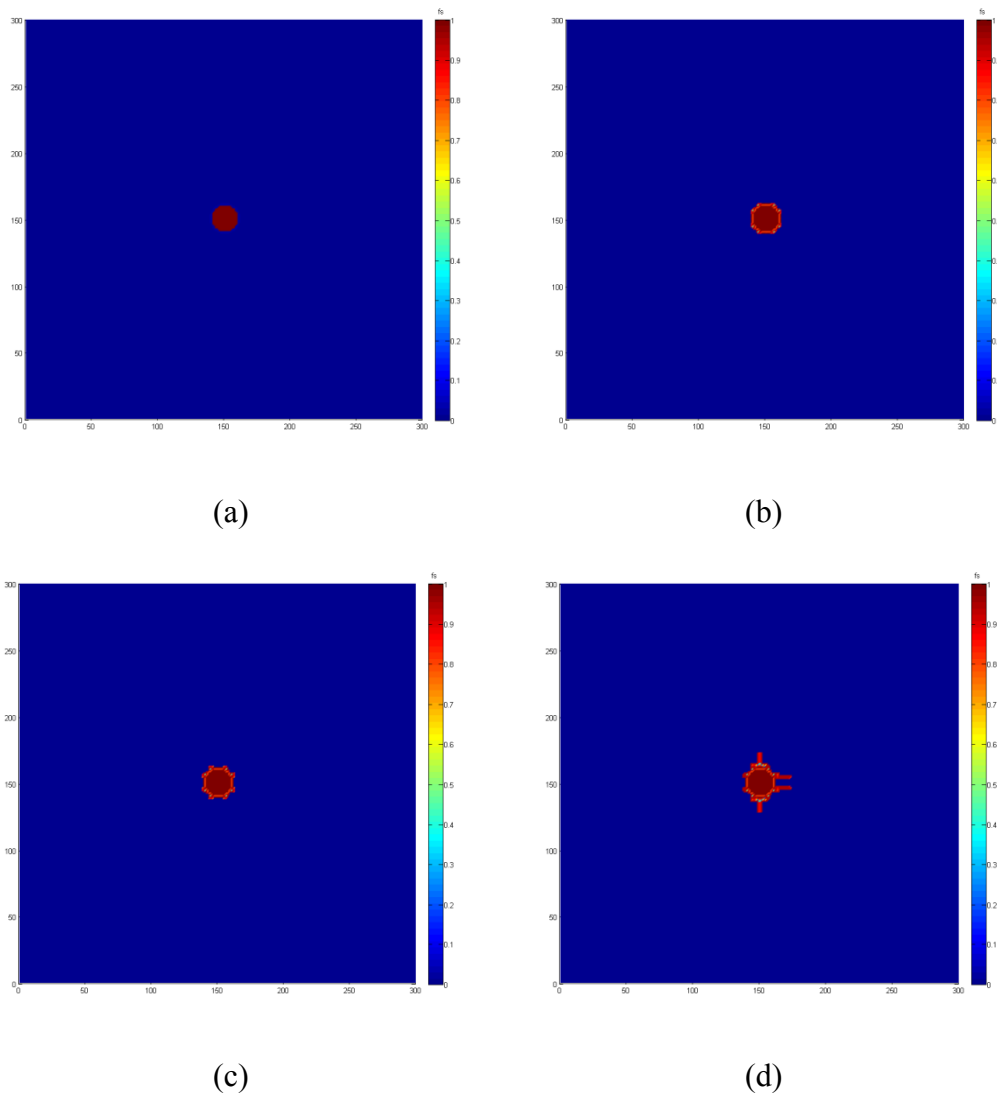


Figure B0.8 Distribution of solid fraction

$\delta=0.04$, $\lambda=4$, $\theta=5\pi/96$, undercooling of 4K

Calculation step (a) 0, (b) 1, (c) 2, (d) 3

In the above results, Figure B0.8(a) is the initial status where a circle seed is set in the domain. After calculation of two steps, in Figure B0.8(b) and (c), it can be found that new interface cells are captured at about $\pi/4$ direction. The grain could not grow as a circle. Although the small size of seed, which makes the S/L interface contain less cells and not smooth enough, may prevent the grain from growing as a circle, it seems that at $\pi/4$ direction, cells have priority to be captured as new interface cells.

In the capture rules, as shown in Figure 3.1(a), L_φ has biggest value $\sqrt{2}\Delta x$ at $\varphi=\pi/4$ and has smallest value Δx at $\varphi=\pi/2$ or $\varphi=0$. Suppose at one time step the S/L interface is a circle as the black line shown in Figure B0.9. As the interface is a circle, the solutal gradient is same at all directions and therefore all S/L interface cells have same value of solid fraction. Then for next time step, theoretically, the new S/L interface should be located as the blue dash line as the grain has same growth speed at all directions. But when applying the capture rules, the new S/L interface should be as the red line. This means that at $\pi/4$ angle, there are additional areas covered by solid. After many time steps calculation, these excess areas could be accumulated and finally the S/L interface protrudes in $\pi/4$ direction, as pink line shown in Figure B0.9. L_φ is introduced to eliminate artificial anisotropy due to square grid. It seems that the definition of L_φ possibly gives priority for cells along $\pi/4$ direction being caught as new interface cells.

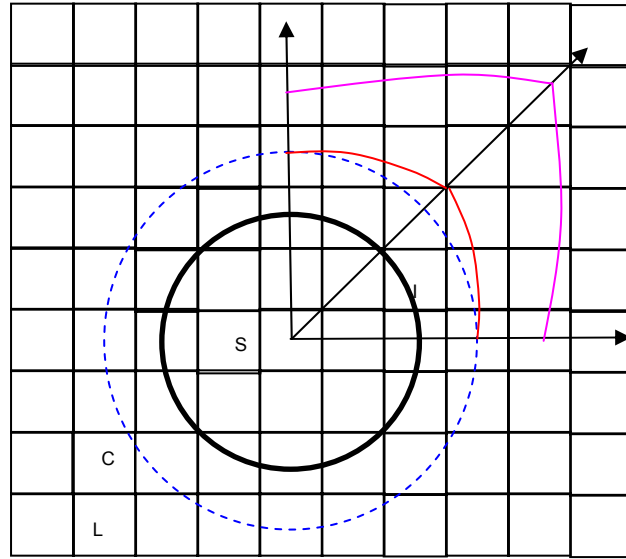
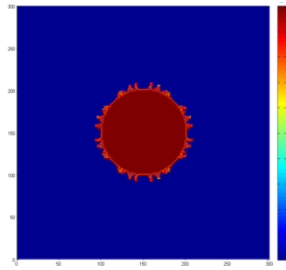
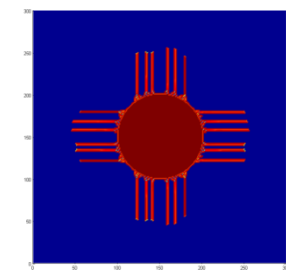
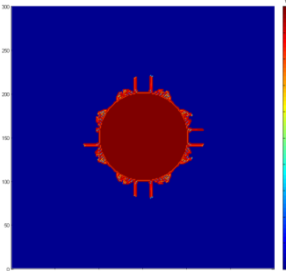
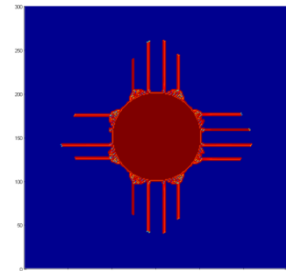


Figure B0.9 Position of S/L interface

As the definition of L_ϕ may be an aspect that causes grain grow faster along $\pi/4$ direction. Calculations are tried with fixing value of L_ϕ . To make the grain grow from a circle and more smooth S/L interface, bigger seed with radius of fifty cells is set in the domain when initialize the system. Anisotropy of surface tension is not taken into account in simulation results as shown as case 1 in Table B0.6. At the very early stages, S/L interface protrudes in some directions. Once the S/L interface could not keep smooth, grain starts to grow faster at tips of sharp interface. Due to the artificial anisotropy caused by square grid, cells can hardly be captured as new S/L interface cells along $\pi/4$ direction and therefore grain could not grow in the direction.

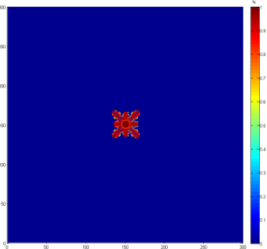
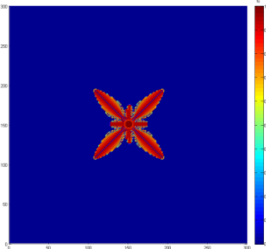
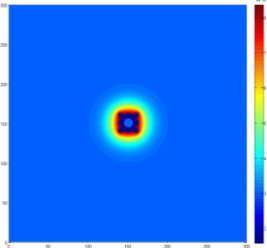
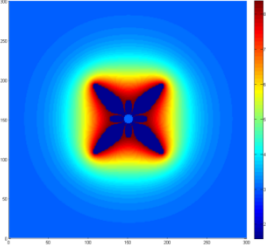
Even with taking into account of anisotropy of surface tension, as results shown as case 2, grain still could not grain along $\pi/4$ direction. The possible reason could be that the artificial anisotropy due to square grid is much stronger than anisotropy of surface tension.

Table B0.6 Investigation of grain growth with fixed L_ϕ

Case No.	Parameters Applied			Results	
	δ	λ	<i>anisotropy</i>	Step 10	Step 30
1	0.04	4	without		
2	0.04	4	with		

For cases of smaller seed with fixing L_ϕ , simulations have also been done. Figure B0.10 shows simulation results of grain growth during first three steps calculation, with taking into account of anisotropy of surface tension, where (a),(c) and (e) in solid fraction distribution, and (b),(d) and (f) in distribution of solutal concentration. Results of later stages of this calculation are plotted in solid fraction distribution as shown as case 1 in Table B0.7.

Table B0.7 Investigation of grain growth with fixed L_ϕ

Case No.	Parameters Applied			Results	
	δ	λ	<i>anisotropy</i>	Step 20	Step 80
1	0.04	4	with		
2	4	4	without		

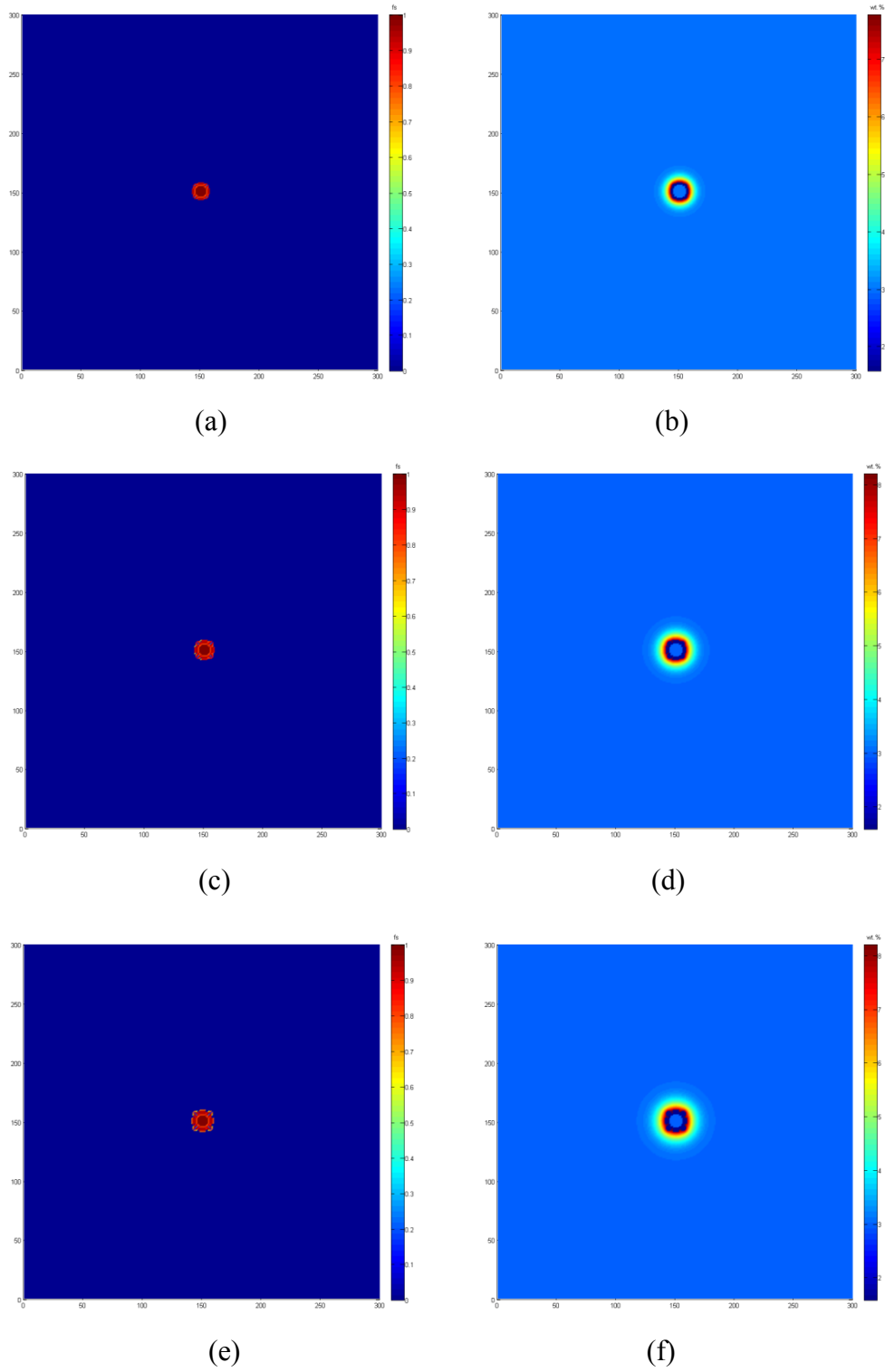


Figure B0.10 Early stages of grain growth

Fixing L_{ϕ} , with anisotropy of surface tension

Calculation step (a) and (b) 1, (c) and (d) 2, (e) and (f) 3

Case 2 in Table B0.7 shows simulation results of grain growth during first three steps calculation, without taking into account of anisotropy of surface tension, where distribution of solutal concentration is plotted. Compared simulation results with and without anisotropy of surface tension, the morphology of dendrite is very close. This means that the artificial anisotropy due to square grid is so strong with fixing L_ϕ , and anisotropy of surface tension, which is much smaller, can hardly affect the grain grow.

In summary of the above results, the anisotropy of surface tension has no significant effect on grain growth. The crystal could not grow along the preferential crystallographic orientation even with one order magnitude bigger of anisotropy. As in the model, the grain growth is mainly controlled by the solute field. The contribution of anisotropy of surface tension to the solute distribution is introduced via curvature undercooling. In the next section, investigation and analysis on the model will start from the solution of solute redistribution. Detailed investigations of effect of curvature undercooling on grain growth are carried out. Simulations are done with enhanced curvature undercooling, where different parameters are applied.

Appendix C. Materials and Process Data Management Program

We were asked by Rolls-Royce to develop a management program, which would be able to keep records of experimental data, to share information among different groups within Rolls-Royce, and to predict materials properties and performance based on the available data. Following the discussion with Rolls-Royce, we developed a small program which has the capacity to do so. Here, a brief introduction on developed program is given.

According to functions, the program primarily contains two parts: 1) interface program, which is used to operate the data, such as adding records into the database, searching existing records and modifying existing records; 2) background database, where to store records. The interface program is developed in Microsoft Visual Basic 6.0® environment and the background database is built in Microsoft Access 2000.

1. Interface Program

The interface program reads data from the background database file and at the same time new data information in the interface program is updated into the background file. It contains four parts: Main Interface, Add Data, Modify Data and Search Data interfaces.

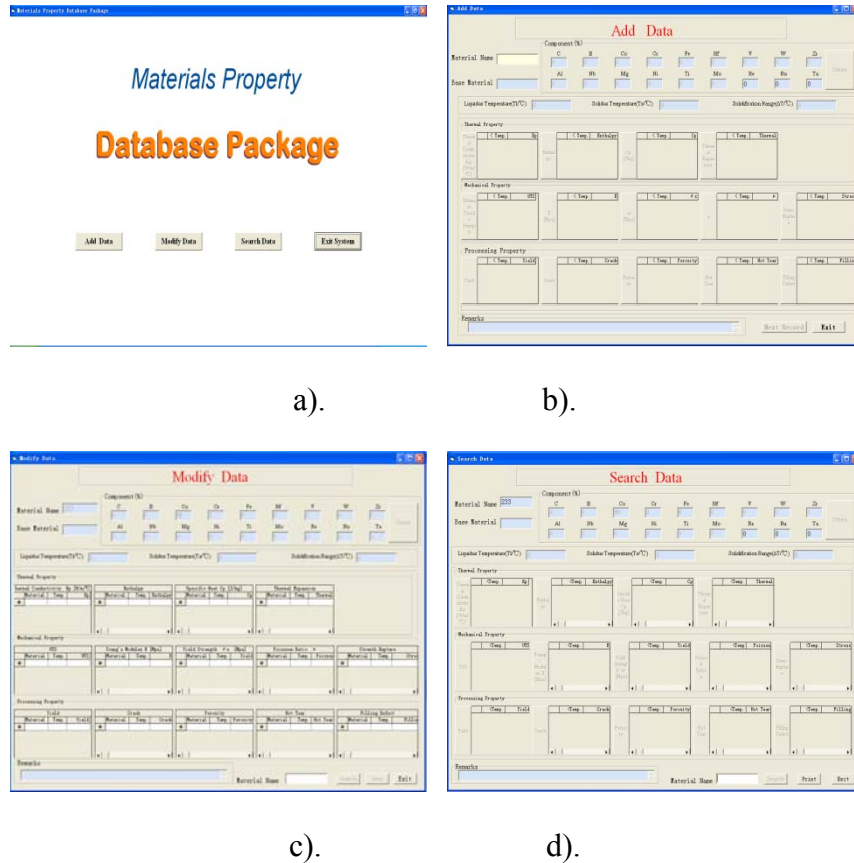


Figure C0.1 Program interfaces

1) Add Data

This interface is used to input new data records into the database file. When the Add Data interface program starts, as shown in Figure C0.1 (b), only "Material Name" field, which is the keyword, and "Exit" button are enabled. We cannot operate others which are locked. With such a lock system, we can avoid missing some parameters of the inputting record.

To input new data record, we need firstly to input the "Material Name". And once we press Enter Key, the program will search the background database file with this material name to find out whether record with this material name has already existed or not. If the record has already existed, a new window will popup to inform you and then the

program will transfer to the Modify Data interface program to allow us to modify the record which exists. If the record does not exist, the following field will be unlocked in turn when we finished the one before each. For each parameter, the program also validates its value, such as type and range, to avoid wrong information. All parameters will be input in turn. For those parameters, which are functions of other parameters, a new window, with both material name and the parameter name displayed, will pop up, as shown in Figure C0.2. The above lock system is also applied in this window.

The screenshot displays the 'Add Data' software interface. The main window has a title bar 'Add Data' and a central title 'Add Data' in red. It features several input fields: 'Material Name' (55454), 'Base Material' (g), and a 'Component (%)' table with columns for C, B, Co, Cr, Fe, Hf, V, W, Zr, Al, Nb, Mg, Ni, Ti, Mo, Re, Ru, Ta, and Others. Below these are fields for 'Liquidus Temperature(Tl/°C)', 'Solidus Temperature(Ts/°C)', and 'Solidification Range(ΔT/°C)'. The interface is organized into sections: 'Thermal Property' (Thermal Conductivity), 'Mechanical Property' (Ultimate Tensile Strength), and 'Processing Property' (Yield, Crack, Porosity, Hot Tear, Filling Defect). A 'Remarks' field is at the bottom. A pop-up window titled '55454: Thermal Conductivity' is open, showing a '< Temperature' field and a 'Thermal Conductivity' field, with 'Input' and 'Finish' buttons.

Figure C0.2 Interface for inputting changeable parameters

2) Modify Data and Search Data

Firstly, we give the material name of the record we want to modify. The program will then search the background database file with this given material name. If the record is found, the data of it will be displayed in the interface, as shown in Figure C0.3. Then,

we can change all of the value of the record. When we press Save Button or Exit Button, all of the value will be updated into the background database file. The Search Data interface is similar with that of Modify Data.

Figure C0.3 Modify data interface

2. Background database

The background database file contains one main table and several subtables. Parameters which have only one value are stored in the main table. Each of the subtables stores one of these which are function of other parameters. The structure is shown in Figure c0.4.

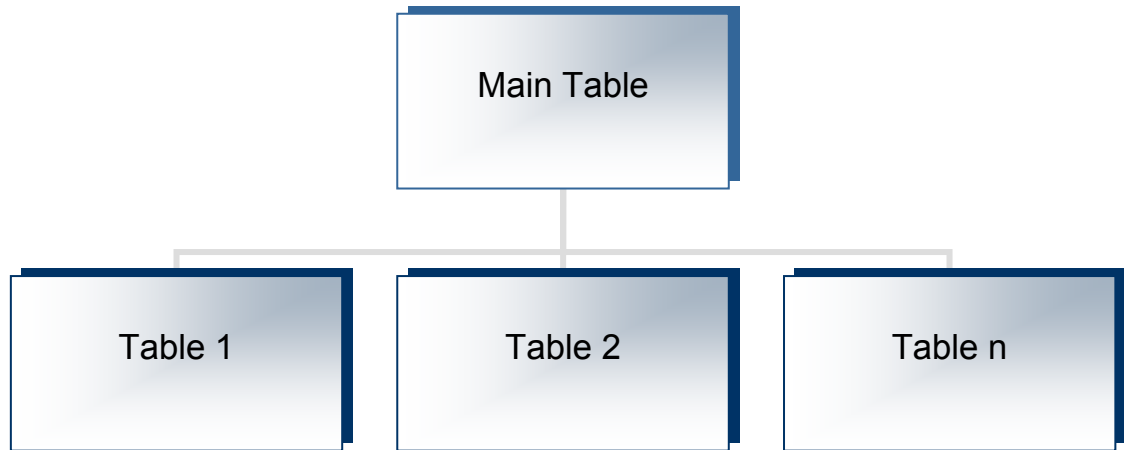


Figure C0.4 Database structure

Reference

Allen, S.M. and Cahn, J.W.(1979), “A microscope theory for antiphase boundary motion and its application to antiphase domain coarsening”, *Acta Metallurgica*, **27**, 1085-1095.

Amar, M.B. and Pelce, P.(1989), “Impurity effect on dendritic growth”, *Physical Review A*, **39**, 4263-4269.

Banaszek, J., Mcfadden, S., Browne, D.J., Sturz, L. and Zimmermann, G.(2007), “Natural convection and columnar-to-equiaxed transition prediction in a front-tracking model of alloy solidification”, *Metallurgical and Materials Transactions A*, **38A**, 1476-1484.

Beltran-Sanchez, L, and Stefanescu, D.M.(2003), “Growth of solutal dendrites: a cellular automaton model and its quantitative capabilities”, *Metallurgical and Materials Transactions A*, **34**, 367-382.

Beltran-Sanchez, L. and Stefanescu, D.M.(2004), “A quantitative dendrite growth model and analysis of stability concepts”, *Metallurgical and Materials Transactions A*, **35**, 2471-2485.

Bi, Z.Q. and Sekerka, R.F.(1998), “Phase-field model of solidification of a binary alloy”, *Physica A*, **261**, 95–106.

Boettinger, W.J., Coriell, S.R., Greer, A.L., Karma, A., Kurz, W., Rappaz, M. and Trivedi, R.(2000), “Solidification microstructures: recent developments, future directions”, *Acta Materialia*, **48**, 43-70.

Boettinger, W.J., Warren, J.A., Beckermann, C. and Karma, A.(2002), “Phase-field simulation of solidification”, *Annual Review of Materials Research*, **32**: p. 163-194.

Boettinger, W.J., Wheeler, A.A., Murray, B.T. and McFadden, G.B.(1994), “Prediction of solute trapping at high solidification rates using a diffuse interface phase-field theory of alloy solidification”, *Materials Science and Engineering A*, **178**, 217–23.

Brody, H.D. and Flemings, M.C.(1966), “Solute redistribution during dendritic solidification”, *Transactions of the Metallurgical Society of AIME*, **236**, 615-624.

Caginalp, G.(1989), “Stefan and Hele-Shaw type models as asymptotic limits of the phase-field equations”, *Physical Review A*, **39**, 5887-5896.

Caginalp, G. and Xie, W.(1993), “Phase-field and sharp-interface alloy models”, *Physical Review E*, **48**, 1897-1909.

Cahn, J.W. and Hilliard, J.E.(1958), “Free energy of a nonuniform system. I. Interfacial energy”, *Journal of Chemical Physics*, **28**, 258-267.

Cha, P.R., Yeon, D.H. and Yoon, J.K.(2001), “A phase field model for isothermal solidification of multicomponent alloys”, *Acta Materialia*, **49**, 3295-3307.

Chen, L., Garimella, S. V., Reizes, J. A. and Leonardi, E.(1997), “Motion of interacting gas bubbles in a viscous liquid including wall effects and evaporation”, *Numerical Heat Transfer, Part A: Applications*, **31**, 629-654.

- Chilton, R.A.(2002), *Experimental Study and Modeling of the Cell/Dendrite Transition*, Ph.D. Thesis, Oxford, University of Oxford.
- Clyne, T.W.(1984), “Numerical treatment of rapid solidification”, *Metallurgical and Materials Transactions B*, **15**, 369-381.
- Clyne, T.W. and Kurz, W.(1981), “Solute redistribution during solidification with rapid solid state diffusion”, *Metallurgical Transactions*, **12A**, 965-971.
- Dantzig, J. A. and Rappaz, M.(2009), *Solidification*, EPFL Press.
- Dilthey, U. and Pivlik, V.(1998), “Numerical simulation of dendrite morphology and grain growth with modified cellular automata”, in *Modeling of Casting, Welding and Advanced Solidification Processes VIII*, edited by Thomas, B.G. and Beckermann, C., TMS, Warrendale, PA, p. 589-596.
- Echebarria, B., Folch, R., Karma, A. and Plapp, M.(2004), “Quantitative phase-field model of alloy solidification”, *Physical Review E*, 2004. **70**(6).
- Flemings, M. C.(1974), *Solidification Processing*, McGraw-Hill.
- Floryan, J.M. and Rasmussen, H.(1989), “Numerical methods for viscous flows with moving boundaries”, *Applied Mechanics Review*, **42**, 323-341.
- Folch, R. and Plapp, M.(2005), “Quantitative phase-field modeling of two-phase growth”, *Physical Review E*, **72**(1).
- Giovanola, B. and Kurz, W.(1986), in *State of the Art Computer Simulation of Casting and Solidification Processes*, edited by Fredriksson, H., pp. 129-135. Les edition de Physique, Paris.

Ginzburg, V.L. and Landau, L.D.(1950), “On the theory of superconductivity”, *J. Exp. Theor. Phys. (USSR)*, **20**, 1064.

Glicksman, M.E. and Koss, M.B.(1994), “Dendritic growth velocities in microgravity”, *Physical Review Letters*, **73**, 573-576.

Glimm, J., Marchesin, D. and McBryan, O.(1981), “A numerical method for two phase flow with an unstable interface”, *Journal of Computational Physics*, **39**, 179-200.

Greer, A. L., Bunn, A. M., Tronche, A., Evans, P. V. and Bristow, D. J.(2000), “Modelling of inoculation of metallic melts: Application to grain refinement of aluminium by Al-Ti-B”, *Acta Materialia*, **48**, 2823.

Jacot, A. and Rappaz, M.(1997), “A two-dimensional diffusion model for the prediction of phase transformations: application to reaustenitisation and homogenisation of hypoeutectoid Fe - C steels”, *Acta Materialia*, **45**, 575-85.

Jacot, A. and Rappaz, M.(2002), “A pseudo-front tracking technique for the modelling of solidification microstructures in multi-component alloys”, *Acta Materialia*, **50**(8), 1909-1926.

Jayaraman, V., Udaykumar, H.S. and Shyy, W.S.(1997), “Adaptive unstructured grid for three-dimensional interface representation”, *Numerical Heat Transfer, Part B: Fundamentals*, **32**, 247-265.

Juric, D. and Tryggvason, G.(1996), “ A front-tracking method for dendritic solidification”, *Journal of Computational Physics*, **123**, 127–148.

Juric, D. and Tryggvason, G.(1998), “Direct numerical simulation of solidification microstructures affected by fluid flow”, in *Modeling of Casting, Welding and Advanced Solidification Processes VIII*, edited by Thomas, B.G. and Beckermann, C., TMS, Warrendale, PA, p. 605.

Karma, A. and Rappel, W.-J.(1996), “Phase-field method for computationally efficient modeling of solidification with arbitrary interface kinetics”, *Physical Review E*, **53**, R3017-R3020.

Karma, A. and Rappel, W.-J.(1998), “Quantitative phase-field modeling of dendritic growth in two and three dimensions”, *Physical Review E*, **57**, 4323-4349.

Kim, S.G., Kim, W.T. and Suzuki, T.(1998), “Interfacial compositions of solid and liquid in a phase-field model with finite interface thickness for isothermal solidification in binary alloys”, *Physical Review E*, **58**, 3316-3323.

Kim, S.G., Kim, W.T. and Suzuki, T.(1999), “Phase-field model for binary alloys”, *Physical Review E*, **60**, 7186-7197.

Kobayashi, R.(1993), “Modeling and numerical simulations of dendritic crystal growth”, *Physica D*, **63**, 410-423.

Koss, M.B., LaCombe, J.C., Tennenhouse, L.A., Glicksman, M.E. and Winsa, E.A.(1999), “Dendritic growth tip velocities and radii of curvature in microgravity”, *Metallurgical and Materials Transactions A*, **30A**, 3177-3190.

Kurz, W. and Esaka, H.(1988), *Solidification microstructures*, *Praktische Metallographie*, **25**(5) 207-13.

Kurz, W. and Fisher, D. J.(1989), *Fundamentals of Solidification*, Trans Tech Publications, Aedermannsdorf, Switzerland, 3rd Ed.

Kurz, W., Giovanola, B. and Trivedi, R.(1986), “Theory of microstructural development during rapid solidification”, *Acta Metall*, **34**, 823-830.

Lafaurie, B., Nardone, C., Scardovelli, R., Zaleski, S. and Zanetti, G.(1994), “Modelling merging and fragmentation in multiphase flows with SURFER”, *Journal of Computational Physics*, **113**, 134-147.

Lan, C.W., Shih, C.J. and Lee, M.H.(2005), “Quantitative phase field simulation of deep cells in directional solidification of an alloy”, *Acta Materialia*, **53**(8), 2285-2294.

Langer, J. S.(1980), *Physicochemical Hydrodynamics*, **1**, 41-49.

Langer, J.S. in: Grinstein, G. and Mazenko, G.(Eds.)(1986), *Directions in Condensed Matter Physics*, World Scientific, Singapore, p. 164.

Li, C.Y., Garimella, S.V. and Simpson, J.E.(2003), “Fixed-grid front-tracking algorithm for solidification problems, part I: method and validation”, *Numerical Heat Transfer, Part B: Fundamentals*, **43**, 117–141.

Lipton, J., Glicksman, M.E. and Kurz, W.(1984), “Dendritic growth into undercooled alloy metals”, *Materials Science and Engineering*, **65**, 57-63.

Losert, W., Stillman, D.A., Cummins, H.Z., Koczynski, P., Rappel, W.J. and Karma, A.(1998), “Selection of doublet cellular patterns in directional solidification through spatially periodic perturbations”, *Physical Review E*, **58**, 7492-7506.

- Löwen, H., Bechhoefer, J. and Tuckerman, L.S.(1992), “Crystal growth at long times: Critical behavior at the crossover from diffusion to kinetics-limited regimes”, *Physical Review A*, **45**, 2399-2415.
- McFadden, G.B., Coriell, S.R, and Sekerka, R.F.(2000), “Effect of surface free energy anisotropy on dendrite tip shape”, *Acta Materialia*, **48**, 3177-3181.
- McFadden, G.B., Wheeler, A.A., Braun, R.J., Coriell, S.R., and Sekerka, R.F.(1993), “Phase-field models for anisotropic interfaces”, *Physical Review E*, **48**, 2016-2024.
- Meiron, D.I.(1986), “Selection of steady-state in the two-dimensional symmetrical model of dendritic growth”, *Physical Review A*, **33**, 2704-2715.
- Nastac, L.(1999), “Numerical modelling of solidification morphologies and segregation patterns in cast dendritic alloys”. *Acta Mater*, **47**, 4253-4262.
- Nobari, M.R.H. and Tryggvason, G.(1996), “Numerical simulations of three-dimensional drop collisions”, *AIAA Journal*, **34**, 750-755.
- Ode, M., Kim, S.G. and Suzuki, T.(2001), “Recent Advances in the Phase-field Model for Solidification”, *ISIJ International*, **41**,1076-1082.
- Oldfield, W.(1966), “A Quantitative Approach to Casting Solidification --Freezing of Cast Iron”, *ASM Trans. Quart.*, **59**, 945-959.
- O’Malley, R.E.(1991), *Singular Perturbation Methods for Ordinary Differential Equations*, Springer, New York.
- Osher, S. and Fedkiw, R.(2003), *Level Set Methods and Dynamic Implicit Surfaces*, Springer, New York.

Patankar, S.V.(1980), *Numerical Heat Transfer and Fluid Flow*, Hemisphere Publishing, Washington, DC.

Penrose, O. and Fife, P.C.(1990), “Thermodynamically consistent models of phase-field type for the kinetics of phase transitions”, *Physica D*, **43**, 44-62.

Rappaz, M., Bellet, M. and Deville, M.(2003), *Numerical Modeling in Materials Science and Engineering*, Springer, Germany.

Rappaz, M. and Gandin, C. A.(1993), “Probabilistic Modelling of Microstructure Formation in Solidification Process”, *Acta Metallurgica et Materialia*, **41**(2), 354-360.

Rebow, M. and Browne, D.J.(2007), “On the dendritic tip stability parameter for aluminium alloy solidification”, *Scripta Materialia*, **56**, 481-484.

Rosam, J. A., Mullis, M. and Jimack, P.K.(2007), “Fully Implicit, Adaptive Grid Methods for Phase-Field Simulation of Solidification in Pure Metals and Alloys”, *Frontiers in Solidification Science*, ed. Hoyt, J., *et al.* TMS.

Rowlinson, J.S. Translation of Van der Waals, J.D.(1979), “The thermodynamic theory of capillarity under the hypothesis of a continuous variation of density”, *Journal of Statistical Physics*, **20**, 197-244.

Saito, Y., Goldbeck-Wood, G. and Müller-Krumbhaar, H.(1988), “Numerical simulation of dendritic growth”, *Physical Review A*, **38**, 2148-2157.

Sethian, J.A.(1996), *Level Set Methods: Evolving Interfaces in Geometry, Fluid mechanics, Computer Vision, and Material science*, Press Syndicate of the University of Cambridge, Cambridge.

Shin, M.R.M.(2001), *Prediction of microsegregation in multi-component alloys*, PhD thesis, University of Oxford.

Sullivan, J. M., Lynch, D. R. and O'Neill, K.(1987), "Finite element simulation of planar instabilities during solidification of an undercooled melt", *Journal of Computational Physics*, **69**, 81-111.

Temkin, D. E.(1962), *Sov. Phys. Crystallogr.*, **7**, 354-357

Thevoz, P., Desbiolles, J. L. and Rappaz, M.(1989), "Modeling of Equiaxed Microstructure Formation in Casting", *Metallurgical and Materials Transactions A*, **20**, 311-322.

Tiaden, J., Nestler, B., Diepers, H.J. and Steinbach, I.(1998,) "The multiphase-field model with an integrated concept for modelling solute diffusion", *Physica D*, **115**, 73-86.

Trivedi, R. and Kurz, W.(1994), "Dendritic growth", *International Materials Review*, **39**(2), 49-74.

Trivedi, R. and Mason, J.T.(1991), "The effect of interface attachment kinetic on solidification interface morphologies", *Metallurgical and Materials Transactions A*, **22**, 235.

Trivedi, R. K. and Tiller, W. A.(1978), "Interface morphology during crystallization, Part II: Unconstrained growth from a binary alloy melt", *Acta Metallurgica*, **26**, 679-687.

Tronche, A. and Greer, A. L.,(2001) “Electron back-scatter diffraction study of inoculation of Al”, *Philosophical Magazine Letters A*, **81**, 321.

Turnbull, D. and Cech, R. E.(1950), “Microscopic observation of the solidification of small metal droplets”, *Journal of Applied Physics*, **21**, 804-810.

Udaykumar, H.S., Shyy, W. and Rao, M.M.(1996), “ELAFINT: A mixed Eulerian-Lagrangian method for fluid flow with complex and moving boundaries”, *International Journal for Numerical Methods in Fluids*, **22**, 691-712; also *AIAA 6th AIAA/ASME Joint Thermophysics and Heat Transfer Conference*, Paper No. 94-1996, June 20-23, (1994), also a shorter version published in the *Proceedings of the 14th International Conference on Numerical Methods in Fluid Dynamics*, Bangalore, India, July (1994).

Unverdi, S.O. and Tryggvason, G.(1992), “A front-tracking method for viscous, incompressible, multi-fluid flows”, *Journal of Computational Physics*, **100**, 25-37.

Van Doormal, J.P. and Raithby, G.D.(1984), “ Enhancements of the simple method for predicting incompressible fluid-flows”, *Numerical Heat Transfer*, **17**, 147–63.

Wang, G.X. and Matthys, E.F.(1992), “Numerical modelling of phase change and heat transfer during rapid solidification processes: use of control volume integrals with element subdivision”, *International Journal of Heat Mass Transfer*, **35**, 141-153.

Wang, S.L. and Sekerka, R.F.(1996), “Computation of the dendritic operating state at large supercoolings by the phase field model”, *Physical Review E*, **53**, 3760-3776.

Wang, S.L., Sekerka, R.F., Wheeler, A.A., Murray, B.T., Coriell, S.R., Braun, R.J. and McFadden, G.B.(1993), “Thermodynamically-consistent phase-field models for solidification”, *Physica D*, **69**, 189-200.

Warren, J.A. and Boettinger, W.J.(1995), "Prediction of dendritic growth and microsegregation patterns in a binary alloy using the phase-field method", *Acta Metallurgica et Materialia*, **43**(2),689-703.

Wheeler, A.A., Ahmad, N.A., Boettinger, W.J., Braun, R.J., MacFadden, G.B. and Murray, B.T.(1995), "Recent Developments in Phase-Field Models of Solidification", *Advances in Space Research*, **16**, 163-172.

Wheeler, A.A., Boettinger, W.J. and McFadden, G.B.(1992), "Phase-field model for isothermal phase transitions in binary alloys", *Physical Review A*, **45**, 7424-7439.

Wheeler, A.A., Boettinger, W.J., and McFadden, G.B.(1993), "Phase-field model of solute trapping during solidification", *Physical Review E*, **47**, 1893-1909.

Wheeler, A.A., McFadden, G.B., and Boettinger, W.J.(1996), "Phase-field model for solidification of a eutectic alloy", *Proceedings of the Royal Society [London] Series A* 452: 495-525.

Yeoh, G.J., de Vahl Davis, G., Leonardi, E., de Groh, H.C. and Yao, M.(1992), "A numerical and experimental study of natural convection and interface shape in crystal growth", *First International Conference Transport Phenomena in Processing*, Honolulu, Hawaii.

Zabaras, N. and Tan, L.(2006), "A level set simulation of dendritic solidification with combined features of front-tracking and fixed-domain methods", *Journal of Computational Physics*, **211**(1), 36-63.

Zhang, X. and Atrens, A.(1992), “A Thermokinetic model for rapid solidification”, *International Journal of Rapid Solidification*, **7**, 83-107.

Zhao, P. and Heinrich, J.C.(2001), “Front-tracking finite element method for dendritic solidification”, *Journal of Computational Physics*, **173**, 765-796.

Zhao, P. and Heinrich, J.C.(2002), “Approximation to the interface velocity in phase change front tracking”, *Communications in Numerical Methods in Engineering*, **18**, 77-88.

Zhao, P., Venere, M., Heinrich, J.C. and Poirier, D.R.(2003), “Modeling dendritic growth of a binary alloy”, *Journal of Computational Physics*, **188**, 434-461.

Zhu, J.Z., Wang, T., Zhou, S.H., Liu, Z.K. and Chen, L.Q.(2004), “Quantitative interface models for simulating microstructure evolution”, *Acta Materialia*, **52**(4), 833-840.

Zhu, M. F. and Stefanescu, D. M.(2006), “Growth of solutal dendrites- a quantitative front tracking model”, in *Modeling of Casting, Welding and Advanced Solidification Processes-XI*, edited by Gandin, C. A. and Bellet, M., TMS.

Zhu, M.F. and Stefanescu, D.M.(2007), “Virtual front tracking model for the quantitative modelling of dendritic growth in solidification of alloys”, *Acta Materialia*, **55**, 1741–1755